THE UNIVERSITY *of* EDINBURGH

Climate and vegetation effects on sediment transport and catchment properties along an arid to humid climatic gradient

Lynsey Elizabeth Callaghan

PhD

The University of Edinburgh

School of Geosciences

College of Science & Engineering

2012

Contents

DECLARATION

This thesis is the result of four and a half years work. The work presented herein is my own; where work has been published or submitted for publication, authorship and contributions have been noted accordingly. This thesis has not been submitted for any other degree or professional qualification.

Lynsey E. Callaghan

ACKNOWLEDGEMENTS

First and foremost, I would like to thank my supervisors, Tibor Dunai and Simon Mudd, for their supervision of my research, in particular for their input and guidance but also for their patience and encouragement over the course of the past several years. I would also like to thank Francis Mayle for his supervisory input, especially for his expertise and assistance during fieldwork in Chile, for his assistance in compiling early thesis chapters and for his reviews of later chapters. Thanks are also due to the following people: Steve Binnie, whose help with fieldwork and lab work in the early stages of my project was invaluable; Rachel Walcott, who was always ready and willing to offer advice and feedback; Guadalupe Buceta, who provided assistance and companionship during the second stint of fieldwork in Chile; and Gabriel Gonzalez of the Universidad Catolica del Norte in Antofagasta, who provided logistical support during fieldwork. Many thanks are due to Elaine McDougall, who provided endless support in the lab and without whom the task of processing samples for cosmogenic analyses would have been long and probably a lot less fun. I would also like to thank several people within the School of Geosciences in Edinburgh who have helped me in many large and small ways throughout the course of the project: Kate Briggs, Andy Hein, Joe Hagg, Martin Hurst, Shiela Wilson, Helena Sim, Chris Place and Caroline Keir.

I was supported in this project by a NERC PhD Scholarship, and would also like to extend my gratitude to the AMS facility at the Scottish Universities Environmental Research Centre (SUERC), for the vital services and support they provided throughout the course of the project and for the additional AMS beam-time supported by Consortium funding. Particular thanks are due to Sheng Xu and Fin Stuart. On a personal note, I would like to thank my parents for their support, financial, practical and emotional, throughout the course of my doctoral studies. I would also like to acknowledge the support of friends who have been there throughout this process and have kept me going; they are too numerous to mention one by one, but thanks go especially to Lynsey Smyth, Marcy Barnes, Sandy Gill, Bomina Yu, Rachel McDermott and Jonathan Todman. Finally, I would like to thank my examiners, Michael Summerfield and Adrian Hartley.

ABSTRACT

Recent attempts to elucidate a climatic effect on erosion rates at the catchment scale have generally found little or no correlation between precipitation and erosion rates, yet climate has been shown to exert a significant control on landscape properties such as drainage density, slope and relief. That erosion rates to do not directly reflect climatic conditions may not come as a surprise, since erosion rates will tend to keep pace with uplift rates in a tectonically active landscape. The interplay between erosion rates and climate may therefore be better understood with reference to the erosional efficiency of the landscape. Erosional efficiency governs how steep the landscape must become to balance uplift rates, and has also recently been postulated to affect the width to length (or spacing) ratio of first order basins, and the distribution of hillslopes within a landscape, via the relative inputs of diffusive and advective transport. This study constrains the efficiency of sediment transport along a climatic transect spanning a precipitation range of over two orders of magnitude in the Chilean Coastal Cordillera (26˚-41˚S), combining long-term erosion rates derived from concentrations of cosmogenic Be-10 in quartz in fluvial sediments with topographic metrics. The effects of changes in the relative input of diffusive and advective processes is investigated by studying the basin spacing ratios and distribution of hillslopes for a variety of natural landscapes and landscapes generated using the CHILD model. Sediment transport efficiency was found to peak at the transition between arid and semiarid climates, where herbaceous vegetation has almost entirely replaced bare ground, and to level off as climate becomes more humid, providing a background sediment transport efficiency value which will be

applicable in both semi-arid and humid landscapes. Basin spacing ratios in natural landscapes show little variation along the transect, suggesting that changes in climate have little effect on this apparently universal catchment property, although maximum basin length attained appears to be linked to sediment transport efficiency. Slopes are consistently lower in the southern region where vegetation and sediment transport efficiency are uniform; here, lower slopes are maintained despite relatively high erosion rates thanks to higher sediment transport efficiency than in the north. Results from the CHILD landscapes show an increase in width to length ratio with decreasing sediment transport efficiency; this relationship is at odds with both the data from the study area and with data from previous studies. Results therefore indicate that, in natural landscapes, climate and vegetation cover exert a first order control on sediment transport efficiency. While climate and vegetation play little or no part in controlling the ratio of catchment dimensions, they may exert some control on the maximum dimensions of catchments and may help to modify the distribution of mean basin slope via their effects on hillslope processes.

1. INTRODUCTION

The correlation between erosion rates and climate, primarily precipitation, has been the subject of much debate. A seminal paper by Langbein & Schumm (1958) hypothesised that erosion rates should be positively correlated with precipitation in arid regions, peaking and becoming negatively correlated with the appearance of landscape-stabilising grasslands. Since then, many authors have sought to prove or disprove this theory, with conflicting results. The emergence of the use of cosmogenic radionuclide (CRN) techniques (see Chapter 4) to calculate catchment averaged erosion rates has allowed comparison of climate metrics with erosion rates on timescales relevant to landscape evolution processes. Yet, despite clear evidence linking climate with sediment transport both directly and indirectly via climatic effects on vegetation at the hillslope scale (see Chapter 2 for a detailed discussion), and qualitative links between large scale variations in relief or hypsometry and climate (e.g. McElroy & Wilkinson, 2005; Montgomery *et al*, 2001), no correlation between precipitation and erosion rates has been found in recent CRN studies (e.g. Riebe *et al*, 2001; von Blanckenburg, 2005). Climate has also been shown to have no effect on the overall geometry of basins, with several authors documenting a striking regularity in the ratio of basin length to width across a diverse range of climatic and tectonic regimes (e.g. Hovius, 1996; Talling *et al*, 1997; Walcott & Summerfield, 2009), yet recent studies (Perron *et al*, 2008; Perron *et al*, 2009) suggest that both the ratio of basin width to length and the spacing of valleys should be affected by the

relative inputs of diffusive and advective transport, which should in turn be affected by changes in climate and vegetation cover.

Crucial to the understanding of how climate and vegetation affect landscapes is the concept of sediment transport efficiency. If a landscape has been uplifting for long enough, at a relatively constant rate, erosion rates will match uplift rates and therefore will not reflect any climatic influence. Instead, topography will steepen to match uplift rates, and the steepness of slopes will tend to be a reflection of how efficient the landscape is at transporting sediment, with more efficient sediment transport producing gentler slopes at a given erosion rate. Typically, slopes have been used as a metric for erosion rates, with a positive correlation between catchment-mean hillslope and erosion rate proposed by most authors (e.g. Ahnert, 1970; DiBiase *et al*, 2010; Binnie *et al*, 2007), but where uplift is spatially and temporally uniform, the influence of climate, via its influence on sediment transport efficiency, should be seen in the topographic form of the landscape.

Recently, Roering *et al* (2007) recognised that hillslope steepness and relief are governed by both erosion rates and sediment transport efficiency, and their analytical relationship provides the basis for a novel approach which allows for the calculation of sediment transport efficiency based on several parameters which can be calculated independently. While we may not expect to see any relationship between precipitation and erosion, it seems intuitive that sediment transport efficiency should be affected by precipitation in much the same way as that predicted by Langbein & Schumm (1958) for sediment yield and precipitation.

Of course, the landscape is shaped not only by processes on hillslopes (diffusive processes, equivalent to the sediment transport efficiency), but also by the relative input of advective processes. Evidence suggests that the interplay of these two competing sets of processes will affect the ratio of basin width to length (Perron *et al,* 2008); since the diffusivity of landscapes can be constrained independently, it should therefore be possible to make some assertions about the changes in advective processes with climate from any changes in basin spacing ratio.

In addition to studying the competing effects of diffusive and advective transport via their effects on basin spacing ratio, it should also be possible to distinguish changes in competing modes of hillslope processes with climate. The distribution of mean slopes can provide information about whether the terrain is erosional or depositional (e.g. Montgomery *et al*, 2001; Burbank, 1992; Burbank *et al*, 1996) and has also been shown to reflect relative inputs of slope failure processes versus creep or wash processes (e.g. Wolinsky & Pratson, 2005). In particular, Wolinsky & Pratson (2005) describe a process-based model which incorporates a diffusivity term and determines the skewness of slope distributions, suggesting that it should be possible to trace changes in slope distribution with changing climate.

Although previous studies have covered a wide range of climatic conditions, there is still a lack of a dataset covering a continuous transition from hyperarid to humid conditions, accompanied by concomitant changes in vegetation cover and type. The Chilean Coastal Cordillera encompasses such dramatic changes in climate and vegetation, and yet has experienced relatively uniform uplift along its entirety, providing the perfect location to untangle the effects of climate on sediment transport and catchment morphology from the effects of tectonics and topography. In order to

make predictions about how future climate will affect sediment transport processes, it is crucial to understand how changes in climate can modulate sediment transport efficiency, and how this parameter relates to drainage basin morphology. This is particularly important in areas where vegetation cover is at a critical level and small changes in climate could lead to destruction or creation of vegetation cover, potentially causing significant changes in sediment yield. This study represents the first attempt to constrain sediment transport efficiency at a regional scale (Chapter 5) and to understand how this parameter can affect, or be reflected in, topographic features of a landscape (Chapters 6 & 7).

2. CLIMATE, SOILS, VEGETATION AND EROSIONAL PROCESSES

2.1 INTRODUCTION

While it seems intuitive that increased precipitation should lead to increased runoff and erosion, this relationship is complicated by other factors, including the presence of vegetation and its pattern, topography, lithology, and the spatial and temporal scale of observation. Work at the plot and hillslope scale has generally found a positive correlation between both vegetation cover and erosion and between precipitation and erosion (e.g. Langbein & Schumm, 1958; Istanbulluoglu & Bras, 2006; Lavee *et al,* 1998; Cerdá, 1997; Puigdefábregas, 2005; Gyssels *et al,* 2005). Continent-scale variations in topography in South America also appear to be qualitatively linked to variations in precipitation (McElroy & Wilkinson, 2005; Montgomery *et al,* 2001; Hebbeln *et al,* 2007). However, recent studies of the relationship between precipitation and erosion at the catchment scale have proven inconclusive, with many authors rejecting any relationship between precipitation and denudation (e.g. Riebe *et al,* 2001; 2003; 2004a; 2004b; von Blanckenburg, 2006; see figure 2.1). In much of this work there has been a tendency to use oversimplified climatic indicators, and while some authors acknowledge the crucial effect of vegetation as a function of climate, temperature and precipitation have generally been used as sole indicators of climatic conditions. Both long-term climate and short-term climatic variability affect sediment yield; erosional response to climatic variability is dynamic and does not depend solely on temperature and precipitation (Mulligan, 1998; Istanbulluoglu & Bras, 2006). In order to fully understand the

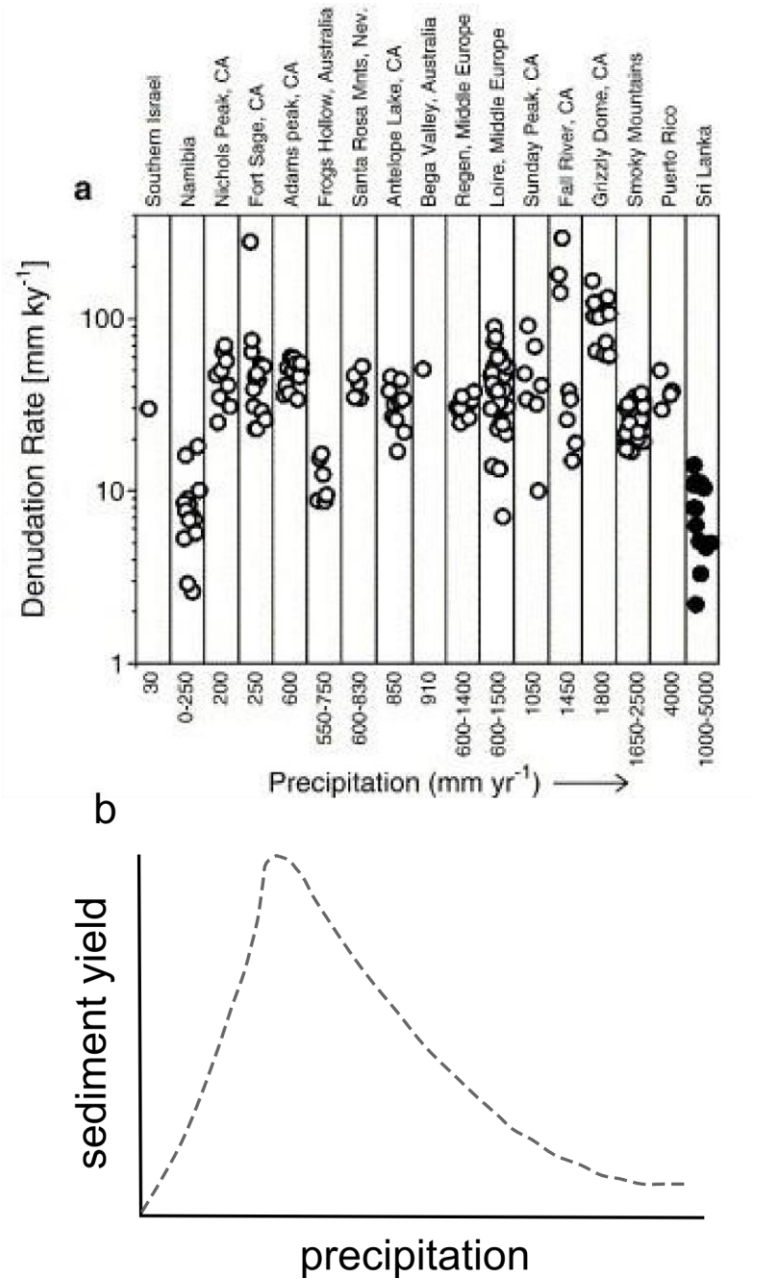

Figure 2.1: Illustration of relationship between erosion/sediment yield and precipitation found in previous studies. a) Results of previous catchment-scale studies, from von Blanckenburg, 2006. b) The measured relationship between sediment yield and effective precipitation, simplified from Langbein & Schumm, 1958.

interaction between climate and erosion, it is essential to document the ways in which climatic variability alters ecosystem function, particularly in regions where climates are more extreme and vegetation cover is at a critical threshold. Since erosion rates will change to reflect uplift rates, it may not even be expected that

erosion rates will provide any indication of climatic conditions. Instead, the effects of climate may be reflected more directly in the steepness of hillslopes, which is governed by the efficiency of sediment transport in the landscape, which is in turn directly affected by climate and vegetation. In particular, studies have suggested that the relative input of diffusive and advective sediment transport processes, and the interaction of competing modes of hillslope transport, can have an effect on basin morphology (e.g. Wolinsky & Pratson, 2005; Perron *et al*, 2008; Perron *et al*, 2009). Sediment transport in channels and on hillslopes can be affected by changes in climate and vegetation, and when the vegetation cover is heterogeneous it can have significant effects on generation of runoff, which will affect both hillslope and channel processes. Climate has also been found to affect the topographic threshold for channelization (Montgomery & Dietrich, 1992). It is therefore clear that while climate and vegetation may not have a discernible effect on erosion rates, they must certainly have an effect on sediment transport and thus in the shaping of landscapes. It is therefore crucial to understand how changes in climate may affect changes in type and cover of vegetation at the regional scale.

Differences in threshold values to be surpassed for runoff generation at different scales could explain the differences between plot scale and catchment scale relationships as discussed above. For example, Cammeraat *et al* (2004) argue that only rare events are likely to produce broad-scale changes, where reaching a geomorphic threshold can cause landscape change, and that these broad-scale changes can be further altered by fine-scale changes over time, with different processes and variables dominating at different scales. Conversely, Vanacker *et al*

(2007) derived a negative exponential relationship between sediment yield and increasing surface cover, indicating a strong control of vegetation cover on soil erosion rates at the catchment scale, a relationship similar to that measured by other authors (Gyssels *et* al, 2005) at the plot scale. These similarities indicate the general character of the exponential decrease of sediment yield with increasing surface cover, regardless of both spatial and temporal scale. Although these studies are primarily concerned with the relationship between vegetation cover and erosion rates, the strong links between precipitation amount and frequency and vegetation cover (as discussed below), particularly in arid and semiarid climates, makes this evidence important.

In an attempt to link processes at different scales and understand the impact of climate change on ecosystem degradation, Imeson & Lavee (1998) studied geo-ecological processes along climatological transects. They concluded that, as temporal and spatial scales change, so does the relative significance of different processes. With increasing spatial scale, the periods of time between the largest sediment transfer events increases, and the most important erosion processes emerge at coarser scales, with thresholds and discontinuities occurring as a result of vegetation-soil interactions, human interaction and the evolution of the system under study. Braud *et al* (2001) also found a decrease in runoff coefficients and increase in rainfall thresholds with increasing catchment size in the Argentinian Andes.

2.2 CLIMATIC EFFECTS ON VEGETATION COVER

Vegetation is important in controlling erosion because it controls the ability of the soil to absorb water and decreases rainsplash erosion, and because root fixation can help slow erosion. In the absence of vegetation, infiltration will decrease and precipitation will instead be converted to runoff. Vegetation can respond to climate via changes in its distribution, cover, structure and physiology and its response to climatic forcing will vary for different functional types of plant (Mulligan, 1998). Environmental change in arid and semiarid areas is largely controlled by unpredictable precipitation events which are both infrequent and discrete (Bertiller *et al*, 1995). Sediment transport is greater for bare soil, as there is no shear stress loss to vegetation roughness, and with increased precipitation allowing for development of grass cover, evapotranspiration increases rapidly, leading to a reduction in runoff and sediment transport (Istanbulluoglu & Bras, 2006). With increasing aridity and decreasing vegetation cover, enhanced evaporation and high soil temperatures on bare ground can negatively affect plant growth (e.g. Rietkerk *et al*, 2002; Rietkerk *et al*, 2004). Vegetation improves the structural and hydrological properties of soils, protecting soil against erosion by wind and water, and holding in nutrients leading to a subsequent increase in plant density because of feedback mechanisms (Rietkerk & van de Koppel, 1997), which leads to the formation of two-phase mosaics in response to water-limited conditions.

Abundant evidence exists for the control of erosion not just by total vegetation cover but also by the distribution of the vegetation present. Vegetation density is controlled

by water and resource availability, whereas its spatial configuration is tuned to storm time patterns and abiotic controls such as topography and soil properties (Puigdefábregas, 2005). Field studies (e.g. Bautista *et al*, 2007) provide evidence of the importance in plant spatial cover and functional diversity in controlling the hydrological functioning of arid-semiarid lands. Modelling studies (e.g., Tongway, 1994) relate vegetation pattern and cover to longer term, average climatic conditions, representing a sort of equilibrium between water availability and vegetation patterning and density. Total vegetation cover and vegetation pattern can be linked to climatic variables, particularly precipitation amount and seasonality, indicating the importance of vegetation in regulating erosional response in arid and semi-arid environments where there may exist a threshold between different controls of erosion, such as the changes from biotic and abiotic control as noted by Ewing *et al* (2006) at the hyperarid-arid transition and by Langbein & Schumm (1958) at the transition from shrublands to grasslands.

Ecosystems can be considered to undergo transition through a sequence of patterns of various forms as rainfall decreases, from continuous cover to gaps, to labyrinths or stripes, and finally to spots, with a catastrophic shift to the bare state if rainfall is decreased beyond a certain threshold (Rietkerk *et al*, 2004). Aguiar & Sala (1999) suggest that there is a critical precipitation threshold (250mm/yr) below which patterns cannot form in a homogeneous landscape, and that below this threshold heterogeneities in the landscape allow for redistribution of resources into the two-phase mosaic to allow vegetation production to occur. Similarly, Buis *et al* (2008) note the formation of regular patterns only in homogeneous semiarid catchments, and

irregular patterns in heterogeneous arid catchments, and suggest that the formation of patterns is governed by sets of scale-dependent processes and structures - in drier areas the position of vegetation is governed by water redistribution which is in turned governed by landscape structure. Several studies have addressed the variation in both plant cover and plant structural type along a precipitation gradient. Bertiller *et al* (1995) describe a steady decrease in grass cover and increase in shrub cover with increasing aridity along a precipitation gradient in western Patagonia. Along a climatic transect in the Negev Desert of Israel, vegetation cover decreases as biotic controls become less important with increasing aridity, with herbaceous plants more common in wetter catchments (Buis *et al,* 2008). Evidence also suggests that for a given climatic condition, the spatial distribution of plant cover may be more sensitive to disturbance or degradation than total vegetation cover (Bautista *et al,* 2007). Modelling results suggest that as climate becomes more arid, vegetation cover can be maximised with a more variable rainfall regime as only large magnitude storms can sustain soil moisture conditions which lead to vegetation development, although grass cover generally increases with humidity regardless of storm frequency (Istanbulluoglu & Bras, 2006). In Australian savanna ecosystems, fine scale vegetation patches have been seen to decrease in size and cover with increasing rainfall, where the cover of patches is negatively correlated to tree canopy cover - with higher rainfall, the size and spacing of ground layer patches is controlled by the tree layer, the effect of which decreases with increasing rainfall (Ludwig *et al,* 1999). Patterned chenopod shrublands in New South Wales, Australia, have been demonstrated to be at least Holocene in age, suggesting that vegetation patterning can be an enduring component in arid environments (Dunkerley & Brown, 1995).

Relationships between annual precipitation and vegetation type and cover are not always simple and may involve other factors such as micro-topography, aspect and soil depth, although many of these additional factors are also tied in with the water balance (Bertiller *et al,* 1995). Aspect, for example, has been demonstrated to have a profound effect on vegetation structure in Mediterranean-type ecosystems, and aspect controls of vegetation contrasts are especially great in the mid-latitudes (Wilkinson & Humphreys, 2006). Armesto & Martínez (1978) reported differences in vegetation structure between north-facing xeric slopes and south-facing mesic slopes in the Mediterranean region of Chile, with higher numbers of evergreen species and larger plant dimensions on south-facing slopes compared to the open scrub vegetation found on north-facing slopes. Patch sizes on south-facing slopes have also been seen to be larger than those on north-facing slopes (Aguiar & Sala, 1999). Badano *et al* (2005) also report plant patterns affected by aspect in the Chilean matorral. Slope aspect influences mesoclimatic conditions and species richness is higher on xeric slopes, perhaps because the importance of competition decreases in stressful environments (Badano *et al,* 2005). Slope gradient can also affect the shape and scale of vegetation patterns as a result of spatial self-organisation caused by the net displacement of surface water to vegetated patches where water infiltration rates are higher (Rietkerk *et al,* 2002).

The emergence of vegetation patterns can be described with reference to local positive interactions, which can induce vegetation patchiness and determine the response of patchiness to environmental change (Kefi *et al,* 2007, Sherratt & Lord,

2007). Vegetation patches are found over a wide range of size scales in the Kalahari, with many small patches and relatively few larger ones. Cluster size of vegetation can be described by a power law distribution (Kefi *et al,* 2007; Scanlon *et al,* 2007), the scaling exponents of which persist over a range of climatic conditions, suggesting that a universal mechanism underlies the organisation of all Mediterranean ecosystems. The power law distribution itself is indicative of self-organisation (Scanlon *et al,* 2007) and comparison of vegetation patterns observed in the field with statistical patterns generated by a cellular automata model indicate that local feedback mechanisms can result in the patterns observed without entailing threshold behaviour such as that invoked in discussions of bistability in such ecosystems (Rietkerk *et al,* 2004; Sherratt & Lord, 2007). Scheffer & Carpenter (2003) suggest that although there may be a local tendency to alternative stable states in water-limited ecosystems, these will be smoothed out at larger scales. While Kefi *et al* (2007) and Scanlon *et al* (2007) imposed a global constraint on spatial coverage of vegetation, Manor & Shnerb (2008) modelled perennial vegetation patchiness and found that this imposed parameter emerged anyway as a result of different rainfall values in their model, such that water competition leads to mutual facilitation and a scale-free distribution of vegetation, whereas in the model of Scanlon *et al* (2007) the power law distribution is only applicable up to a particular length scale.

Initial conditions also play a part in how an ecosystem will respond to changes in external conditions. Under either arid or humid conditions, the vegetation cover is unaffected by small changes in external conditions, but in semiarid conditions even very small changes in rainfall can produce considerable changes in vegetation cover,

to which the landscape responds (Carson & Kirkby, 1972). Herbaceous vegetation in particular is highly sensitive to amount of rainfall (Van de Koppel *et al*, 1997).

2.3 CONTINENT-SCALE STUDIES

McElroy & Wilkinson (2005) used the latitudinal gradient as a proxy for first order changes in temperature and precipitation and found that land surface slope covaries with latitude, such that steeper slopes are generally found at higher latitudes, and attribute this distribution to changes dependent on climate. They also found that maximum elevations attained on the continents generally decreases polewards. Similarly, Montgomery *et al* (2001) suggest that climatically influenced gradients in erosion rates contribute to latitudinal variation in range width and crustal volume in the Andes, and that non-uniform erosion due to large-scale climate pattern is a first-order control on the topographic evolution of the Andes. They illustrate a distinct contrast in hypsometric profiles along the length of the Andes, with concave-up profiles indicative of fluvially dissected landscapes in the northern Andes, convex profiles indicative of a weakly incised tectonic wedge in the central Andes (where low precipitation may limit erosion) and a concave-up profile with evidence of selective erosion at higher elevations reflecting glacial erosion in the southern Andes. Hebbeln et al (2007) note the existence of a long-standing, pronounced latitudinal precipitation gradient in the Andes, and consider this a determining factor in driving changes in erosion with latitude.

2.4 LANDSCAPE SCALE AND CATCHMENT SCALE

Many recent studies on the effects of climate on erosion at the catchment scale have focussed on the use of catchment-averaged denudation rates derived from cosmogenic nuclide techniques. While cosmogenic nuclide-derived erosion rates incorporate both mechanical and chemical denudation, a combination of cosmogenic nuclide and geochemical mass balance methods can be used to disentangle rates of chemical weathering and denudation in catchments. Riebe *et al* (2003) used this method for a study in Rio Icacos, Puerto Rico, and found a tight coupling of chemical weathering and erosion rates, a result also found by von Blanckenburg (2006), and Riebe *et al* (2004a). Riebe *et al* (2004a) produced a series of plots to determine whether a correlation exists between precipitation, temperature and denudation and the chemical depletion fractions (CDF) and chemical weathering rates, while Riebe *et al* (2004b) plotted altitude (and consequently mean annual temperature) against CDF, denudation rate and chemical weathering rate. Riebe *et al* (2004b) found that chemical weathering rates decreased rapidly with increasing altitude (interpreted to indicate increasing effect of physical erosion with altitude), at a greater rate than predicted by weathering kinetics. The authors interpret this to be an indication that weathering rates at higher altitudes may also be affected by the progressive decline in vegetation and increasing snow depth. This can be interpreted to reflect a threshold altitude above which changes in temperature, vegetation and snow cover could work together to enhance physical erosion at the expense of chemical weathering. The authors indicate that this threshold could vary in different mountain ranges depending on latitude, local vegetation distribution and topographic

factors (e.g. rain shadow effects, orientations relative to prevailing storm patterns, etc.). While Riebe *et al* (2004b) consider this change as a function of altitude, the relationship could also be considered in terms of climatic variability and associated changes in vegetation assemblages, and could therefore be extended to apply to different climatic settings.

Riebe *et al* (2001) plotted average precipitation and mean annual temperature against erosion rate, and found that erosion rates vary by a factor of 2.5 across their sites (which have a temperature range of 11ºC and an 8-fold range in average precipitation), and conclude that this smaller-than-expected variation in erosion rates indicates that climate is a weak regulator of erosion rates across their sites, results which are also reported by Kirchner *et al* (2001). Von Blanckenburg (2006) compiled a worldwide dataset of spatially averaged denudation rates calculated using cosmogenic methods, finding no obvious relationship between precipitation or mean annual temperature and total denudation, and thus providing support to some of the results discussed above from studies by Riebe *et al* (2001). In these studies, relationships are determined solely by plotting erosion and weathering (and weathering indicators) against temperature and precipitation, and the results are therefore subject to some limitations, namely that the methods do not take into account factors such as vegetation effects, seasonality of precipitation and evapotranspiration ratios, all of which may affect long-term erosion rates.

Whipple *et al* (1999) state that in tectonically active mountain belts, uplift of peaks and ridges in response to climate change is likely to be minimal, and that an increase

in erosivity of the fluvial system would instead lead to a reduction in relief of both the trunk stream and tributary. Similarly, Montgomery & Brandon (2002) describe a non-linear relationship between long-term erosion rates and mean slope for the Olympic Mountains, and results of a global analysis suggest that erosion rates adjust to high rates of tectonic uplift.

Dedkov & Moszherin (1992) carried out a comparative assessment of erosion intensity (based on suspended sediment yield) in mountain regions of the world, and state that erosion depends on climate and runoff, landscape character, relief, and recent tectonic activity and underlying geology. They consider climate to influence erosion processes via runoff and degree of surface vegetation cover, and note that the greatest mechanical denudation rates (outwith glacial and subnival zones) occurs in the subtropical Mediterranean zone, where runoff is considerable due to limited protection of soils by vegetation.

Yair & Kossovsky (2002) studied the climate and surface properties of small arid and semiarid watersheds in Israel with annual precipitation of 100-300mm/yr and found that changes along the climatic gradient were not limited to purely climatic factors, suggesting that runoff generation and rate in arid and semiarid areas is primarily controlled by surface properties rather than absolute amounts of storm or annual rainfall such that the same regional climatic change could have opposite effects on the hydrological response of adjoining surface units. Although the authors generally agree with the results of Langbein & Schumm (1958), they note that the situation is complicated in arid and semiarid areas where rapid alteration of surface properties

(e.g. the extent of rocky cover, and the porosity and absorbing capacity of the soil) can occur, and that surface properties are only indirectly linked to climate in these areas.

Experimental modelling of landscape response to climate changes (Bonnet & Crave, 2003) suggests that changing rainfall while keeping uplift constant will lead to a change in mean elevation as the landscape adjusts to a new steady state: increasing rainfall will induce an increase in denudation rate resulting from a combination of high inherited topography and high rainfall, leading to a lower mean elevation, while decreasing precipitation will lead to climatically-induced uplift and higher mean elevations. However, the experiments do not reproduce all the erosional processes, and ignore vegetation effects and natural feedbacks, merely demonstrating that climatic forcing can have the same effects on geomorphic systems as tectonic forcing. As with the studies by Riebe *et al*, the study modelled geomorphological/erosion responses to only certain climatic variables (rainfall, in this case), and the authors note that their results are only valid if they do not consider the effect of vegetation development with climate.

Langbein & Schumm (1958) studied the relationship between mean annual sediment yields and annual precipitation on decadal timescales using sediment yield data from gauging stations and reservoirs. This study provided empirical evidence for an important relationship between sediment yield and precipitation, namely that sediment yield increases with precipitation to ~300mm/yr, after which it begins to tail off. The turning point can be related to a transition from shrubland to grassland,

and a concomitant increase in evapotranspiration and reduction in runoff, highlighting the importance of vegetation in controlling erosion. These results are replicated by model simulations (e.g. Istanbulluoglu & Bras, 2006) which suggest that the interplay between vegetation and precipitation control of erosion changes with mean annual precipitation: with low precipitation, vegetation cover is minimal and sediment transport is controlled directly by climate; with vegetation increasingly favoured as annual precipitation becomes greater, climatic forcing and vegetation growth contribute to control of sediment yields; and where precipitation is abundant and vegetation growth is no longer limited by water availability sediment transport potential is again dominated by climatic forcing.

Indirect evidence of climatic control on erosion rates at the catchment scale can be garnered from studies of how vegetation cover and distribution (which are directly controlled by climate, primarily precipitation) affect erosion and sediment yields. Vanacker *et al* (2007) and Molina *et al* (2008) provided evidence to show that vegetation cover exerts a first order control over present day erosion rates at the catchment scale, with fractional vegetation cover explaining 57% of the variance in sediment yield in their study. Comparison of catchment-averaged denudation rates from cosmogenic nuclide methods with modern-day sediment yields from reservoir sedimentation rates and classification and percentage cover of vegetation reveals a decrease in average sediment yields with increasing fractional vegetation cover (Vanacker *et al*, 2007; Molina *et al*, 2008). The cosmogenic-derived denudation rates reflect the natural benchmark erosion rates, and the authors found that where vegetation cover was high, modern sediment yields were very similar to the natural

benchmark, suggesting that vegetation cover can reduce erosion rates to near-natural levels, regardless of whether the vegetation is native or anthropogenic. Bautista *et al* (2007) measured runoff and sediment yield at the hillslope scale, and found an inverse relationship between patch density and runoff, with increasing runoff and sediment yield as the spatial pattern of vegetation became coarser. Fine-grained vegetation patterns are more efficient at trapping water and sediment flux than coarser patterns, and hillslopes with clumpy distributions of vegetation yield more water and sediment than those with uniform distribution of vegetation.

Modelling studies also provide some insight into processes operating at the catchment scale, both in terms of the role of mean annual rainfall and of the role of rainfall variability. Tucker & Bras (2000) published model simulation results which suggest that catchments which undergo a shift to more variable climatic conditions will tend to have an increased sediment transport capacity and thus higher erosion rates, higher drainage density and lower relief. Model simulations also suggest differences between the response to climatic variability (or vegetation disturbance) in different ecosystems. Collins & Bras (2008) presented results which suggest that if climate abruptly becomes wetter, arid landscapes will produce most sediment, but semiarid landscapes will also produce significant sediment because of a high proportional increase in runoff in areas of runoff-limited erosion and in these areas changes in rainfall will play their greatest role in modulating runoff via the effects of rainfall on vegetation. Many models rely on a dynamically generated vegetation cover, where changes in climate can affect geomorphic processes indirectly through changes in vegetation (Kirkby, 1995).

2.5 HILLSLOPE AND PLOT SCALE

In order to understand the processes operating in arid and semiarid regions, it is important to make a distinction between the processes operating in arid and humid regions. In arid ecogeomorphic systems, processes are dominated by abiotic factors, in contrast to the strongly biotic control evident in humid regions (Lavee *et* al, 1998). In arid and semiarid climates, sediment transport is directly controlled by climate, and rainfall is particularly important as it exerts a dominant control on the most important geomorphic processes and causes changes in soil organic matter content, soluble soil content and aggregate stability. As vegetation cover increases, sediment transport decreases, and runoff and sediment transport are controlled by the interaction of climatic forcing versus vegetation growth. Model simulation results presented by Istanbulluoglu & Bras (2006) reproduce the sediment transport versus mean annual precipitation curve of Langbein & Schumm (1958), which indicates that sediment yield in arid and semiarid climates will increase with increasing precipitation, to a maximum of approximately 300mm/yr, after which sediment yield declines with increasing precipitation. Langbein & Schumm (1958) link this peak in sediment transport potential to the transition from shrubland to grassland, subsequently reducing runoff and rainsplash erosion, both of which are important erosion processes in arid and semi-arid climates. Istanbulluoglu & Bras (2006) extend this concept and suggest that in arid and semiarid climates with sparse or no vegetation, sediment transport is directly controlled by climate, generating erosive runoff. As vegetation is favoured by growing precipitation, sediment transport diminishes abruptly because of a reduction in both runoff and sediment transport. With precipitation amounts of more than 1000mm/year, vegetation growth is no

longer water-limited and sediment transport is again controlled by climate (see figure 2.2).

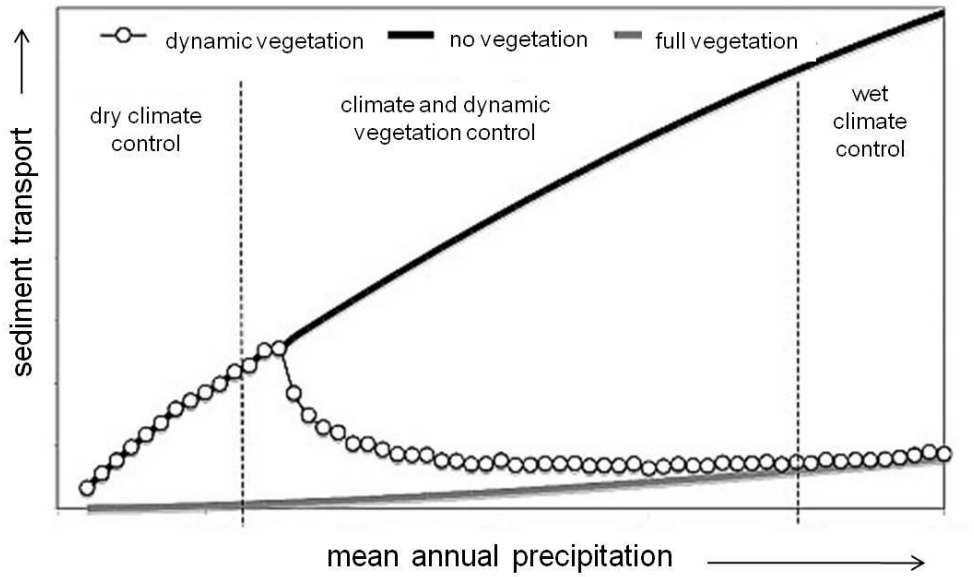

Figure 2.2: Results of modelling studies illustrating changes in controls of sediment transport with increasing mean annual precipitation. The 'dynamic vegetation' scenario replicates the results of Langbein & Schumm (1958). Adapted from Istanbulluoglu & Bras (2006).

Changes in vegetation and soil properties under different climatic conditions are important in governing erosion and sediment yield. Under a moderate to dense vegetation cover, there is little overland flow generation and infiltration is dominant at the hillslope scale, but in arid regions, where vegetation cover and thus infiltration tend to be low, runoff is high but generally homogeneous at the hillslope scale. In semiarid regions, however, overland flow is discontinuous at the hillslope scale due to heterogeneous surface and rainfall properties, and the high spatial and temporal variability of organic matter content and soil stability leads to a mosaic-like pattern (Lavee *et al,* 1998). On natural hillslopes, vegetation plays an important part in reducing runoff by reducing flow velocity, increasing residence time and allowing reinfiltration (Dunne *et al,* 1991). Boix-Fayos *et al* (1998) evaluated the effects of climate on soil properties at the site, slope and patch scale along a climatic transect in

Alicante, Spain, noting that runoff coefficients and erosion become higher as climate becomes more arid. Rainfall simulation experiments on patchy distributions of *Stipa tenacissima L.* in SE Spain (Cerda, 1997) illustrate that in areas with patchy vegetation, surface runoff and erosion is negligible in vegetated tussocks and high in bare, unvegetated patches due to higher infiltration rates and deeper wetting fronts in the vegetated patches, dividing the landscape into water source (runoff) and sink (runon) areas. Similarly, Boix-Fayos *et al* (1998) found that vegetated patches on north-facing slopes in Alicante exhibited higher aggregation and infiltration capacity than bare slopes.

The influence of vegetation on spatial structuring of runoff and sediment flux is more noticeable in extreme environments where plant cover is scattered (Puigdefábregas, 2005). Studies have suggested that below 30-40% vegetation cover, runoff and soil loss will increase dramatically (Bartley *et al*, 2006), but that the arrangement of patches within the hillslope are more important than average ground cover, such that at the hillslope scale the mosaic of vegetation cover overrides the effect of average cover. Hillslope flume experiments suggest that hillslopes with a relatively high mean cover but with small bare patches can exhibit 6-9 times more runoff and up to 60 times more sediment loss than similar hillslopes without bare patches and the closer these patches are to the base of the slope the greater the opportunity for sediment trapping and conservation (Bartley *et al*, 2006). Gyssels *et al* (2005) studied the impact of plant roots on the resistance of soils to water erosion, and found that water erosion rates decrease exponentially with increasing root mass at the plot scale, similar to the exponential decrease of erosion rates with increasing vegetation

cover, suggesting that for splash and inter-rill erosion, vegetation cover is the most important vegetation parameter, whereas for rill erosion the rooting properties are of paramount importance.

Analysis of topographic data in New Mexico reveals that aspect can have an effect on landscape morphology because soil and vegetation properties and local microclimatic and hydrological properties vary with aspect: north-facing slopes are steeper and have greater curvatures than south-facing slopes, suggesting south-facing slopes are sparsely vegetated, more erodible, and can therefore maintain long-term erosion rates equal to base-level fall with shallower slopes (Istanbulluoglu *et al,* 2008). It has been suggested that under conditions of negligible water exchange, aspect and slope can be the key factors in determining hydrological behaviour (Ivanov *et al,* 2008).

Geomorphologic evidence also exists for past climatically-induced changes in erosion rate. Hunt & Wu (2004) present evidence for accelerated soil loss and topographic roughening in the Mojave desert during the early Holocene, associated with loss of vegetation due to increased aridity following the cooler, wetter Pleistocene.

2.6 SUMMARY

While there seems to be little doubt that climate can have a profound effect on erosion rates at the plot, hillslope, and continent scales, the effect of climate on erosion at the catchment scale is much less clear. Evidence suggests that climate, especially precipitation, directly affects vegetation cover and patterning and that this relationship is particularly strong in arid and semiarid areas. Since the presence of vegetation, and indeed the orientation of patches of vegetation, have been demonstrated to have an effect on erosion (or sediment yield) at the catchment scale, it seems logical that precipitation could exert a first-order control on erosion rates at the catchment scale. However, difficulties arise when the results of many recent catchment-scale studies of the effects of climate on long-term erosion rates are considered, because these studies indicate a weak (if any) correlation between erosion rates and climatic variables. Previous studies may, however, be obscuring a relationship between climate and erosion by sampling over a relatively limited climatic range, or by neglecting to consider how threshold behaviour in vegetation may affect erosion rates. The current study aims to address these issues by studying long-term erosion rates at the catchment scale, sampling catchments of similar lithology and morphology along a continent-scale transect which has experienced relatively uniform uplift along its length. The study will therefore give a clearer indication of how long-term erosion rates vary along a climatic transect as mean annual precipitation, and vegetation cover and patterning, change.

3. STUDY AREA

3.1 CLIMATE

3.1.1 Controlling Factors of Climate

The Chilean climate is dominated by the influence of Andes and the Pacific Ocean, and receives little input from the eastern part of the South American continent. The topographic structure of Chile leads to a decrease of air temperatures, increase in precipitation and lowering of the snowline with increasing latitude (Caviedes, 1990). The coastal cordillera feels the full force of maritime influences and shifts in position of winds, whereas the climate of the interior is disrupted by rainshadow and continentality effects. The main factors affecting Chilean climate lead to a north-south climatic zonation, while a strong east-west climatic gradient is imposed by the topography. The width of the Andes is greater in the northern Chilean sector, with decreasing width and mean elevation with increasing latitude. The coastal cordillera also presents a considerable barrier, particularly north of ~33ºS and less so in the southern sector, where the range becomes fragmented (Miller, 1976).

The tapered shape of the South American continent limits the effect that continentality can have on climate, and this is particularly true in Chile, where the effects of oceanic and atmospheric factors offshore can have a profound effect on the climate onshore, moderated by the topography of the Andes (which block transport of moisture related to the tropical easterly winds) and the coastal cordillera. Both the dominating winds and the coastal upwelling off the coast of Chile are directly linked to the strength and location of the South Pacific Anticyclone (SPA), which is centred off the coast of Chile at ~27ºS in winter and 30ºS in summer (Caviedes, 1990).

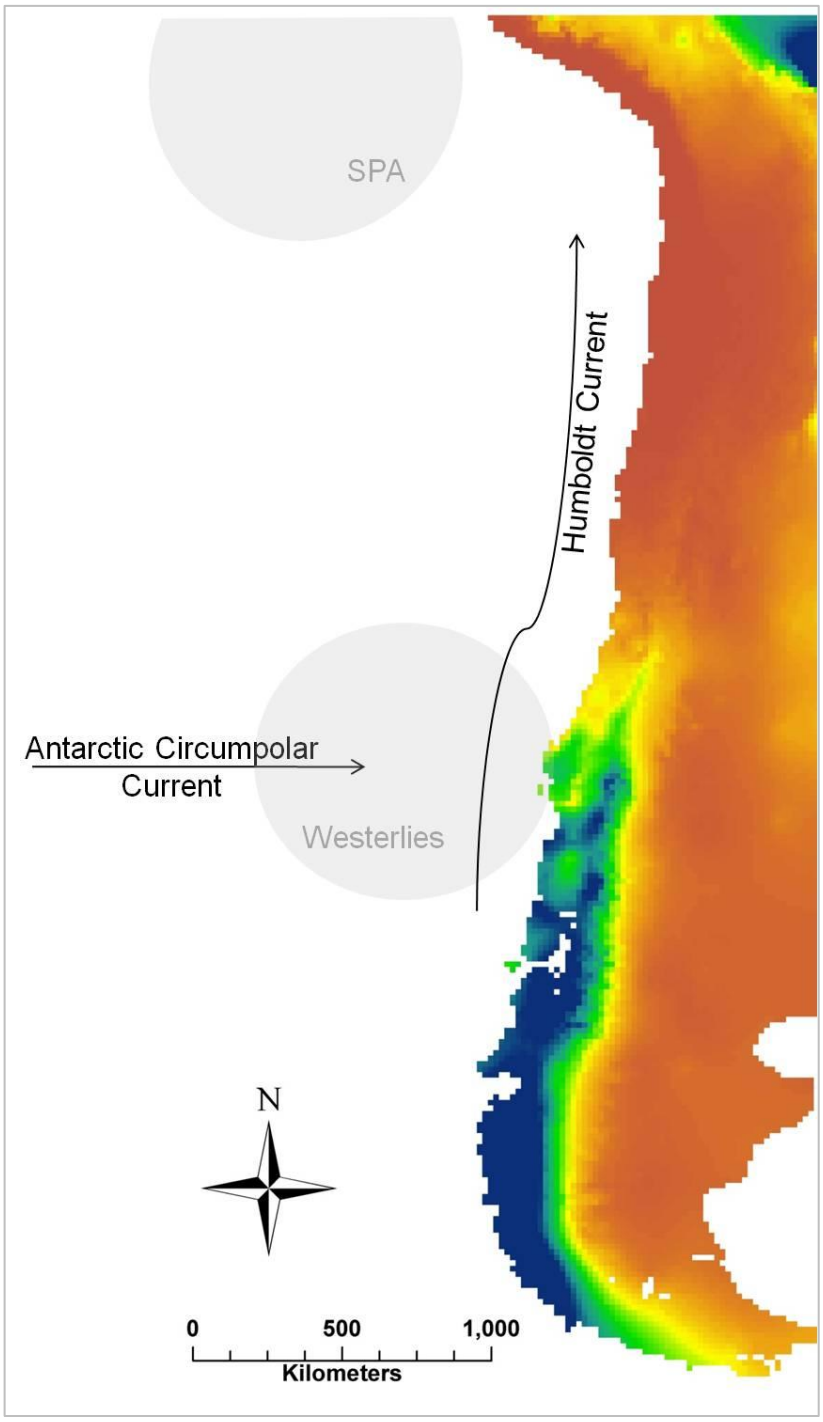

Figure 3.1: Summary of factors controlling the climate along the Chilean coast. In addition to the Humboldt Current, the Chile Coastal Current flows equatorward along the coast, and these two currents are separated by the poleward-flowing Peru-Chile Counter Current. Land surface is coloured according to mean annual precipitation (see Figure 3.2 for legend).

Oceanic currents near the surface have a direct effect on the climate of South America (Fig. 3.1). On the west coast, this comprises one major oceanic current system: the equatorward Peru-Chile Current (PCC), or Humboldt Current, and the Chile Coastal Current (CCC), separated by the poleward-flowing Peru-Chile Countercurrent (PCCC) (Cerveny, 1998; Lamy *et al*, 1998a, Lamy *et al*, 1999). The PCC is one branch of the Antarctic Circumpolar Current (ACC), which approaches the South American continent between 40-45ºS and then splits into the poleward-flowing Cape Horn Current and the equatorward flowing PCC (Mohtadi & Hebbeln, 2004). The PCC upwells along the coast of northern Chile, allowing cool Subsurface Water to reach the surface (Hebbeln *et al*, 2000) and inhibiting the moisture capacity of onshore winds (Houston & Hartley, 2003), resulting in the arid climatic conditions present in northern Chile, where the only moisture comes from fog and drizzle in the coastal zone, also related to the coastal upwelling.

Atmospheric circulation is also of paramount importance in controlling the Chilean climate, in particular the circulation systems relating to the southern westerly wind belt which brings rain to the region. The location and intensity of the Westerlies is related to the strength and position of the subtropical anticyclone in the south-eastern Pacific (SPA) and the circum-Antarctic low pressure belt (Markgraf, 1998), and seasonal latitudinal shifts in the westerly belt and changes in ocean currents (the PCC) reflect interaction between the subtropical high and subpolar low pressure systems (Heusser *et al*, 2006b). The SPA exhibits an annual shift of ~10° of latitude and is in its southernmost position in austral summer, blocking the paths of storm fronts moving towards central Chile (Muñoz *et al*, 2007). The SPA eliminates all

traces of westerly activity north of 31ºS, although frontal systems occasionally reach as far north as 27ºS in midwinter (Miller, 1976), but south of here the Westerlies play a large part in controlling Chile's climate, particularly in the coastal cordillera. Westerly storm tracks are centred around 40ºS in winter due to greater sea ice extent and a strengthened subtropical anticyclone, and around 45ºS in summer when the subtropical anticyclone is weakened and sea ice extent is reduced (Markgraf, 1998), such that the southern third of Chile is under Westerly influence throughout the year (Miller, 1976).

The Westerlies also control the coastal climate indirectly, through their effects on coastal upwelling. North of 35ºS, upwelling occurs year round and results in the arid to hyperarid climate with coastal fog and drizzle. Between 35-42ºS, the southward migration of the Westerlies during the austral summer allows coastal upwelling, while south of 42ºS the intense, year-round Westerlies prevent the occurrence of coastal upwelling (Hebbeln *et al*, 2000). In this southern region, the Westerlies arise from relatively simple circulation cells, with the cold Antarctic air to the south and warmer tropical waters to the north producing a steep thermal gradient and powerful oceanic circulation (Cerveny, 1998). North of 40ºS the Andes disrupts the dominant zonal flow, resulting in two large anticyclones: the South Pacific Anticyclone to the west and the South Atlantic Anticyclone to the east. The South Pacific Anticyclone is the dominant controlling factor of the climate in northern Chile, although the northern Andes experience some climatic effects from east of the cordillera (Cerveny, 1998).

3.1.2 Climatic Zones

3.1.2.1. Precipitation

The climate in Chile ranges from hyperarid in the north to cool temperate in the south. Overall zonation of mean annual precipitation is illustrated in figure 3.2. North of 27ºS the climate can be considered to be hyperarid, and the climate is predominantly arid north of 31ºS (Miller, 1976), with precipitation increasing from ~25mm at 27ºS to ~200mm at 31ºS due to rare passages of frontal systems of the Southern Westerlies in midwinter (Miller, 1976; Lamy *et al*, 2000). Winter rainfall is extremely rare north of 27ºS and the only reliable source of moisture along the northern coast is drizzle from stratus clouds, and even fog is relatively infrequent (Miller, 1976). The few rivers present in the axial region generally have larger flows in summer due to the influence of Andean rains (Muñoz *et al*, 2007). Stratus occurs along the coast north of 27ºS in summer, confined to the early mornings, and occurs almost daily in winter. An extreme climatic gradient exists which makes the region very sensitive to changes in climate induced by latitudinal shifts in the position of the Southern Westerlies (Lamy *et al*, 2000).

The warm temperate zone of Chile begins south of ~31ºS, seeing a steady increase in frequency and intensity of the southern Westerlies and an associated increase in annual rainfall and wetter summer months (Clapperton, 1993). Summers are dry, as the subtropical high-pressure system blocks the Westerlies, and winters are cooler and humid when the Westerlies reach the area (Valero-Garces *et al*, 2005), although monthly river discharge variations occur due to summer snowmelt in the Andes

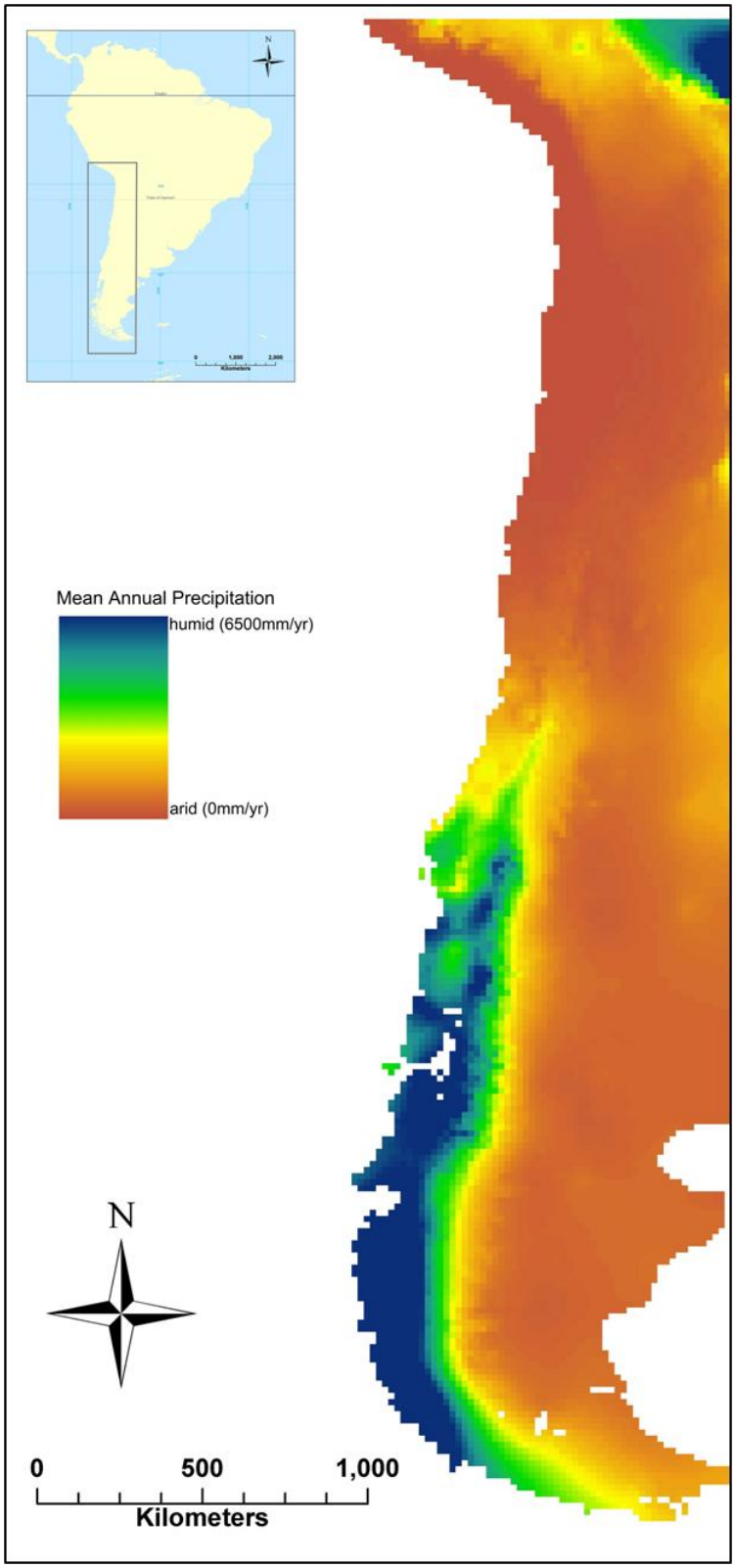

Figure 3.2: Distribution of mean annual precipitation in Chile. Created using the 1km-resolution WorldCLIM dataset of Hijmans *et al* (2005).

(Muñoz *et al*, 2007). From 31-37ºS the amount of winter rain grows significantly with an increase in frequency and intensity of the Westerlies, and the climate can be classified as semiarid Mediterranean. Summer dryness disappears south of ~37ºS and a humid temperate climate is developed with precipitation up to 2000mm/a in low elevations (Miller, 1976).

The abrupt change in climate at 37ºS can be attributed to the fact that the Westerlies here split into two branches, with one flowing northward along the Pacific anticyclone and part flowing southeastward (Miller, 1976), and to the fact that the coastal range becomes increasingly fragmented to the south, making it less effective as a barrier to flow from the west. Southern Chile (south of 42ºS) is characterised by continuously humid, cool temperate conditions throughout the year with heavy precipitation varying depending on the exposure towards the very strong westerly winds in this region (Lamy *et al*, 1998a), with the Westerlies year-round and intense (Miller, 1976).

3.1.2.2. Temperature

Temperature shows a relatively uniform distribution, both seasonally and from north to south along the coast of Chile, and of South America as a whole, with generally high temperatures near the equator and low temperatures near the poles (Cerveny, 1998; Miller, 1976). Temperature variation is, however, minimal compared to the more dramatic latitudinal variations in precipitation. Onshore, mean annual temperatures at the coast decrease from 19°C in the far north of the country, to ~15°C at 34°S, to ~11°C at 40°S, and to 5°C in the extreme south of the country

(Miller, 1976; Heusser *et al,* 2006a). Temperature in central Chile is largely controlled by how effective the coastal range is at acting as a barrier to cool oceanic air masses.

3.1.2.3. Fog/Stratus

The coastal deserts of Chile and Peru have high atmospheric moisture, but very little precipitation, similar to other West coast deserts (Cerveny, 1998) and large parts of the Chilean coast are subject to regular and persistent stratus and fog, particularly between 30º and 40º (Miller, 1976). Atmospheric stability induced by the Humboldt Current and subsidence generated by a permanent high-pressure area over the Pacific lead to low cloud decks and fogs on the coastal mountains, with development of precipitation inhibited by well-developed trade wind inversion (Larrain *et al*, 2002). Fog and stratus clouds are an almost daily occurrence in the coastal hills of central Chile, with differences in fog distribution attributable to changes in ocean proximity, altitude, orientation of the coastal range and local relief (Larrain *et al*, 2002).

3.1.3 Climatic variability and palaeoclimate

The climatic gradient in Chile, especially central Chile, is particularly steep, and even small shifts of the climatic zones can result in profound changes in the terrestrial environment. Palaeoclimate studies have provided evidence for significant northwards shifts of the climatic zones along the coast during glacial periods, such that climate and vegetation characteristics currently found in southern Chile were present in central Chile during the Last Glacial Maximum (LGM). While the climate in northern Chile has been arid-hyperarid since at least the Pliocene (Hartley & Chong, 2002; Dunai *et al,* 2005) and has been relatively stable since the Jurassic (Hartley *et al*, 2005), central Chile has been subject to climatic variability on glacial timescales, and these frequent, rapid climatic changes could have a significant effect on erosion rates by frequent addition and removal of vegetation cover.

3.1.3.1. ENSO

The ENSO phenomenon refers to a surface pressure oscillation in the South Pacific, the Southern Oscillation, and its related oceanic aspects, El Niño and La Niña (Cerveny, 1998), and leads to interannual climatic variability in South America (Markgraf, 1998). The El Niño term refers to warming of the coastal waters in tropical and subtropical coastal waters on the Pacific coast of south America, disrupting the usual cold upwelling processes and replacing fog and drizzle along the coast by torrential rain (Cerveny, 1998). The La Niña term refers to a reinforcement of cold upwelling conditions and is thus the antithesis of El Niño (Cerveny, 1998). El Niño phases bring warmer than average temperatures to most of Chile and the rest of South America (Markgraf, 1998). Modern ENSO events have an average recurrence

of 3-6 years (Maldonado & Villagran, 2006).

Most authors agree that there was little or no ENSO influence during the early-mid Holocene, but there is significant evidence for an increase in frequency of ENSO events since ~3.2ka (Maldonado & Villagran, 2006). Some authors suggest that ENSO conditions may have been present since as early as 6ka (Villa-Martinez *et al*, 2003) which could support the idea that ENSO-like events have simply intensified over the last ~3000 years (Villa-Martinez *et al*, 2004). Maldonado & Villagran (2002) present swamp forest pollen analyses from ~32°S which they interpret to reflect increased rainfall from 4.2ka as a result of changes in position and/or frequency of the Westerlies linked to ENSO events. Varve analyses of Lago Puyehue at ~40°S in the Chilean Lake District indicate that the region was subject to climatic variability with ENSO periodicities over the past 600 years (de Batist *et al*, 2008). Diatoms from Lago Puyehue highlight ENSO-type activity in the Chilean Lake District since at least 3ka (Sterken *et al*, 2008).

3.1.3.2. The Holocene

Patterns of Holocene climate are characteristic of interglacial climates (Markgraf, 1998). The climate of Chile has become generally warmer and drier since the LGM, although some brief climatic reversals have been noted, although these Holocene changes in climate are minor compared to the change from glacial to interglacial climate. Swamp forest records from ~32°S indicate increasingly drier conditions since ~10ka (Villagran & Varela, 1990), with a humid phase from 9.9-8.7ka, followed by aridity until 5.7ka, an increase in moisture followed by a less intense

drought from 3-2.2ka, and subsequent swamp forest expansion and more variable climate at ~2ka (Maldonado & Villagran, 2006), which the authors attribute to variations in the extent of the Southern Westerlies, but which has also been postulated to relate to the inception of ENSO dynamics at this time.

Pollen records from Laguna Aculeo, a lake in the eastern foothills of the Coastal Cordillera at 34°S, similarly indicate an increase in moisture at ~5.7ka and a more variable climate from 3.2ka as a result of ENSO phenomenon (Villa-Martinez *et al,* 2003), and decadal-centennial scale changes in the frequency of the Westerlies over the last 2500 years (Villa-Martinez *et al,* 2004).

Further south, records from Lago Puyehue in the Andean foothills (~40°S) also indicate a general warming and drying of the region until the Late Holocene (Sterken *et al,* 2008), with the exception of a brief climatic reversal between 13.1-12.3ka (Bertrand *et al,* 2008). A similar reversal is noted at 41°S from 14-12ka (Heusser *et al,* 2006b). Varve thickness analyses from Lago Puyehue indicate rapid climatic fluctuations superimposed on the general warming trend (de Batist *et al,* 2008) and Late Holocene increases in precipitation in the region have been attributed to the increased frequency of El Niño events and the related increase in winter moisture (Sterken *et al,* 2008).

3.1.3.3. Glacial-interglacial variability

Analysis of terrigenous marine sediments from the continental slope at 27.5ºS (Lamy *et al,* 2000; Lamy *et al,* 1998a) show both a precession-driven variability in

precipitation and rapid changes in weathering in the coastal cordillera. These datasets contain a record of input of material from the Andes, and record primarily medium- to large-scale shifts of the Southern Westerlies and small-scale shifts in circulation patterns which are reflected in variations in chemical weathering intensity. Records here indicate an equatorward shift of the southern Westerlies during glacial periods, resulting in higher seasonal precipitation derived from frontal winter rains (Lamy *et al*, 1998a), and superimposed climatic variability representing latitudinal shifts of the Westerlies on smaller temporal and spatial scales (Lamy *et al*, 2000). Grain-size distributions of the same core indicate humid conditions (i.e. increased fluvial input relative to aeolian input) from 27-17ka, a time period which encompasses the LGM (Stuut & Lamy, 2004) and a generally increased humidity during glacial periods over the past 120kyr, providing support for an equatorward migration of the Westerlies at these times, probably controlled by increased Antarctic sea ice, an enhanced polar vortex and increased thermal gradients between the poles and equator (Stuut & Lamy, 2004).

Grain size distributions and clay mineralogy from two sediment cores from the continental shelf at ~33ºS indicate a generally cold-humid glacial climate from 28-18ka, with a cold but semiarid interval from 26-22ka and the LGM from 22-18ka (cal), providing further support for an equatorward migration of the Westerlies during glacial cycles (Lamy *et al*, 1999).

Cooler and more humid intervals on orbitally-controlled timescales are also recorded in pollen studies throughout Chile. Pleistocene vegetation around Laguna de Tagua

Tagua (~34ºS) comprised *Nothofagus dombeyi* type trees and podocarp species, indicating much higher precipitation and much lower temperatures than present, similar to those currently experienced south of 39ºS (Heusser, 1983), providing support for a northwards displacement of the southern Westerlies of around 5º of latitude during glacial times. Caviedes (1990) suggests a 7º northwards shift of the Westerlies based on multiregressive modelling of changes in the snowline in semiarid northern Chile. Sedimentologic, geochemical and palynological evidence from Laguna de Tagua Tagua all favour cooler, more humid conditions during the Last Glacial: pollen records from that time contain species now representative of the Valdivian rainforests from 39º-41ºS (*Lomatia, Myrtaceae, Lauraceae, Drimys* and ferns), while sedimentologic and geochemical evidence points to high lake level at the same time (Valero-Garces *et al*, 2005).

Evidence from pollen and oxygen isotope data from a marine sediment core (ODP Site 1234) at ~36ºS also indicates a northwards migration of the Westerlies during the last glacial cycle. Pollen assemblages indicate that the area, which is currently covered by xeric lowland deciduous forest, was once covered in mesic Valdivian Evergreen Forest and Subantarctic Evergreen Rainforest. Subantarctic Evergreen Rainforest is primarily composed of southern beech (*N. Dombeyi*) and is currently found at latitudes greater than 47ºS, and would require annual precipitation ~2000mm higher than presently found at the study site (Heusser *et al*, 2006a). This evidence suggests a possible northwards shift of the Westerlies of more than 10º at this latitude during the last glacial cycle, or a lesser northwards shift combined with intensification of the Westerlies.

A similar core from ODP Site 1233, at ~38ºS, provides a record of deposition at the present boundary between the northern, summer-green lowland forest to the north and the southern evergreen rainforest to the south (Heusser *et al*, 2006b). Palynological evidence from this core points to the existence of hyper-humid vegetation (e.g. North Patagonian and Sub-Antarctic forests), implying sustained northward migration of the westerlies and the prevalence of climatic conditions presently found more than 10º further south. Coldest, wettest conditions in this area appeared to be ~20-17ka (Heusser *et al*, 2006b), i.e. coincident with the LGM. Information gleaned from fossil pollen records and beetle assemblages from 41º-43ºS suggests cold and humid (snowy) conditions at the LGM (Heusser *et al*, 1996).

During the LGM, enhanced precipitation onshore was accompanied by lower water temperatures and higher marine productivities (Mohtadi & Hebbeln, 2004), suggesting a coupling between the atmospheric and oceanic systems off the coast of Chile (i.e. the southern Westerlies and PCC/ACC respectively). Romero *et al* (2006) also found evidence for increased surface water productivity in central Chile (35ºS) at the LGM, indicative of a northward shift of the climate zones (and of the ACC and the Westerlies) at this time.

3.2 VEGETATION

The vegetation of Chile is controlled primarily by precipitation (Veblen *et al*, 1981), and displays a strong latitudinal and altitudinal zonation. Present day vegetation distribution is therefore a result of the relatively stable, interglacial climate of the past ~10ka (Clapperton, 1993). The dominant woody vegetation changes along the aridity gradient, from open deserts dominated by drought-resistant and spinose forms, to a more closed, low-growing mesophytic stage, then to dense sclerophyllous evergreen shrubs and finally to broadleafed shrub and tree forms (Parsons & Moldenke, 1975; see figure 3.3).

The vegetation of the study area, from ~25°S to ~40°S, consists of three main ecoregions, defined by the World Wildlife Fund (WWF): deserts and xeric shrublands (the Atacama desert), Mediterranean forests, woodlands and scrub (the Chilean matorral) and the temperate coniferous and deciduous forests (southern Valdivian forests) (Olson *et al*, 2001). In each of these eco-regions, endemism is high due to the isolation of Chilean flora from the rest of South America.

The Atacama desert forms a continuous strip along the Chilean coast, with an average width of ~100km between ~18ºS and ~29ºS, with climate becoming less arid towards the south of the region. The northern coastal region has almost no vegetation, with annual and short-lived perennial species and woody scrub surviving on coastal lomas, with trees and shrubby and herbaceous plants being limited to quebradas (small gullies or ravines) and coastal plateaus in fog zones.

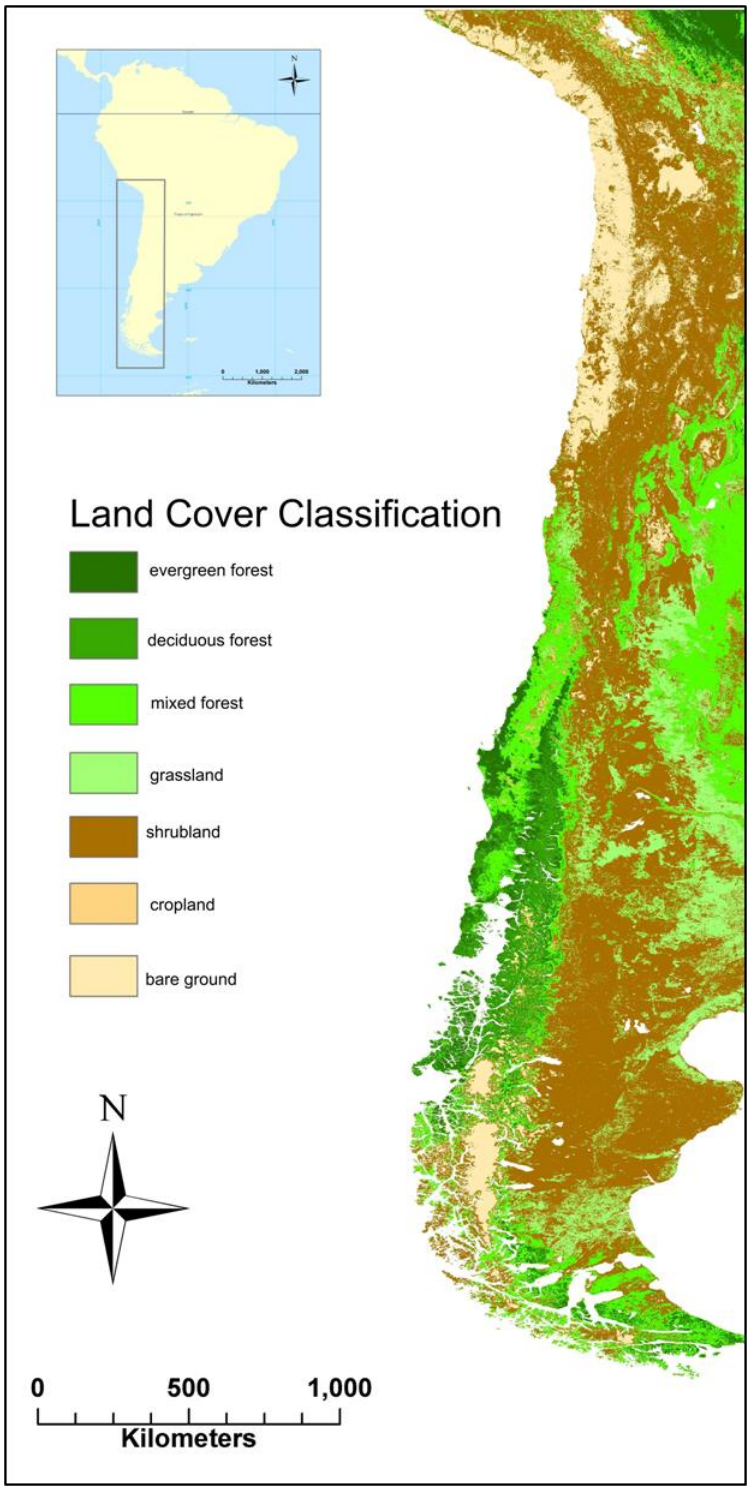

Figure 3.3: Landcover classification in Chile. Adapted from the data described by Hansen *et al* (2000).

The Chilean matorral forms a 100 km wide strip along the central Chilean coast, consisting of mostly evergreen shrubs and a seasonal cover of herbaceous perennials and some annuals. The higher precipitation of this region supports evergreen broadleaf forests and evergreen bushes in the Central Valley and adjacent slopes (Clapperton, 1993). This zone extends south to the Rio Bio Bio at 38ºS, and south of here the more persistent Westerlies support dense Valdivian rainforest. The natural coastal vegetation of central Chile is a mosaic of xeric *Nothofagus obliqua* forest, sclerophyllous woodlands, and mesic *N. dombeyi* and myrtaceous forests where humidity is high enough (Veblen *et al*, 1983). Littoral deposits support sclerophyllous and myrtaceous forests, wetlands and halophytic shrubs and herbs (Heusser *et al*, 2006).

Deciduous forests represent a transition from the Mediterranean forests of the Chilean matorral to the wet temperate forests further south (WWF), although the ecotone between the subtropical sclerophyllous woodland of the matorral and the southern rainforest is broad and uneven (Heusser *et al*, 2006). This ecoregion is also home to several stands of what is considered to be relict Pleistocene forest (Caviedes, 1990; Hinojosa *et al*, 2006), where humidity-loving species survive on moisture derived from coastal fogs. The best-developed of these occur at Fray Jorge, Talinay, Huentelauquen and Mantagua (Villagran & Armesto, 1980). These forests occur primarily on the ocean-facing slopes and ravines of the Coastal Cordillera between 33ºS and 43ºS, with isolated pockets occurring north of 33ºS where supported by coastal fogs and are floristically similar to Valdivian temperate rainforests (del-Val *et al*, 2006). The coastal plains also support small patches of floristically homogeneous

swamp forest, comprising mostly myrtaceous species (Villagran & Varela, 1990; Maldonado & Villagran, 2006). Plant communities are typified by *Cryptocarya alba,* arboreal species such as *Schinus latifolius and Peumus boldus,* and *Beilschmiedia miersii* in cloud-covered parts of the coast (Heusser, 1990). In drier locations, *Lithrea caustica* and the overstory species *Quillaja saponaria* and *Kageneckia oblonga* can also be found (Heusser, 1990). Villa-Martinez *et al* (2003) describe an altitudinal zonation of vegetation in the Coastal Cordillera at ~34ºS, with the dominant espinal vegetation (savanna-like scrub characterised by *Acacia cavens*) giving way to sclerophyllous forests up to 1250m asl, sclerophyllous mountain matorral to 1900m, and then to monospecific stands of *N. obliqua* and high elevation scrubland. The dominant vegetation type in the semiarid coastal region is the Jaral Costero (Maldonado & Villagran, 2002), an open scrub vegetation dominated by *B. vernalis* and *Schinus polygama* with sand dune and salt marsh herbaceous vegetation common. Vegetation in this ecoregion is profoundly affected by slope aspect, with north-facing slopes bearing open scrub vegetation with spiny shrubs and small trees and south-facing slopes bearing evergreen sclerophyllous woodland (di Castri, 1968), and with evergreen species representing 19% cover on north-facing slopes compared to over 90% on south-facing slopes (Armesto & Martinez, 1978).

The temperate coniferous forests of southern Chile extend from 35-48ºS and cover a narrow strip of land between the Andes and the Pacific Ocean and comprise a heterogeneous mosaic of different forest types. The dense Valdivian rainforest comprises mostly the evergreen southern beech species, *Nothofagus dombeyi*, and there is a well-defined latitudinal and altitudinal zonation of *Nothofagus* species in

this area (Clapperton, 1993). Natural forested regions can be divided into the northern lowland deciduous forests (36-40ºS) and the southern evergreen forests (Schmithüsen, 1956, cited in Heusser *et al*, 2006). Deciduous beech forests extends to ~41ºS where it merges with Valdivian evergreen forest (Heusser *et al*, 2006; Heusser, 2003; Heusser *et al*, 2000). At greater latitudes, and up into the main Andean cordillera, North Patagonian evergreen forest, Subantarctic forests and Magellanic moorlands can be found. Lowland deciduous beech forests comprise several species of southern beech (*N. obliqua, N. glauca and N. alpina*) along with conifers including *Podocarpus saligna*, and exhibit an altitudinal zonation in both the Coastal Cordillera and the Andes. The winter-deciduous beech forests are accompanied by sclerophyllous forests, *Acacia caven* matorral and scrub formations in the central coastal region (Villagran & Varela, 1990).

3.3 GEOLOGY AND GEOMORPHOLOGY

The South American continent has long drifted to the west, and its western margin has been the leading edge of the continent since at least the Late Ordovician (Lucassen *et al*, 1996). Almost uninterrupted subduction since the Jurassic (e.g. Kukowski & Oncken, 2006; Farias *et al*, 2008a) culminated in increased shortening in the overriding plate, leading to the elevation of the Andes during the Cenozoic. Convergence initially took place between the Farallon Plate and the South American Plate; breakup of the Farallon Plate ~25Ma (Lonsdale, 2005) led to formation of the Cocos and Nazca plates and subsequent subduction of the Nazca Plate beneath the South American Plate. The Nazca plate has to its southern edge a divergent margin with the Antarctic plate (the Chile Rise), to its western side a divergent margin with the Pacific plate (the East Pacific Rise) and to its northern edge a divergent margin with the Cocos plate (the Galapagos Rise). The Chile Triple Junction occurs at the intersection of the Nazca, South American and Antarctic plates. The South American plate forms a complex boundary with the Antarctic and Scotia plates to the south and has a boundary with the Caribbean plate to the north. The evolution of the Andean plateau has been a subject of much debate, and various models have been proposed for the temporal and spatial evolution of the Andes (e.g. Isacks, 1988; Silver *et al*, 1998; Lamb & Davis, 2003). Current knowledge suggests that plateau uplift was slow and steady and that plateau growth took ≥40 Myr (Barnes & Ehlers, 2009; Sobolev *et al*, 2006; Ehlers & Poulsen, 2009) with the rate of tectonic shortening in the central Andes increasing since ~50Ma (Sobolev *et al*, 2006). Modelling studies by Sobolev & Babeyko (2005) suggest that Andean orogeny was primarily controlled

by accelerating westward drift of the South American Plate, as postulated by Silver *et al* (1998), but that other contributing factors were also essential for extreme orogeny in the central Andes: high overriding rate over the past 30Myr and especially the last 10Myr; thick crust in the backarc as a result of tectonic shortening prior to 30Ma; and a high coefficient of friction in the subduction channel. Where these conditions are not in existence, orogeny is much less intense, similar to conditions in the southern Andes (Sobolev & Babeyko, 2005).

The Andes as a whole, and Chile itself, have a strong geological and morphological segmentation, both on the continent and on the continental shelf, slope and trench (Clapperton, 1993; Lamy *et al*, 1998b). The curve in the outline of the continent at ~19°S, south of the Nazca Ridge intersection, corresponds to a change in orientation of the trench and the Andes from NW-SE to NNE-SSW (Clapperton, 1993) and a widening of the Andes. The other main features causing segmentation of the Chilean margin are the Chile Rise at 46°S and the Juan Fernandez Ridge at 33°S (Melnick & Echtler, 2006; Charrier *et al*, 2007). North of the Juan Fernandez Ridge the margin is sediment-starved, with a thinly sedimented ocean crust and a trench fill of less than 0.5km (Yañez *et al*, 2001, cited in Melnick & Echtler, 2006; von Huene & Ranero, 2003) and can be classed as erosive. Subduction erosion is indicated by outcrops of Mesozoic volcanic arcs in coastal cliffs and the landward migration of volcanic arcs during the past 100Myr (Hervé *et al*, 2007; von Huene & Ranero, 2003). North of 27.5°S, the trench reaches its greatest depth of up to 8000m with sediment thickness increasing to the south (Lamy *et al*, 1998). South of the Juan Fernandez Ridge, the margin is accretionary and the trench contains 1.5-2.3km of terrigenous sediment

(Bangs & Cande, 1997). South of 38°S the trench is completely filled with turbidites (Lamy *et al*, 1998), and where the Chile Ridge collides with the trench, thin trench sediments again correspond with an erosive margin, characterised by non-accretion and tectonic erosion and a narrowing of the forearc region (Bangs & Cande, 1997). Between the Juan Fernandez Ridge and the Chile Rise, the elevation of the Andes decreases rapidly and the crust is much thinner and younger (Clapperton, 1993).

The physiographic units of Chile are arc-parallel and parallel to each other (Caviedes, 1990), Fault systems and magmatic, volcanic and basin development are also arc-parallel and decrease in age from west to east (Riquelme *et al*, 2003). In the Norte Grande (north of ~27°S), the physiographic units comprise the Coastal Cordillera, the Central Depression, and the present volcanic arc of the Andes. The Nazca Plate subducts at ~30° (Gregory-Wodzicki, 2000), conducive to the development of Plio-Quaternary volcanism. The Coastal Cordillera is ~60km wide, has a mean elevation of 1100m and is separated from the Pacific Ocean by an inactive coastal scarp (Riquelme *et al*, 2003), rising rapidly from sea level to 2000-2500m (Lamy *et al*, 1998). The Central Depression forms a forearc alluvial basin supplied by clastics and volcaniclastics from the Andes. The volcanic arc consists of pre-Pliocene rhyolites and ignimbrites, overlain by Pliocene-Quaternary volcanoes (Lamy *et al*, 1998). The region is crossed by few rivers (only the Rio Loa crosses the driest desert areas) and there are regionally extensive subplanar topographic surfaces which are inferred to have developed during episodic uplift of the Andes and deep canyons which characterise the latest erosional phase (Tosdal *et al*, 1984; Mortimer, 1973). Drainage is therefore dominated by enclosed drainage basins, formed from

tectonic subsidence of crustal blocks bounded by major fractures (Clapperton, 1993) and containing salars, salt marshes, saline lakes or clay playas.

In the Norte Chico (~27-33°S) , Rio Copiapo, Rio Huasco and Rio Elqui all traverse the Coastal Cordillera (Cooke *et al*, 1993). The Coastal Cordillera here reaches altitudes of up to 2000m above sea level (Cooke *et al*, 1993). From ~28-33°S, flat slab subduction leads to a lack of Pliocene-Quaternary volcanism and a lack of alluvial forearc basins (Gregory-Wodzicki, 2000; Lamy *et al*, 1998; Pankhurt & Hervé, 2007). The Central Depression is absent in this region, replaced by a region of transverse valleys which are drained by rivers which flow directly from the Andes to the sea (Segerstrom, 1964). Elevation increases constantly from the coast to the Andes, where there are more abundant plutonites, older sedimentary and volcanic rocks, and outcrops of metamorphic basin, than further north.

In the Coastal Cordillera between 33-35°S, the main rivers display a minor channel slope and alluvial beds, and bedrock rivers appear in a belt of 20-40km width along the coastline (Farías *et al*, 2008). The highest summits of the Coastal Cordillera in this region are flat-shaped, representing relict erosion surfaces, and are evident mostly in intrusive rocks (Farías *et al*, 2008). The Central Depression reappears south of ~33°S, where dip of the subducting slab again increases, allowing the development of Plio-Quaternary volcanics and forearc basins (Lamy *et al*, 1998; Gregory-Wodzicki, 2000). From here, elevation in both the Andes and the Coastal Cordillera decreases systematically towards the south, density of river systems increases and catchments become shorter and steeper (Lamy *et al*, 1998a) and

elevation of erosion surfaces decreases (Farias *et al*, 2008). The Coastal Cordillera also becomes less continuous with increasing latitude (Miller, 1976; Lamy *et al*, 1998a). In south-central Chile (36-42°S) the Coastal Cordillera emerges directly from the shoreline and reaches altitudes of up to 1500m (Glodny *et al*, 2008) and south of Puerto Montt (41°S) the Central Depression is drowned by the sea and the Coastal Cordillera there forms the island of Chiloe (Segerstrom, 1964).

The Coastal Cordillera consists of the remnants of a Mesozoic volcanic arc, comprising Jurassic to early Cretaceous dioritic-granodioritic plutons and Jurassic volcanics, with minor amounts of Upper Cretaceous to Tertiary marine sediments, Mesozoic marine volcanics, and with a basement of Palaeozoic sediments and Precambrian metamorphic rocks (Allmendinger *et al*, 2005; Lamy *et al*, 1999; SERNAGEOMIN, 2003). The crystalline basement is comprised of metamorphic complexes and associated magmatic rocks formed during the Proterozoic, Palaeozoic and Triassic (Hervé *et al*, 2007), cropping out discontinuously in northern Chile and almost continuously from 34-42°S. In southern Chile, the coastal zone is mainly represented by Mesozoic metasedimentary turbidites and since the Central Valley is drowned by the sea in this region, there is a transition from these turbidites to the Mesozoic-Cenozoic Patagonian batholith of the Andes (Pankhurst & Hervé, 2007). Mantle-derived plutonic and volcanic rocks in the Triassic and Jurassic were emplaced in an extensional tectonic regime which marked the onset of the Andean cycle (Lucassen *et al*, 1996). The western Coastal Cordillera is often covered by Late Miocene to Recent marine deposits (Farias *et al*, 2008), while the eastern side tends to display an irregular mountain front embayed with the sedimentary infill of the

Central Depression (Allmendinger *et al,* 2005). Sedimentary rocks are relatively scarce in the Coastal Cordillera because it was a morphological high in the Mesozoic (Lucassen *et al,* 1996).

3.3.1 Uplift History

Despite differential Miocene uplift between the central and southern Andes (Sobolev & Babeyko, 2005), and proposed decoupling of uplift in the eastern and western Coastal Cordillera in the Miocene-Pliocene (Farias *et al,* 2008), evidence suggests that the Coastal Cordillera has undergone remarkably spatially uniform Plio-Quaternary uplift. The coastline of South America is characterised by Quaternary marine terraces that have been uplifted along much of the Pacific margin, suggesting a continent-scale uplift mechanism (Hsu *et al,* 1989) combined with more regional local and tectonic processes (Ortlieb *et al,* 1996). Vertical uplift of 100s of m has occurred in places, while only up to 100m can be ascribed to eustatic sea level change (Segerstrom, 1964). Several authors have provided estimates of uplift rates based on these marine terraces (fig. 3.4).

In northern Chile, Plio-Quaternary marine terraces are described by Hartley & Jolley (1995), Ortlieb *et al,* (1996), Gonzalez *et al* (2003), Marquardt *et al* (2004) and Cembrano *et al* (2007). Published uplift rates include 0.05-0.5m/kyr for the northern coastal segment (Cembrano *et al,* 2007) and ~0.24m/kyr at ~23°S (Marquardt *et al,* 2004), an estimate which the authors consider to representative of the entire coastal sector as far north as 20°S. Marquardt *et al* (2004) consider this uplift to have been

continuous over at least the last 330kyr, and evidence suggests uplift rates in the Early Pleistocene may have been much slower (Ortlieb *et al*, 1996).

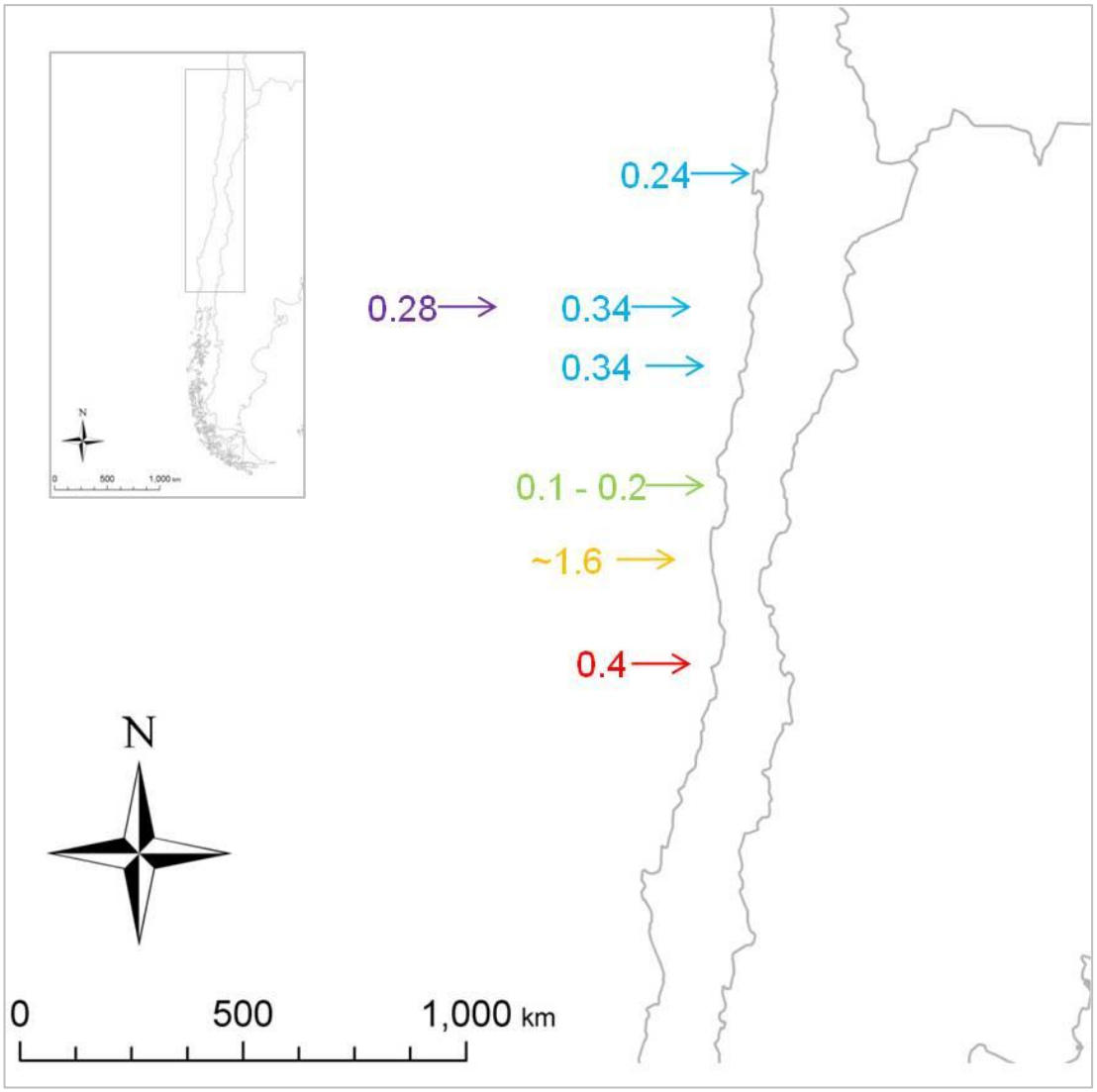

Figure 3.4: Previously published estimates of uplift along the coast of Chile based on marine terraces. Values in blue are from Marquardt *et al* (2004) and are averaged over the last 500ka. Values in purple are from Quezada *et al* (2007) and are averaged over 750ka. Values in green are from Leonard & Wehmiller (1992) and are averaged over 1-100ka. Values in yellow are from Saillard *et al* (2009) and are averaged over 6ka. Values in red are from Encinas *et al* (2006) and are averaged over at least the past 6.5ka.

In the vicinity of Caldera and Bahia Inglesa (~27°S), Marquardt *et al* (2004) calculated average uplift rates of ~0.34m/kyr over the last 500kyr, and cite evidence

for similar uplift rates at ~28°S, attributing the small variation to local faulting, and in the absence of marine terraces between 24-26°S, Marquardt *et al* (2004) consider their calculated uplift rates to be representative of the coastal segment continuing north to ~24°S. Uplift rates of ~0.28m/kyr were reported for the Caldera-Bahia Inglesa area by Quezada *et al* (2007), averaged over the past 750kyr, and the discrepancy between the two estimates is attributed to lower uplift rates during the period from 750-400ka.

Leonard & Wehmiller (1992) report uplift rates calculated from mollusc aminostratigraphy for the Coquimbo Bay (~30°S) area over the last 1-100kyr. Their rates range from 0.1m/kyr to no more than 0.2m/kyr, and are distinctly lower than other uplift rates estimates in the Coastal Cordillera. At Altos de Talinay (~31°S), wave-cut platforms formed during interglacials at 6ka, 122ka, 232ka, 321ka and 690ka (Saillard *et al*, 2009), based on ^{10}Be exposure ages, indicating that uplift rates varied from ~0.1m/kyr between 122-6ka to ~1.2m/kyr between 321-232ka. The absence of platforms during other highstands is interpreted to reflect slow uplift rates. Encinas *et al* (2006) calculated an uplift rate of 0.4m/kyr over at least the past 6500 years for a Holocene marine layer in Algarrobo, at ~33°S.

3.4 SUMMARY

The Coastal Cordillera of Chile provides the ideal setting to investigate the effect of climate, particularly precipitation, on long-term erosion rates. The combination of atmospheric and oceanic factors controlling climate in the region leads to a stark latitudinal gradient in climate, and yet geological and geomorphological features along the continental margin are remarkably uniform and allow sampling in similar geological and geomorphological settings along the climatic transect. The Coastal Cordillera represents a Mesozoic volcanic arc and is primarily composed of dioritic to granodioritic plutons and volcanics, and samples in the present study were specifically collected from catchments which were entirely or almost entirely composed of the plutonic rocks. Despite the morphological segmentation of Chile, it is possible to select small, first order catchments of similar geometry along the entire length of the climatic transect, in order to minimise differences between sampling sites. In addition, Plio-Quaternary uplift rates throughout the study area are of the same magnitude, with small lateral variation which can be attributed to localised tectonic processes.

4. METHODS

4.1 COSMOGENIC ISOTOPES

4.1.1 Overview

Sediment yields determined from sediment loads and accumulation of sediment behind checkdams have traditionally been used as a proxy for erosion rates, but since they typically average rates over years or decades they can be dominated by anthropogenic effects or changes in sediment storage, and may not be representative of the long-term mean erosion rate, particularly where erosion is driven by episodic processes or extreme events (Granger *et al,* 1996; Clapp *et al,* 2000; Kirchner *et al,* 2001). Erosion rates can be estimated over longer timescales from volumes of sediment trapped in basins or fans, but these techniques require additional dating techniques in order to be useful. Cosmogenic nuclides, meanwhile, can be used to measure long-term erosion rates integrated over periods of at least millenia (Lal, 1988; Bierman & Nichols, 2004).

Cosmogenic nuclides such as ^{10}Be build up in rocks near the surface of the earth due to bombardment by cosmic radiation, and the concentration of these nuclides in target minerals can indicate the near-surface residence time of the rock, and therefore the rate at which a landscape is eroding. Attenuation of cosmic radiation in matter limits production of ^{10}Be in quartz to the upper few metres below the surface of the Earth and so the ^{10}Be concentration in quartz grains is a function of the near-surface residence time of these grains. Early use of the technique (e.g. Lal, 1988; 1991) focussed on the interpretation of erosion rates and exposure ages at the outcrop scale,

and more recent refinements to the technique have allowed the calculation of catchment-scale erosion rates from concentrations of ^{10}Be in quartz in fluvial sediments exiting a basin. Seminal papers by Brown *et al* (1995), Bierman & Steig (1996) and Granger *et al* (1996) provided the basis for use of this technique, which has been used widely in recent years. Reviews of subsequent studies utilising the technique are provided by von Blanckenburg (2005), Cockburn & Summerfield (2004) and Bierman & Nichols (2004).

4.1.2 Production Systematics

Earth is bombarded by galactic cosmic radiation which largely originates within the Milky Way galaxy and is primarily composed of high energy nucleons, mostly protons with minor amounts of heavier nuclei, electrons and positrons (Niedermann, 2002), with energy between ~1GeV and ~10^{10}GeV (Gosse & Phillips, 2001). These primary rays interact with the Earth's magnetic field and those with a high enough momentum to penetrate the magnetic field then interact with N and O atoms in the upper atmosphere to produce cascades of lower energy secondary particles, which in turn impact on the ground surface to produce most atmospheric nuclides and all in-situ nuclides (Granger & Riebe, 2007). As these reactions propagate down through the atmosphere, and in turn the lithosphere, the composition of the nuclear particles becomes dominated by neutrons and muons, which subsequently produce cosmogenic nuclides in the atmosphere, hydrosphere and lithosphere (Gosse & Phillips, 2001). Cosmogenic nuclides are produced within a characteristic depth scale of ~1m and so the measured concentration of nuclides at the surface is a reflection of the integrated denudation history while the material passed through this depth interval (von Blanckenburg, 2005).

Variation in the intensity of cosmic rays occurs for several reasons. The most important determinant of the intensity of radiation reaching the Earth's surface is the influence of the geomagnetic field on the charged, primary particles whose rigidity (i.e. momentum per unit charge) and angle of incidence determine whether they are deflected or admitted by the geomagnetic field (Gosse & Phillips, 2001; Dunai,

2001; Pigati & Lifton, 2004). In order to pass through the geomagnetic field the primary particles must have a rigidity exceeding that of the cutoff rigidity (R_c) at that location, and R_c is greatest at the equator and decreases towards the poles (Niedermann, 2002; Gosse & Phillips, 2001; Dunai, 2000), such that cosmic ray flux increases towards the poles until R_c is below the minimum energy of particles in the radiation, and so cosmic ray flux does not increase further above 60° latitude (Simpson *et al*, 1953, cited in Dunai, 2000). Production rates decrease exponentially with increasing atmospheric depth although the attenuation length varies with both latitude and altitude (Desilets & Zreda, 2003; Dunai, 2000; Dunai, 2001). Fluctuations in solar activity influenced by solar cycles and longer-term variability primarily affect low-energy cosmic radiation (< 1 GeV), and so variations on these timescales are only significant in high latitude regions where cut-off rigidity is low and where low-energy particles are able to pass through the geomagnetic field (Lifton *et al*, 2005; Dunai, 2001a). On timescales of 10^4 to 10^7 ka, variations may also occur in relation to interstellar medium or effects of nearby supernovae (Gosse & Phillips, 2001), although these changes are much less significant than those due to modulation of the cosmic ray flux by solar and geomagnetic factors. The geomagnetic field also varies with time, for example, at 20ka the intensity was ~60% of today (von Blanckenburg, 2005; Dunai, 2001). Production rates over the past 100kyr may have differed by up to 30% (Gosse & Phillips, 2001; Dunai, 2001).

Lal & Peters (1967) estimated production rates of thermal and fast neutrons in the atmosphere based on experimental and observational data and these measurements form the basis for calculation of production rates within rocks (Lal, 1988). Although

early work (e.g. Lal, 1988; 1991) treats the Earth's magnetic field as a dipole field (which is true as a first-order approximation), the geomagnetic field has a considerable non-dipole component which varies regionally.

Near the Earth's surface, the secondary cosmic ray flux which causes the bulk of cosmogenic nuclide production is split almost evenly between neutrons and muons (Granger & Riebe, 2007). Production of cosmogenic isotopes in-situ (terrestrial cosmogenic nuclides or TCNs) occurs by three principal mechanisms: high energy nucleon spallation, neutron capture reactions and muon-induced nuclear disintegrations (Lal, 1988). In spallation reactions, the target nucleus is broken by the kinetic energy of impact, producing a lighter nucleus; in negative muon capture, muons are captured by charged nuclei, e.g. reacting with protons to form neutrons with the excess energy breaking up the target nucleus (Gosse & Phillips, 2001; Granger & Riebe, 2007). In both cases, cosmogenic ^{10}Be is produced from oxygen in quartz; ^{10}Be is not produced by neutron capture in quartz. Cosmogenic ^{10}Be is a radioactive nuclide which is also present as atmospheric and meteoric nuclides, but is virtually non-existent in rocks prior to emerging into the cosmic ray field. Quartz is an ideal mineral for study as it is resistant to chemical weathering and loss of nuclides, and because it is abundant in silicate rocks and has a simple target chemistry (von Blanckenburg, 2005).

Negative muon capture is responsible for only ~2% of ^{10}Be production at the ground surface but is the dominant process at depths greater than ~3m (Granger & Riebe, 2007), and fast muon reactions become important at greater depths (Heisinger *et al,*

2002a). At sea level and high latitude, spallation reactions are responsible for ~96% of cosmogenic ^{10}Be production at the surface (Heisinger *et al*, 2002b; see figure 4.1).

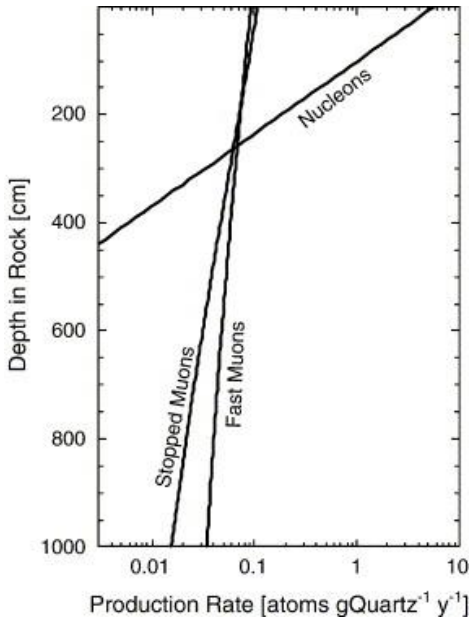

Figure 4.1: Change in production rates with depth below the rock surface for nucleons (spallation reactions) and stopped and fast muons. Source: von Blanckenburg, 2005.

In order to model the concentration of nuclides in a landscape, it is essential to understand the depth dependence of production rates within the lithosphere, and the absorption mean free path, or attenuation length (Λ), is central to this concept. The mean free path is defined as the range within which the number of particles is reduced to 1/e, or the thickness of a slab or rock required to attenuate the intensity of the cosmic ray flux by a factor of 1/e, and is expressed in g/cm^2 (Gosse & Phillips, 2001). The mean attenuation path length, or absorption depth scale, z* can be described as an absorption law (Lal, 1991; von Blanckenburg, 2005) thus:

$$z^* = \frac{\Lambda}{\rho} \qquad [4.1]$$

where, where ρ is the bulk density of the rock (~2.6g/cm^3 for granite). For nucleons, Λ≅150g/cm^2 (e.g. Gosse & Phillips, 2001) and so in silicate rocks z* is typically ~60cm. At 2m depth the nucleonic production rate is only about 3% of that at the surface (von Blanckenburg, 2005) and muonic production becomes dominant. For the purpose of the erosion rate calculator produced by Balco *et al* (2008), Λ=160g/cm^2.

Lal (1991) describes the change in production rate with depth thus:

$$P_x = P_o e^{-(\frac{x\rho}{\Lambda})} \quad [4.2]$$

P_x is the production rate at depth x, P_o is the surface production rate and ρ is the density of material.

4.1.3 Denudation Rate Models

4.1.3.1 Exposure Age/Erosion Rate Model

Interpretation of isotopic data to produce useful denudation rates requires the use of a feasible model. Lal (1991) described such a model based on two variables, exposure time and erosion rate, and which forms the basis of current denudation rate models and for the basin-wide denudation rate model. Lal (1991) derived equations to calculate the concentration of cosmogenic nuclide, N, for a surface sample as follows (assuming that sufficient time has passed for the surface to be at steady state):

$$N = \frac{P_o}{(\lambda + \frac{\varepsilon\rho}{\Lambda})}$$

[4.3]

where P_o is the production rate at the surface, λ is the nuclide decay half-life, and ε the erosion rate. Solving this for ε gives:

$$\varepsilon = \frac{\Lambda}{\rho\left(\left(\frac{P_o}{N}\right) - \lambda\right)} = z^* \left(\left(\frac{P_o}{N}\right) - \lambda\right)$$

[4.4]

If loss of nuclides from the surface through erosion is much greater than loss through radioactive decay, i.e. for erosion rates greater than 1mm/kyr for ^{10}Be (Brown *et al*, 1998), the decay term can be ignored and the equation becomes further simplified:

$$\varepsilon = \frac{z^* P_o}{N}$$

[4.5]

Erosion rates calculated in this manner are model values and generation of these rates depends on underlying assumptions implicit in the models. Lal's (1988; 1991) erosion rate models are underpinned by the following assumptions:

- production rates have been constant over time
- denudation rate has been constant for long enough to allow the cosmogenic nuclide concentration to have achieved secular equilibrium with respect to production by incoming cosmic radiation and loss through decay and denudation
- minerals at the surface have no prior exposure history
- denudation is occurring at the surface

Although production rates are unlikely to have been constant over time, the scaling factors of Dunai (2001) account for secular variation of the geomagnetic field and a correction can therefore be applied. There are many situations where the nuclide concentration will not have reached secular equilibrium, e.g. where erosion is occurring episodically rather than continuously or where climate has changed abruptly, and corrections can also be made in these situations (e.g. Muzikar, 2009; Muzikar, 2008; Schaller & Ehlers, 2006; Granger & Riebe, 2007). Exposure history of samples can be determined using paired nuclides such as ^{10}Be and ^{26}Al (e.g. Nishiizumi *et al,* 1991; Bierman & Caffee, 2001).

4.1.3.2 Catchment-Averaged Denudation Model

While the above erosion rate model simply provides a means to calculate erosion rate

at a specific point on the landscape, it also forms the basis of a model to calculate the erosion rate of an entire catchment based on the average concentration of cosmogenic nuclide in sediment exiting the basin, e.g. in quartz. Assuming hillslope surfaces are contributing sediment in proportion to their erosion rate, the average nuclide concentration in the quartz should reflect the erosion rate of its contributing area. In this way, fluvial processes provide a natural means of averaging the erosion rate (Bierman & Steig, 1996; Granger *et al*, 1996).

The interpretative model for calculating catchment-scale erosion rates is used on the same basis as that for outcrop-scale erosion, but comes with its own specific set of assumptions. Although it is inevitable that some assumptions will not be strictly met, the accuracy of the method is usually sufficient to yield useful results (von Blanckenburg, 2005). Assumptions for the basin-scale model are as follows:

- denudation is uniform over time, such that the basin is in isotopic equilibrium; this may never be strictly achieved and steady erosion rates may be difficult to verify (Bierman & Steig, 1996), but changes in sediment generation over time can be buffered by the soil mantle (Bierman & Nichols, 2004)
- each area of the catchment contributes quartz in proportion to its erosion rate and contributing rock types contain similar grain size distributions; these are reasonable assumptions in areas of constant lithology
- sediment storage is minimal
- sampled sediment is spatially and temporally representative of all sediment leaving the basin

- mass loss from the basin is primarily through surface lowering

The assumption that sampled sediment is representative of all sediment leaving the basin is likely to be valid where there is no strong relationship between grain size and nuclide concentration. Assuming this is the case, and that changes in denudation rate are either buffered by the soil mantle or can be compensated for, all other assumptions can be satisfied by careful selection of sampling sites.

The spatially averaged denudation rate is described by the same equation (Lal, 1991) that governs concentration in bedrock surfaces and vertically mixed soils (Equation 4.5), assuming that there is little variation in P_o (such that a single production rate is appropriate for all locations in the basins), that erosion is rapid enough that the decay term can be neglected, and that long term sediment storage is minimal (Brown *et al*, 1995). The decay term can be neglected where erosion rates are more than a few m/Ma and sediment storage times are less than several 100kyr (Bierman & Steig, 1996).

Nuclide concentrations reflect the total mass lost from a basin, by both chemical weathering and physical erosion, but chemical weathering can preferentially enrich quartz in bedrock, leading to quartz having a longer residence time and therefore underestimating erosion rates (Small *et al*, 1999). If the enrichment of quartz from bedrock to soil can be quantified, an equation provided by Granger & Riebe (2007) following the logic of Small *et al* (1999) can be used to compensate for the effects of quartz enrichment:

$$N = \Sigma P \Lambda \varepsilon \left\{ \left(\frac{f_s}{f_b} \right) + \left[1 - \frac{f_s}{f_b} \right] e^{\frac{-\rho h}{\Lambda}} \right\}$$

[4.6]

where f_s is the fractional quartz concentration in soil, f_b is the fractional quartz concentration in bedrock, and h is the soil thickness. The quartz enrichment factor, f_s/f_b, can be easily estimated using the enrichment of an insoluble element such as zirconium as a proxy (Granger & Riebe, 2007). Unless the weathering environment is extreme, bias in erosion rates due to dissolution will be a small part of the overall uncertainty in erosion rate calculations (Riebe *et al*, 2001).

Changes in erosion through time can affect nuclide concentration, although these changes can be damped by the residence time of quartz in the soil (Granger & Riebe, 2007). When a surface is eroding, underlying material is continually replacing material that is removed from the surface by erosion, and as this underlying material moves closer to the surface it is exposed to more intense cosmic radiation. This means that the nuclide concentration in a surface sample will have built up over the time taken for the sample to be brought from depth to the surface. The concentration is therefore moderated by denudation rate (i.e. the rate at which the sample is moved towards the surface), the nuclide production rate, and the depth scale, z*. Lal (1991) introduced the concept of 'apparent exposure age', T_{eff}, which is calculated thus:

$$T_{eff} = \frac{N_o}{P_o} = \frac{1}{\lambda + \frac{\varepsilon \rho}{\Lambda}}$$

[4.7]

and the decay constant, λ, is usually insignificant for moderate to fast erosion, as discussed above. T_{eff} can also be considered to be the timescale over which the

denudation rate is averaged. The averaging time is therefore a function of the denudation rate, and corresponds to the time the sample spends in the rock or soil within z* of the surface (von Blanckenburg, 2005).

Cosmogenic averages are exponentially weighted over time, and tend to reflect primarily erosion during the last several thousand years (Riebe *et al,* 2001), depending on the erosion rate, but the denudation rate dictates how long the surface retains a 'memory' of previous denudation rates, and so this averaging time scale is significant when we are dealing with regions which have been subject to change in denudation rate, such as the transition from glacial to interglacial climate in the study area. In order to completely erase any memory of previous denudation signals, 2-3m (or 3-5 absorption depth lengths) must be removed (Bierman & Steig, 1996) under a constant weathering regime (Reinhardt *et al,* 2007), although removal of ~1m of material would be sufficient to damp the change in most cases (von Blanckenburg, 2005). Otherwise the denudation rate determined will be a composite or average of the two different rates rather than a true representation of the present steady-state erosion rate. When considering the less dramatic Holocene climatic fluctuations in the study area, this concept is useful, because these small changes are damped (von Blanckenburg, 2005), however, the memory of higher denudation rates during the last glacial may not have been erased (e.g. Schaller & Ehlers, 2006).

The disparity between the calculated erosion rate and 'true' erosion rate, introduced by a change in erosion rate or by episodic erosion, depends on the denudation rate itself, the depth and temporal spacing of erosion events, and the isotope half-life

(Bierman & Steig, 1996). With increasing denudation rates, the disparity between the nuclide-derived and 'true' erosion rates decreases (Schaller & Ehlers, 2006; Granger & Riebe, 2007). Where erosion style changes dramatically, e.g. from landsliding to non-landsliding erosional regimes, there may be transients in nuclide concentration lasting tens of thousands of years, and the response time of the landscape is a function of bedrock weathering rate and landsliding rate (Niemi *et al,* 2005).

The relationship between grain size and ^{10}Be concentration can provide information about geomorphic processes. In humid regions, where deep-seated landslides are abundant, Brown *et al* (1995) found a distinct correlation between grain size and ^{10}Be concentration in quartz, such that coarser grains had a much lower concentration than finer material. Conversely, Clapp *et al* (2002) found ^{10}Be concentration and grain size to be independent of each other in arid regions, where sediment tends to be transported in discrete pulses relating to infrequent large storm events which move all grains sizes equally. Large bedrock landslides can incise to depths greater than the attenuation lengths of cosmic rays, and can therefore mobilise sediments with little or no nuclide abundance (Niemi *et al,* 2005). Numerical simulations (Niemi *et al,* 2005) indicate that the temporal stability of erosion rates decreases with increased ratios of landsliding to bedrock weathering within a catchment, suggesting that sediment sampling is more appropriate than bedrock sampling in regions dominated by mass-wasting processes. With increasing proportion of bedrock weathering, nuclide-derived erosion rates become closer to the volumetric erosion rate for any catchment scale (Niemi *et al,* 2005). Reinhardt *et al* (2007) combined numerical analyses and ^{10}Be in fluvial sediments from high relief, rapidly eroding terrain and concluded that

mean catchment erosion rates can still be reliably estimated from ^{10}Be where erosion is primarily accomplished through shallow (<3m) spalling processes; where landsliding is more deep-seated the nuclide-derived erosion rate will only be a minimum rate. Anthropogenic erosion can also remove near surface soils to average depths of ~500mm in developed catchments; this is comparable to the apparent attenuation length for nuclide production, and so concentration of ^{10}Be in river sediments should retain a memory of pre-development conditions (Brown *et al*, 1998).

4.1.4 Production Rate Calculations

4.1.4.1. Measuring Production Rates

Although production rates of ^{10}Be by muons are specified (e.g. Heisinger *et al,* 2002a; 2002b), production rates of ^{10}Be in quartz have to be determined from sites of known age and scaled to the sampling site. Production rates have been determined on glacially polished surfaces, glacial deposits and landslides of known age. In order to derive a reference production rate at sea level and high latitude, these scattered measurements must be normalised using a particular scaling scheme, and the reference production rate can then be scaled to any sample site. Balco *et al* (2008) have provided an online calculator, codifying previously published procedures, to help derive erosion rates and exposure ages in a consistent manner. A full description of the normalisation process, including a list of published calibration measurements used in the calculator, is provided by Balco *et al* (2008).

4.1.4.2 Calculating Basin-Averaged Rates

For basins with high relief and which span several degrees of latitude, it will usually be necessary to calculate a spatially weighted average production rate. However, where elevation and latitude do not change more than several hundred metres or several degrees, and slopes are <20°, a mean elevation may be sufficient (Bierman & Steig, 1996; Bierman & Nichols, 2004).

4.1.4.3 Scaling Factors

Scaling factors allow for description of the altitudinal and latitudinal dependence of production rates for in situ cosmogenic nuclides. When using the calculator provided

by Balco *et al* (2008), production due to muons is independent of latitude or time, and so the scaling factors used are solely for nuclide production by spallation. Balco *et al* (2008) provide a description of the five different scaling schemes used with the online calculator; the current study will use the scaling factors of Dunai (2000; 2001). Methods for calculating the elevation, latitude and geometry corrections have been presented and are based on theory and neutron flux data (Lal, 1991). Calculation of scaling factors based on Lal (1991) were based only on the dipole field, whereas the scaling factors of Dunai (2000) also incorporate the influence of non-dipole contributions to the geomagnetic field. At sea level and latitudes of 20-40°, the factors of Dunai (2000) are up to 18% lower, and at high altitudes more than 30% higher, than those of Lal (1991). The scaling factors of Dunai (2000) use the same approach as Lal (1991), except that only absorption mean free path lengths obtained at elevations relevant for exposure age dating are considered. The latitudinal dependence of cut-off rigidity of geomagnetic field also causes different values of absorption mean free path length at different geomagnetic latitudes, because absorption of primary and secondary particles is energy-dependent (Dunai, 2000). In addition, since the dipole and non-dipole field are known to have varied in intensity and position in the past, Dunai (2001) has produced scaling factors which fully describe production rates.

4.1.4.5 Shielding

Topography can reduce nuclide production both by shielding a proportion of incoming radiation, and by modifying the effective attenuation length by changing the angle of incidence for sloping surfaces (Dunne *et al*, 1999; Gosse & Phillips,

2001), and for steep terrain, an additional scaling factor is required for topographic shielding. Dunne *et al* (1999) derived equations for calculating geometric shielding by thick objects, and shielding by surface slope. If we assume that shielding by distant objects is negligible in relation to shielding by surface slope, we can use the following equation from Dunne *et al* (1999) to calculate the shielding factor at a sample point:

$$S = 1 - (3.6 \times 10^{6}\ \alpha^{2.64}) \qquad [4.8]$$

where S is the shielding factor and α is the dip angle of the slope (Figure 4.2).

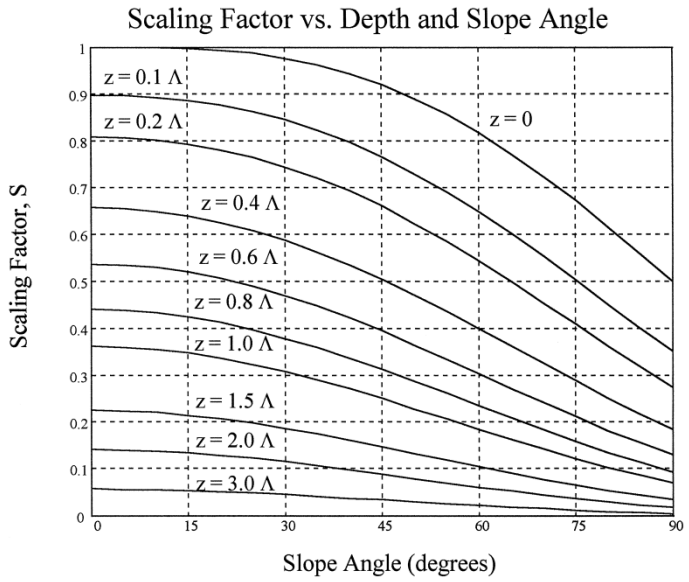

Figure 4.2: Variation in scaling factors for topographic shielding as a function of dip angle of slope. Source: Dunne *et al,* (1999).

The situation becomes more computationally intensive when we consider the case of basin-averaged shielding factors. Codilean (2006) has described a less labour-intensive method for calculating topographic shielding based on relief shadow modelling over large areas, using a high-resolution DEM. The method described by Codilean (2006) agrees well with the method of Dunne *et al* (1999) when a DEM of

10m resolution is used. However, the highest resolution DEM available for the study area is 30m, and increasing DEM grid size can cause an artificial increase in basin-averaged topographic shielding factors (Norton & Vanacker, 2009). Binnie *et al* (2006) utilised the equation of Dunne *et al* (1999) to calculate slope angle shielding, but applied it to a hypothetical plane projected across the drainage divides of a basin, using the maximum and minimum elevation of the basin to derive an approximation for α. This approach assumes that variations in slope within the basin will not average production rates across the basin since the total flux through the projected plane will be the same regardless of internal morphology of the basin (Binnie *et al,* 2006). In the present study, the approach of Binnie *et al* (2006) and Binnie *et al* (2008) to calculating slope shielding factor is utilised. Shielding can also occur in relation to surface cover, e.g. by snow, sand, soil or peat, or vegetation (Gosse & Phillips, 2001), although snow shielding is irrelevant for the current study. Attenuation of the cosmic ray flux in temperate forests can diminish secondary radiation due to absorption by trees, and spatial and temporal variability in production could result from a heterogeneous distribution of biomass (Plug *et al,* 2007). Corrections for vegetation shielding will typically be small, but where basins are heavily vegetated, an additional correction factor should be applied for rays absorbed by organic matter; the cosmic ray flux can be decreased by as much as 4% in extremely dense forest (Cerling & Craig, 1994). Shielding by biomass in most terrestrial environments is minimal (Brown *et al,* 1995) and changes in vegetation shielding over time should also have a small effect. While temporal variability in vegetation shielding may have an effect on dating experiments, it will not affect derivation of catchment-wide erosion rates (Plug *et al,* 2007).

4.1.5 Sampling and Measurement

4.1.5.1 Sample Collection Strategy

Sample intervals were chosen primarily to reflect the full range of precipitation along the length of the Chilean Coastal Cordillera, while individual catchments were chosen in order to satisfy the assumptions made for the basin-wide erosion rate model. There were several criteria for sample selection:

- Catchment located in granitic lithology (predominantly granodiorite), although some catchments were primarily schist with quartz veining (fig. 4.3)
- Catchments of similar morphology were sampled and samples were always taken above the knickpoint
- Catchments which exhibited any evidence of landsliding or mass movements were avoided
- Only small catchments were sampled, and only those with no input from the Andes
- Catchments with no evidence of sediment storage were selected
- Samples were sieved in the field (mostly dry sieved) and only the 250µm to 4mm size fraction was returned to the lab

Samples were taken from accumulations of quartz-rich sand within the active channel, although the exact site of sample collection varied depending on the abundance of quartz and the most common grain size in the channel, on whether the channel was dry or wet and on the speed of water flow in the channel, and on the

degree of riparian vegetation. Photos of the variation in sampling sites across the study area are shown in Figure 4.4.

Sample sites were also selected to encompass the full range of vegetation characteristics within the study area, and the density of sample sites was therefore particularly high in the climatic transition zone, where there were rapid changes in the character of the vegetation cover with latitude. The primary changes in vegetation are related to percentage cover, percentage of herbaceous vegetation, and percentage of tree cover. Photos showing areas of characteristic vegetation are shown in Figure 4.5.

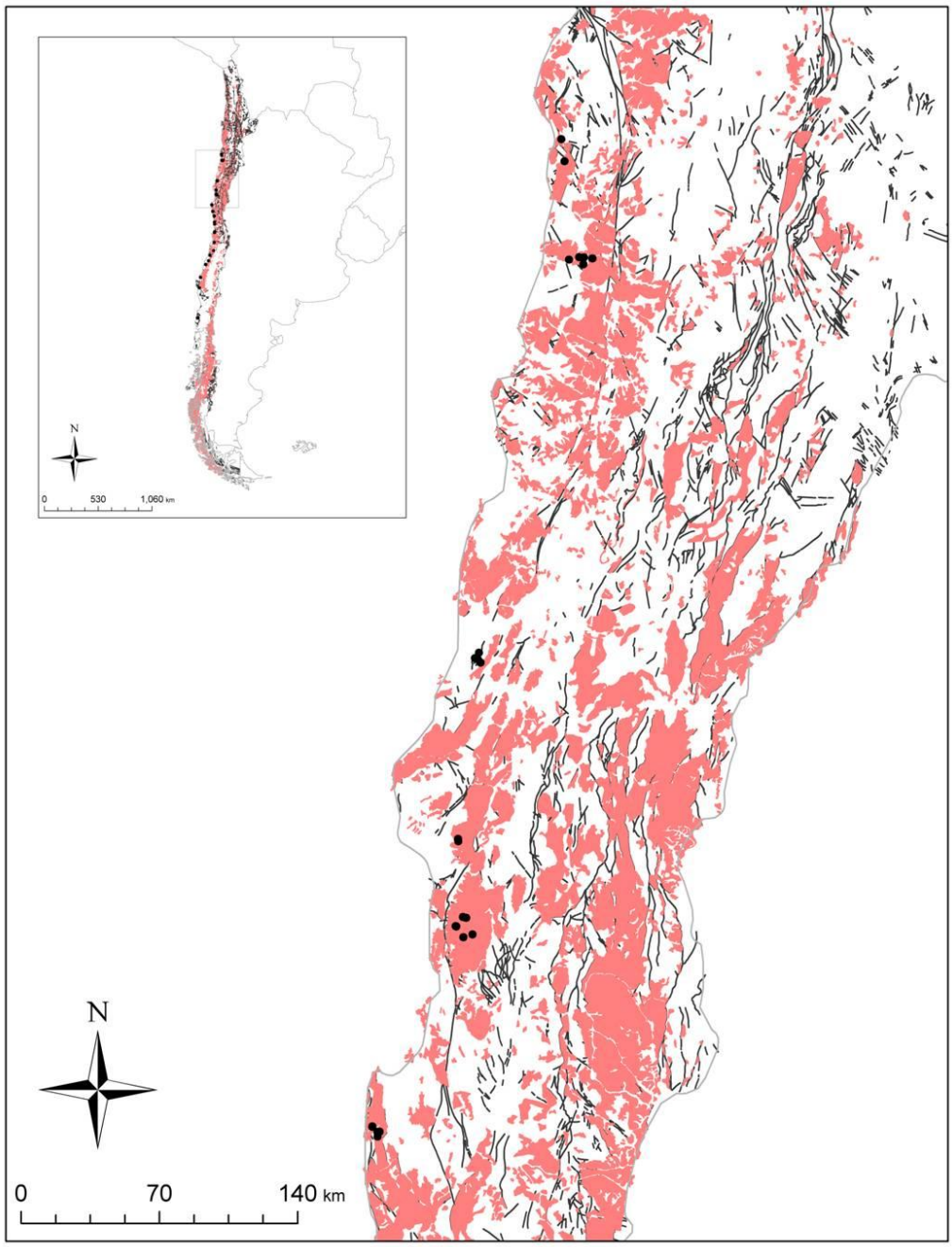

Figure 4.3(a): Northern part of study area. Sample locations are shown by black dots and faults by black lines. Pink represents the occurrence of granitoid rocks (primarily granite, granodiorite and monzonite) throughout Chile. Samples were collected primarily from catchments draining areas underlain by these granitoid rocks, except in rare cases where underlying lithology was schist with abundant quartz veins.

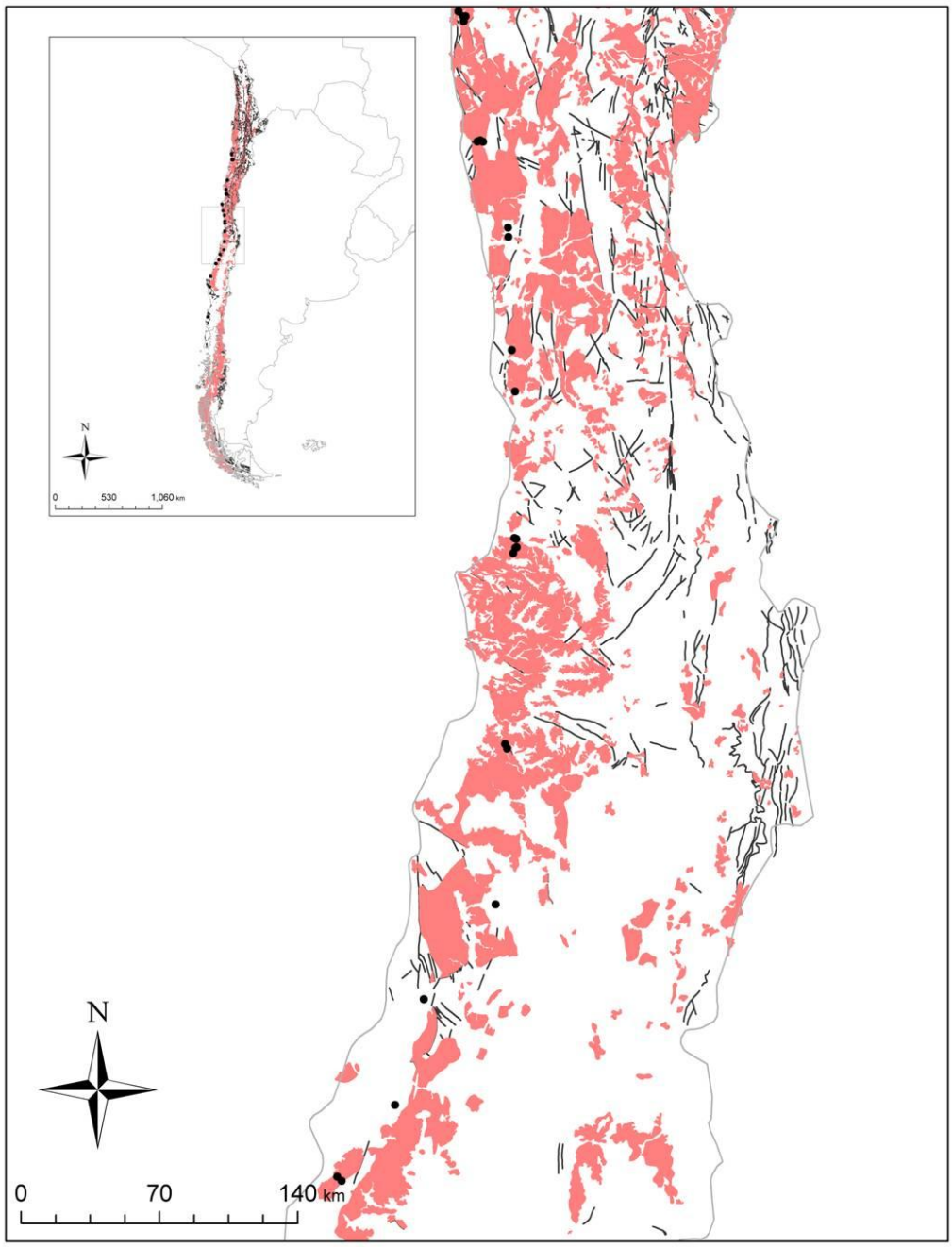

Figure 4.3(b): Central part of study area. Sample locations are shown by black dots and faults by black lines. Pink represents the occurrence of granitoid rocks (primarily granite, granodiorite and monzonite) throughout Chile. Samples were collected primarily from catchments draining areas underlain by these granitoid rocks, except in rare cases where underlying lithology was schist with abundant quartz veins.

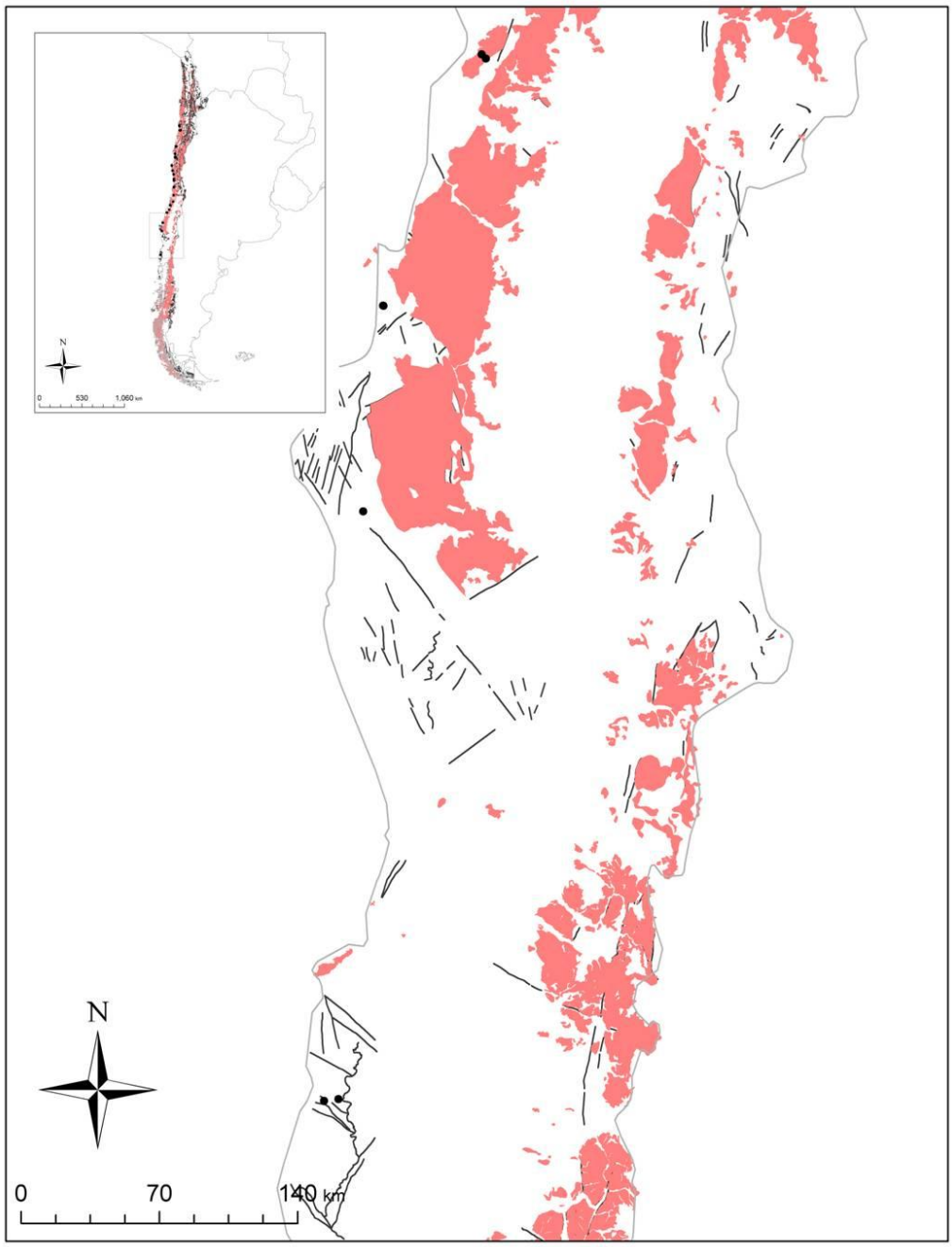

Figure 4.3(c): Southern part of study area. Sample locations are shown by black dots and faults by black lines. Pink represents the occurrence of granitoid rocks (primarily granite, granodiorite and monzonite) throughout Chile. Samples were collected primarily from catchments draining areas underlain by these granitoid rocks, except in rare cases where underlying lithology was schist with abundant quartz veins.

Figure 4.4(a): Example of sites sampled for cosmogenic isotope analysis. This example is from sample site LC07-60 (~26˚7'S) and illustrates a sample collected in a dry channel with large accumulations of quartz-rich sand.

Figure 4.4(b): Example of sites sampled for cosmogenic isotope analysis. This example is from sample site LC07-47 (~26˚33'S) and illustrates a sample collected in a dry channel which is dominated by coarser, more angular material. Sample was collected from the finer-grained, interstitial, quartz-rich material.

Figure 4.4(c): Example of sites sampled for cosmogenic isotope analysis. This example is from sample site LC07- 37 (~29˚13'S) and illustrates a sample collected in a narrow dry channel where the bed is mainly quartz-rich sand.

Figure 4.4(d): Example of sites sampled for cosmogenic isotope analysis. This example is from sample site LC07- 11 (~31˚7'S) and illustrates a sample collected from sand bars or small pockets of sand in a channel dominated by coarser material and with some ephemeral vegetation in the channel.

Figure 4.4(e): Example of sites sampled for cosmogenic isotope analysis. This example is from sample site LC07- 10 (~32˚56'S) and illustrates a sample collected from sandy material in a moist stream bed with leaf litter and dense riparian vegetation.

Figure 4.4(f): Example of sites sampled for cosmogenic isotope analysis. This example is from sample site LC07- 03 (~32˚59'S) and illustrates a sample collected in a stagnant pool where we were able to gain access to the channel (the rest of the channel was inaccessible due to dense riparian vegetation).

Figure 4.4(g): Example of sites sampled for cosmogenic isotope analysis. This example is from sample site LC08-20 (~34˚36'S) and illustrates a sample collected in a narrow damp channel comprising mainly coarser material, with leaf litter, riparian vegetation and lichen and herbaceous vegetation growing in channel. Sample taken from pockets of sandier material.

Figure 4.4(h): Example of sites sampled for cosmogenic isotope analysis. This example is from sample site LC08-10 (~36˚23'S) and illustrates a sample collected in a narrow channel with dense riparian vegetation and moderate to fast flow. The sample was collected from accumulations of sand behind large boulders.

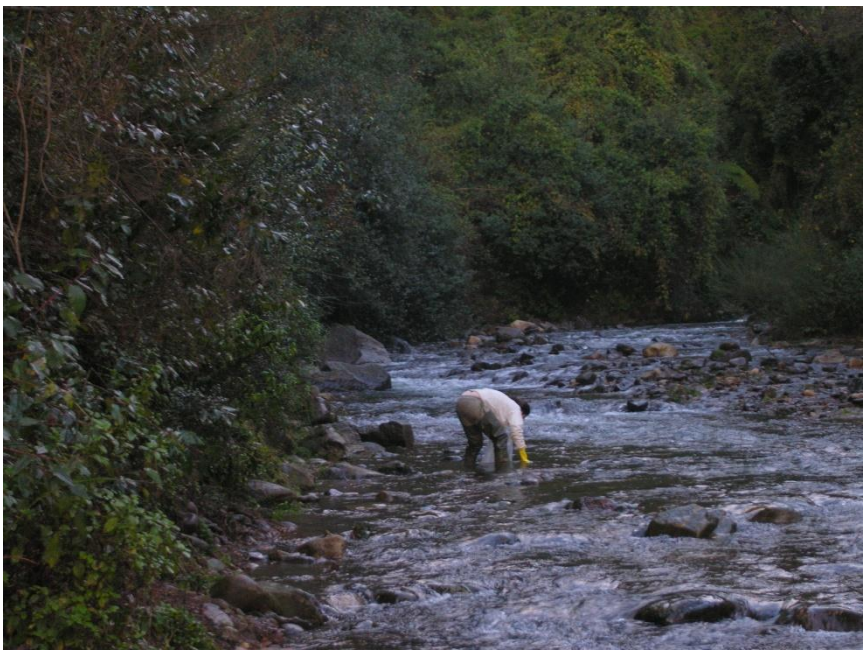

Figure 4.4(i): Example of sites sampled for cosmogenic isotope analysis. This example is from sample site LC08-07 (~37˚16'S) and illustrates a sample collected in a wider channel with moderate to fast flow and dense riparian vegetation. The sample was collected from accumulation of sand behind large boulders and in sand banks.

Figure 4.4(j): Example of sites sampled for cosmogenic isotope analysis. This example is from sample site LC08-01 (~40˚35'S) and illustrates a sample collected in a narrow channel with fast flowing stream and dense riparian vegetation. The sample was collected from accumulations of sand around large boulders in the stream bed.

Figure 4.5(a): Photo showing characteristic vegetation in the hyperarid far north of the study area. This photo was taken at sample site LC07-60. Mean annual precipitation is in the range 0-20mm. Vegetation is almost entirely absent in this region, except where coastal fogs support a patchy vegetation cover. Where scattered shrub cover exists, vegetation is dry and woody.

Figure 4.5(b): Photo showing characteristic vegetation in the arid part of the study area. This photo was taken at sample site LC07-41. Mean annual precipitation is approximately 40mm. Vegetation comprises patchy shrub cover, mainly dry/dead bushes, with large bare patches in between.

Figure 4.5(c): Photo showing characteristic vegetation in the arid part of the study area, as precipitation increases with latitude. This photo was taken at sample site LC07-22. Mean annual precipitation is 60-70mm. Vegetation comprises patchy shrub cover, often with flowering bushes, with smaller bare patches in between, and possibly includes herbaceous vegetation during rainy periods.

Figure 4.5(d): Photo showing characteristic vegetation in the arid part of the study area, as precipitation increases with latitude. This photo was taken at sample site LC08-36. Mean annual precipitation is 100-120mm. Vegetation cover is almost complete, and comprises shrubs and succulents with some interstitial herbaceous cover and small bare patches.

Figure 4.5(e): Photo showing characteristic vegetation in the semi-arid part of the study area. This photo was taken at sample site LC08-33. Mean annual precipitation is approximately 200mm. The climate supports a continuous soil cover, and bare ground gives way to herbaceous vegetation and increased tree cover.

Figure 4.5(f): Photo showing characteristic vegetation in the semi-arid part of the study area as precipitation increases with latitude. This photo was taken at sample site LC07-06. Mean annual precipitation is approximately 400mm. The climate supports a continuous vegetation cover with large areas of Mediterranean forest. Large parts of this area are covered in eucalyptus plantation.

Figure 4.5(g): Photo showing characteristic vegetation in the semi-arid to humid part of the study area. This photo was taken at sample site LC08-13. Mean annual precipitation is approximately 1000mm. The climate supports a continuous, lush vegetation cover with large areas of forest.

Figure 4.5(h): Photo showing characteristic vegetation in the humid part of the study area. This photo was taken at sample site LC08-01. Mean annual precipitation is approximately 2000mm. The climate supports a continuous, lush vegetation cover with large areas of forest which support ferns.

4.1.5.2 Laboratory Work

The end product of laboratory work carried out at the University of Edinburgh is a copper cathode filled with a mixture of beryllium oxide and niobium, which is in turn sent to the AMS facility at SUERC for analysis. In order to produce the cathode sample, pure quartz must first be extracted from the bulk sample, and this quartz must then be treated to isolate the BeO.

Quartz Extraction

Bulk samples were sieved in the lab in order to collect the 250-710µm size fraction, which was then subjected to several junk etches using HCl, to remove carbonates and Al and Fe coatings on quartz grains (Kohl & Nishiizumi, 1992), and H_2SiF_6, to dissolve non-quartz components (Bourlés, 1988). Three to four quartz etches were then carried out to remove meteoric ^{10}Be and chemically isolate the quartz in the sample (Kohl & Nishiizumi, 1992). Many samples contained mafic minerals, and these were removed with a magnet where possible, or removed by separation in heavy liquid.

Isotope Extraction

Small amounts of sample were dissolved to estimate the Al content of the sample in order to check the purity of the quartz. The sample was subsequently dissolved and ^{9}Be carrier added to set the $^{10}Be/^{9}Be$ ratio, before perchloric fuming to convert insoluble fluorides to perchlorates (Yokoyama *et al*, 1999), to reduce boron levels and to liberate Al from fluorides (Binnie, 2005) and samples were then passed through anion exchange chromatography columns to remove contaminants (such as

Fe). Titanium was removed from the sample by precipitation in order to prevent its interference with AMS measurements due to contamination or reduction of the beam current (Bierman *et al*, 2002). Samples were passed through a cation exchange chromatography column to separate the Be and Al fractions, and a final perchloric fume was performed to further reduce boron levels, before the samples was precipitated as a BeOH gel which helps purify the final sample. Finally, the sample was fired to convert the BeOH gel to BeO, and the oxide was mixed with Nb and pressed into a copper cathode to produce the AMS target.

4.1.5.3 AMS Measurements

As nuclides occur in extremely low concentrations, the technique requires sensitive detection techniques. Accelerator mass spectrometry (AMS) directly measures the isotopic ratio of $^{10}Be/^{9}Be$ in the sample, and from this measurement the ^{10}Be concentration in the sample can be calculated. The particle accelerator effectively acts as a large mass spectrometer. The formation of a negatively charged ion and its subsequent acceleration to MeV energies allows the separation of ions based on their mass to charge ratio, allowing measurement of the number of ions per second in a detector (Elmore & Phillips, 1987). The high energies involved allow measurement of isotopes lower than otherwise possible (Elmore & Phillips, 1987).

All samples in this study were analysed at the Scottish Universities Environmental Research Centre (SUERC), using a National Electrostatic Corporation (NEC) 5MV Pelletron based AMS (see figure 4.6). The facility and its operation are described in detail by Freeman *et al* (2004; 2007) and Maden *et al* (2007). The sample material

(BeO mixed with Nb) is mounted in a target cathode, and the cathode is sputtered by a 6keV Cs^+ primary bream to produce a beam of negatively charged secondary ions which is then accelerated towards the high voltage terminal of the accelerator. Electrons are removed from the incoming negative ions, producing positively charged $^{10}Be^{3+}$ and $^{9}Be^{3+}$ which are then accelerated away from the terminal towards a magnetic analyser. The ions are then deflected, depending on their weight, with $^{10}Be^{3+}$ analysed with an electrostatic deflector and passed through a gas absorber cell before each atom is counted, and $^{9}Be^{3+}$ deflected into Faraday cups to measure the electrical current and determine abundance.

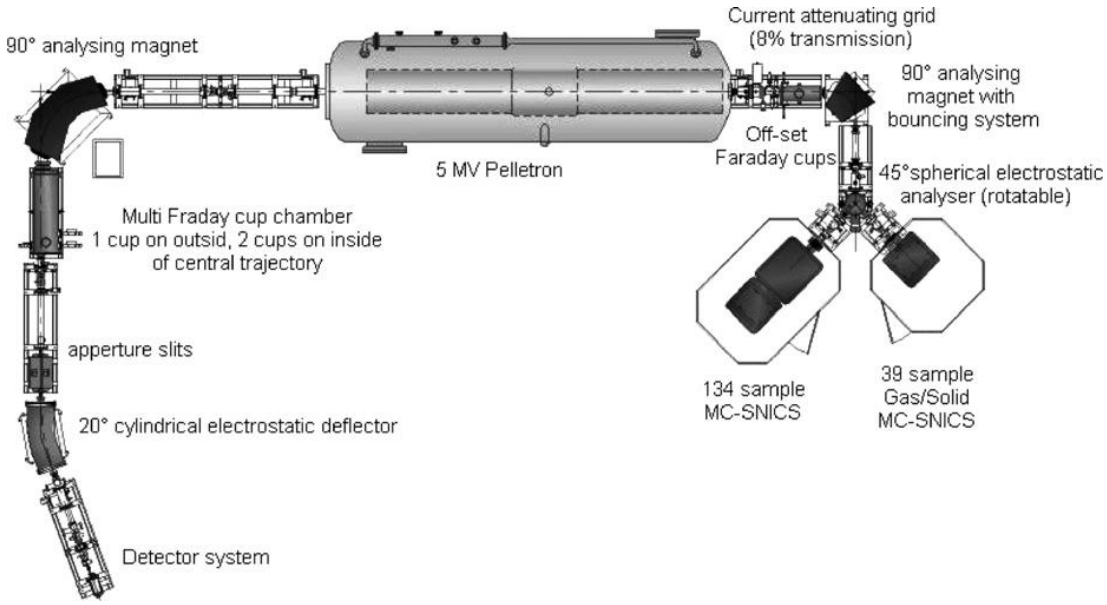

Figure 4.6: Schematic of AMS at SUERC. Source: Maden *et al,* 2007.

4.1.5.4. Nuclide Concentration Calculations

The AMS facility at SUERC returns a $^{10}Be/^{9}Be$ ratio and this must subsequently be converted to a measure of ^{10}Be in the sample. The $^{10}Be/^{9}Be$ ratio will also contain any additional ^{10}Be which has been introduced into the sample after dissolution, and

so a blank must be run with each batch of samples to account for this. Calculation of the concentration of ^{10}Be in the sample is then possible from the $^{10}Be/^{9}Be$ ratio, given the mass of ^{9}Be carrier (m_c) added and two constants: Avogadro's number, N_A = 6.02214179 +/- 0.00000030 x 10^{23} $mole^{-1}$ and the atomic weight of Beryllium, A_{Be} = 9.012182. ^{10}Be concentration can be calculated using the following equation:

$$\frac{[^{10}Be/^{9}Be_{(sample)}\, m_{c(sample)}\, (N_A/A_{Be})]-[^{10}Be/^{9}Be_{(blank)}\, m_{c(blank)}\, (N_A/A_{Be})]}{m_{qtz}} \qquad [4.9]$$

4.1.5.5 Erosion Rate Calculator

Erosion rates were calculated using the online calculator described by Balco *et al* (2008).

Inputs & Outputs

The calculator is designed to take mainly observed or measured values, with the exception of two input parameters: the ^{10}Be concentration in the sample, and the shielding factor. The calculator is strictly intended to calculate surface erosion rates at a particular site but, assuming that the range of elevation and latitude is small, can also be used for calculation of catchment-averaged rates (Balco *et al*, 2008). The calculator reports erosion rates derived using five different scaling schemes: St, based on the scaling factors of Lal (1991) and revised by Stone (2000); De, from the scaling factors of Desilets *et al* (2006); Du, using the scaling factors of Dunai (2001);

Li, using the scaling factors of Lifton *et al* (2005); and Lm, which is an adapted version of the St scheme which also uses the palaemagnetic corrections of Nishiizumi *et al* (1989). The current study at all times uses the scaling factors of Dunai (2001). In addition to the outputs reported in the table, the calculator also reports surface production rates due to spallation for the St scheme; this is not reported for the other scaling schemes as corrections are made for the variation in spallogenic production with time. Inputs and outputs of the calculator are included in Appendix 1.

4.1.5.6. Errors/Uncertainties

Uncertainty stated should consist of both internal and external uncertainties. Internal uncertainty is that resulting from measurement of nuclides and is directly available from AMS measurements, whereas external uncertainty comprises the uncertainty in scaling schemes and the uncertainty in input parameters such as the reference production rate, atmosphere pressure and the magnetic field reconstruction used (Balco *et al*, 2008).

The AMS facility returns a 1σ uncertainty for the $^{10}Be/^{9}Be$ ratio for each sample and blank analysed. In addition, there will be an uncertainty associated with each term included in the equation used to calculate ^{10}Be concentration above. Quality assurance tests carried out in the cosmogenic lab facility at the University of Edinburgh estimate error of ~3.8%, including errors and uncertainties from both lab work and AMS analysis; when assigning uncertainty to measurements the highest of the two error estimates was used in each case.

The calculator produces a combined external uncertainty to account for both scaling scheme error and input parameter error. Since most of the scaling schemes provide only a general estimate of uncertainty, Balco *et al* (2008) have utilised another approach, assuming that the scaling schemes and magnetic field reconstructions are precise and thus that any uncertainty introduced by this assumption will be discernible in the scatter among reference production rates inferred from calibration sites. This scatter can then be used to provide uncertainty for the reference production rate, taking into account scaling scheme used and the input parameters. In addition, the uncertainty associated with muogenic production, according to Heisinger *et al* (2002a; 2002b), is included in the calculator. A more detailed explanation of the associated error and uncertainty is provided by Balco *et al* (2008). It is also worthwhile to note that these systematic uncertainties have little effect on intersample comparisons (von Blanckenburg, 2006).

4.2. GIS/REMOTE SENSING PRODUCTS

4.2.1 Climate and vegetation datasets

The values of mean annual precipitation used in this study are derived from the interpolated WorldCLIM climate dataset of Hijmans *et al* (2005). The dataset has a resolution of 1km. Climate and vegetation datasets with the same spatial resolution were chosen for simplicity, and classification of vegetation for the purposes of the study was derived from the MODIS Vegetation Continuous Fields dataset described by Hansen *et al* (2000). This dataset contains proportional estimates for three different vegetation cover types: woody vegetation, herbaceous vegetation and bare ground (Figure 4.7). This type of continuous classification scheme is likely to be a more representative depiction of heterogeneous vegetation cover (Hansen *et al*, 2003). For comparison with cosmogenic data, this information was extracted for individual catchments, whereas for comparison with distribution of landscape metrics over greater areas, trends for each vegetation cover type were approximated based on climate and vegetation data extracted across the whole study area (Figure 4.8).

4.2.2 Digital Elevation Model

The 30m-resolution ASTER global DEM was used for topographic analysis of the study area. Channel networks were initially extracted in ArcGIS using a constant drop method (Tarboton *et al*, 1992) but comparison of extracted channel networks with satellite imagery highlighted the fact that this method produced unrealistically

short channel networks. Channel networks were therefore extracted using the Peuker-Douglas algorithm (Band, 1986), which determines stream source using an accumulation threshold of concave-up pixels. The appropriate threshold was chosen by varying the threshold for each group of samples and comparing the resulting networks to georeferenced satellite photos and the best estimate, given the 30m-resolution of the DEM, was used (Figure 4.9). Watersheds for the stream networks were then extracted using the TauDEM software package (http://hydrology.usu.edu/taudem/taudem5.0/downloads.html), and these watersheds were used for further analysis. Watersheds were extracted for first to fourth order streams, based on the Strahler stream order system: when two first order streams join together, they form a second order stream; when two second order streams join they form a third order stream; and so on.

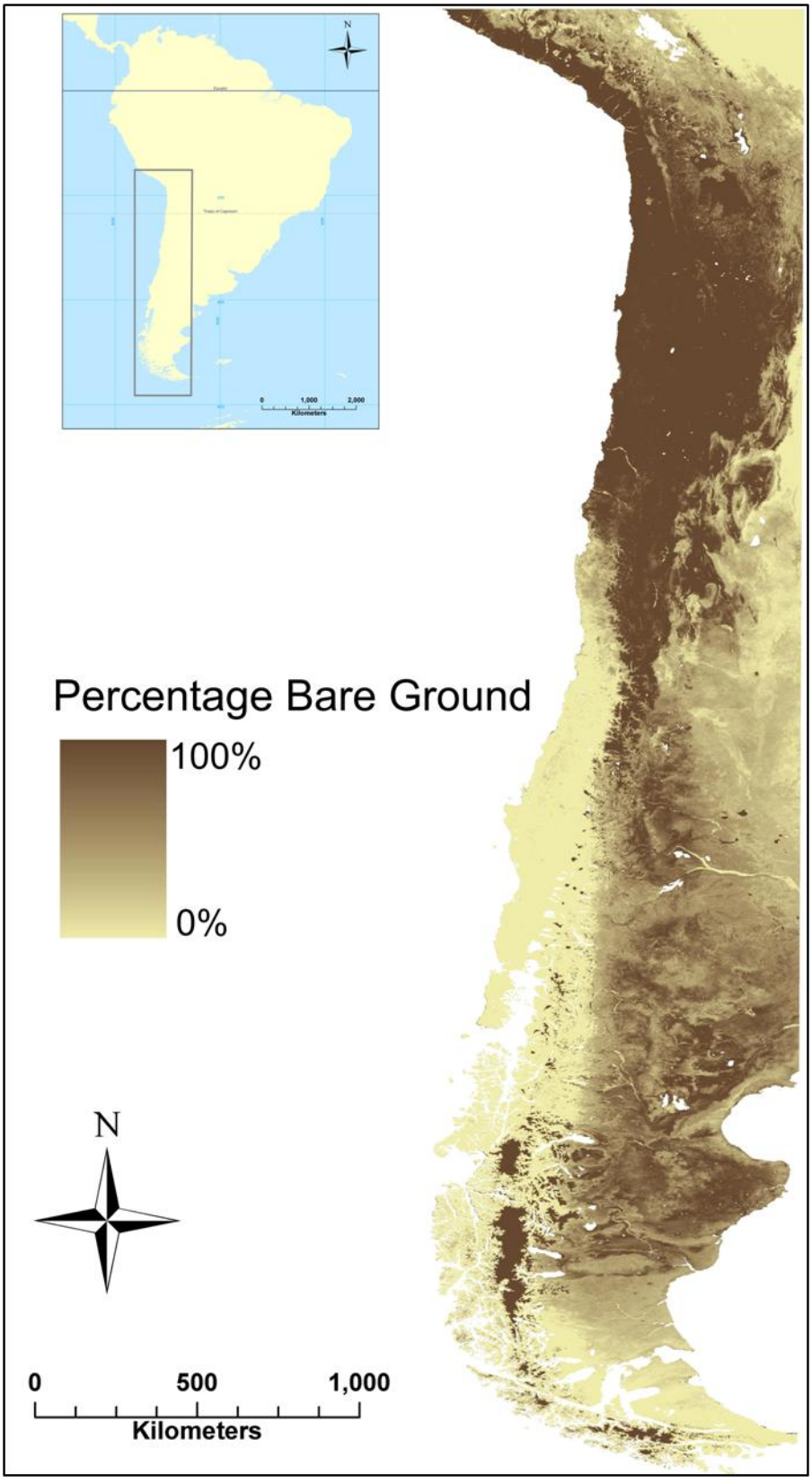

Figure 4.7(a): Distribution of bare ground for the study area. Created using the MODIS Vegetation Continuous Fields data described by Hansen *et al* (2000), which contains proportional estimates of bare ground for each pixel.

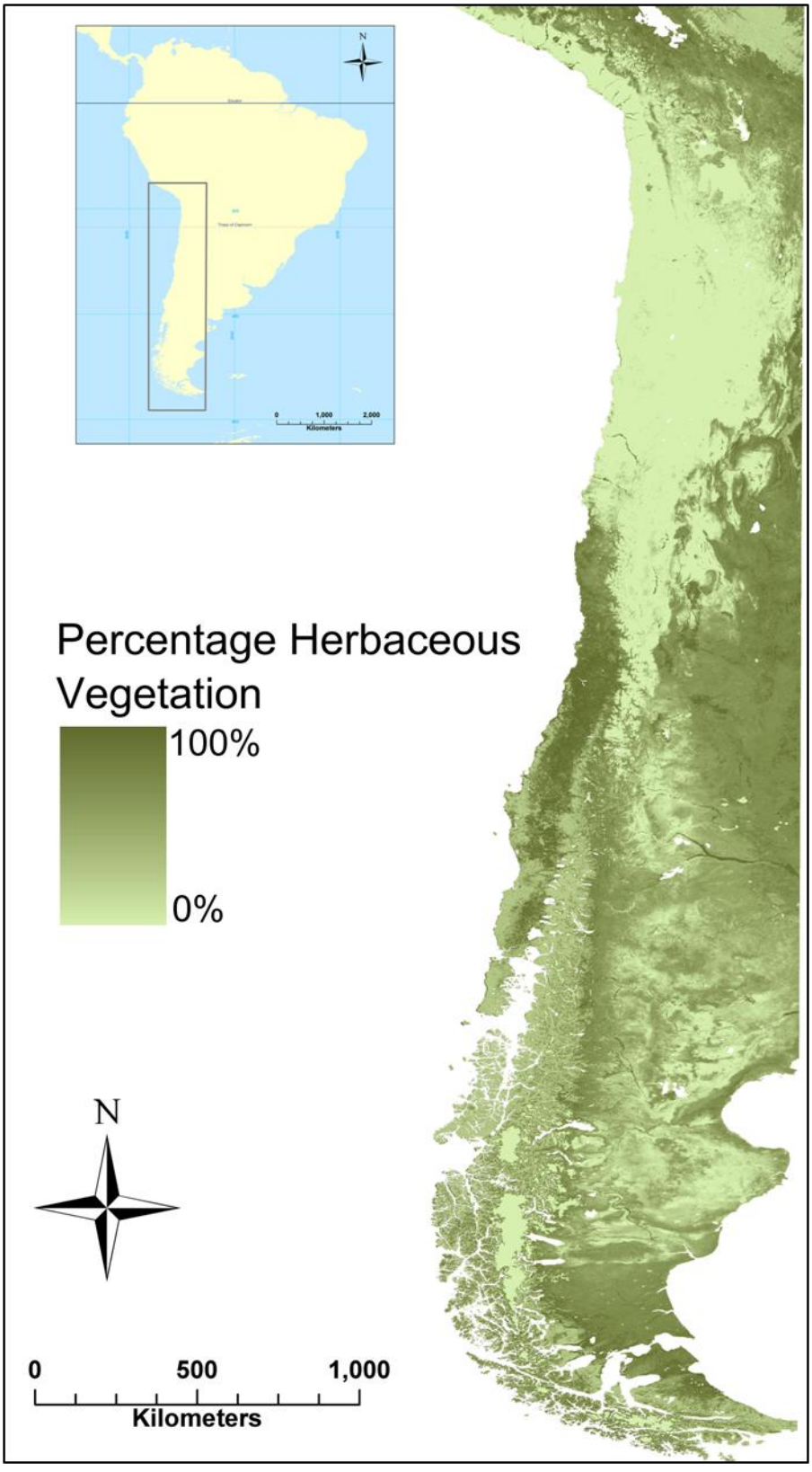

Figure 4.7(b): Distribution of herbaceous vegetation for the study area. Created using the MODIS Vegetation Continuous Fields data described by Hansen *et al* (2000), which contains proportional estimates of herbaceous vegetation for each pixel.

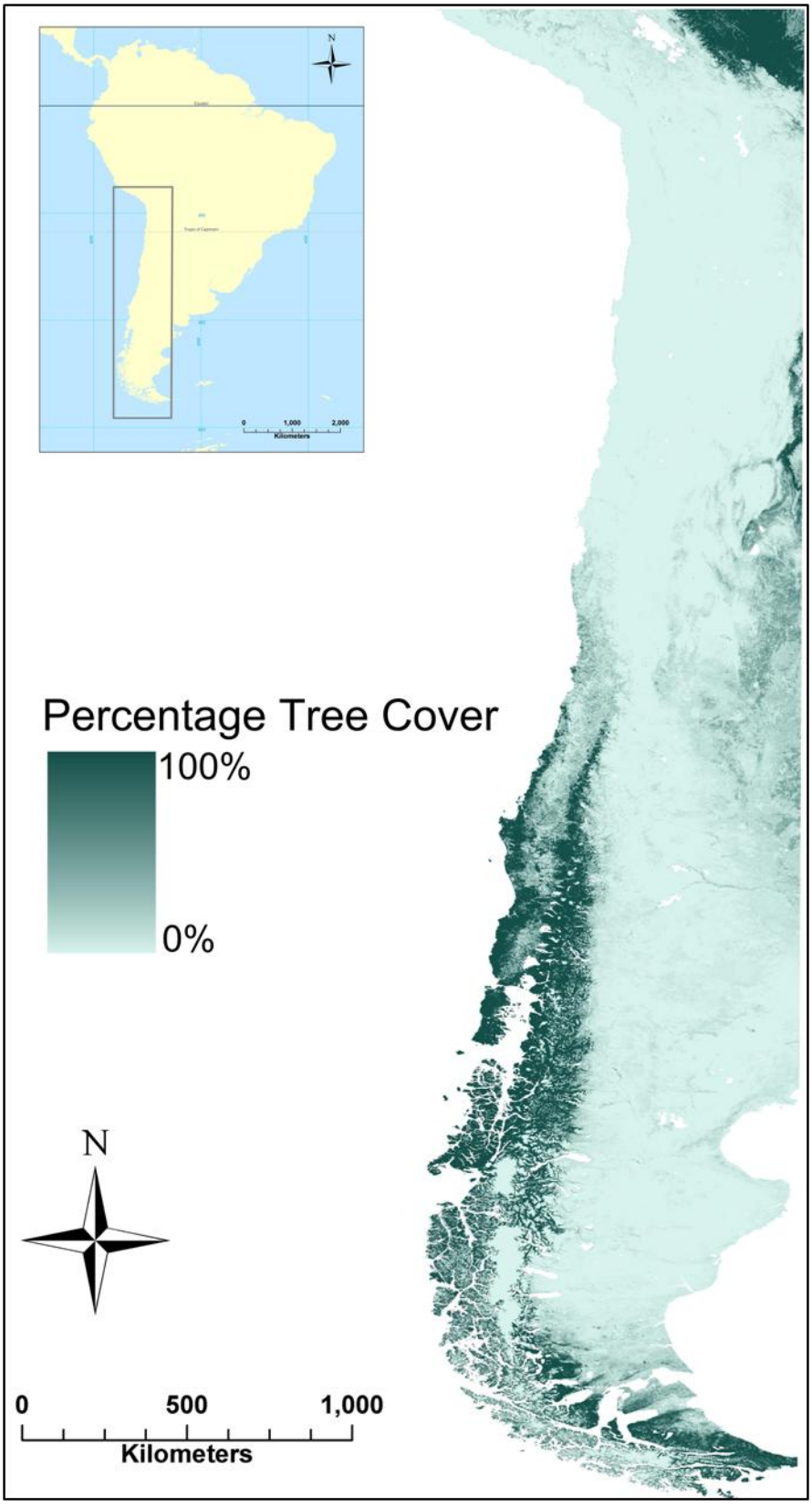

Figure 4.7(c): Distribution of woody vegetation for the study area. Created using the MODIS Vegetation Continuous Fields data described by Hansen *et al* (2000), which contains proportional estimates of woody vegetation for each pixel.

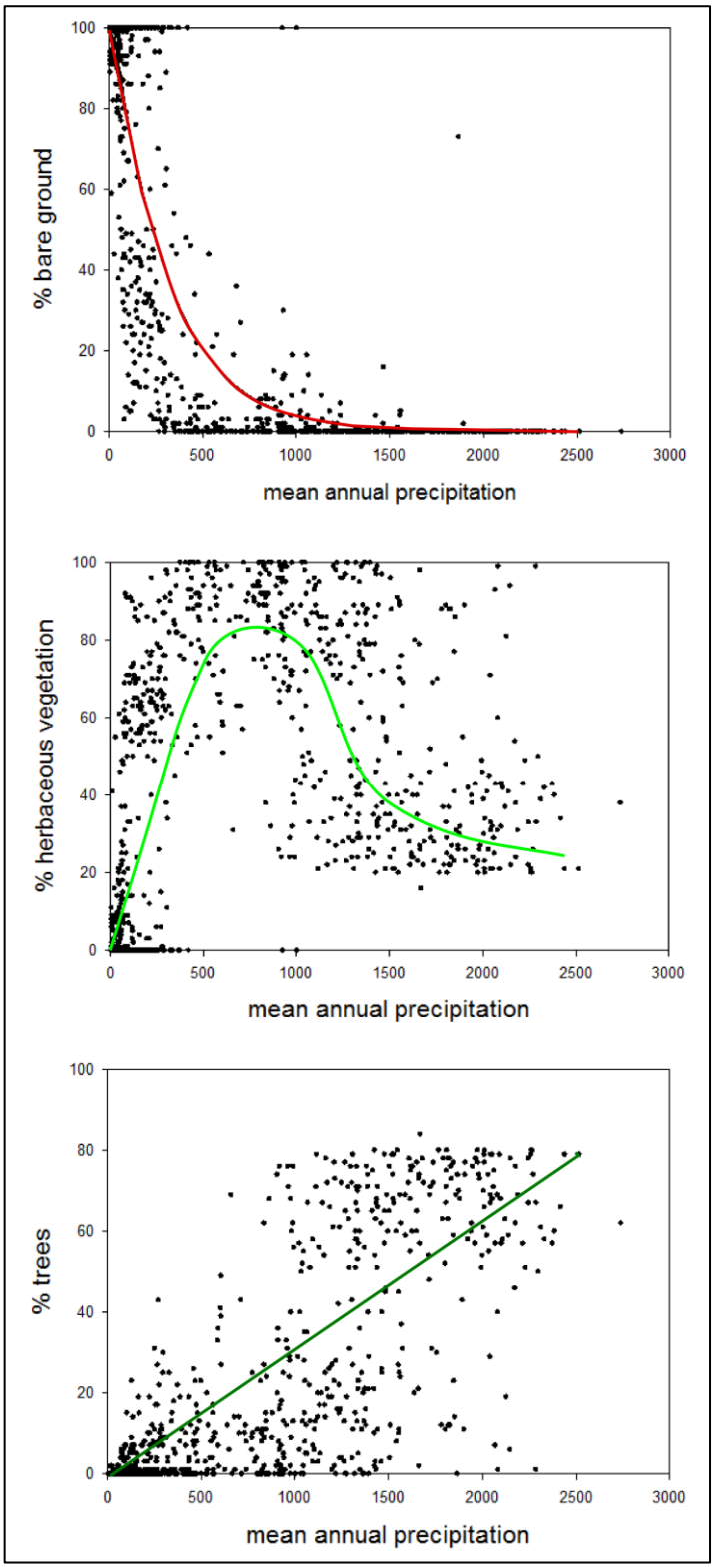

Figure 4.8: Variation in percentage of vegetation cover type with mean annual precipitation. Values were extracted for each pixel in the study area, from the datasets described by Hansen *et al* (2000) and Hijmans *et al* (2005). Approximate trends have been overlaid for comparison with DEMs.

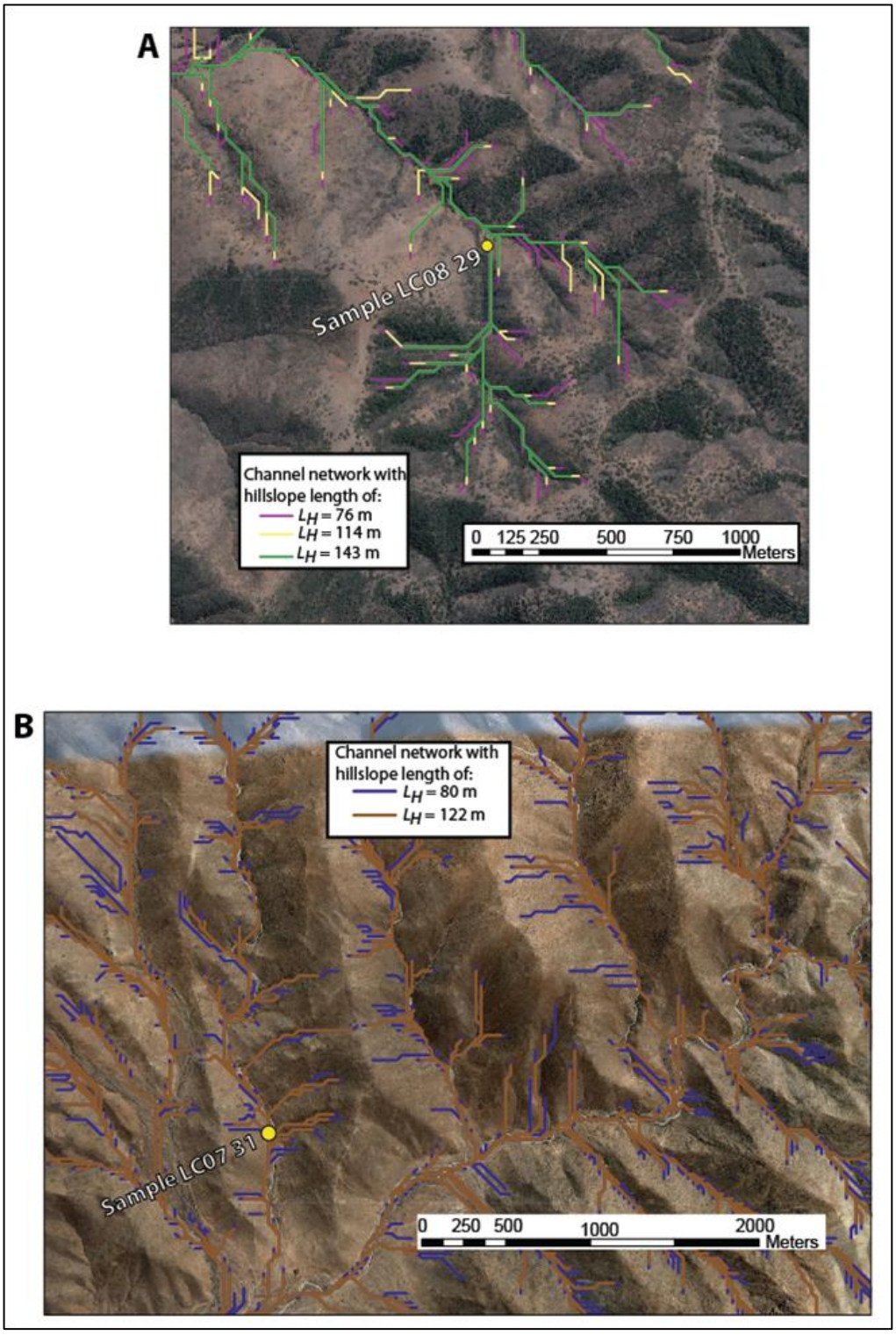

Figure 4.9: Extracted channel networks. For sample LC08-29, L_H was estimated to lie between 70m and 120m (A). For sample LC07-31, L_H was estimated to lie between 80m and 120m (B). Figure created by Simon Mudd.

Chapter 5: Declaration of co-authorship

This chapter is currently being submitted for publication and is presented in its final form with minor alterations to fit the format of the rest of the thesis. I declare that I was the first author of this chapter, and that the final version presented here has benefitted from the input of several co-authors: Tibor J. Dunai (now at Institut für Geologie und Mineralogie, Universität zu Köln, Germany), Simon M. Mudd and Francis E. Mayle (both from the School of Geosciences, Edinburgh) and Sheng Xu (from the Scottish Universities Environmental Research Centre, East Kilbride).

5. CLIMATE AND VEGETATION CONTROL OF SEDIMENT DELIVERY FROM HILLSLOPES

5.1. ABSTRACT

Recent attempts to elucidate a distinct climatic effect on erosion rates at the catchment scale have found that there is little or no correlation between precipitation and erosion rates. This, perhaps, is unsurprising because in tectonically active regions, topography will tend toward steepening until erosion rates match tectonic uplift rates. How steep the landscape must become for erosion rates to match uplift rates, however, depends on the efficiency of sediment transport in a landscape. Landscapes with inefficient sediment transport will be steeper than those with efficient sediment transport, all else equal. We constrained the efficiency of sediment transport processes on hillslopes along a latitudinal climatic transect in the Chilean Coastal range (26˚-41˚S) by combining long-term erosion rates, derived from concentrations of cosmogenic ^{10}Be in quartz in fluvial sediments with topographic measurements. Precipitation changes by two orders of magnitude along this transect and vegetation cover ranges from permanently barren to permanently vegetated. We find that sediment transport efficiency climbs over two orders of magnitude, from as low as $2x10^{-4}$ m^2 per year in hyperarid environments (<20mm per year precipitation) to over 10^{-2} m^2 per year in semiarid environments (~100 mm per year precipitation), with transport efficiency peaking where herbaceous vegetation has mostly replaced bare ground. Transport efficiencies beyond this arid to semiarid transition average at $6.0\pm2.8 \times 10^{-3}$ m^2 per year in both semi-arid and humid environments. We conclude that climate has a first order control on sediment transport at the catchment scale in

the arid section of our study area, and that vegetation cover is a crucial, climate-dependent sediment transport modulator on the regional scale.

5.2. INTRODUCTION

In a landmark paper, Langbein & Schumm (1958) hypothesised that erosion rate is positively correlated with precipitation in arid regions, but once there is enough precipitation to sustain grasslands, which stabilise the landscape, erosion rates peak or become negatively correlated with precipitation. Many authors have sought to either confirm or disprove this seminal work with inconclusive results. For example, Fournier (1960) found that erosion rates were slowest for intermediate precipitation rates, whereas others found peaks at over a wide range of precipitation rates from 400 mm yr^{-1} to 1600 mm yr^{-1} (see summary figure in Riebe *et al*, 2001). Studies in the decades following (Langbein & Schumm, 1958) used short-term sediment yield data to calculate erosion rates, which may be subject to both anthropogenic perturbation (e.g. Milliman *et al*, 1987) or underestimation of long term rates because they do not capture infrequent, large magnitude events (Kirchner *et al*, 2001). In order to overcome the limitations of sediment yield studies, more recent authors have used cosmogenic radionuclide (CRN) techniques to estimate erosion rates (e.g. Riebe *et al*, 2001; von Blanckenburg, 2005); CRN based erosion rate estimates have the advantage of averaging erosion rates of hundreds to thousands of years (e.g. von Blanckenburg, 2005). Both Riebe *et al* (2001) and von Blanckenburg (2005) found no correlation between erosion rates and precipitation for precipitation rates ranging from 30 to 5000 mm yr^{-1}.

Despite the apparent lack of correlation between precipitation and erosion rates, other landscape properties, such as large scale variations in relief or hypsometry, can be qualitatively linked to variations in precipitation (e.g. McElroy & Wilkinson,

2005; Montgomery *et al*, 2001). In addition, large-scale studies of sediment yield have indicated a strong vegetation control on erosion rates (Molina *et al*, 2008; Vanacker *et al*, 2007; Bautista *et al*, 2007) while modelling studies (e.g. Istanbulluoglu & Bras, 2006) have found that the interplay between vegetation and precipitation control of erosion changes with mean annual precipitation, and that climate exerts a strong control on vegetation cover and distribution in arid and semi-arid landscapes (e.g. Kefi *et al*, 2007).

One may not, however, expect a simple relationship between precipitation and erosion rate, if any. When a landscape is uplifted at a reasonably fixed rate for long enough, the landscape will adjust so that its slopes are steep or gentle enough to balance the tectonic uplift rate: this is the basic conceptual model of geomorphic steady state (e.g. Roering *et al*, 2007; Hack, 1960). In a landscape at or near topographic steady state, erosion rates will reflect tectonic uplift rates and not climate (by definition). Whether the hillslopes are gentle or steep, however, is governed by the erosion efficiency of the landscape system, which in turn may be influenced by climate and vegetation. For a given erosion rate, if sediment transport is efficient, hillslopes will be gentle, and where sediment transport is inefficient hillslopes will be steep. If meaningful predictions about sediment yields under future climate scenarios are to be made, it is essential to understand the sediment transport efficiency. We focus on hillslopes because they are the source for the vast majority of sediment delivered to the channel network. In addition, changes in hillslope transport efficiency would affect the entire landscape at once, in contrast to changes in channel erosion which can take tens of thousands to millions of years to propagate across from a channel to a drainage divide (e.g. Mudd & Furbish, 2007). If precipitation

rates change, will the landscape be too steep, e.g., have slopes that were adjusted to less efficient sediment transport, resulting in enhanced sediment transport, or vice versa? Yet there has been no systematic study of how sediment transport efficiencies, averaged over landscape evolution timescales (i.e., 10^2-10^5 years), might change as a function of precipitation.

Recognizing that hillslope steepness, and similarly relief, are governed not just by erosion rates but also, crucially, by the sediment transport efficiency, Roering *et al* (2007) derived an analytical relationship capable of quantifying the relationship between topographic properties of a landscape (relief, steepness) and the factors that drive them (denudation, which equals uplift at steady state, and sediment transport efficiency).

$$\frac{R}{S_c L_H} = \frac{1}{E^*}\left(\sqrt{1+\left(E^*\right)^2} - \ln\left[0.5\left(1+\sqrt{1+\left(E^*\right)^2}\right)\right] - 1\right)$$

[5.1]

where R is local relief, S_c is the critical hillslope angle at which downslope sediment fluxes become infinite, L_H is the mean hillslope length, and

$$E^* = \frac{2E(\rho_r / \rho_s)L_H}{KS_c}$$

[5.2]

where E is the erosion rate, ρ_r and ρ_s are the densities of parent material and regolith, respectively, and K is the sediment transport efficiency in dimensions $L^2\ T^{-1}$. Roering *et al*. (2007) tested this analytical model on two landscapes in the western United States and showed it was able to accurately discriminate between steep, landslide

dominated landscape and landscapes with gentle and broadly convex slopes. In this study, we invert equation [5.1] to estimate sediment transport efficiency, or diffusivity (hereafter referred to as D, in common with Chapter 6 and Chapter 7), in a series of Chilean landscapes that have similar lithologies but have precipitation rates that span two orders of magnitude. Using this novel approach we are able to separate sediment transport efficiency from influences that spatially variable tectonic forcing and changing topography may have on erosion rates. Consequently our results are not specific to the study area but may be generalized for use in areas with a similar range in climatic conditions.

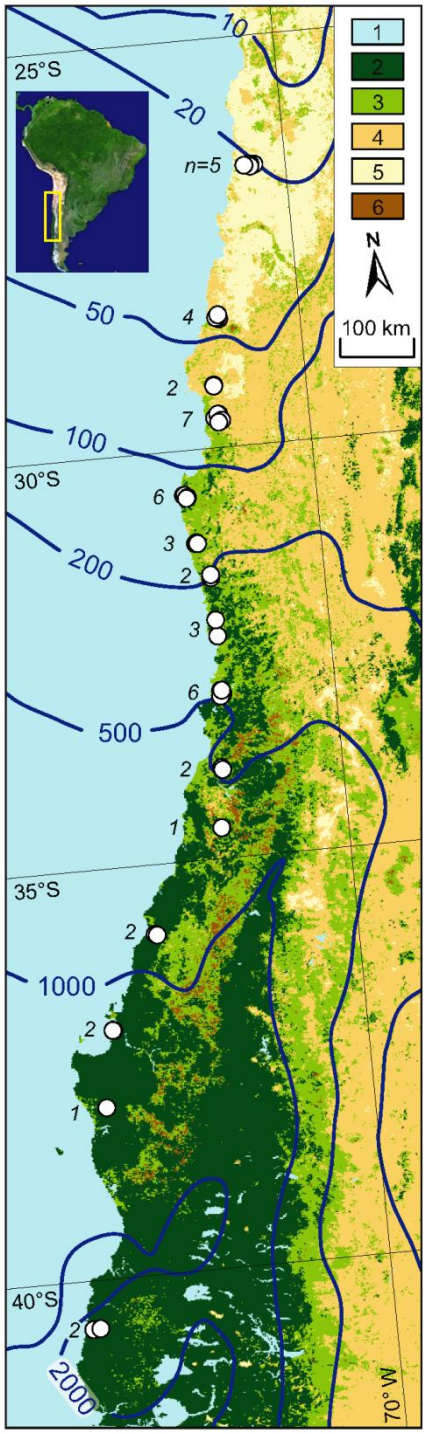

Figure 5.1: The 48 catchments investigated (white circles, number of catchments indicated by numbers) represent all land-cover types in the study area (Hansen *et al*, 2000) ranging from forest (2), grassland (3), and shrubland (4) to bare ground (open water (1) and cropland (6) are also indicated on the map for completeness), and span two orders of magnitude change in average precipitation (indicated as isohyets of mm annual rainfall; (Hijmans *et al,* 2005). Figure created by Tibor Dunai.

5.3. STUDY AREA

The coastal cordillera of Chile experiences an increase in mean annual precipitation with increasing latitude, and changes in precipitation are accompanied by changes in vegetation type and cover (Figure 5.1). Climate ranges from hyperarid north of 27˚S, with an arid zone from 27-31˚S and a warm temperate zone from 31-37˚S, to cool temperate climate south of 37˚S (Miller, 1976). Increased frequency and intensity of the Westerlies from 31˚-37˚S leads to a pronounced latitudinal precipitation gradient of more than two orders of magnitude (20 mm/a - >2000 mm/a; (Fuenzalida et al, 2008; Hijmans et al, 2005) in the study region between 26º and 41ºS. Although temperature decreases from the tropics to the higher latitudes this variation (annual mean range between 16-11ºC (Hijmans et al, 2005)) is minimal compared to the variation in precipitation. Consequently vegetation zonation in Chile is largely controlled by precipitation (Veblen et al, 1981), and the present day vegetation is a result of the interglacial climate of the past ~12 ka (Clapperton, 1993). Glacial climates were wetter than interglacial (modern) climates in the study area, with present day climate and vegetation zones shifted at least 2º to the North during glacials (Lamy et al, 2000; Heusser et al, 2006). The current vegetation of the study area can be divided into 3 ecoregions (Olson et al, 2001): the deserts and xeric shrublands of the Atacama region (18˚-29˚S); the Mediterranean forests, woodlands and scrub of the Chilean matorral (29˚-35˚S); and temperate coniferous and deciduous forests (south of 35˚S) (Figure 5.2). The ecotone between the matorral and the southern forests is broad and uneven (Heusser et al, 2006) (Figure 5.1). The Coastal Cordillera of Chile represents the remnants of a Mesozoic volcanic arc and

comprises Jurassic to early Cretaceous dioritic-granodioritic plutons and Jurassic volcanic (SERNAGEOMIN, 2002).

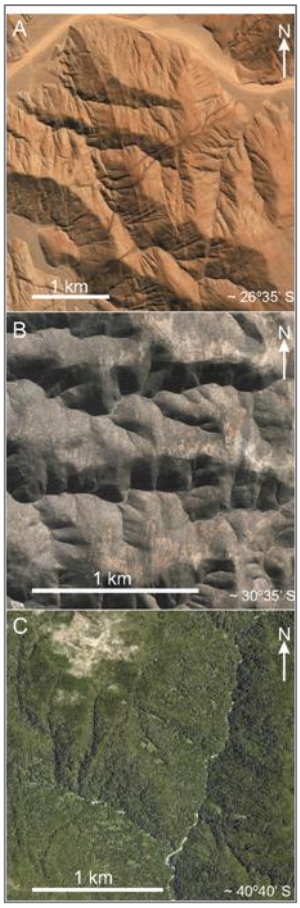

Figure 5.2: Aerial photographs of the three main ecotypes in the Chilean Coastal Range in landscapes of granitic lithology. Arid (A) and humid-temperate (C) landscapes reflect the isotropic nature of the granitic basement rocks, whereas semi-arid landscapes (B) often show anisotropic vegetation and asymmetric hills due to aspect. Vegetation native in wetter ecozones can survive in shaded areas (south facing) in the semi-arid ecozone. This denser vegetation on south-facing slopes reduces erodibility and can maintain steeper hillslopes than the adjacent north-facing dryland vegetation. Aspect-related vegetation heterogeneities therefore contribute to the broad and uneven ecotone between the matorral and the southern forests and may cause a heterogeneous response to changes in climate parameters. Figure created by Tibor Dunai.

5.4. METHODS

Transport efficiency parameters. To invert equation [5.1], several parameters must be constrained. The concentration of the cosmogenic radionuclide ^{10}Be in fluvial sediments was used to estimate erosion rates (von Blanckenburg, 2005; Bierman & Steig, 1996; Granger *et al*, 1996). Sediment samples were taken along a climatic transect of almost 2000km in length, spanning the range of climatic zones along the Chilean coast. Only catchments originating in the Coastal Cordillera were sampled, in order to eliminate the effects of any input from the Andes, and samples were taken above any knickpoints or pronounced convexities in the channels networks to ensure that catchments had not felt the influence of base level fall that was evident in the main channels. All samples were taken in areas where the predominant lithology was granitoid and only catchments with no evidence of landsliding, intensive agricultural activity (forest and pasture only; no ploughing) or sediment storage were sampled. The samples were sieved to obtain the 250-710 µm size fractions for in-situ cosmogenic ^{10}Be analysis.

The parameters R and L_H were calculated based on 30m ASTER DEM. To characterize L_H, we extracted drainage networks using the Peukar-Douglas algorithm reported by Band (1986). This algorithm links upwardly concave pixels in the DEM and requires the user to define channel heads by setting a threshold number of contributing concave pixels. We vary the threshold values and compared the extracted channel networks with georeferenced satellite images of the study area. Once these channel networks are extracted for each field location, we divide the total extracted basin area (extracted basins include both the sample basin and nearby

basins) by twice the total length of the channel network to arrive at L_H (e.g. Horton, 1932). To calculate local relief, R, we follow the method of Roering *et al* (2007) and calculate relief within a moving window with a diameter that is equal to L_H. The 30m resolution of the DEM (which is the highest resolution available in our field area) precludes exactly matching extracted networks with the true channel network. We therefore included this uncertainty in our calculations by estimating a minimum, maximum, and 'best estimate' channel network. Watersheds were then extracted for these channel networks using the TauDEM software package (http://hydrology.usu.edu/taudem/taudem5.0/downloads.html). Uncertainties in mean hillslope length are propagated through our calculations of the *D* value. To calculate local relief, we followed the methodology of Roering *et al* (2007) and determined the range in elevation values within a moving window that has the same diameter as L_H. We used cubic interpolation of topography within this window, sampling at 5-metre spacing when calculating elevation ranges. Relief was also calculated over the full range of L_H values: it takes into account the uncertainty in the extracted drainage density. Because relief only occurs in conjunction with L_H in equation [5.1], Roering *et al* (2007) noted that this could be cast as an effective slope. Despite the large uncertainty in L_H, effective slopes are very consistent; effective slopes typically vary by less than 1% for individual sample basins. These effective slopes are also consistent with extracted mean basin slopes, although mean basin slopes are systematically gentler by 3-4% because mean basin slope calculations include low relief channel pixels.

Sampled catchments are in granitoid terrain, and we take ρ_r = 2.6g/cm^3 and ρ_s = 1.3g/cm^3 following Riebe *et al* (2004); note that only the ratio, rather than the

absolute values, of these densities impacts the estimated D value. We use S_c = 1.2, following the reasoning of Roering *et al* (1999). With these parameters, we solve equation [5.1] for D using the Powell hybrid algorithm (Powell, 1970).

Mean annual precipitation values are extracted from the 1km-resolution WorldCLIM dataset (Hijmans *et al*, 2005). Vegetation classifications are based on 1km-resolution Advanced Very High Resolution Radiometer (AVHRR) satellite data (Hansen *et al*, 2000). The latitudes of boundaries between climatic zones ~31°S and ~37°S are based on the descriptions of (Miller, 1976). The latitudes were transformed into corresponding estimates of annual precipitation, of ~150 mm/yr and ~1200 mm/yr, respectively (Figure 5.4), using the WorldCLIM dataset (Hijmans *et al*, 2005).

5.5. RESULTS

5.5.1. Erosion rate, transport efficiency and climate.

The erosion rates we obtain from cosmogenic nuclide analysis range between 2-70 m/Ma (assuming $\rho_r = 2.6 g/cm^3$; Figure 5.3)

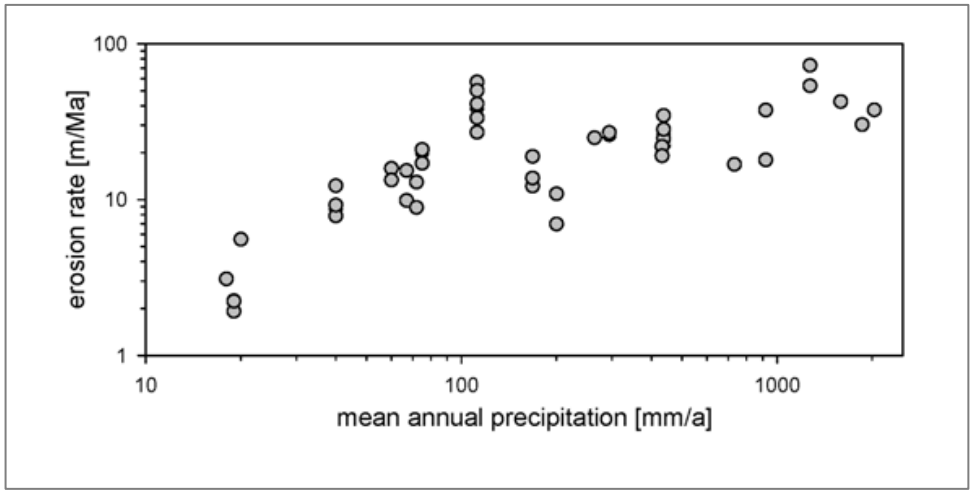

Figure 5.3: The ^{10}Be-derived erosion rate in granitic catchments of the study area increases with precipitation, particularly below 100 mm rainfall per year. The finer structure that is visible in the data at higher precipitation, such as an apparent rise above 150 mm rainfall per year, is probably due to changes in topography, channel processes and/or differential tectonic forcing, as it disappears in the signal of the sediment transport efficiency (Fig. 5.4) that screens out the effects of these features/processes. Analytical uncertainties are smaller than the symbol size. Figure created by Tibor Dunai.

The rates lower than 10 m/Ma are exclusively found in the arid areas (<100 mm/a). These erosion rates indicate that in the semi-arid to humid climate zones 10-30 cm of rock has been removed during the Holocene (i.e. the last 11.5 ka). Since more than 50 cm of rock must be removed to fully obliterate the memory of a previous exposure regime (e.g. Bierman & Steig, 1996) the cosmogenic erosion data contain a remaining pre-Holocene signal. Consequently the climate-erosion relationships derived from this data may mimic the response to a somewhat wetter climate than is

indicated by the present day climate data used. While the blurring effect of this inheritance may affect the quantitative position of transitions observed, however, it does not affect the nature of the transitions. It has been postulated that the ratio of glacial to Holocene erosion rates will vary along the coast, and Hebbeln *et al* (2007) deduced the ratio of glacial to Holocene accumulation of terrigenous sediments; their ratios can be used to estimate glacial erosion rates in the study area and therefore to test the sensitivity of *D* to possible inheritance of glacial erosion rates (fig. 5.4). Results indicate that even if the present day erosion rate was completely obscured by the glacial erosion rate, the trend in diffusivity would still be clearly defined (fig. 5.4B).

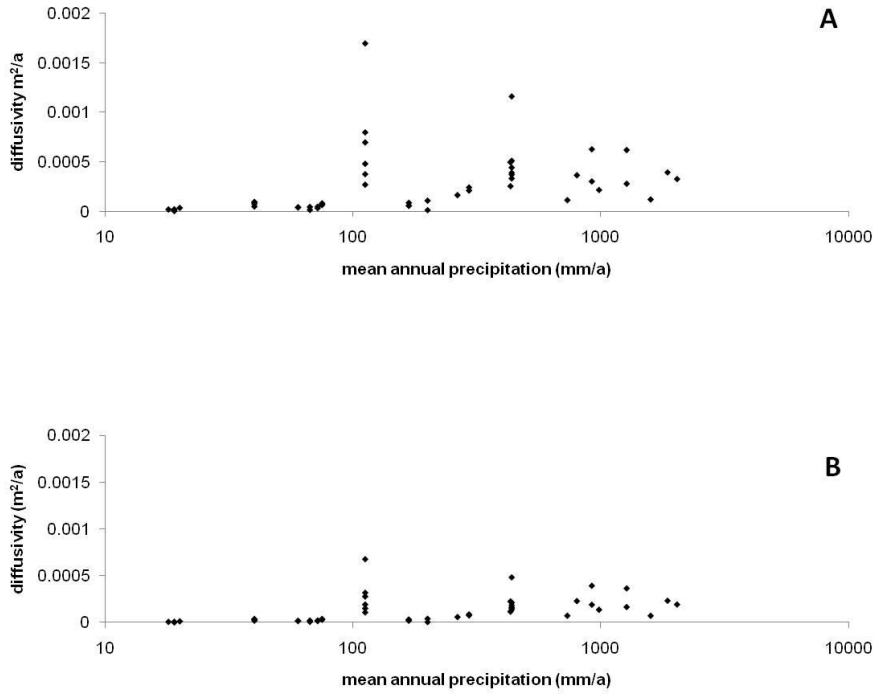

Figure 5.4: Sensitivity analysis to show effects of inheritance of pre-Holocene erosion rates on the nature of the relationship between *D* and mean annual precipitation. Results indicate that even if the erosion rates derived from cosmogenic isotope studies (A) were reflecting a glacial erosion rate, the 'real' erosion rates (B) would still produce a *D* plot of similar form.

Results indicate that sediment transport is most inefficient in the most arid environments (~ 20 mm per year precipitation). Transport efficiency, *D*, then increases by nearly two orders of magnitude to peak at an annual precipitation rate of ~100 mm/year (Figure 5.5).

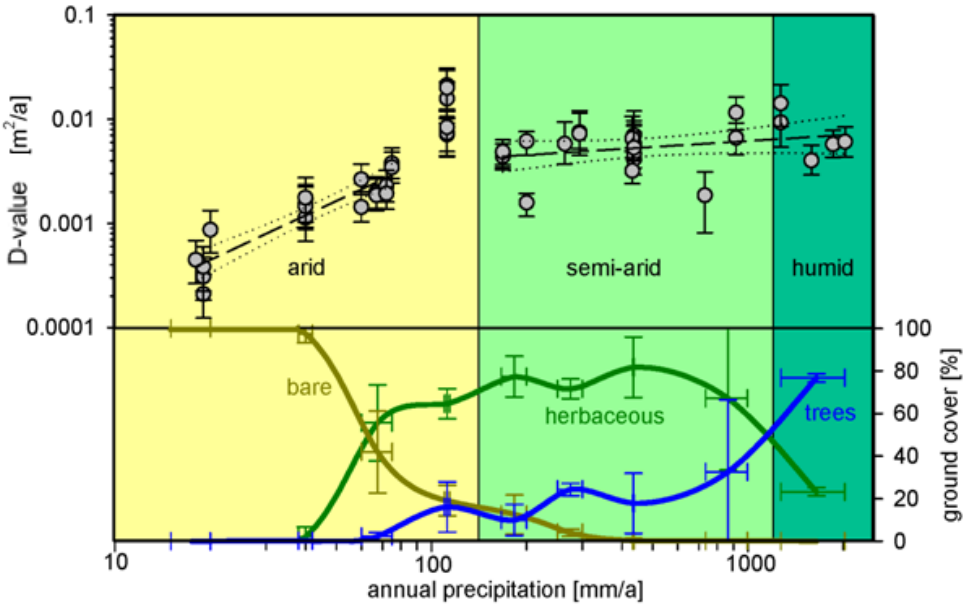

Figure 5.5: The sediment transport efficiency (*D*) increases with increasing precipitation in arid landscapes, peaking near the transition to a semi-arid climate. At higher rates of precipitation, *D*-values become invariant. The region with invariant *D*-values is characterized by the near, to complete, absence of bare ground; the sediment transport efficiency in the region with predominantly bare ground (50-100%) correlates linearly with precipitation. Envelopes around the regression lines denote the 95% confidence interval. Error bars on *D*-values include the analytical uncertainties and the uncertainties associated with the extraction of topographic parameters from digital elevation models. Ground cover classes were determined for all catchments; the horizontal bars denote the precipitation range for which individual mean values of ground cover types were derived for groups of catchments; the vertical bars denote the standard deviation of these means. The coloured areas in the background provide the approximate range of arid, semi-arid and humid environments (Miller, 1976); the actual boundary areas are broad and uneven (Heusser *et al,* 2006). Figure created by Tibor Dunai.

This precipitation rate corresponds approximately with the transition from arid to semi-arid climate as described by Clapperton (1993). *D* values then decrease by about half to remain essentially stable across the semi-arid climatic zone and across

the transition to a more humid climate until at least ~2000mm/year mean annual precipitation.

5.6. DISCUSSION

5.6.1. Sediment transport efficiency and vegetation cover

Changes in the land cover classes (Figure 5.5) mirror the changes in precipitation. The profound changes in *D* near the arid semi-arid transition coincide with the virtual disappearance of bare ground at higher precipitation. In areas with predominantly bare ground (~50-100 %) the *D*-values are linearly correlated with precipitation (r^2=0.78, < 100 mm/a; value for linear plot, not shown). In areas with near-complete vegetation cover (>80%) we find no significant change in *D*-values with increasing precipitation or changes in type of vegetation cover. The mean *D*-value for these areas is 6.0±2.8 x 10^{-3} m^2 per year (±1σ, n=24). The area with the highest *D*-values (mean 1.3±0.7 x 10^{-2} m^2 per year, n =6) has significant bare ground (~ 20%) and a predominantly herbaceous vegetation cover (~60%) (Hansen *et al,* 2000; Gutierrez *et al,* 2010).

Our large scale results (Figure 5.1) are supported by detailed local studies (e.g. Molina *et al,* 2008; Vanacker *et al,* 2007) which indicate that the percentage of vegetation cover exerts a first order control on erosion rates at the catchment scale, regardless of vegetation type. Consequently the peak in *D*-values near arid/semi arid transition (Figure 5.5) occurs due to the observed sensitivity of ephemeral vegetation cover there (Gutierrez *et al,* 2010) to precipitation changes (Gutierrez *et al,* 2010; van de Koppel *et al,* 1997). Numerical modelling results predict a change in the dominant control of sediment transport with changing precipitation (Istanbulluoglu & Bras, 2006). Istanbulluoglu & Bras (2006) foresee a change from direct climatic control where precipitation is low and vegetation cover minimal, to a combined

vegetation and climatic control when mean annual precipitation increases and favours vegetation growth, until vegetation growth is no longer limited by water availability. This is reflected in the position of the peak in *D* value near the arid to semi-arid transition (Figure 5.5), where vegetation becomes the dominant control and reduces sediment transport. Istanbulluoglu & Bras (2006) further predict a near linear increase of sediment transport potential for arid climates, a peak near the arid/semi-arid transition where vegetation cover becomes permanent, which is followed by a sharp decrease in sediment transport efficiency. These predictions are coherent with our data. In the model of Istanbulluoglu & Bras (2006), sediment transport potential may or may not resume a gentle rise at very high precipitation rates, depending on grain-size, a feature which we cannot resolve with the current data.

As precipitation increases from a hyperarid environment, the computed *D* values increase and the percentage of bare ground decreases in the arid areas. This observation apparently contrasts with Dunne *et al* (2010) who find a strong decrease in the efficiency of transport with increasing plant cover, per cm of rainfall. However, Dunne *et al* (2010) investigated specifically situations without overland flow, whereas sediment transport in arid environments is commonly associated with overland flow during storm events (Istanbulluoglu & Bras, 2006). Our *D* values integrate over many storm-events, demonstrating that the increase in vegetation cover associated with an increase in rainfall is not enough to offset the erosive power by the increased number in storm events; the peak in *D*-values appears at the current northern limit where regular Westerly storm events occur (Fuenzalida *et al*, 2008). Transport efficiency in fact does not decline until the landscape is nearly 100% covered by vegetation.

The constancy of sediment transport efficiency in fully vegetated environments (Figure 5.5), covering a precipitation range of 150-2000 mm, suggests that the mean *D*-value ($6.0 \pm 2.8 \times 10^{-3}$ m^2 per year) is typical for soil mantled hillslopes in granitiod catchments in a wide range of climatic conditions. This mean *D*-value can therefore be used as a natural baseline for sediment transport efficiency to assess changes in sediment transport in areas that have been affected by human activity that has removed previously complete vegetation cover (e.g. logging, fire-clearing, ploughing etc.). Extrapolating the near-linear increase of sediment transport efficiency with increasing precipitation for areas with (naturally) significant bare ground (Figure 5.5; also Istanbulluoglu & Bras, 2006), indicates that artificially cleared areas in semi-arid to humid environments will develop one to two orders of magnitude higher sediment transport efficiencies than their natural counterparts. This general conclusion is in agreement with local studies, which confirm such large effects (e.g. Vanacker *et al*, 2007; Hewawasam *et al*, 2000) and provides a tool for predictive erosion forecasts for environments in danger of losing their vegetation cover, be it from climate change or from more direct forms of human activity.

5.6.2. General applicability

When translating the results of this study to other areas, care should be taken if the numeric values for annual mean precipitation, rather than the completeness of vegetation cover, are used, as climate in Chile is relatively temperate, even in the arid areas, and is characterized by frequent coastal fogs (Clapperton, 1993). Evapotranspiration is therefore lower than in many regions supporting a similar range in ecotypes (Hijmans *et al,* 2005; Olson *et al,* 2001). The arid to semi-arid transition, or better the transition from incomplete to complete natural vegetation cover, may therefore occur at higher mean annual precipitation in other areas. While the numeric value at which the change in sediment transport efficiency occurs might be different, mean *D*-values for regions with complete vegetation cover should be the same.

Our calculated *D* values are consistent with the only two other values reported in granitic environments. Heimsath *et al* (2000) reported a value of $4x10^{-3}$ m^2 per year for a site in SW Australia (Nunnock River) that experiences ~910 mm per year precipitation, and Reneau (1988) reported a value of $3x10^{-3}$ m^2 per year for a site in coastal California (Point Reyes) that experiences ~430 mm per year precipitation. Both areas support a complete vegetation cover.

5.7. CONCLUSIONS

The efficiency of sediment transport determines the steepness of a landscape for a given erosion rate, or alternatively the sediment yield for a given steepness. We have determined the sediment transport efficiency of hillslopes across granitic landscapes in Chile that experience precipitation rates spanning two orders of magnitude. Our results show that this sediment transport efficiency climbs nearly two orders of magnitude from hyperarid to semi-arid environments. The results also indicate that there is no correlation between sediment transport efficiency and precipitation beyond precipitation rates of ~200 mm per year; humid environments seem to be no more efficient at transporting sediment than semiarid landscapes, but these wetter environments are all much more efficient at transporting sediment than very dry environments (with < 100 mm precipitation per year). These results can help in the prediction of changes to sediment yields as a function of climate over longer timescales (10^2-10^5 years). While an e.g. 30% increase of precipitation in an arid environment would result in a strong increase in sediment yields, a similar increase in humid environments would not have an effect. Again, landscapes at the climatic transition supporting discontinuous to complete vegetation cover have a strong non-linear response to changes in precipitation: changes to the drier and the wetter can decrease sediment yields. Sediment transport in arid regions is by far the most sensitive to fluctuations in precipitation rates when compared to more humid environments that support a continuous vegetation cover. On the other hand semi-arid to humid environments are most sensitive to destruction of vegetation cover, be it natural (e.g. wild fires) or anthropogenic (e.g. agriculture, logging). Destruction of

the vegetation cover in these environments will increase sediment transport efficiency by one to two orders of magnitude.

6. CLIMATE AND VEGETATION CONTROLS ON DRAINAGE BASIN MORPHOLOGY

6.1. INTRODUCTION

Drainage basin morphology can provide vital information regarding earth surface processes, with the morphology of fluvial landscapes representing the product of interactions between climate and tectonics and surface processes. Understanding the controls on basin morphology is therefore crucial in order to understand how climate and tectonics can act to shape the landscape. The striking regularity of drainage basin morphology across diverse climatic and tectonic regimes has long been documented. In particular, several authors have described a relatively constant ratio of basin length to width for linear compressional orogens (Hovius, 1996), fault blocks (Talling *et al,* 1997) and passive margin settings (Walcott & Summerfield, 2009), where the outlet spacing is proportional to range width. This uniform spacing occurs even in the absence of significant control by bedrock structure or tectonic history and ratios appear to persist even where differences in climate, vegetation and slope are evident (Talling *et al,* 1997), although exceptions have been noted in an active orogenic setting in the Himalayas (Walcott & Summerfield, 2009). Yet no comprehensive mechanism has been invoked to explain this apparently uniform property of natural landscapes, although evidence suggests that the mechanisms underlying this universal spacing mechanism may be similar to those which underlie Hack's law of stream length and basin area (Hack, 1957; Hovius, 1996; Walcott & Summerfield, 2009). Conversely, modelling results (Perron *et al,* 2008) suggest that, at least for first order basins, the spacing ratio of basins should be affected by the ratio of

diffusive to advective transport processes within the basin; these competing modes of erosion have also been invoked to explain changes in valley wavelength in natural landscapes (Perron *et al,* 2009).

As sediment transport processes change with climate and vegetation cover (e.g. Saunders & Young, 1983), the results of Perron *et al* (2008) suggest that changes in diffusive and advective transport with climate should be reflected in changes in spacing ratios of basins. The Chilean Coastal Cordillera, where the magnitude of landscape diffusivity has already been constrained (see Chapter 5), provides the ideal setting to test this theory. The model of Perron *et al* (2008) suggests that, unless changes in diffusive transport are somehow compensated for, basin spacing ratios should be positively correlated with diffusivity and should therefore change significantly with latitude in the study area. Since the diffusive processes at work in the study area have already been constrained, any changes in basin spacing ratio should therefore provide information about the magnitude of advective processes. In addition, the applicability of the model of Perron *et al* (2008) to basin-wide geometry of basins of different order can be tested using the CHILD landscape evolution model. The CHILD model is based on the same parameters and equations as the model employed by Perron *et al* and is therefore ideal to test whether changing the relative input of diffusive transport while keeping advective transport fixed will affect basin spacing ratio calculated using the major and minor axes of basins.

Similarly, Perron *et al* (2009) report precipitation-dependent changes in characteristic ridge-valley wavelength in low-relief, soil-mantled landscapes, which they interpret to reflect changes in the ratio of soil creep (diffusive transport) to channel incision (advective transport), with shorter wavelengths in drier climates and

vice versa. However, the observation of these ridge-valley wavelengths rests on the use of high-resolution LIDAR data which can be difficult to obtain. If this relationship between climate and ridge-valley wavelength can be observed at a coarser scale (using basin width as a proxy for ridge-valley wavelength), the model described by Perron *et al* (2009) can be tested and applied in a greater variety of landscapes without the need for such high-resolution elevation data. The results should also be replicated by the CHILD model.

6.2. STUDY AREA

Drainage basin morphology was studied along a climatic transect in the Coastal Cordillera of northern and central Chile (see Chapter 3 for detailed description of study area). Climate within the study area ranges from hyperarid in the north to humid temperate in the south (Miller, 1976; Lamy *et al*, 2000; Clapperton, 1993), with a dramatic latitudinal precipitation gradient and a pronounced, but less dramatic, temperature gradient. The changes in climate with latitude are mirrored by changes in vegetation distribution, with vegetation distribution primarily controlled by amounts of precipitation (Veblen *et al*, 1981). The study area spans three main ecoregions (Olson *et al*, 2001): the deserts and xeric shrublands of the Atacama Desert; the Mediterranean forests, woodlands and scrub of the Chilean matorral; and the temperate forests of the Southern Valdivian Forests. The Coastal Cordillera consists of the remnants of a Mesozoic volcanic arc, comprising Jurassic to early Cretaceous dioritic-granodioritic plutons and Jurassic volcanics, with minor amounts of Upper Cretaceous to Tertiary marine sediments, Mesozoic marine volcanics, and with a basement of Palaeozoic sediments and Precambrian metamorphic rocks (Allmendinger et al, 2005; Lamy et al, 1999; SERNAGEOMIN, 2003). Evidence suggests that the Coastal Cordillera has undergone relatively uniform Plio-Quaternary uplift: the coastline of South America is characterised by Quaternary marine terraces that have been uplifted along much of the Pacific margin, indicating an orogen-scale uplift mechanism (Hsu *et al*, 1989) combined with more local tectonic processes (Ortlieb *et al*, 1996). Uniform uplift has been recorded from at least 23˚S to at least 33˚S (Cembrano *et al*, 2007; Marquardt *et al*, 2004; Ortlieb *et al*, 1996; Quezada *et al*, 2007), with the exception of a region of anomalous uplift

~31˚S (Saillard *et al,* 2009). The study area therefore provides the ideal setting to study the effect of pronounced and continuous changes in climate and vegetation, set against a background of relatively spatially uniform geology and rates of uplift.

6.3. METHODS

In order to study the effects of changing climate and vegetation on basin spacing ratios, 16 tiles were extracted from DEMs generated using 30m-resolution ASTER data. In order to maintain consistency, these tiles were clipped to enclose the catchments sampled for cosmogenic analyses and the surrounding areas (Figure 6.1). Channel networks were defined in ArcGIS using the TauDEM software, with networks being extracted using a Peuker-Douglas algorithm (Band, 1986; see Chapter 4 for further discussion of extraction of stream networks). Watersheds of first to fourth order were defined using these stream networks and zonal statistics (primarily major axis and minor axis, or basin length and width) were calculated for each tile and the basin spacing ratio, defined in this study as the ratio of basin width to basin length, was calculated for each basin. Frequency distributions of basin width and basin spacing ratio were plotted for each tile and formed the basis for further comparisons.

The CHILD landscape evolution model (see Tucker *et al*, 2001 for more detailed description of the model) is one of few landscape models able to incorporate a biological component into a numerical framework with geomorphologic and hydrological processes. The model was used to generate three equilibrium landscapes using diffusivity parameters which varied over three orders of magnitude while keeping the advective transport rate constant. Input parameters for the three landscapes are summarised in Table 6.1 and the landscapes generated using the CHILD model are illustrated in Figure 6.2. The CHILD landscapes were processed

in exactly the same manner as the DEMs and the same zonal statistics extracted for further study.

Where reference is made to climate or vegetation cover, these descriptions are based on classifications made using the MODIS Vegetation Continuous Fields data set (Hansen *et al*, 2000) and the WorldCLIM dataset (Hijmans *et al*, 2005), and specific values of precipitation or vegetation cover refer to values extracted from catchments sampled for cosmogenic analysis, unless otherwise stated.

Parameter	Value
Grid Spacing	25m
Mean storm precipitation P	4.5mm/hr
Mean storm duration T_r	4000yr
Mean interstorm duration T_b	1000yr
Erodibility coefficient k_b	3.17×10^{-14} m s^{-1} Pa^{-1}
Stream power coefficient k_t Manning's roughness coefficient n_m	1196 Pa m^{-2} s^{-1} 0.03
Channel width coefficient k_w	$5.0 m^{-1/2}$ $s^{1/2}$
Exponent p	1
Stream power coefficient K ($K = k_b k_t k_w^{-1} P^{0.5}$)	2.7×10^{-7} $m^{-1/2}$ $s^{-1/2}$
Diffusivity coefficient D	0.215, 0.0239, 0.00215m^2 yr^{-1}

Table 6.1: Input parameters for CHILD model. All parameters were kept constant except the diffusivity constant, D. CHILD1 = 0.215, CHILD2 = 0.0239, CHILD3 = 0.00215.

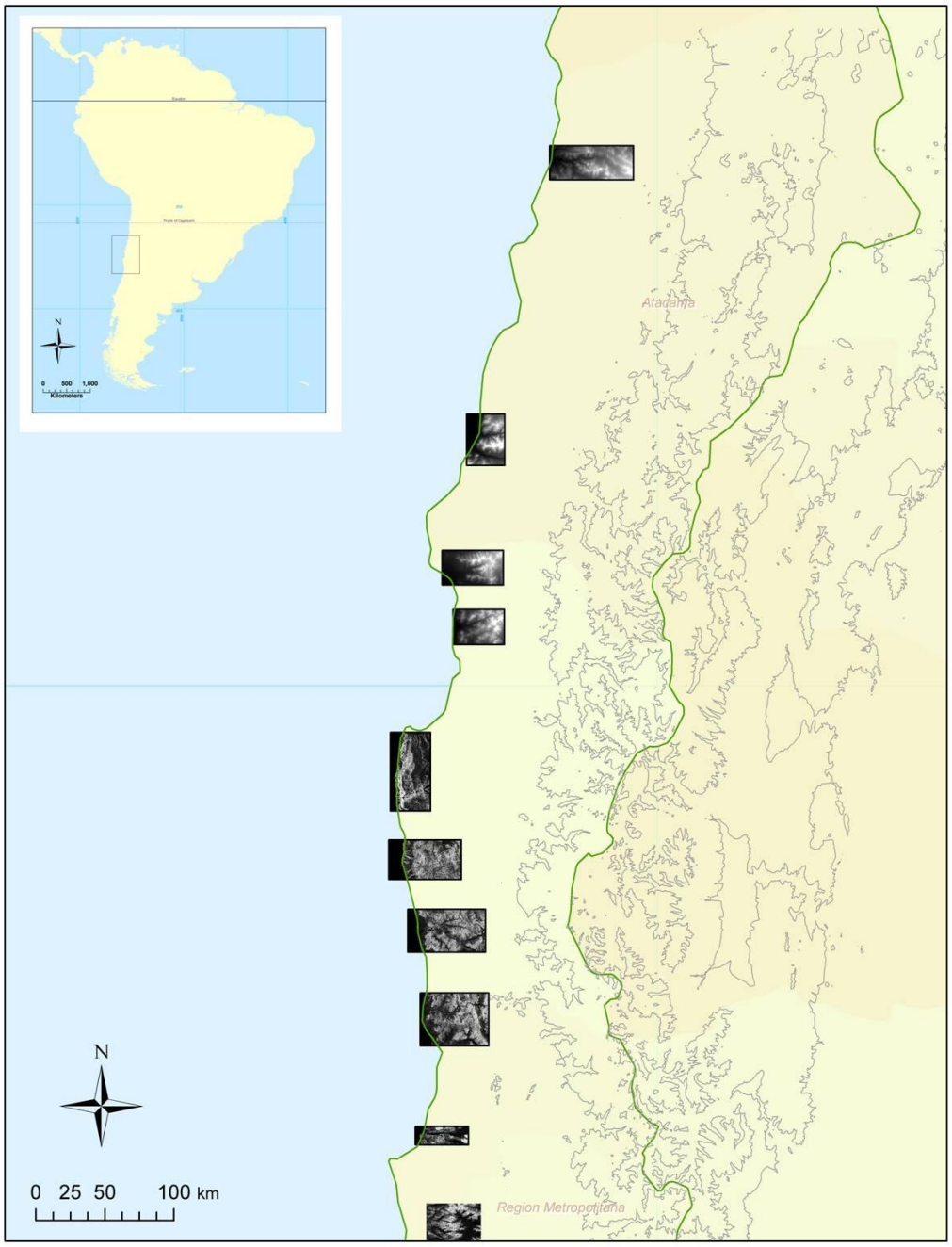

Figure 6.1(a): Distribution of DEM tiles clipped to enclose catchments sampled for cosmogenic analysis (see Chapter 5) in the northern part of the study area. Grey lines are 2km contours.

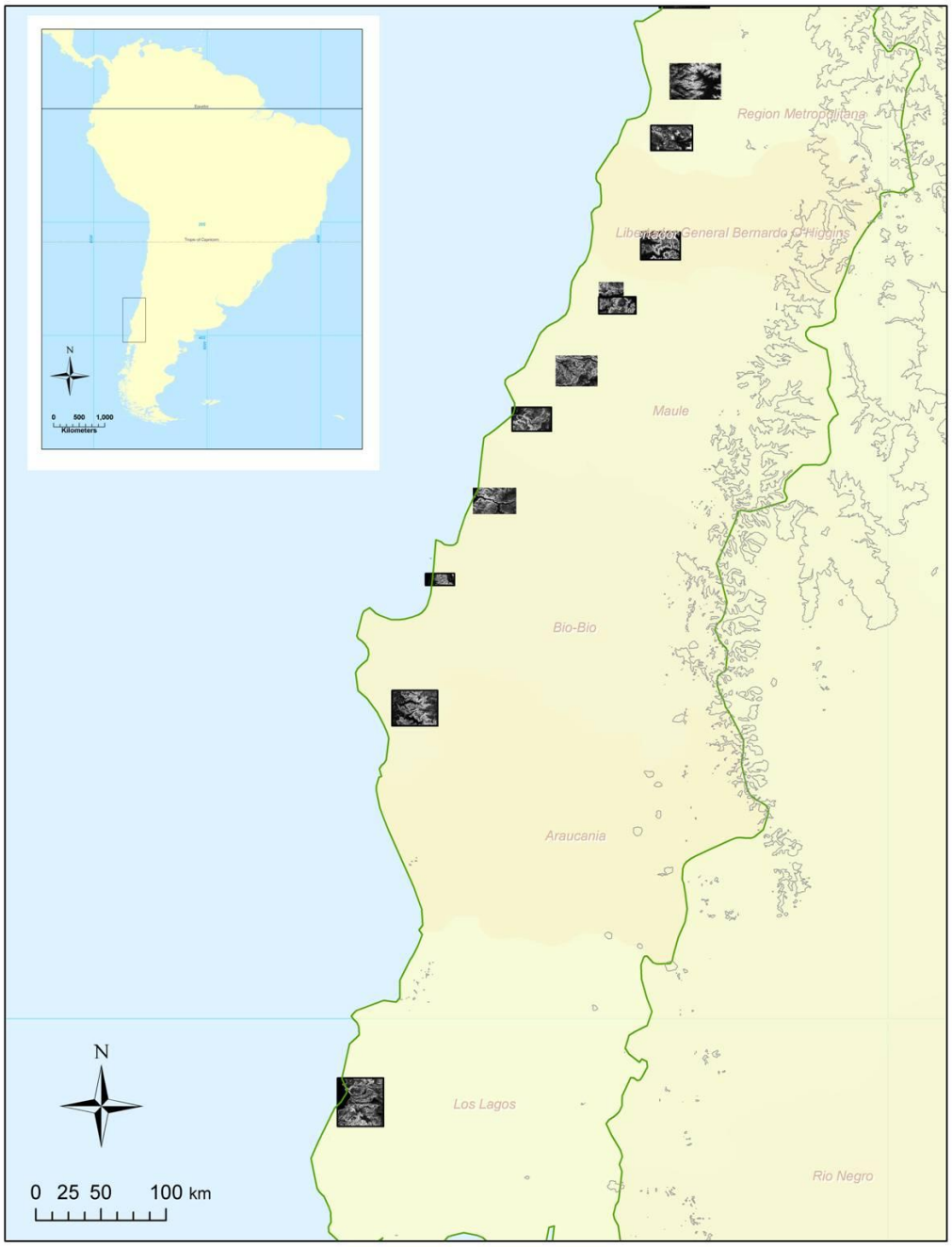

Figure 6.1(b): Distribution of DEM tiles clipped to enclose catchments sampled for cosmogenic analysis (see Chapter 5) in the southern part of the study area. Grey lines are 2km contours.

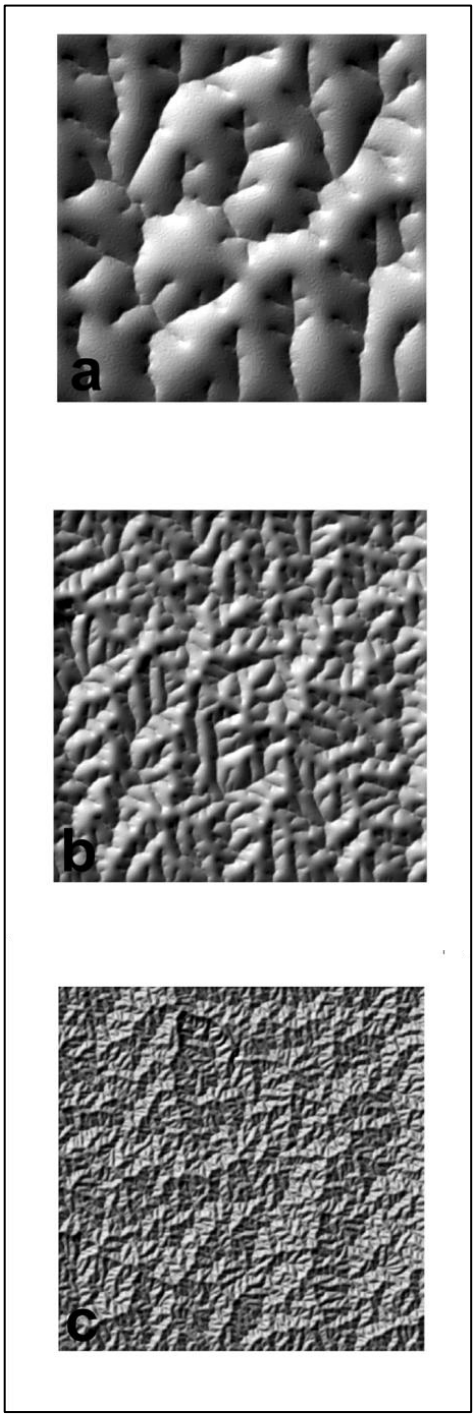

Figure 6.2: Hillshade view of the three landscapes generated using the CHILD model. Each landscape is approximately 10km by 10km. a) CHILD1; b) CHILD2; c) CHILD3

6.4. RESULTS

6.4.1. Distribution of median width to length ratio

The diffusivity, *D*, of the landscapes has been constrained using cosmogenic ^{10}Be in fluvial sediments and is illustrated in Figure 6.3.

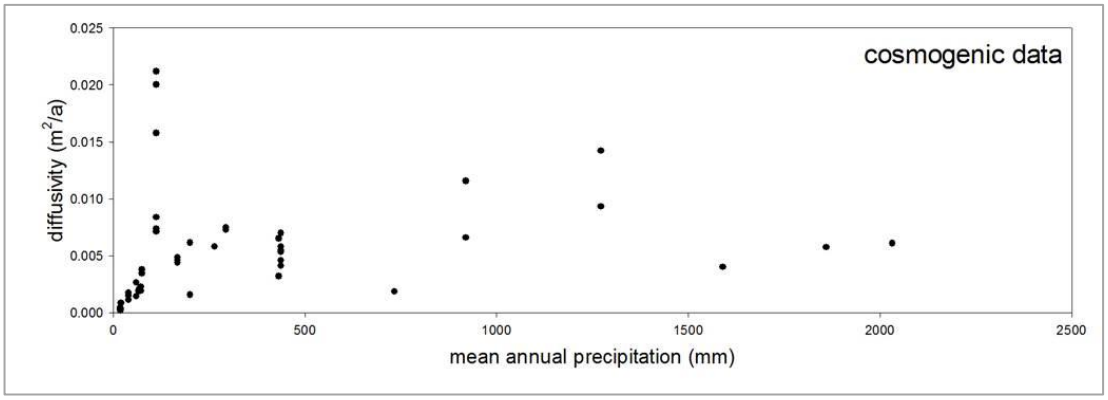

Figure 6.3: Changes in diffusivity with mean annual precipitation in the study area. Each data point represents a sampled catchment. See Chapter 5 for further discussion on calculation of diffusivity from cosmogenic isotope data.

Given the pronounced changes in diffusivity (over two orders of magnitude) in the study area, the modelling results of Perron *et al* (2008) would suggest that, all else being equal, the changes in diffusivity should be reflected in changes in basin spacing ratio with latitude. However, the distribution of width to length ratios is remarkably uniform across a wide range of climatic conditions and for basins of different order (a selection of width to length ratio histograms are included for reference in Appendix 2), although the median values of first order basins are slightly lower than basins of higher order (Figure 6.4). The results indicate no systematic variation in median width to length ratio with latitude, and also show that the variability between regions decreases as order of catchments increases. Although

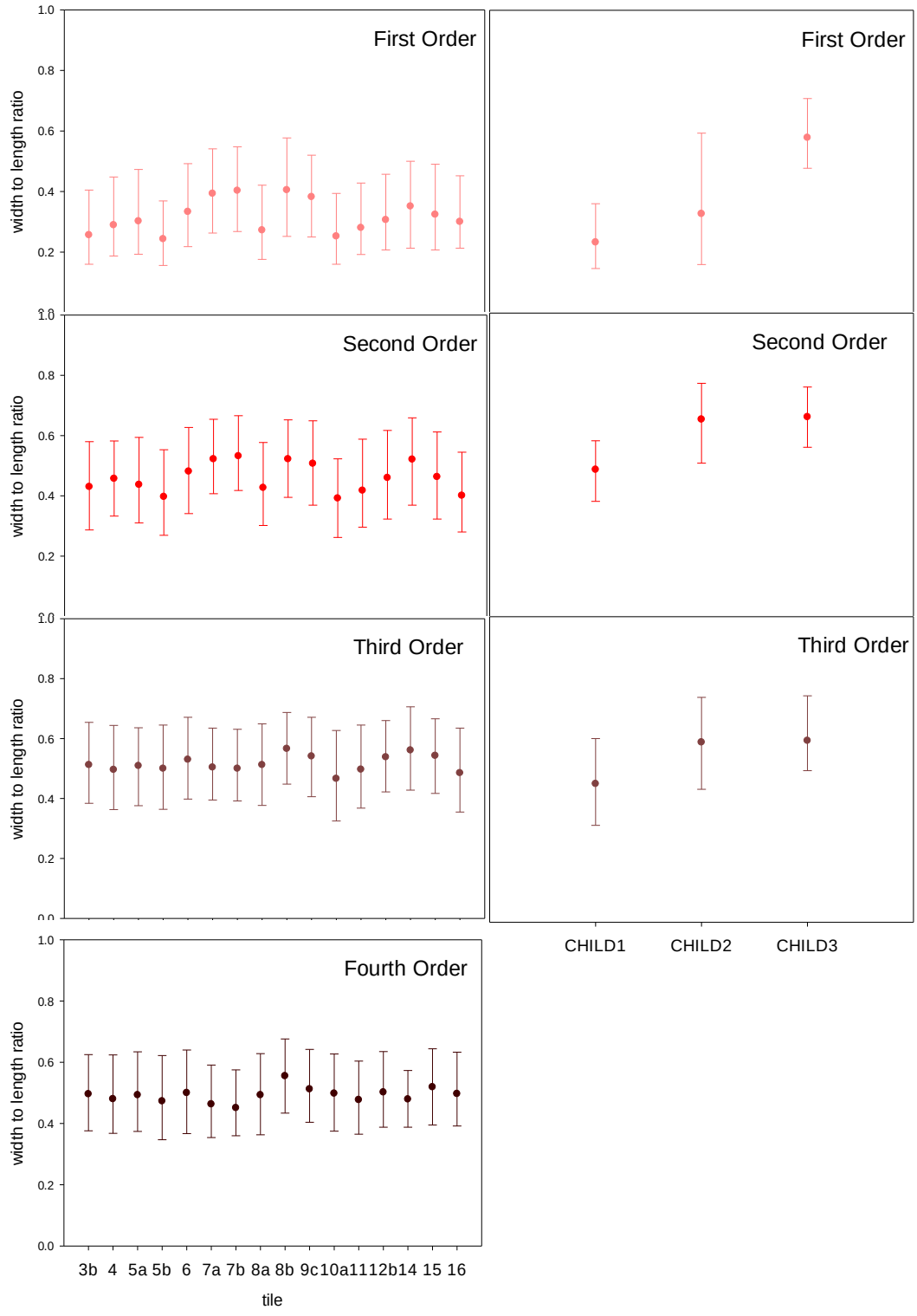

Figure 6.4: Median width to length ratios for each tile (DEM tiles on left, tiles generated using CHILD model on right) for first to fourth order basins.

there is more variability in median width to length ratio between tiles for the first order catchments, values tend to cluster around the 0.3-0.4 mark, which is considerably lower than the ~0.5 ratio for the higher orders. Median width to length ratios (Figure 6.4) are similarly much higher in the second and third order basins for the CHILD landscapes than for first order basins, and second order basins seem to have a slightly higher spacing ratio than third order basins. This is not necessarily at odds with the median ratios for the DEM tiles, since second order medians show more inter-tile variability and in some cases these second order basins also have greater spacing ratios than the third order basins from the same tiles. For all orders, decreasing the diffusivity constant in the CHILD model leads to an increase in the spacing ratio, an effect which is particularly pronounced in the first order basins. The change in median spacing ratio between CHILD2 and CHILD3 for the higher order basins is fairly small, which may suggest that further decreasing the relative input of diffusive processes is unlikely to result in further increases in the width to length ratio of basins, even in these idealised landscapes.

6.4.2. Relationship between width and length: Increasing stream order

Plotting median width to length ratio in natural landscapes reveals little change in ratio from tile to tile. More information can perhaps be gleaned from looking at the relationship between basin width and basin length for all extracted basins rather than considering simple mean or median values (see Figure 6.5). Plotting the data in this way highlights some interesting features. Firstly, the overall distribution of basin characteristics is relatively constant both within tiles and between tiles, with all basins falling within a clearly defined width/length range, and a slight transition from higher to lower width/length ratios with decreasing order such that the higher ratios are predominantly found in the fourth order basins and the lower ratios predominantly in the first order basins, although there are no clearly defined boundaries between basins of different orders. Secondly, the only major deviation from this trend can be found in a significant number of first order basins which have very low width to length ratios, a fact which is unsurprising considering that a large number of smaller basins are likely to be rill-like in nature. These basins are responsible for the fact that the median spacing ratios of first order basins are considerably lower than larger order basins, despite the fact that many first order basins are similar in character to these larger order basins. Thirdly, there are some changes in maximum widths and length attained by basins. Basins in the northern part of the study area tend to reach maximum lengths of ~1500m and widths of approximately ~1000m for the highest order streams studied, with the exception of tile 7a, which has some basins reaching lengths of ~2000m. The transition from tile 8a to tile 8b sees an abrupt change in the maximum lengths and widths attained by

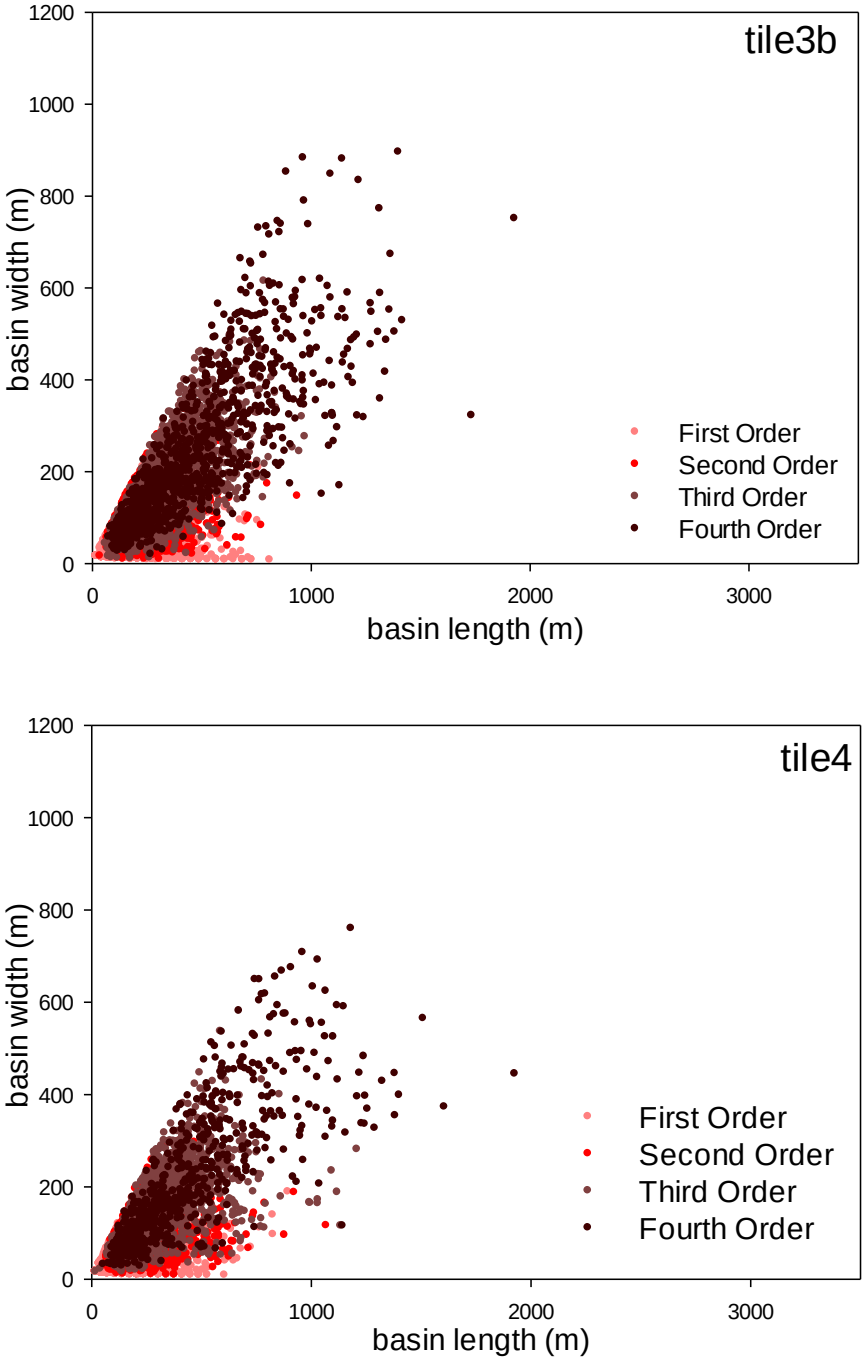

Figure 6.5: Plots of basin width against basin length for every basin in each tile, separated and colour-coded with respect to stream order. Note the overall decrease in maximum widths and lengths attained by basins in the south of the study area (south of tile8a) with some exceptions.

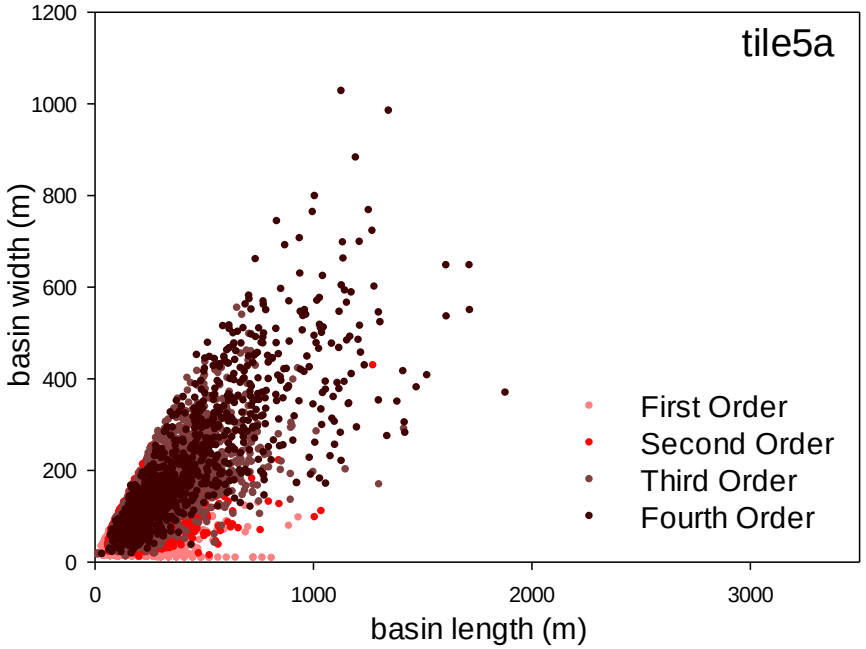

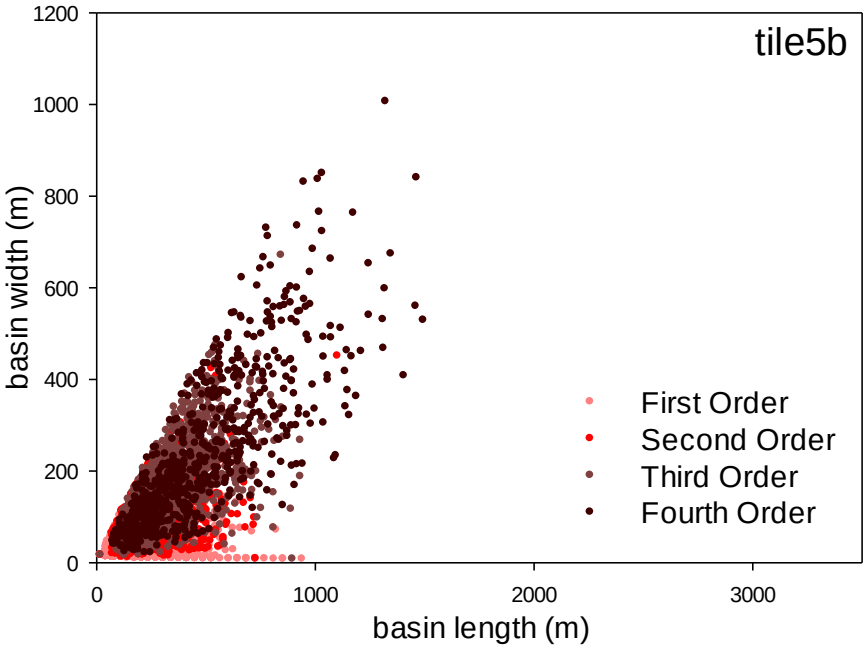

Figure 6.5 (continued)

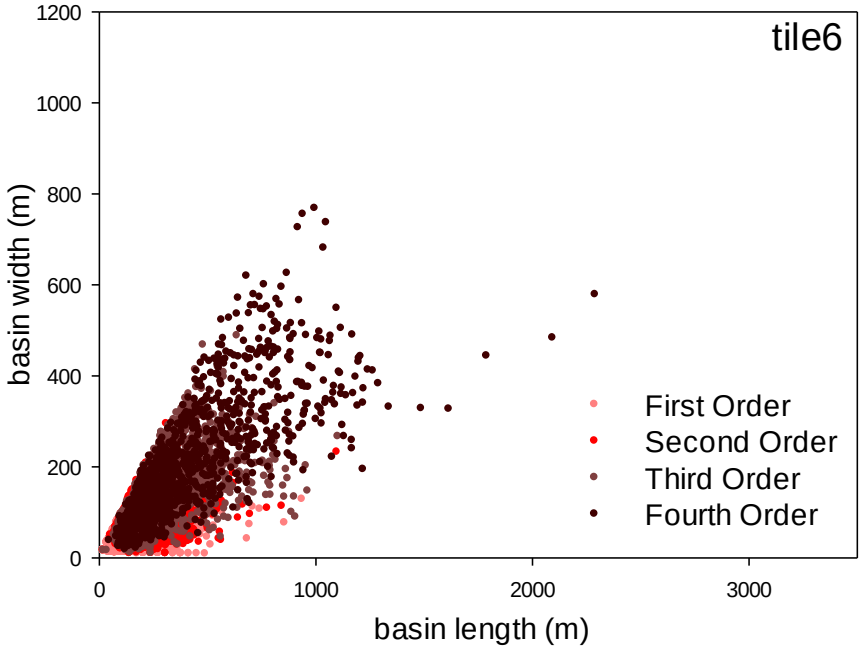

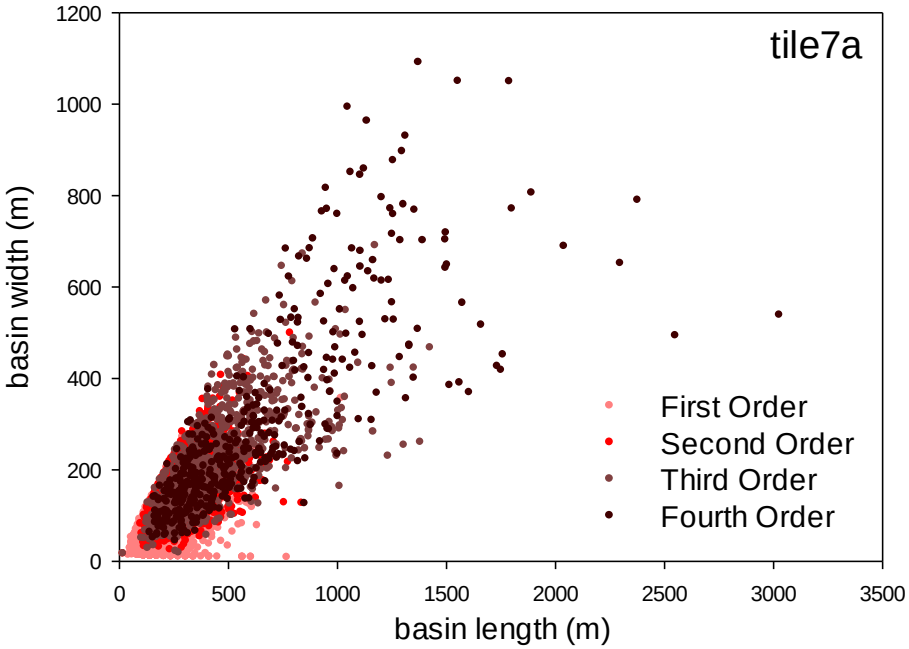

Figure 6.5 (continued)

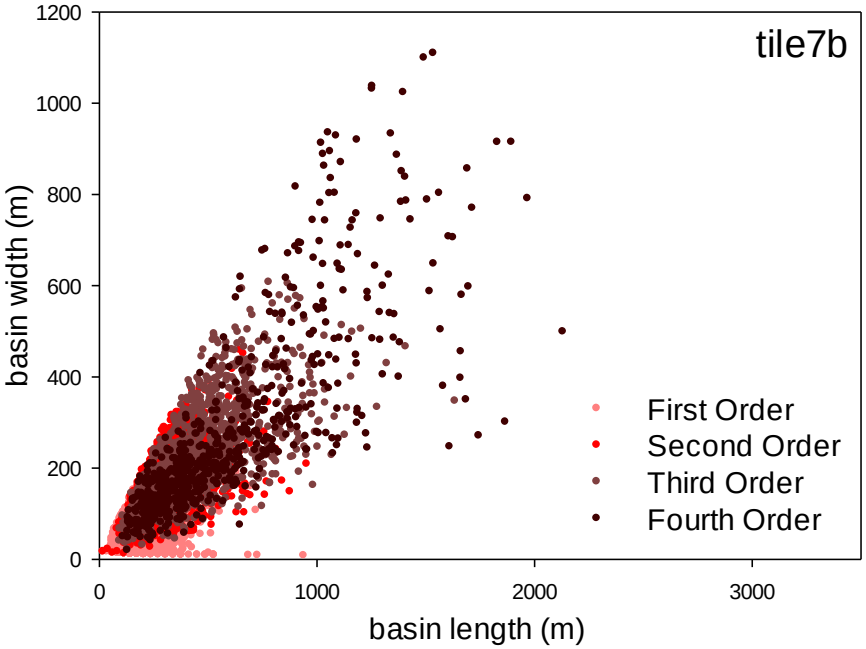

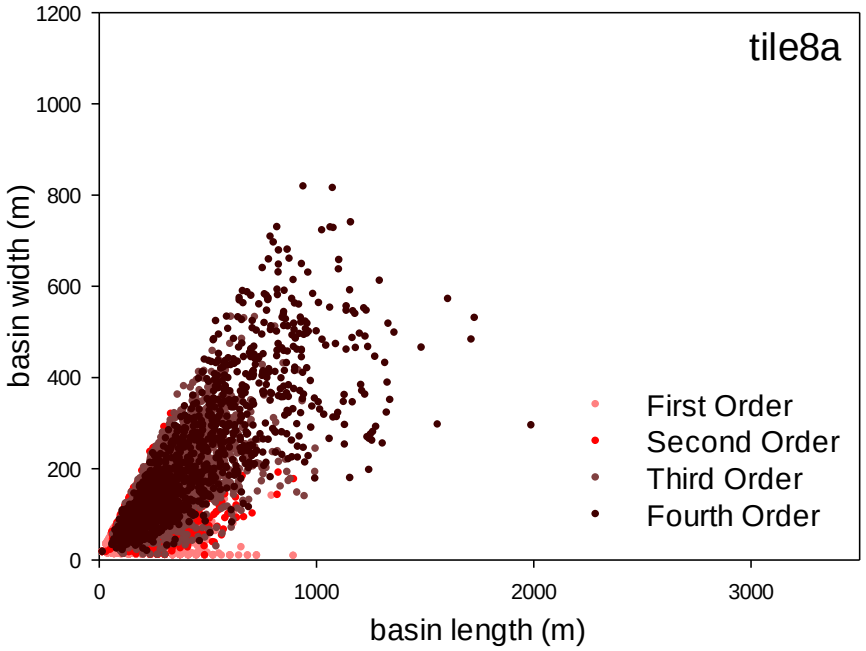

Figure 6.5 (continued)

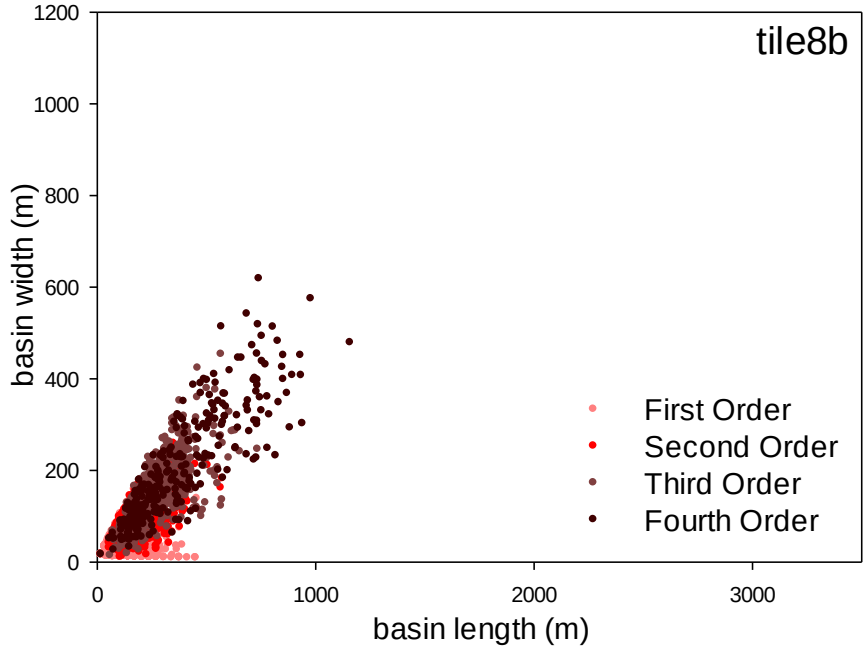

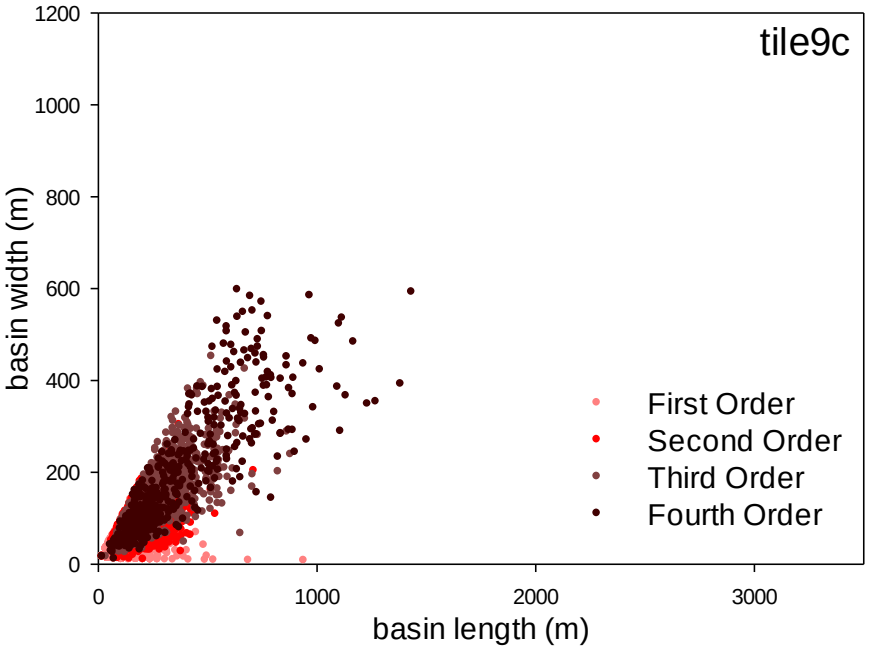

Figure 6.5 (continued)

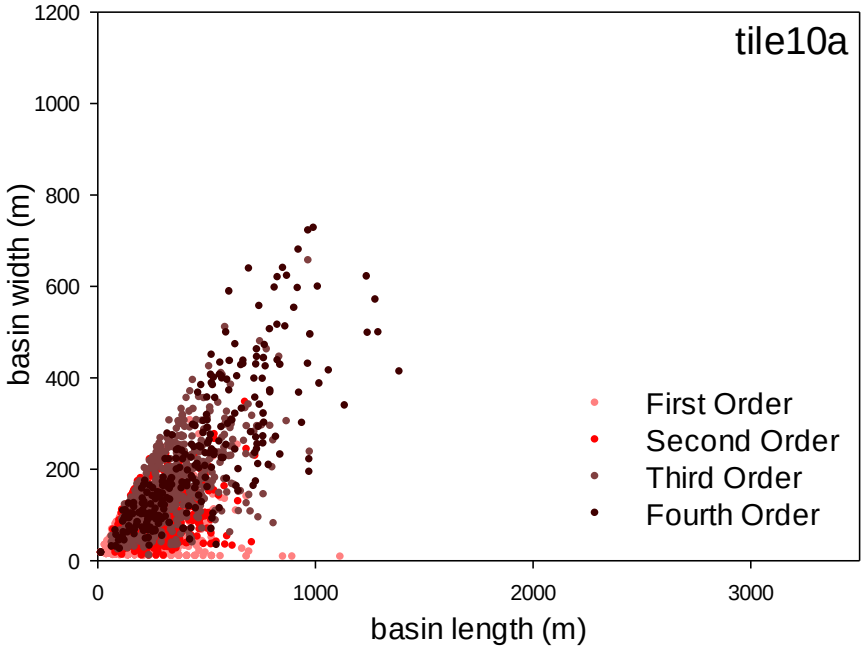

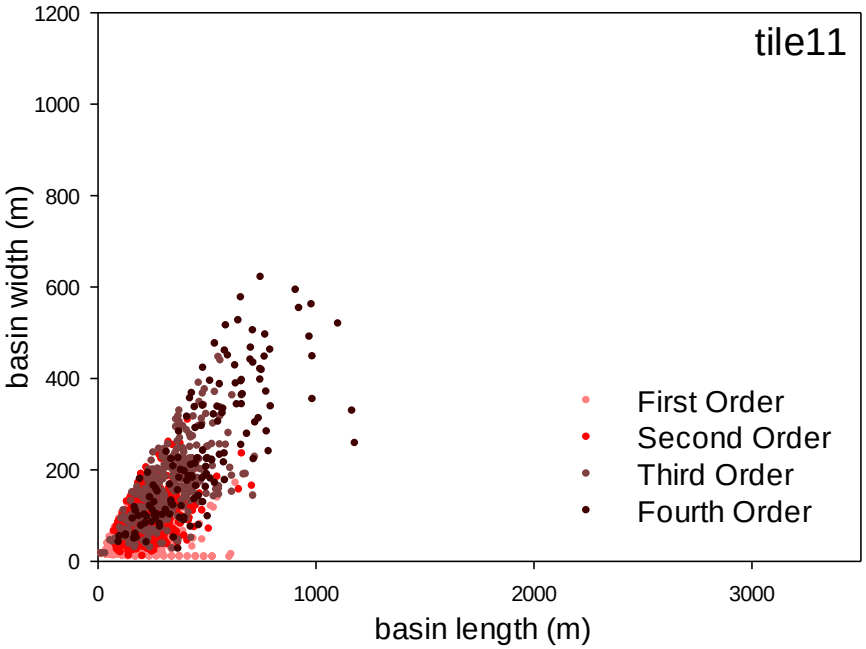

Figure 6.5 (continued)

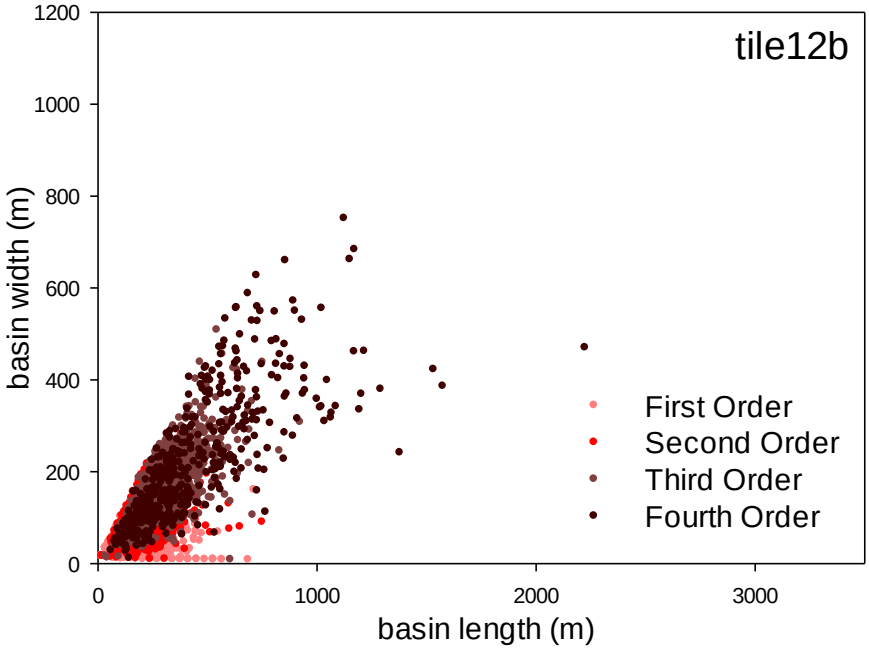

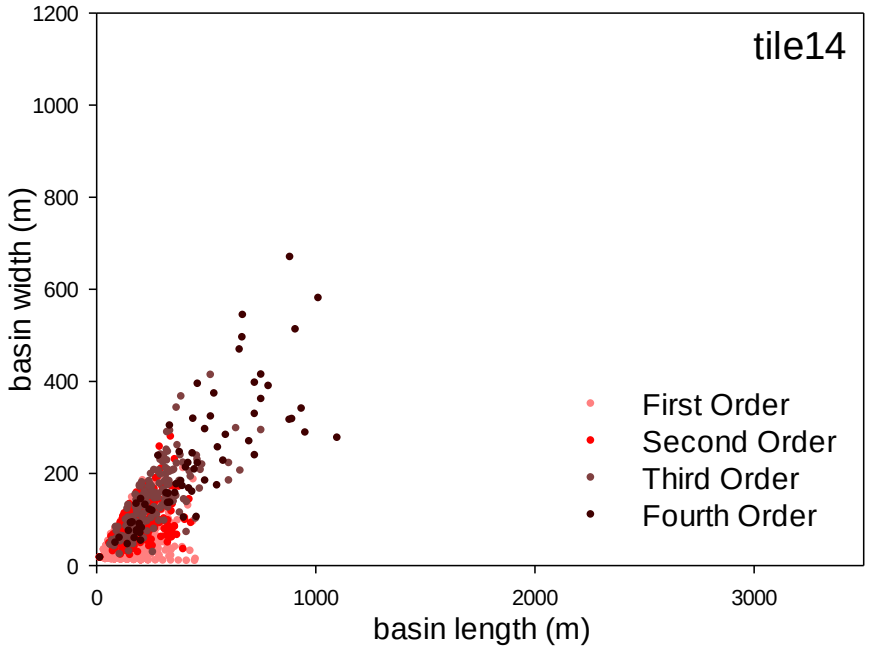

Figure 6.5 (continued)

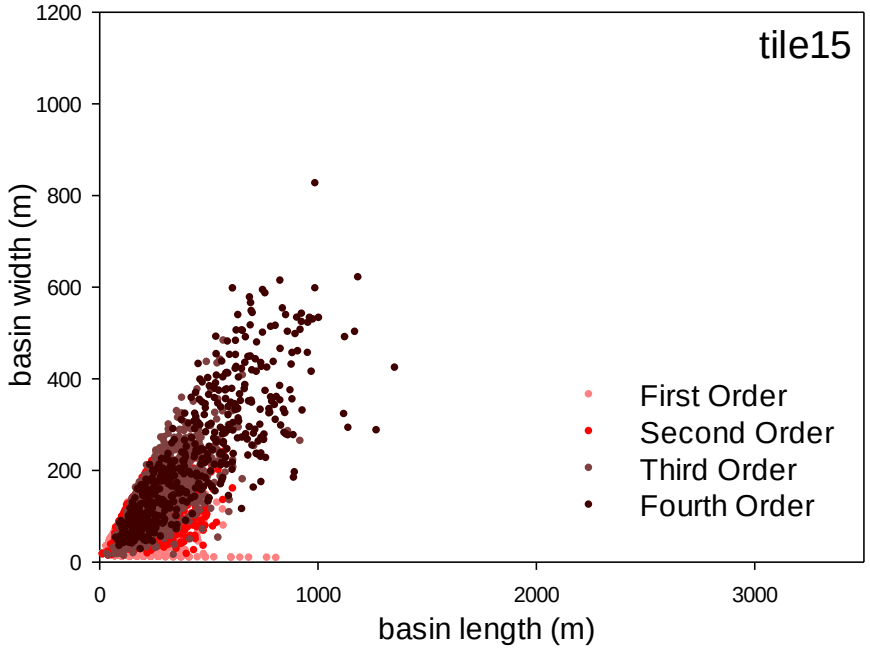

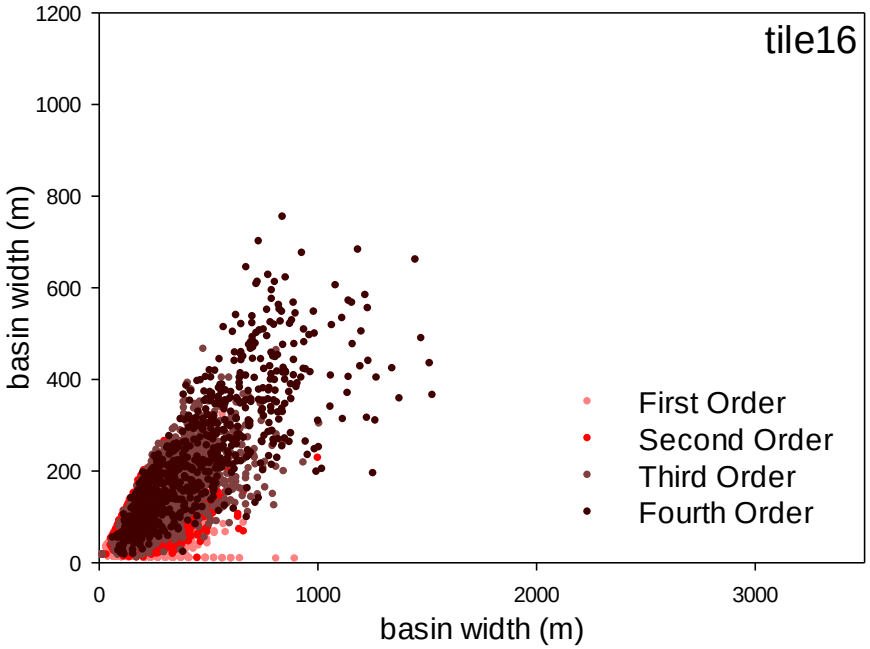

Figure 6.5 (continued)

basins, with maximum lengths of ~1000m and maximum widths of ~600m. This restriction in maximum dimensions persists to the south of the study area.

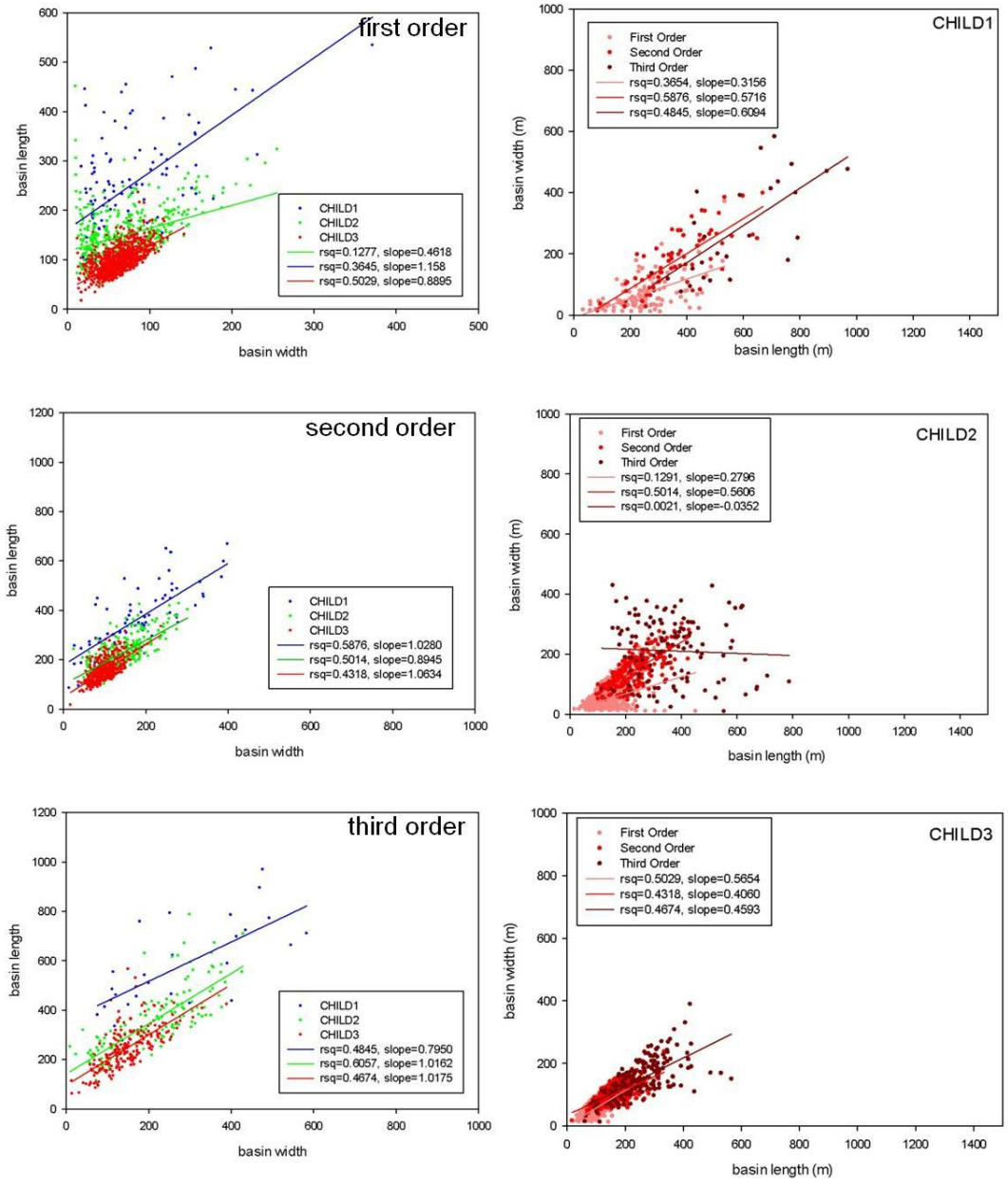

Figure 6.6: Width vs length plots for all basins extracted from the CHILD landscapes. (a-c) illustrate that increasing D (CHILD1 has the highest D value, CHILD3 the lowest) will tend to increase maximum basin dimensions, for all orders. (d-f) illustrate the overall restriction of basin dimensions with decreasing D, suggesting that basins can become larger with increasing ratios of hillslope to channel transport.

Plotting width against length for all basins extracted from the CHILD landscapes (Figure 6.6, a-c) shows that the distribution of ratios becomes more restricted with decreasing *D*, or with greater input of advective transport relative to diffusive transport, suggesting that basins can become larger with increasing ratios of hillslope to channel sediment transport. Figure 6.6(d-f) illustrates directly the effect that increasing diffusive transport has on basin dimensions in first, second and third order basins: increasing *D* will tend to increase basin length. The slope of the regression lines in Figure 6.6, however, shows no systematic change with either basin order or diffusivity; this indicates that there is no systematic change in width to length ratio with either of these variables.

6.4.3. Relationship between DEM tiles and CHILD landscapes

The relationship between the basins generated using the CHILD model and the basins generated in the natural landscapes can provide an indication of the applicability of the model to natural landscapes such as those in the study area (see Figure 6.7). The change in maximum basin length between the north and south of the study area persists even at the scale of first order basins. Distribution within the natural landscapes is much more heterogeneous than within the CHILD landscapes, which is to be expected; that the results of the CHILD model runs fall well within those of the natural landscapes indicates the applicability of the model in this setting. There are some exceptions to the general trend of restricted basin dimensions in the southern part of the study area, when first order basins are considered: tile 6 shows a much more restricted distribution than the adjacent areas, while tiles 15 and 16 contain catchments which attain greater dimensions than the areas immediately adjacent. In areas where the dimensions of basins are referred to as 'restricted', the distribution in natural landscapes broadly corresponds to that of the three CHILD runs combined. The plots of first order basins also reveal that there are, in general, more elongated (i.e. lower width: length ratio) basins in the northern parts of the study area; this may be due to the fact that short-wavelength channels are more difficult to observe in humid climates where response times are rapid and these channels are obliterated by prolonged precipitation (Simpson & Schlunegger, 2003).

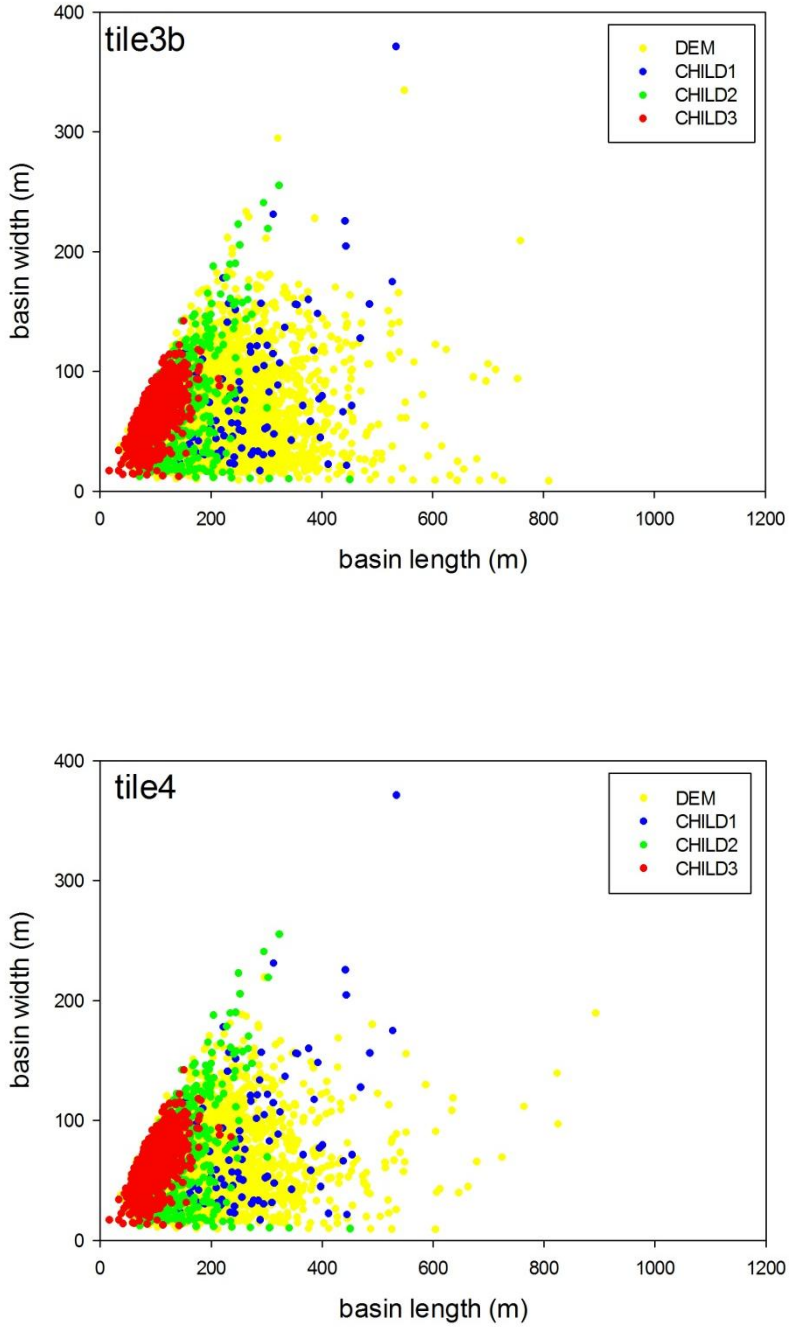

Figure 6.7: Plots of basin width versus basin length for all first order basins generated from DEM tiles and CHILD landscape tiles. These plots illustrate the fact that almost all basins generated using the CHILD model fall within the range of basins in natural landscapes, indicating that the model is generally applicable, particularly in areas with a homogeneous vegetation cover.

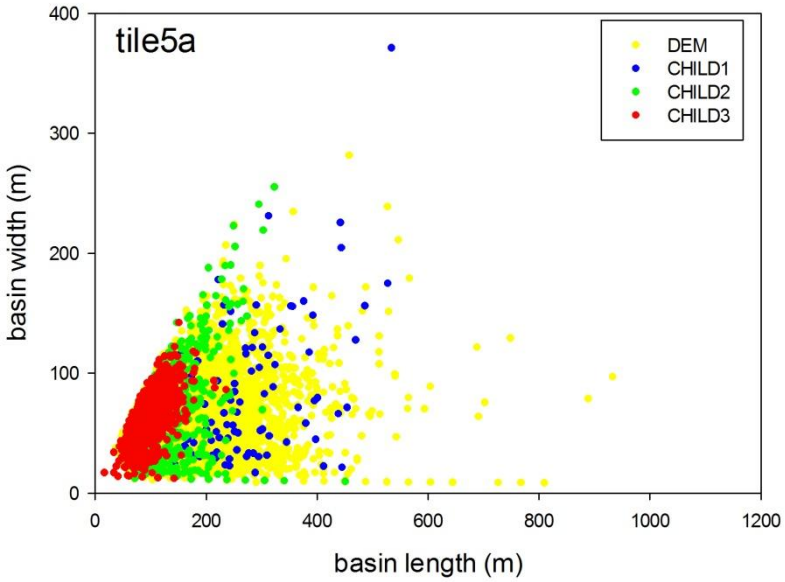

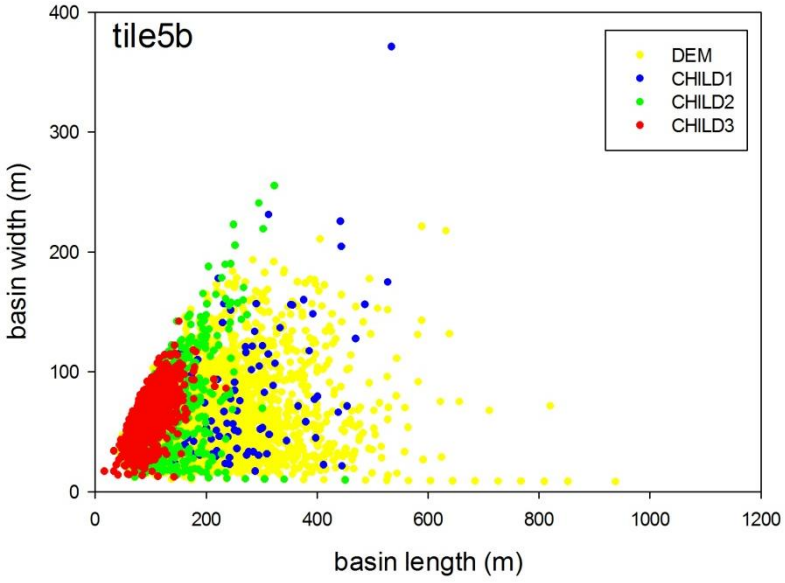

Figure 6.7 (continued)

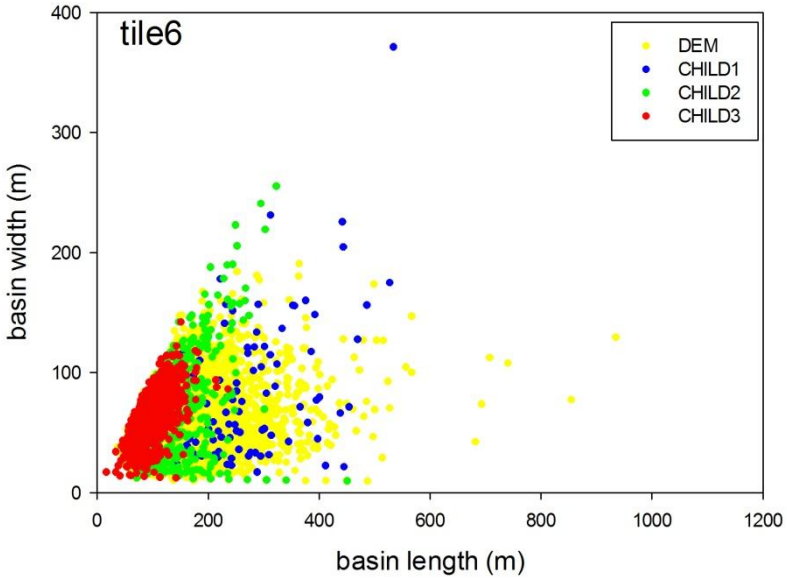

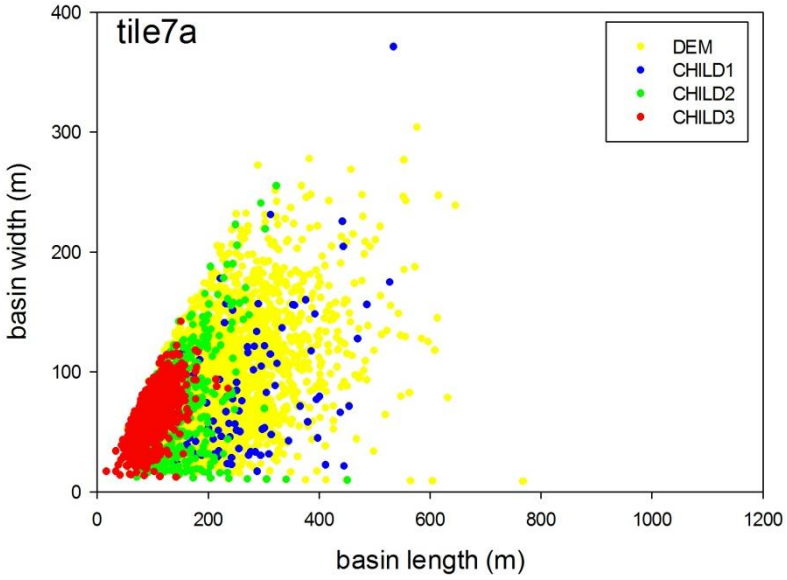

Figure 6.7 (continued)

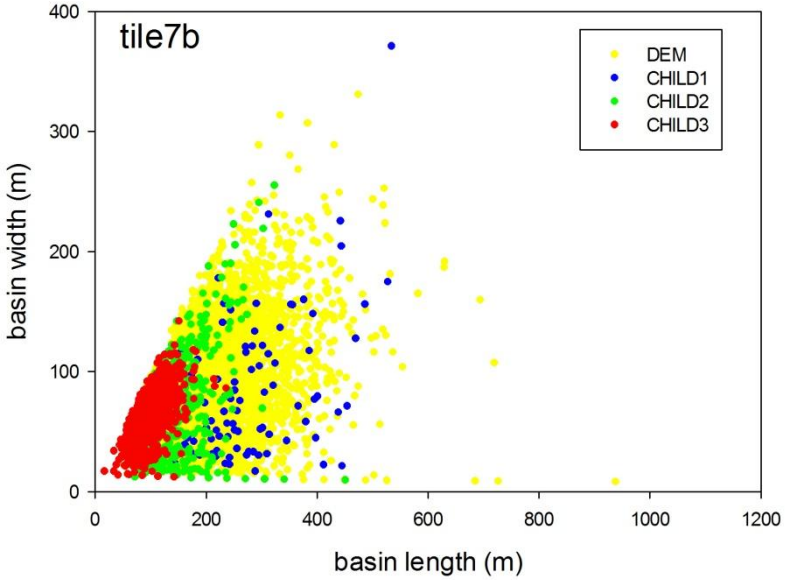

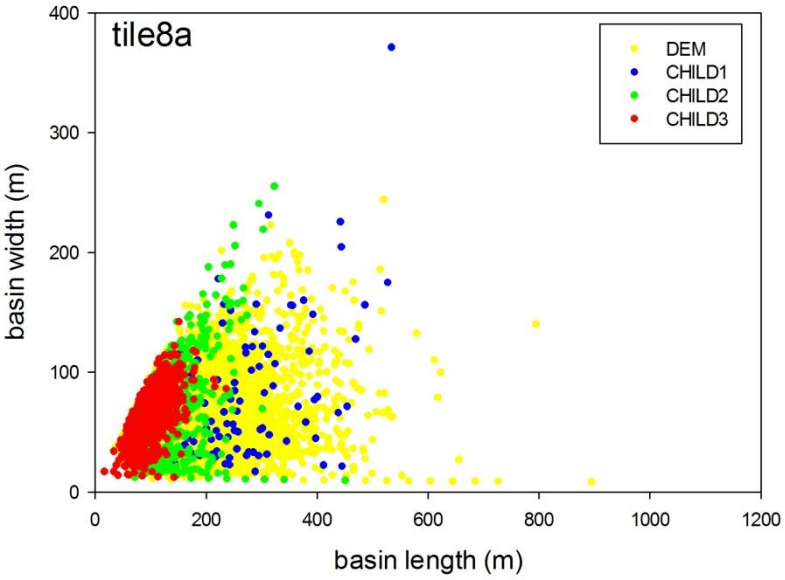

Figure 6.7 (continued)

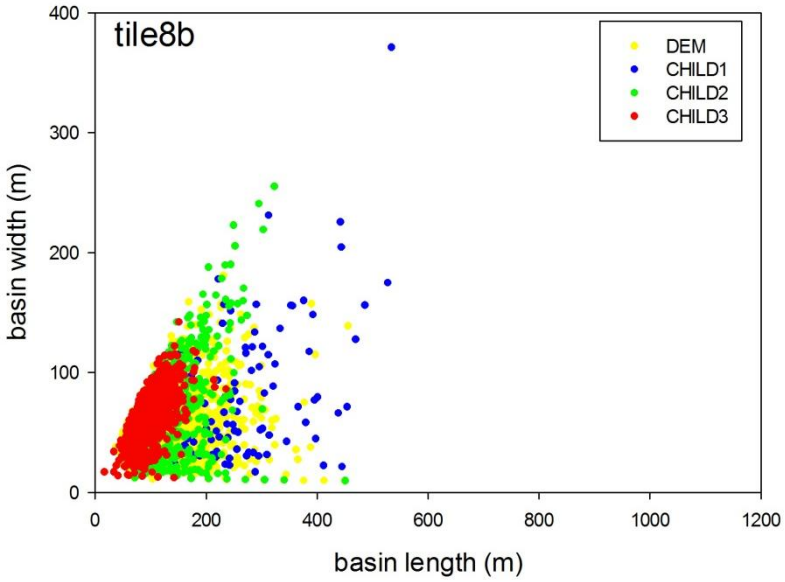

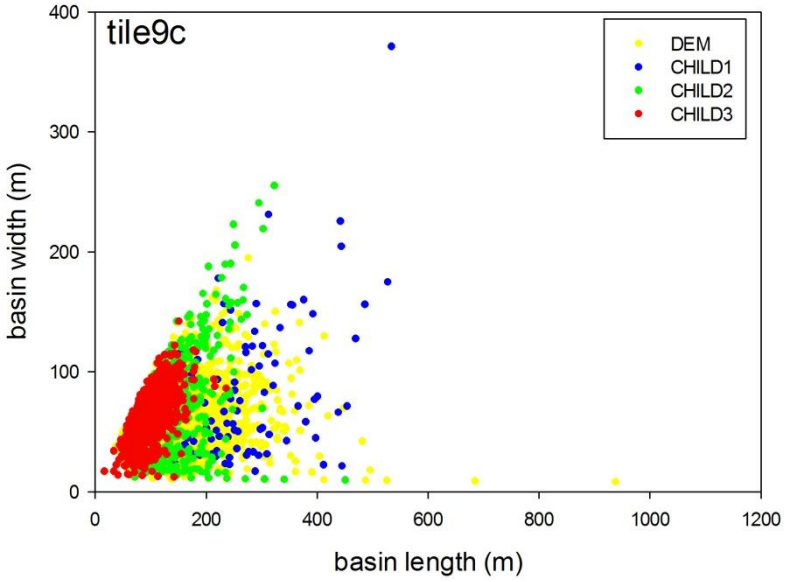

Figure 6.7 (continued)

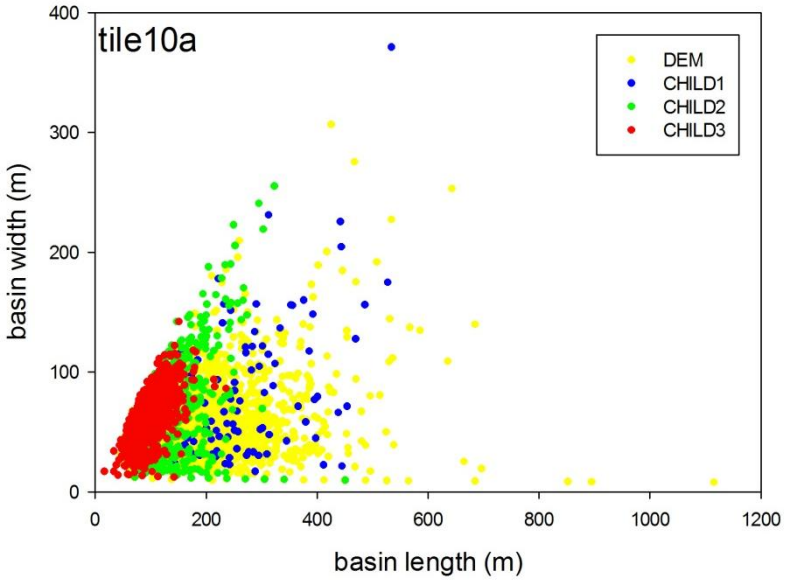

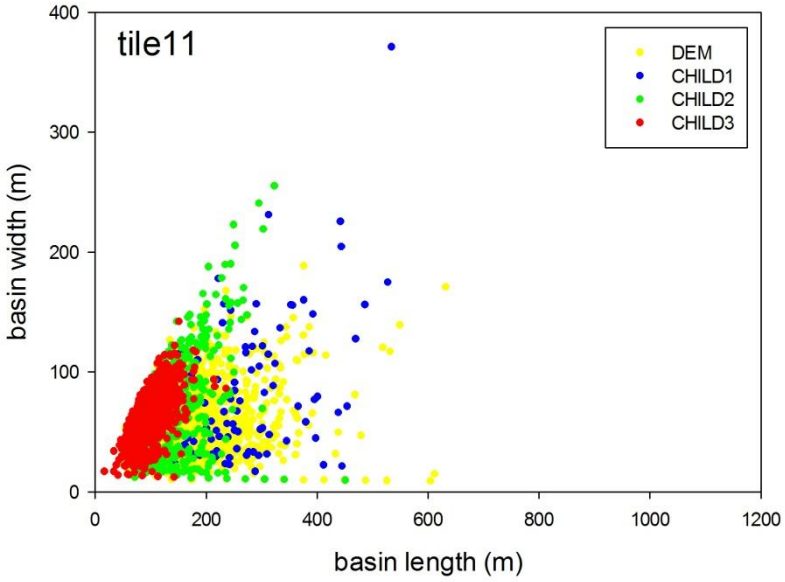

Figure 6.7 (continued)

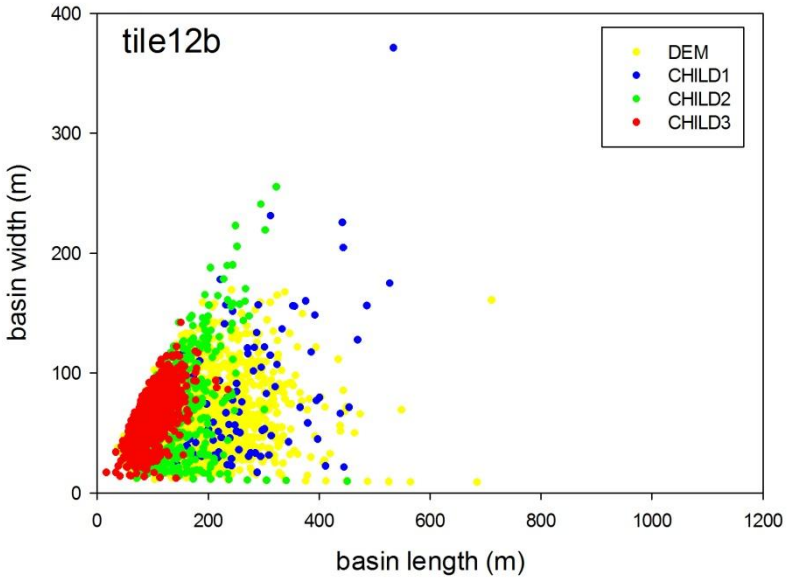

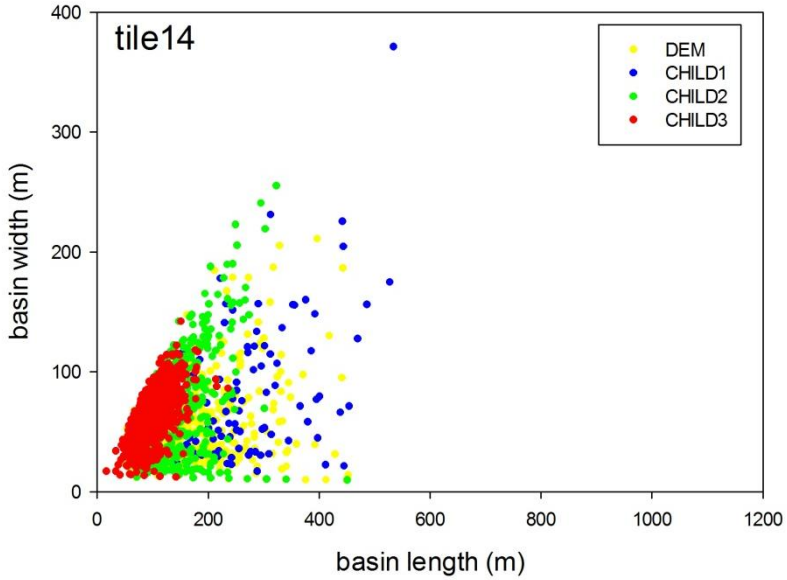

Figure 6.7 (continued)

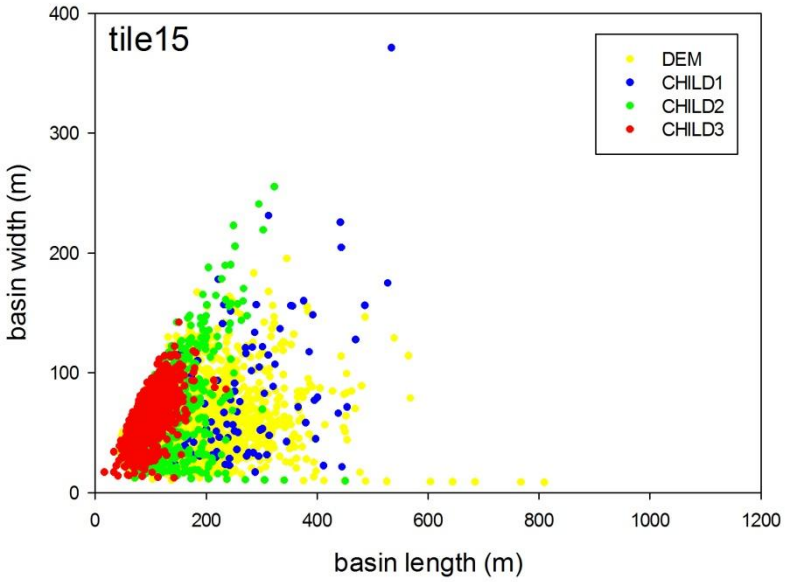

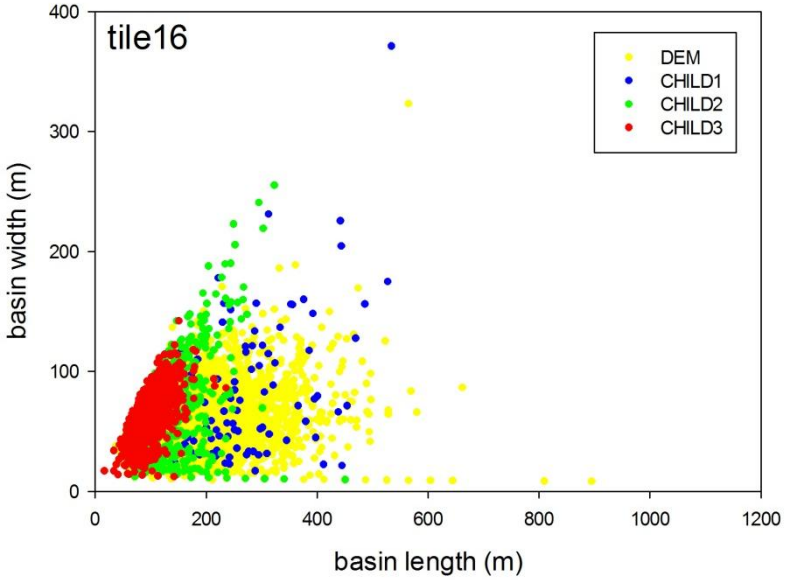

Figure 6.7 (continued)

6.4.4. Changes in maximum basin length with latitude

This change in maximum basin dimensions with latitude can best be illustrated by plotting maximum basin length against mean annual precipitation (Figure 6.8).

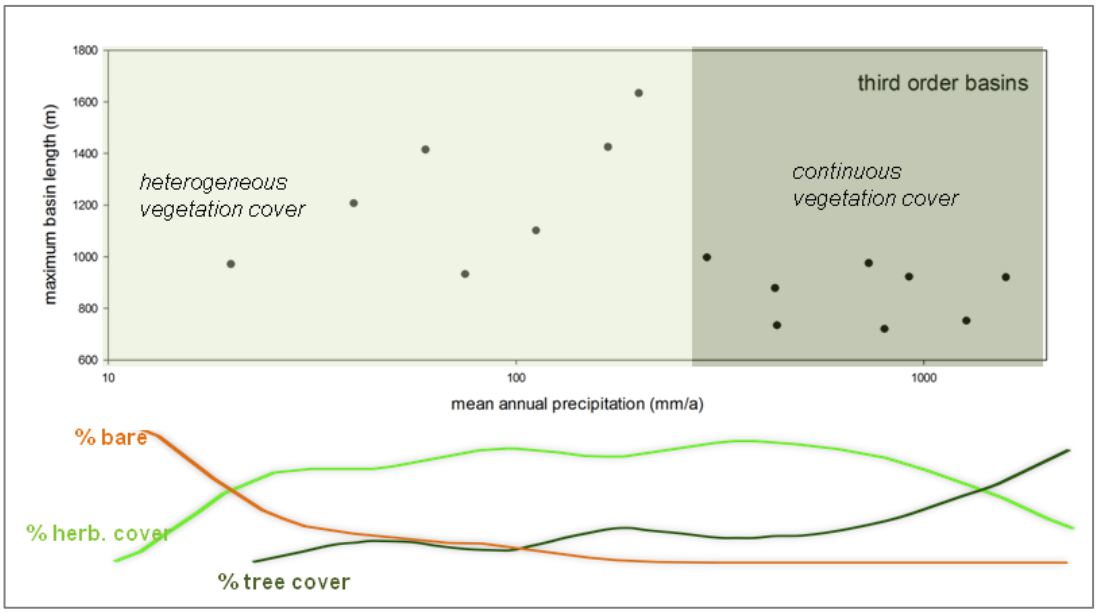

Figure 6.8: Plot of maximum basin length attained for each tile against mean precipitation for the region, for third order basins. This illustrates the greater variability in maximum basin length where vegetation cover is discontinuous, and the relatively stable (and lower) maximum lengths attained once vegetation cover is continuous, regardless of changes in vegetation cover composition or increases in precipitation. Vegetation curves are simplified from Figure 5.4.

This reveals a relationship which persists across first to fourth order streams, becoming more pronounced as basin order increases. Maximum basin length increases with precipitation to ~100-150mm/yr, before decreasing and starting to level off at ~400mm/yr and remaining relatively constant into the humid area. This trend is weak for first and second order basins, but becomes more pronounced in third and fourth order. This trend is similar in nature to that observed between

diffusivity and precipitation. A general increase in maximum basin length with increasing *D* is also observed in the CHILD landscapes (Figure 6.9), although in this case the differences are less pronounced in higher order basins. This relationship between maximum basin length and diffusivity may not seem like such a surprise considering the use of drainage density both to calculate *D* for the cosmogenic samples and as an input parameter in the CHILD model; however, both of these inputs require the use of local drainage density/hillslope length measures, and as such the use of maximum basin length may still provide some useful information.

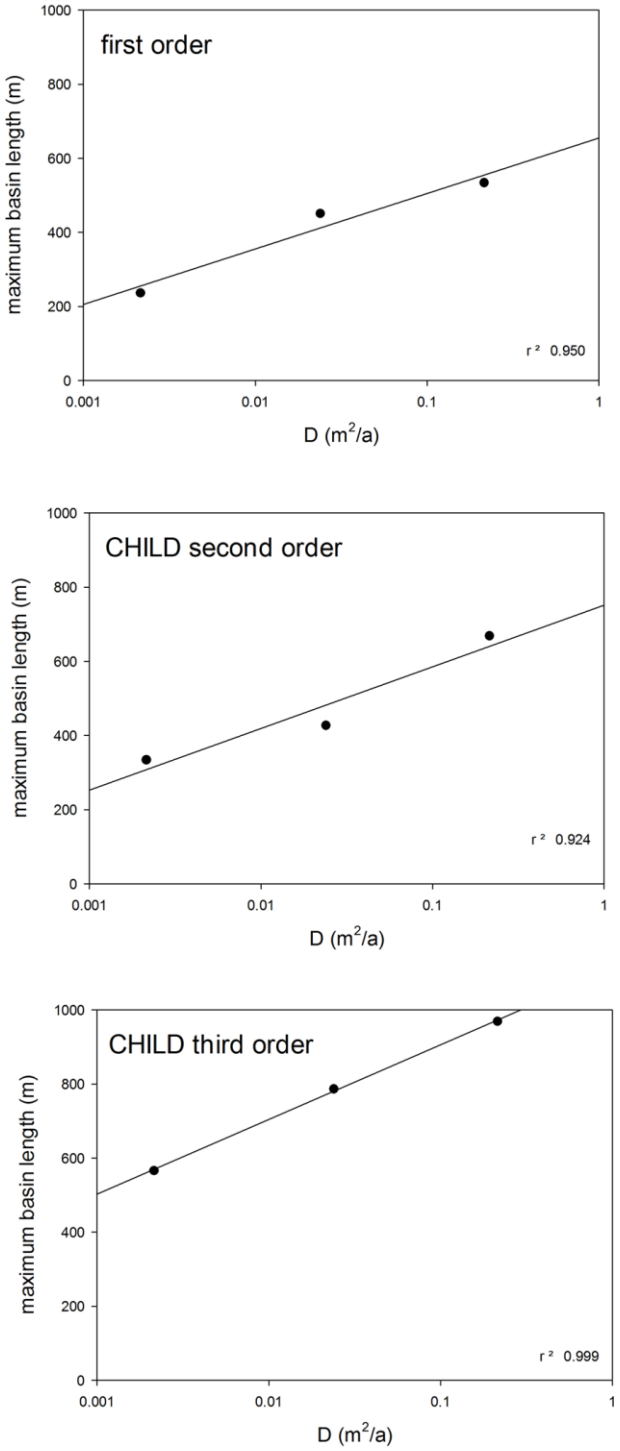

Figure 6.9: Increasing the diffusivity constant, *D*, in the CHILD model increases maximum basin length attained at a rate that is roughly equivalent over first, second and third order basins, although in general larger maximum dimensions are attained at higher orders.

6.5. DISCUSSION

6.5.1. Uniform Spacing Ratio

The results indicate a positive linear relationship between basin width and basin length in the natural landscapes of the Chilean Coastal Cordillera; average spacing ratios vary little along the transect, although there is significant variance in ratios within each specific region. Results are consistent with those seen in previous studies of natural landscapes. Hovius (1996) found that basin width was approximately 0.46 times basin length, while Walcott & Summerfield (2009) found that basin width was approximately 0.53 times basin length; results from the Chilean Coastal Cordillera fall broadly within this range, with the exception of first order basins which have significantly lower median width to length ratios. Talling (1997) reports a width to length ratio of ~0.5 for fault blocks, a value which also corresponds with the present study, providing further evidence that average spacing ratio is constant over a wide variety of tectonic and climatic settings, regardless of the location and orientation of catchments within the main mountain belt. The lower average spacing ratios in first order basins is perhaps unsurprising: these basins will include a significant number of longer, narrower basins associated with rill erosion and more transitory erosion features. These basins are likely to skew the results towards lower ratios, but these small scale features are likely to be unimportant at greater spatial scales. Likewise, the variability of median spacing ratios is greater for first order (and, to a lesser extent, second order) basins, a fact which can be attributed to the input of factors which are most important at the hillslope scale and unimportant in larger systems. The heterogeneity of vegetation cover at the hillslope scale, for example, can have a

significant effect on structuring runoff, affecting efficiency of both fluvial and hillslope transport.

6.5.2. Assertions about advective transport rates

Perron *et al* (2008) found that valley spacing was most sensitive to the relative rates of advective processes (such as stream incision) and diffusion-like processes such as soil creep, and defined a dimensionless valley spacing, analogous to the width to length ratio in this study, and a quantity, Pe, which represents the ratio of advective to diffusive processes. Their models suggest that the dimensionless valley spacing should increase linearly with the inverse of this number, ie with the ratio of *D/K*, in first order basins. However, in the study area there is no systematic change in width to length ratios with changing latitude, yet it would be expected that the significant changes in climate and vegetation cover with latitude would result in changes in the relative inputs of different erosion processes. It seems unlikely, given the significant range in climate and vegetation throughout the study area, that a systematic change in width to length ratio would not be noticed in the data if the results agreed with the model results of Perron *et al* (2008). However, the mechanisms by which *D* and *K* interact in natural landscapes is poorly constrained, and evidence suggests that the introduction of a heterogeneous vegetation cover can affect both diffusive and advective transport in a range of ways. In particular, in arid landscapes where sediment transport is sporadic, erosion tends to be highly fluvial despite the lack of precipitation (Simpson & Schlunegger, 2003) and increasing mean annual precipitation may lead to a concomitant increase in both *D* and *K* as the increased moisture supports vegetation growth and thus encourages sediment transport on hillslopes, at the same time as enhancing advective channel processes (Figure 6.10). In fact, modelling results for landscapes experiencing periodic climate forcing (Rinaldo *et al*, 1995) do suggest that channel incision can be positively correlated

with the extent of landscape convexity, and thus with rates of diffusive sediment transport.

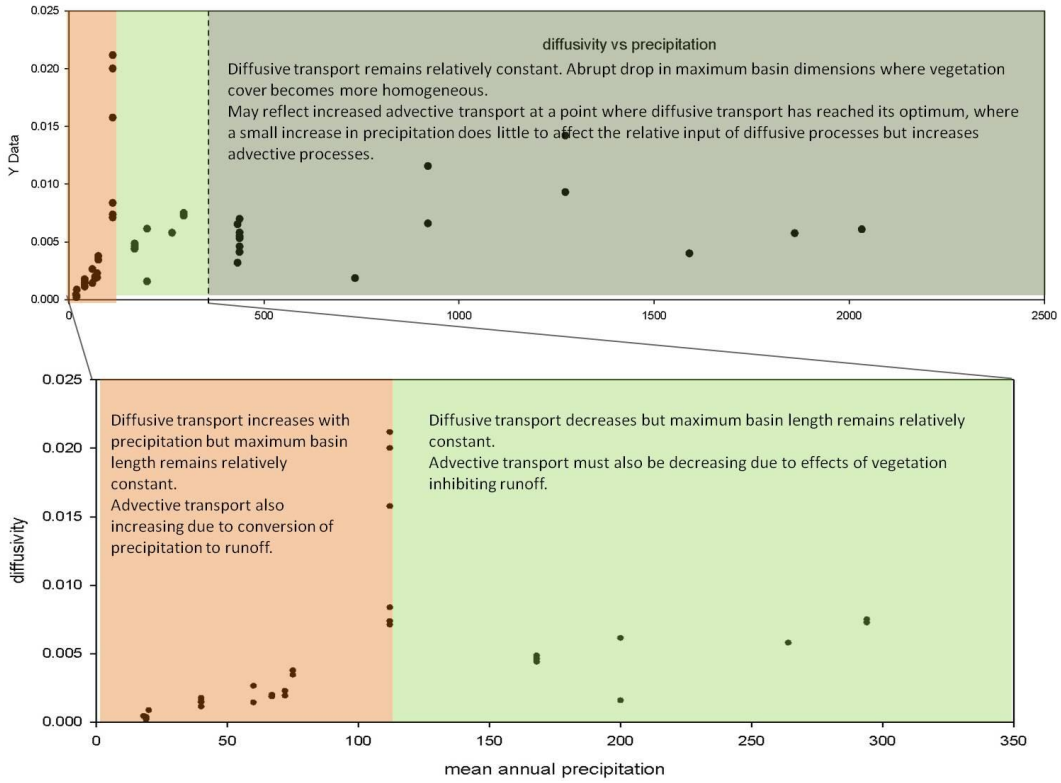

Figure 6.10: Assertions that can be made about the relative changes in diffusive and advective transport with precipitation, if a uniform basin spacing ratio is maintained due to no change in the ratio of diffusive to advective transport.

6.5.3. Possible mechanisms for controlling width to length ratio

Although it has been suggested that the range of basin spacing ratios represents an optimal or most probable geometry (Hovius, 1996; Leopold & Langbein, 1962), there is no generally accepted explanation for why this might be. It has been suggested (Hovius, 1996) that, since the relationship between drainage basin outlet spacing and mountain-belt half-width can be expressed in the same form as Hack's law of stream length and drainage area, the same mechanisms may explain both relationships, yet there is no generally accepted explanation for Hack's law either. Nevertheless, this feature of natural landscapes is spatially and temporally persistent, and modelling results suggest that channels will split in response to shortening in order to maintain this optimum spacing ratio (e.g. Bonnet, 2009). Hovius (1996) suggested that this uniform spacing ratio may arise from the competition between hillslope and fluvial processes during uplift, an idea also considered by Simpson & Schlunegger (2003), whose modelling results suggest that this competition between hillslope and fluvial transport imposes a finite landscape morphology where fluvial processes generate relief and hillslope processes impose an upper limit on relief generation. This is also described at a much smaller scale by Smith & Bretherton (1972), who show that finite dissection of landscapes results due to an instability of hillslopes which is introduced where advective transport dominates diffusive transport. This self-regulation of catchment morphology, combined with the channel splitting mechanism described by Bonnet (2009) provides a plausible explanation for the uniform basin spacing ratios witnessed along the climatic transect, and may also explain the restriction of maximum basin lengths in the southern part of the study area. Furthermore, Hovius (1996) notes that spacing ratios do not appear to differ

depending on range age, suggesting that the regular spacing develops early in mountain belt evolution and is preserved despite competition between fluvial and hillslope transport; this would explain the development of a uniform median spacing ratio in the Chilean Coastal Cordillera, despite changes in climate and vegetation, both spatially and temporally. The distribution of basin spacing ratios becomes more uniform for basins of third order and above, which may suggest this is the scale at which the stable basin configuration as described by Hovius (1996) becomes effective (a length to width ratio of 2 – 2.2, or width to length ratio of 0.45 – 0.5), or may equally indicate that erosion processes are sufficiently different at the scale of first order streams that a lower width to length ratio is considered more 'stable'.

6.5.4. Agreement between CHILD and previous modelling results

The results obtained from analysis of the landscapes generated using the CHILD model indicate the opposite of that predicted by Perron *et al* (2008): increasing the diffusivity constant used in generating the landscapes leads to a decrease in width to length ratio. This relationships persists for second and third order basins, but is particularly pronounced in first order basins. The relationship is also counter-intuitive, since it would be expected that longer, thinner basins would emerge from a relative increase in advective transport rather than diffusive transport. Decreasing *D* is the same as a relative increase in *K* (i.e. more fluvial erosion) but still leads to an increase in width to length ratio of first order basins. Higher order basins also have a higher width to length ratio when *D* is kept constant. Perhaps decreasing *D* in the model allows the *K* term to become dominant, and the consequent increase in fluvial erosion allows expansion of catchment boundaries before these split off into smaller catchments as they rearrange (see Attal, 2009; Bonnet, 2009). This may represent an intermediate stage between first order and second order catchments, and could also explain the significant overlap of first and second order data points in the CHILD data and the shift to higher width to length ratios with higher order basins. The effect of decreasing *D* becomes much less pronounced at higher orders, which suggests that this mechanism has limited effect on higher order basins. This effect is not noted in the natural landscapes. In addition, results from the CHILD model runs should be interpreted with caution, as the method of extraction of stream networks could not be verified as being wholly appropriate in the same way they could be for the natural landscapes; in particular, the first order basins extracted from the CHILD model runs may be unreliable.

6.5.5. Restriction of maximum basin dimensions

Although there is no systematic change in width to length ratio with latitude in the study area, there is one notable change in basin morphology: the maximum dimensions of the natural landscapes appear to be suddenly restricted between tile 8a and tile 8b. In the CHILD landscapes, decreasing *D* leads to a more restricted distribution of basin length (Figure 6.11).

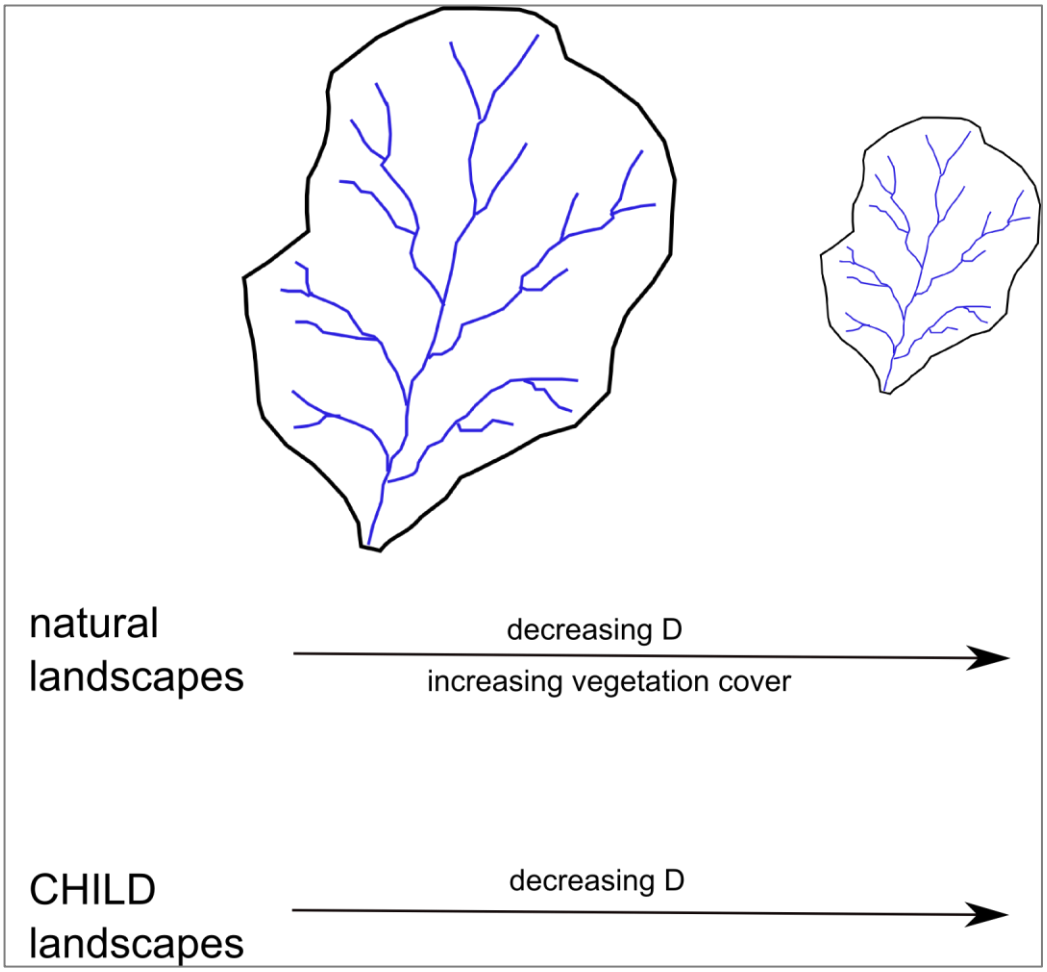

Figure 6.11: Summary of the effects of decreasing the diffusivity constant, D, in both natural landscapes and landscapes generated using the CHILD model. Decreasing D in natural landscapes appears to be buffered by concomitant changes in advective transport, K, and width to length ratios of basins remains constant, but overall basin dimensions are restricted with the introduction of a continuous vegetation cover.

This is an intuitive relationship, since increasing *D* will increase the ratio of hillslope to channel processes, allowing the development of larger basins. This decrease in maximum basin length in the natural landscapes corresponds to the disappearance of bare ground and the development of a constant, homogeneous vegetation cover and can also be linked qualitatively to the independently-determined measure of diffusivity, or sediment transport efficiency, suggesting that while relative ratios of diffusive and advective transport do not affect average basin spacing ratios, they may have an effect on maximum basin dimensions and internal catchment morphology. Montgomery & Dietrich (1992) relate the finite dissection of landscapes to the lower boundary of an empirically determined topographic threshold for channelization of hillslopes, and demonstrate that spatial and temporal variations in climate can affect the source area required for channel initiation via changes in hydrological and erosional processes; this could be interpreted to suggest that these properties have a more significant effect on internal morphology of catchments (i.e. channel development) while having little effect on valley morphology. Perron *et al* (2009) describe precipitation-dependent changes in characteristic ridge-valley wavelength in low-relief, soil-mantled landscapes, which they interpret to reflect changes in the ratio of soil creep to channel incision, with drier climates leading to increased dominance of channel incision and smaller wavelengths, and wetter climates leading to dominance of soil creep processes and thus longer wavelengths. The CHILD results show an increase in maximum basin length with increasing *D*, in agreement with the results of Perron *et al* (2009). In an idealised landscape, this is an intuitive relationship, since an increase in *D/K* ratio represents a landscape increasingly dominated by diffusive transport at the expense of channel incision and acts to

smooth the landscape rather than dissect it. The results from the natural landscapes, at first glance, appear to disagree with these findings, because it would be expected that valley spacing would increase with wetter climates, due to the reduction of runoff and increase in diffusive transport that should occur with increased vegetative cover (Perron *et al*, 2009; Whipple, 2009). There is no systematic increase in maximum basin dimensions with increased precipitation or vegetation cover in the study area. In fact, the opposite occurs: the maximum basin dimensions are significantly lower in the southern, wetter part of the study area. This effect may not be surprising if there is no systematic, linear change in landscape diffusivity with increasing precipitation and vegetative cover, and Chapter 5 indicates that this is indeed the case (see Figure 5.4): diffusivity is found to increase with precipitation in arid landscapes, peaking in semiarid landscapes, before decreasing and levelling off in the more humid regions where both precipitation and vegetation become relatively homogeneous.

The relatively constant distribution of width versus length in the north and the south of the study area, and the sudden change between the two regions can be attributed to the effect of a threshold for channel incision, which is not incorporated into the study of Perron *et al* (2009). A threshold could act to buffer the effects of competing D and K on valley spacing, by acting in the opposite direction (Whipple, 2009), up to a crucial point at which the vegetation cover becomes critically high, after which the threshold has little effect on valley spacing because modes of sediment transport are considerably different. Once there is sufficient precipitation that the threshold can be exceeded, smaller source areas are needed for channel initiation, leading to smaller basins whose absolute size is governed solely by competition between D and K.

Development of a homogeneous vegetation cover could significantly affect the channelization threshold described by Montgomery & Dietrich (1992), and thus vegetation may effectively impose an upper limit to channel network extent in the manner seen in the study area (Tucker & Bras, 1999).

The results of this study do not necessarily contradict those of Perron *et al* (2009) when several factors are taken into account. Firstly, the landscape properties considered by Perron *et al* (2009) are studied at a much finer resolution, and over a more limited spectrum of climate and vegetation properties, than this study; fine-scale changes in catchment morphology in the semiarid region may therefore be obscured in a continent-scale study. Secondly, the model of Perron *et al* (2009) is only strictly applicable in low-relief, soil-mantled landscapes, and does not account for a channel incision threshold which may be crucial in governing maximum extent of catchments at larger scales. Thirdly, if a landscape is not strictly in equilibrium, landscape properties may be defined by a composite of present climatic conditions and those inherited from previous climatic conditions; since the climate of the Coastal Cordillera has changed drastically, particularly in the central region, since the Last Glacial period it cannot be ruled out that the landscape here does not retain some pre-glacial signal.

6.5.6. Applicability of CHILD model

The distribution of basin dimensions for the more 'restricted' regions broadly correspond to the data for the combined CHILD runs for first order basins, suggesting that in these landscapes with homogeneous vegetation cover and climate

characteristics, the CHILD model provides a good estimation of how basin dimensions track changes in diffusivity. The model becomes less reliable at predicting the behaviour of natural landscapes when the effects of a heterogeneous vegetation cover are involved in modulating the response of the landscape to changing climate. One of the limitations of the CHILD model is that it models a single species of vegetation, so vegetation parameters remain constant along a climatic gradient; in reality the changing climatic conditions would foster a different community structure and competition, changing the balance of advective and diffusive processes in a slightly unpredictable way and leading to different hydrological and geomorphic behaviour (Collins & Bras, 2010).

7. CLIMATE AND VEGETATION EFFECTS ON SLOPE DISTRIBUTIONS

7.1. INTRODUCTION

Catchment-mean hillslope has been found to increase with erosion rate in a wide variety of catchments, until erosion rates reach ~300m/Ma (DiBiase *et al*, 2010) and when hillslopes are below threshold slopes (Ouimet *et al*, 2009; Binnie *et al*, 2007). Yet erosion rates derived from concentrations of cosmogenic ^{10}Be in fluvial sediments in the Chilean Coastal Cordillera exhibit the opposite relationship with mean basin slope: increasing erosion rate leads to a decrease in mean slope (Figure 7.1). However, in a landscape where uplift is spatially and temporally uniform, erosion rates will instead be adapted to keep pace with uplift and it therefore would not be expected to see a positive correlation between erosion rates and mean slopes. While topography will tend towards steepening to match uplift rates, how steep the landscape must become to do this depends on the sediment transport efficiency of the landscape, with landscapes with low sediment transport efficiency leading to steeper slopes (Figure 7.1). Ouimet *et al* (2009) state that it is channels which ultimately drive landscape response to base level fall, so while channel steepness may indeed be positively correlated with erosion rates at this regional scale, the steepness of hillslopes appears to be affected by factors other than erosion rate, and studying the distribution of these slopes may provide some insight into what these factors are.

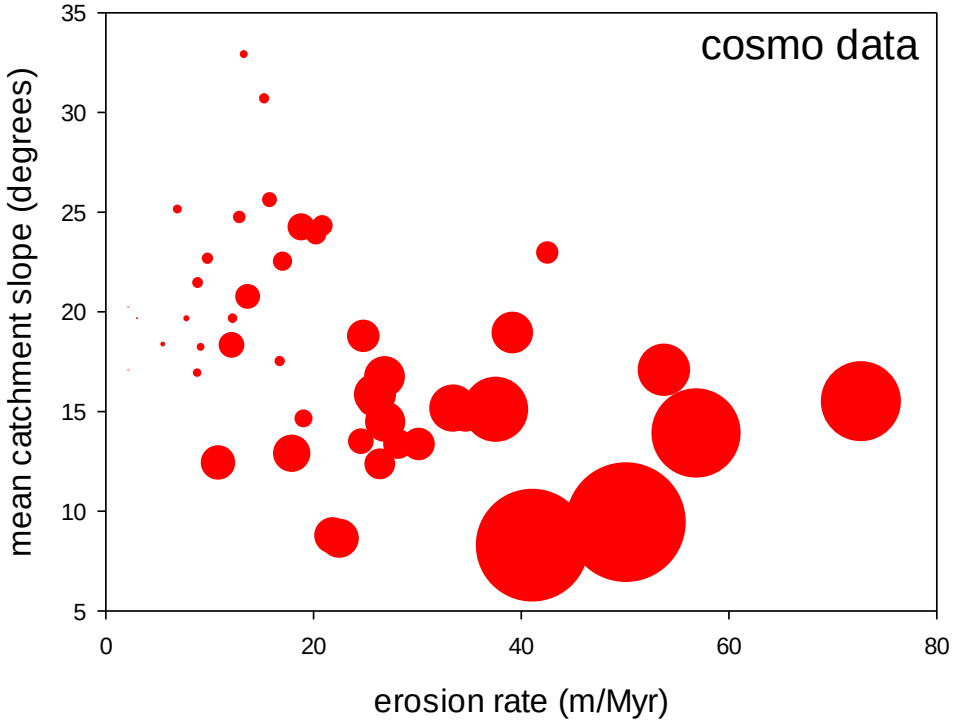

Figure 7.1: Mean catchment slope versus catchment averaged erosion rate calculated from concentration of cosmogenic ^{10}Be in fluvial sediments (see Chapter 5 for more discussion of data). Size of data points reflects sediment transport efficiency, *D*, and illustrates that slopes are steepest where sediment transport is least efficient.

In the same way that the width and length of basins can provide information about the processes at work in a landscape, the statistical distribution of slopes can also indicate which processes may be acting on the landscape. Slope-area studies have been widely used to study channel processes, and previous studies of slope distributions in natural landscapes have produced notable results. Many authors have studied the skewness of slope distributions in different terrain. Skewness is a statistical measure which characterises the degree of asymmetry of a distribution around the mean. Positive values indicate a distribution with an asymmetric tail which extends out to more positive values (fig. 7.2), while negative values indicate a distribution with a tail extending towards more negative values. It is thought that

different types of terrain might have different skewness characteristics. For example, Montgomery (2001) and Burbank (1992) have suggested that depositional terrain should have a positively skewed slope distribution, while threshold slopes and mass failure processes have been linked to negatively skewed slope distributions (Burbank *et al*, 1996; Densmore *et al*, 1998; Roering *et al*, 1999; Wolinsky & Pratson, 2005). It has also been suggested that, for some regions, slopes are distributed exponentially under depositional conditions and normally when uplift/erosion is dominant (Montgomery, 2001), although other evidence suggests that erosional terrain can produce positively or negatively skewed slope distributions (e.g. Speight, 1971; Burbank *et al*, 1996; Densmore *et al*, 1998; Roering *et al*, 1999). That mass failure processes are linked to negatively skewed slope distributions is perhaps unsurprising. In regions dominated by landsliding, mean slope will be high but the slope distribution will be limited by threshold slopes at its upper end (fig. 7.2). Similarly, in areas dominated by depositional terrain, mean slopes will tend to be concentrated at the lower end of the distribution and the slope distribution will be limited at zero slope. Although slope distributions are generally unimodal, multimodal frequency curves have been reported in heterogeneous landscapes, and as well as the overall distribution of slopes, information about landscape processes can be gleaned from statistical data including mean or median slope, the standard deviation and the skewness of the slope distribution (Wolinsky & Pratson, 2005; Vico & Porporato, 2009).

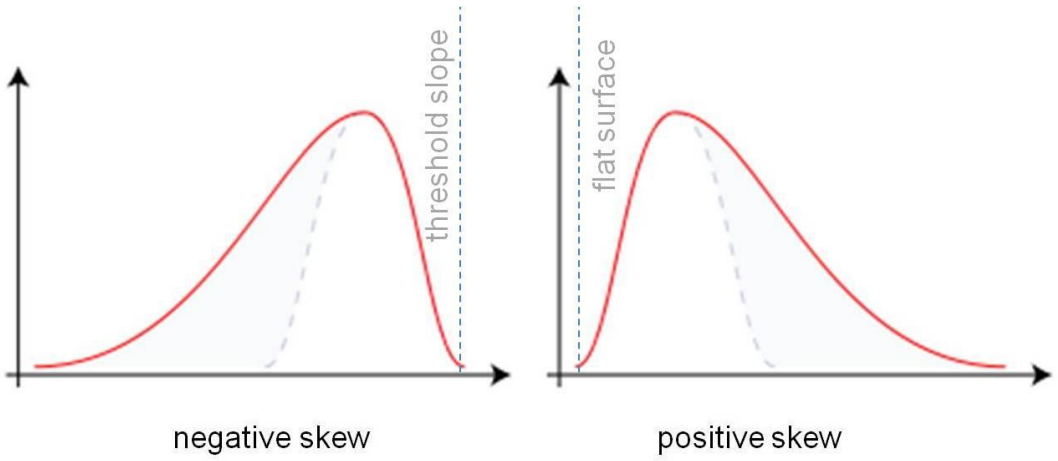

Figure 7.2: Illustration of negatively-skewed and positively-skewed slope distributions. Dashed line indicates normal (unskewed) distribution.

While the basin spacing ratio discussed in Chapter 6 can provide information about the relative ratio of diffusive and advective processes, or between hillslope and channel processes respectively, there are a variety of hillslope processes which are not explicitly described by this ratio; the distribution of hillslopes in a landscape may be able to provide further information about the competition between different hillslope processes. Wolinsky & Pratson (2005) studied slope histograms from DEMs of landscapes across the USA, and found that the skewness of the slope distribution changed from positive to negative with increasing mean slope, a trend reproduced by a process-based landscape model and which the authors suggest reflects a change in dominant hillslope processes with increasing mean slope. Their landscape model indicates that skewness is primarily governed by a dimensionless uplift number, defined thus:

$$\boldsymbol{U} = \frac{UA_L}{\mu K_0} \qquad [7.1]$$

where U represents uplift or stream incision, A_L is a typical hillslope length scale, μ is a critical failure slope and K_0 is a diffusivity term; increasing this uplift number in the model represents a transition from landscapes dominated by creep and/or wash processes to those dominated by failure processes, increasing the mean slope and decreasing the skewness of the slope distribution.

Landscape diffusivity, or sediment transport efficiency, has been shown to vary by two orders of magnitude along a climatic transect in the Chilean Coastal Cordillera (Chapter 5); there is also evidence to suggest that diffusivity has an effect on controlling the dimensions achieved by river basins (Chapter 6). Following the logic of Wolinsky & Pratson (2005), the changes in diffusivity, constrained using catchment-averaged cosmogenic ^{10}Be erosion rates, should be reflected in a systematic change in skewness of slope distributions across the study area. Uplift (U) along the Coastal Cordillera is relatively uniform, and although hillslope length (A_L) varies across the region it does not do so in a systematic manner. Assuming that any changes in the critical failure slope, μ, will be small in comparison with the two orders of magnitude changes in the diffusivity term, K_0, it can be assumed that any changes in the uplift number (and therefore in the skewness of the slope distribution) can be attributed to changes in diffusivity. It is therefore expected that results from the study area will not only exhibit the characteristic mean slope-slope skewness relationship described by Wolinsky & Pratson (2005), but will also show changes in slope skewness related to changes in mean annual precipitation, similar to that seen in diffusivity results in Chapter 5.

7.2. STUDY AREA

Statistics of third order basins were studied along a climatic transect in the Coastal Cordillera of northern and central Chile. Climate within the study area can be classed as hyperarid north of ~27˚S, and arid, with rainfall occurring only in midwinter, north of ~31˚S (Miller, 1976; Lamy *et al*, 2000). The warm temperate zone begins south of ~31˚S, and precipitation increases rapidly to the south as well as becoming markedly seasonal with dry summers (Clapperton, 1993; Valero-Garces *et al*, 2005). The climate can be classified as semiarid-Mediterranean until ~37˚S, where summer dryness disappears and the climate is classed as humid temperate (Miller, 1976). The distribution of temperature also shows a pronounced latitudinal variation, with higher temperatures nearer the equator and lower near the poles (Cerveny, 1998; Miller, 1976) although differences in temperature are minimal compared to the dramatic latitudinal variations in precipitation (Miller, 1976; Heusser *et al*, 2006a).

Vegetation distribution in the study area is primarily controlled by amounts of precipitation (Veblen *et al*, 1981) and shows a strong latitudinal and altitudinal zonation. The study area can be split into three main ecoregions (Olson *et al*, 2001): the deserts and xeric shrublands of the Atacama Desert; the Mediterranean forests, woodlands and scrub of the Chilean matorral; and the temperate forests of the Southern Valdivian Forests. The northern part of our study area is comprised of deserts and xeric shrublands. The Chilean matorral extends to ~38˚S, and the appearance of temperate forests at ~35˚S results in a broad and uneven transition to the Southern Valdivian Forests (Heusser *et al*, 2006).

The Coastal Cordillera consists of the remnants of a Mesozoic volcanic arc, comprising Jurassic to early Cretaceous dioritic-granodioritic plutons and Jurassic volcanics, with minor amounts of Upper Cretaceous to Tertiary marine sediments, Mesozoic marine volcanics, and with a basement of Palaeozoic sediments and Precambrian metamorphic rocks (Allmendinger et al, 2005; Lamy et al, 1999; SERNAGEOMIN, 2003). Evidence suggests that the Coastal Cordillera has undergone relatively uniform Plio-Quaternary uplift: the coastline of South America is characterised by Quaternary marine terraces that have been uplifted along much of the Pacific margin, indicating an orogen-scale uplift mechanism (Hsu *et al,* 1989) combined with more local tectonic processes (Ortlieb *et al,* 1996). Uniform uplift has been recorded from at least 23˚S to at least 33˚S (Cembrano *et al,* 2007; Marquardt *et al,* 2004; Ortlieb *et al,* 1996; Quezada *et al,* 2007), with the exception of a region of anomalous uplift ~31˚S (Saillard *et al,* 2009). That these remarkable changes in climate and vegetation are paralleled by such uniform lithology and uplift history makes the Chilean Coastal Cordillera the ideal place to study the effects of climate and vegetation changes on slope distributions at the regional scale.

7.3. METHODS

30m-resolution DEMs derived from ASTER data were used in order to generate statistics for first to third order basins across a range of climate and vegetation characteristics. In order to maintain consistency and reflect the full range of conditions within the study area, DEM tiles were clipped to enclose the regions sampled for cosmogenic analyses (fig. 7.3).

Channel networks were defined in ArcGIS using the TauDEM software, with networks being extracted using a Peuker-Douglas algorithm (Band, 1986; see Chapters 4 and 5 for further discussion of extraction of stream networks). Watersheds of first to third order were defined using these stream networks and zonal statistics (primarily mean basin slope) were calculated for each tile. The distribution of mean basin slopes was found to be consistent across all three orders; statistics for third order basins were then used for further analysis. Although calculation of mean basin slope in this manner is not ideal since it includes channel pixels, any effect of these pixels on mean basin slope should be consistent across the study area (mean basin slopes were found to be systematically gentler than effective slopes; see Chapter 5 methods) and therefore should not affect comparisons between tiles. Frequency distributions were plotted for each tile and statistical properties, including mean and median slope, standard deviation and skewness, were calculated. For each of the samples collected for CRN analysis, Wolinsky & Pratson's (2005) uplift number can be collected; A_L and K_o values were calculated in Chapter 5 (referred to as L_H and D), μ is taken as ~50˚ based on the reasoning of Roering *et al* (1999) and

uplift is estimated to be ~0.34m/kyr based on the information presented by Marquardt *et al* (2004).

Where reference is made to climate or vegetation cover, these descriptions are based on classifications made using the MODIS Vegetation Continuous Fields data set (Hansen *et al*, 2000) and the WorldCLIM dataset (Hijmans *et al*, 2005), and specific values of precipitation or vegetation cover refer to values extracted from catchments sampled for cosmogenic analysis, unless otherwise stated.

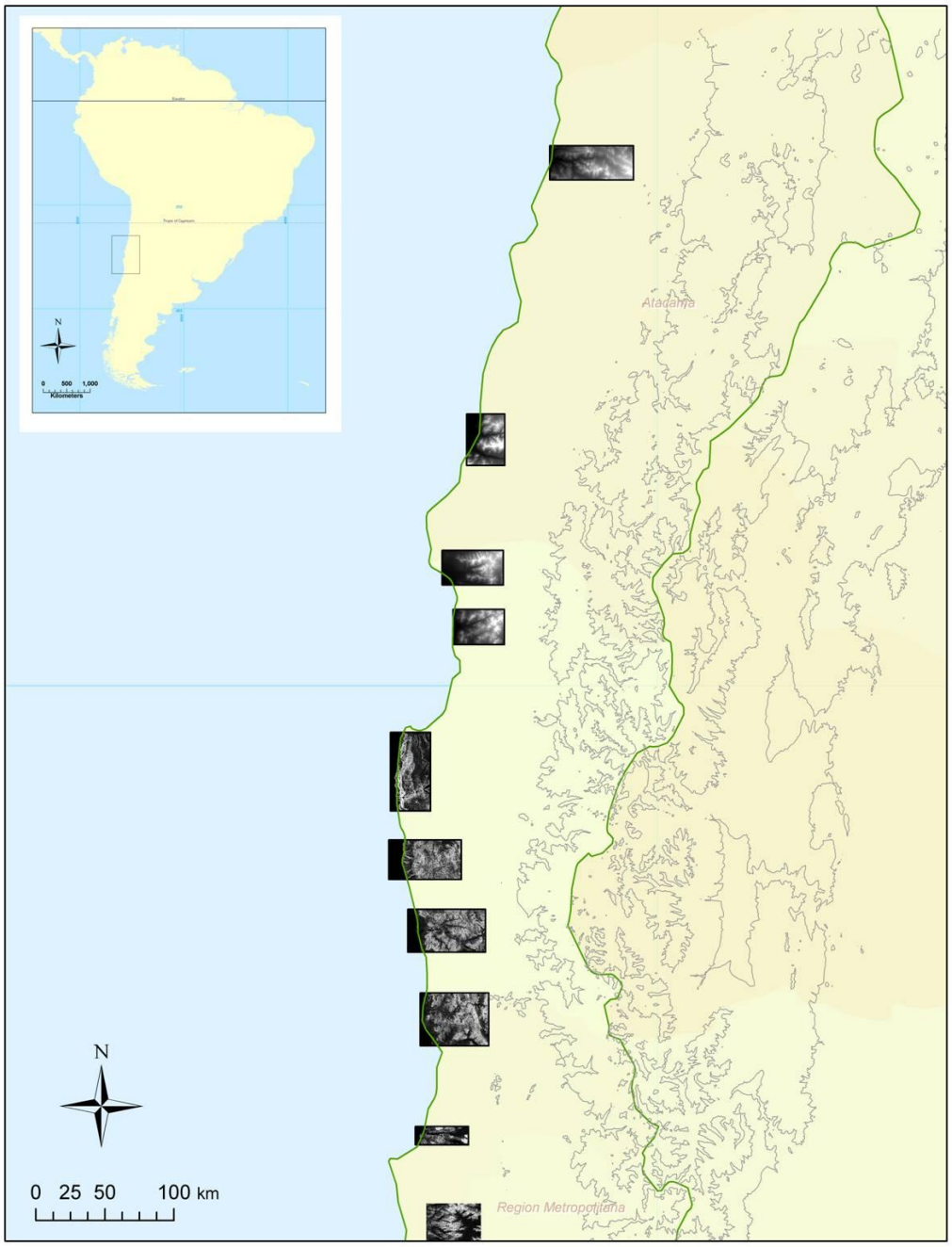

Figure 7.3(a): Distribution of DEM tiles clipped to enclose catchments sampled for cosmogenic analysis (see Chapter 5) in the northern part of the study area. Grey lines are 2km contours.

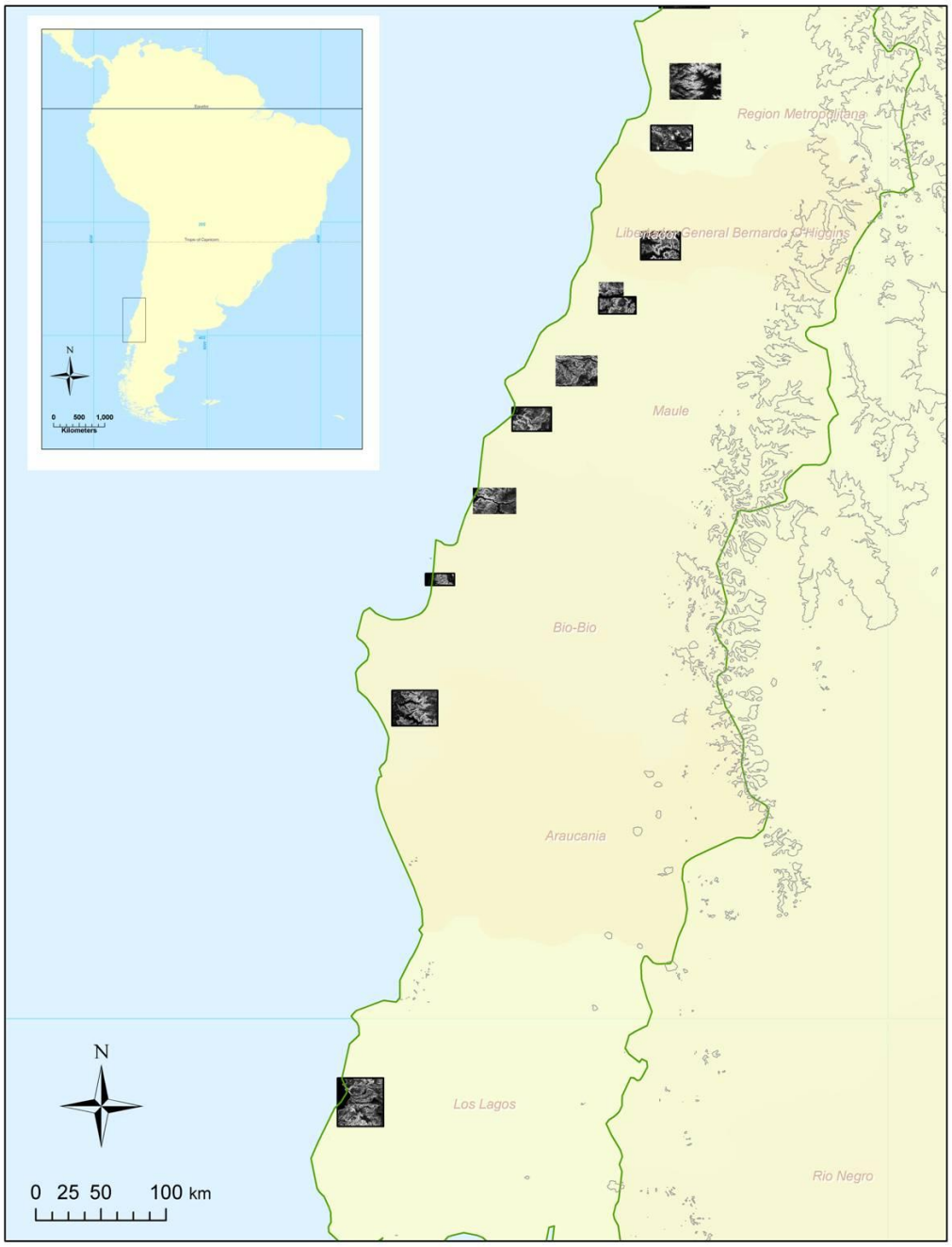

Figure 7.3(b): Distribution of DEM tiles clipped to enclose catchments sampled for cosmogenic analysis (see Chapter 5) in the southern part of the study area. Grey lines are 2km contours.

7.4. RESULTS

Figure 7.4 shows the mean and median slopes for each tile; these results mirror the catchment averaged erosion rates determined using cosmogenic ^{10}Be and show a weak decrease in mean and median slope with increasing latitude. These results, however, reveal little about the specific processes at work in the study area.

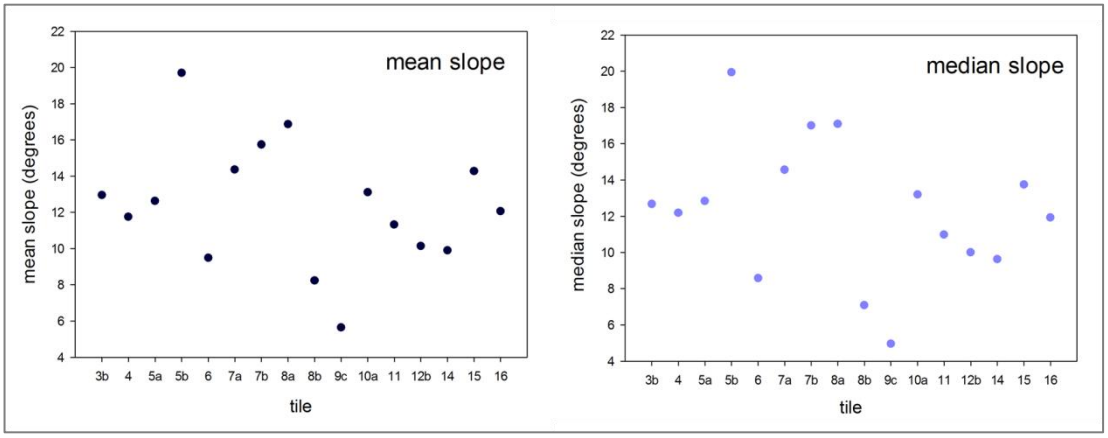

Figure 7.4: Plot of catchment-mean and median slope for each DEM tile in the study area.

According to Wolinsky & Pratson (2005), skewness should decrease with increasing mean slope, and this relationship is replicated by results from the study area (Figure 7.5), confirming that their process-based model is applicable in the study area. The slope of the regression line for the study area is significantly lower than the average data trend described by Wolinsky & Pratson (2005), but this is perhaps unsurprising considering the restricted distribution of mean slopes in the Chilean data compared to the data of Wolinsky & Pratson's study, and considering the relatively uniform lithology and tectonic character of the sampled landscapes in Chile.

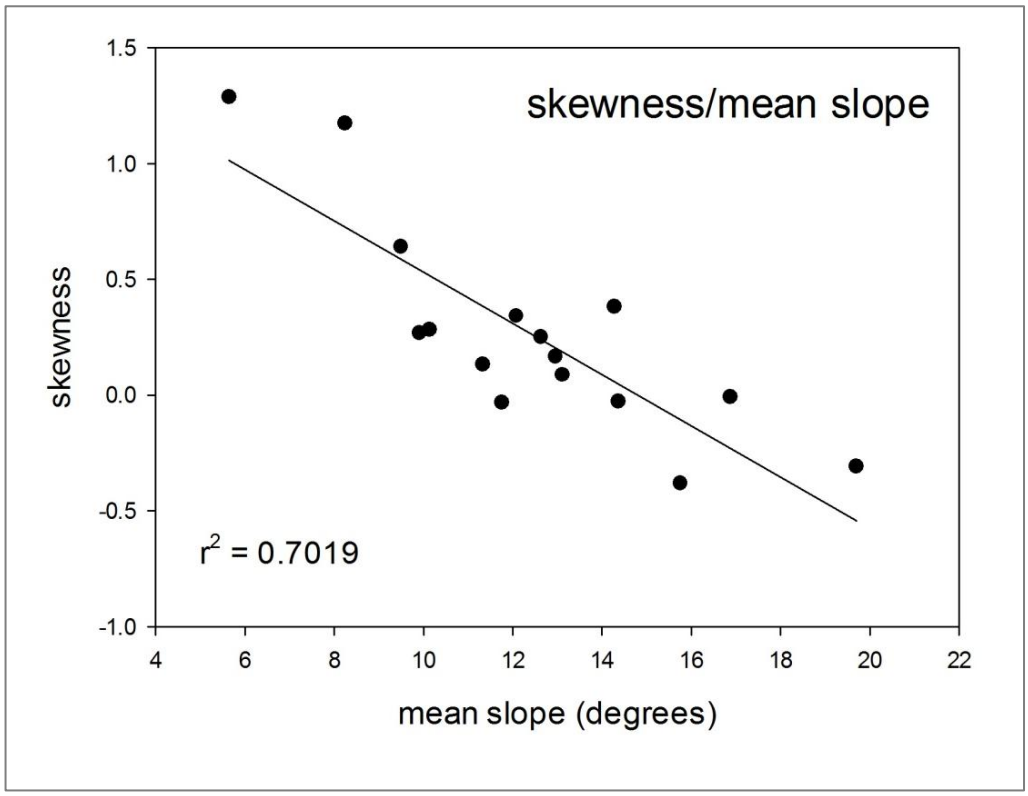

Figure 7.5: Plot of skewness of slope distribution and catchment-mean slope for each DEM tile in the study area. Results replicate those of Wolinsky & Pratson (2005) and confirm that their process-based model is applicable in these landscapes.

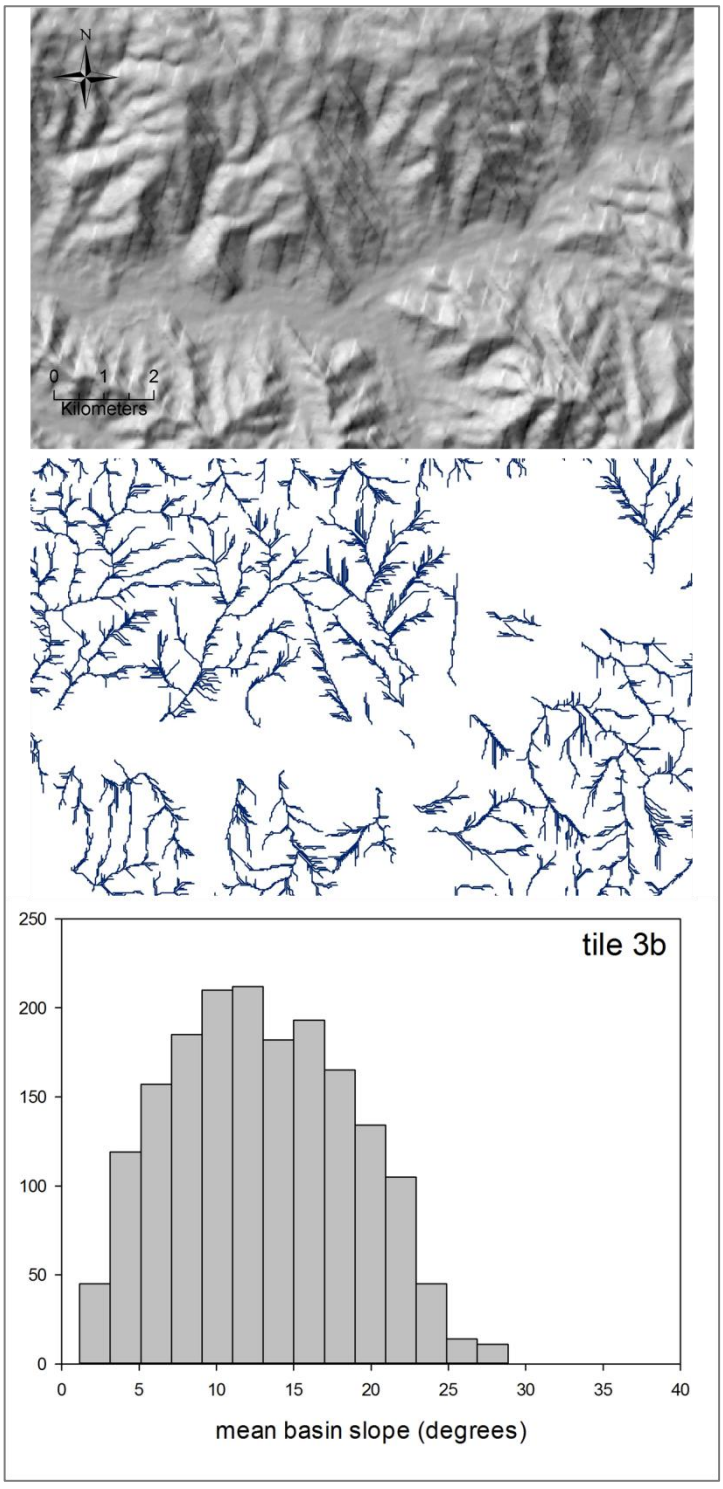

Figure 7.6: Representative extract of DEM tiles showing topography, and extracted stream network. Histogram illustrates distribution of mean basin slope for each tile.

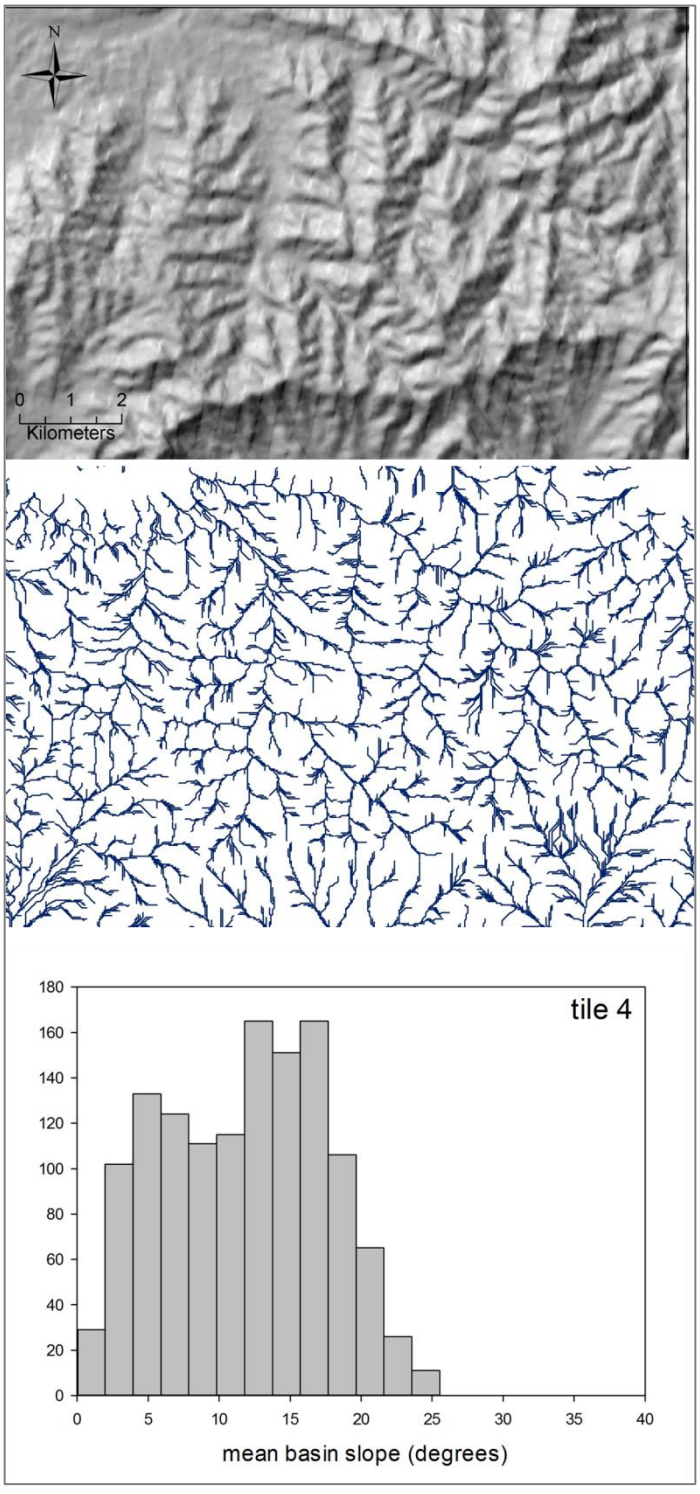

Figure 7.6 (cont.)

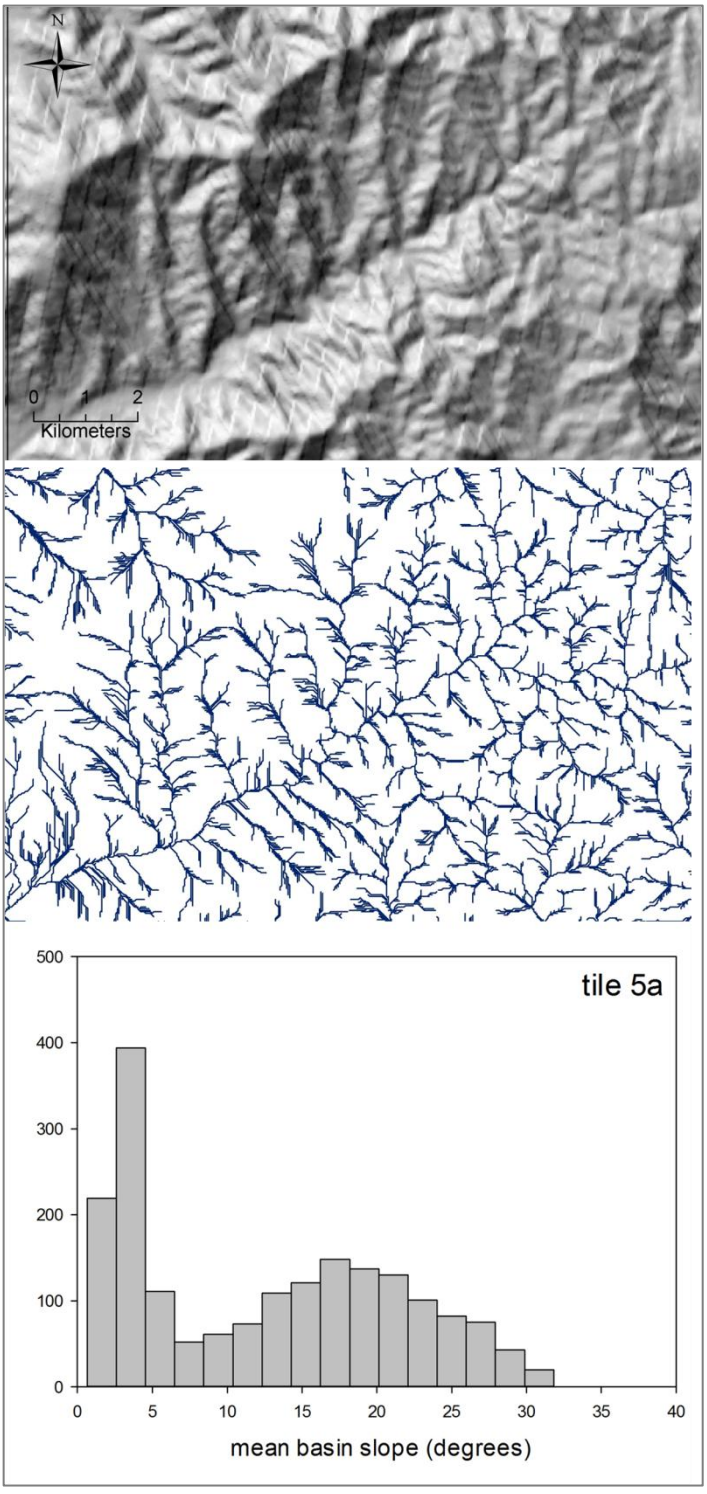

Figure 7.6 (cont.)

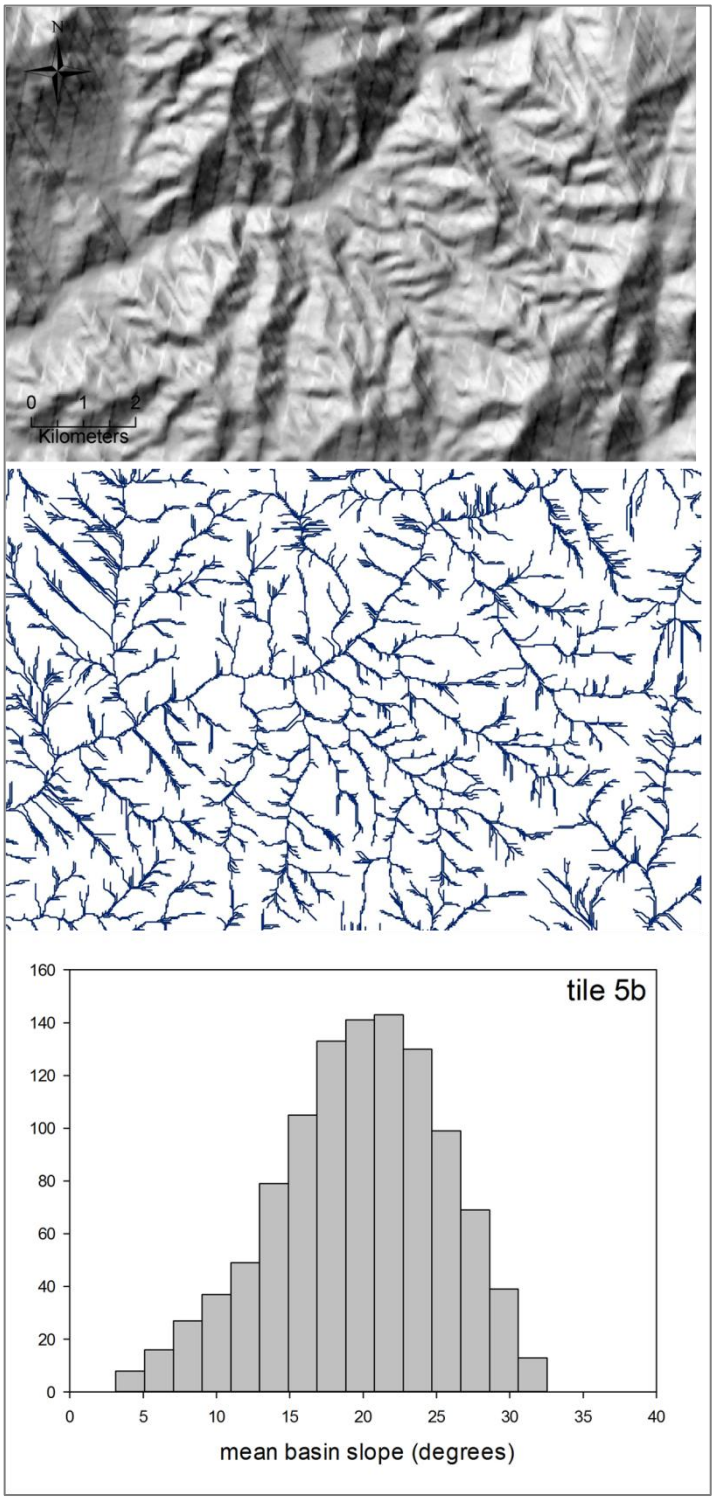

Figure 7.6 (cont.)

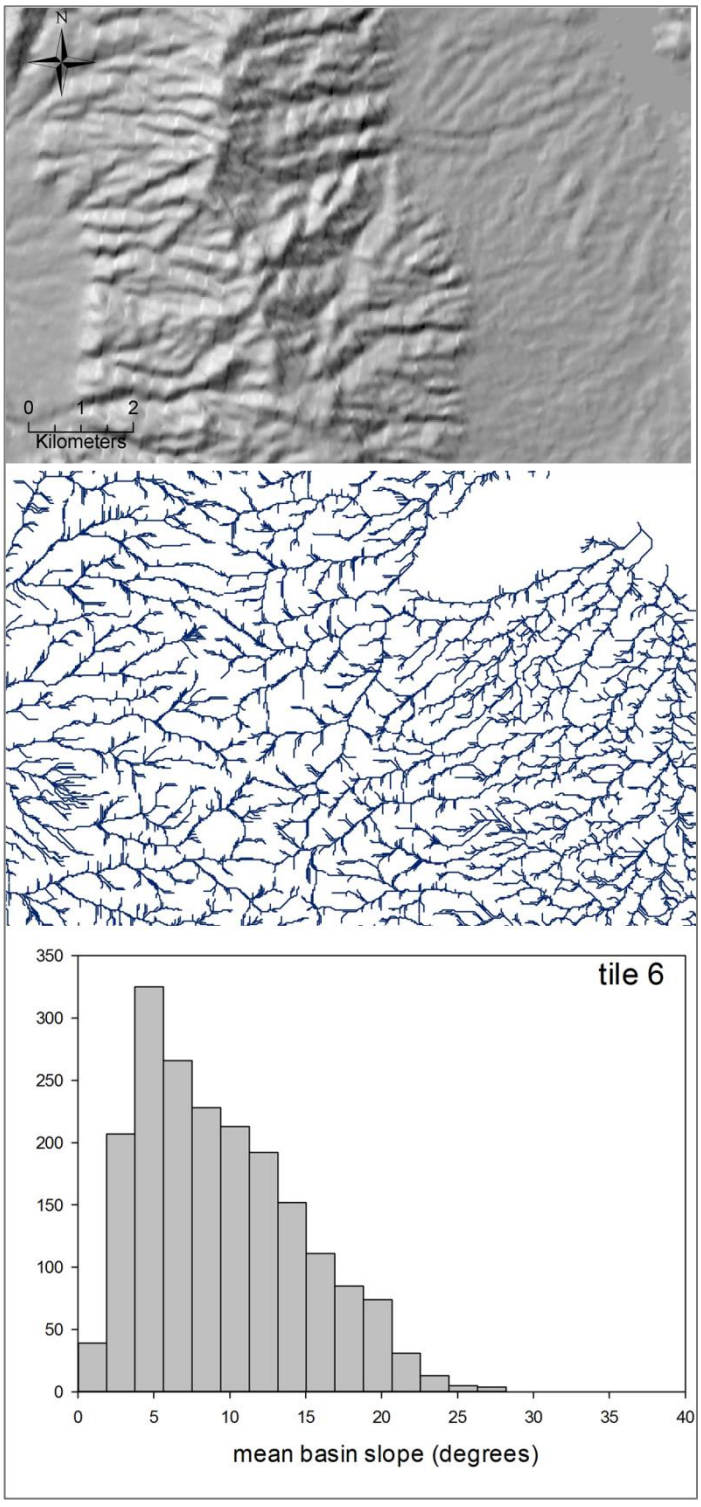

Figure 7.6 (cont.)

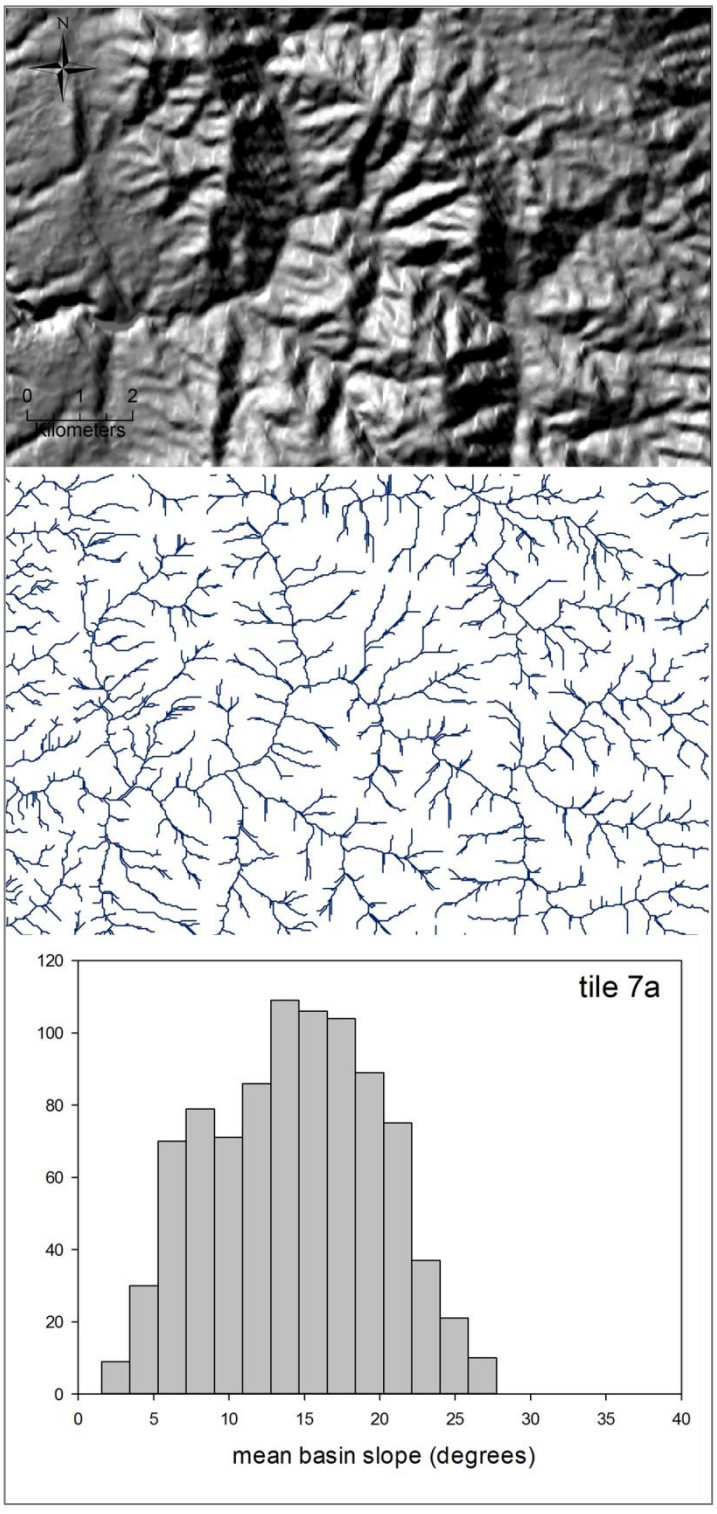

Figure 7.6 (cont.)

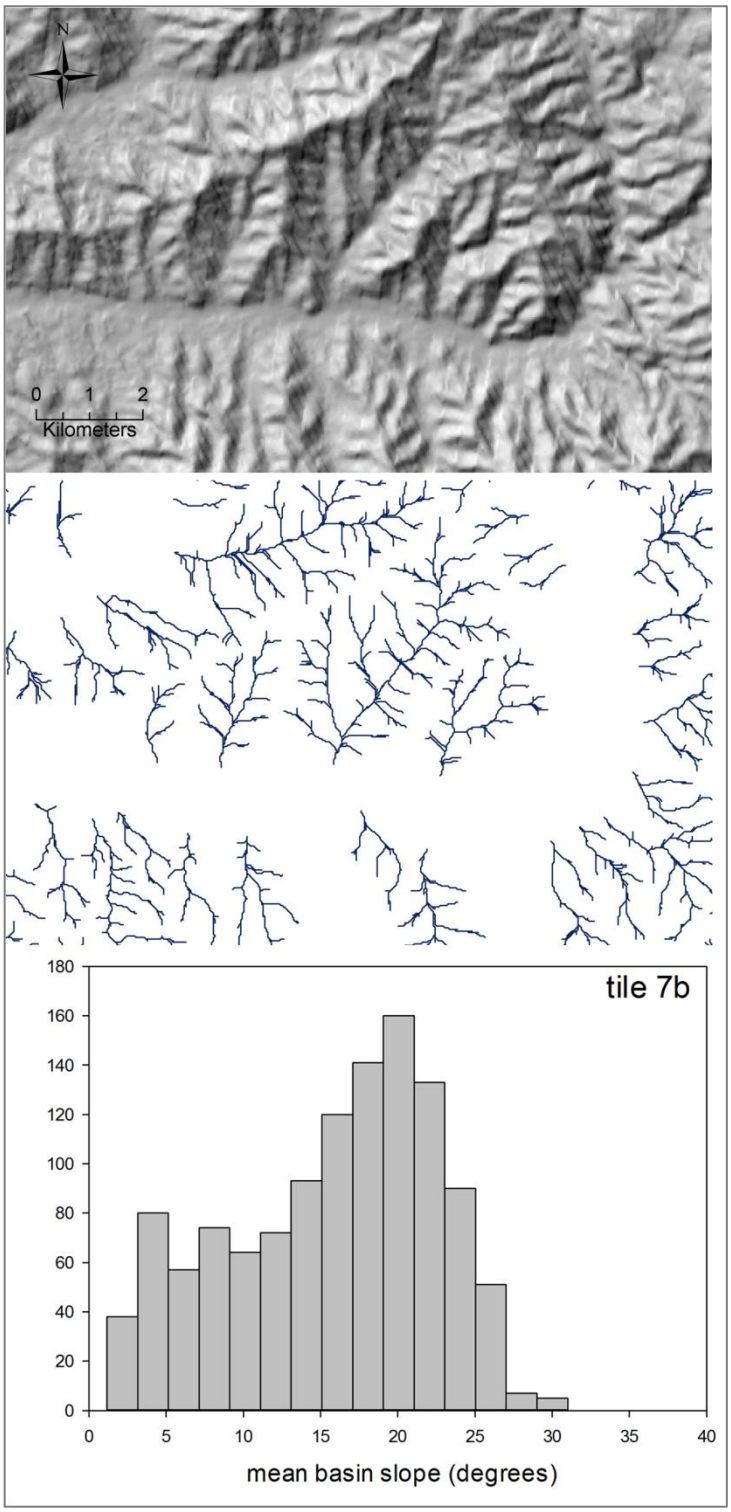

Figure 7.6 (cont.)

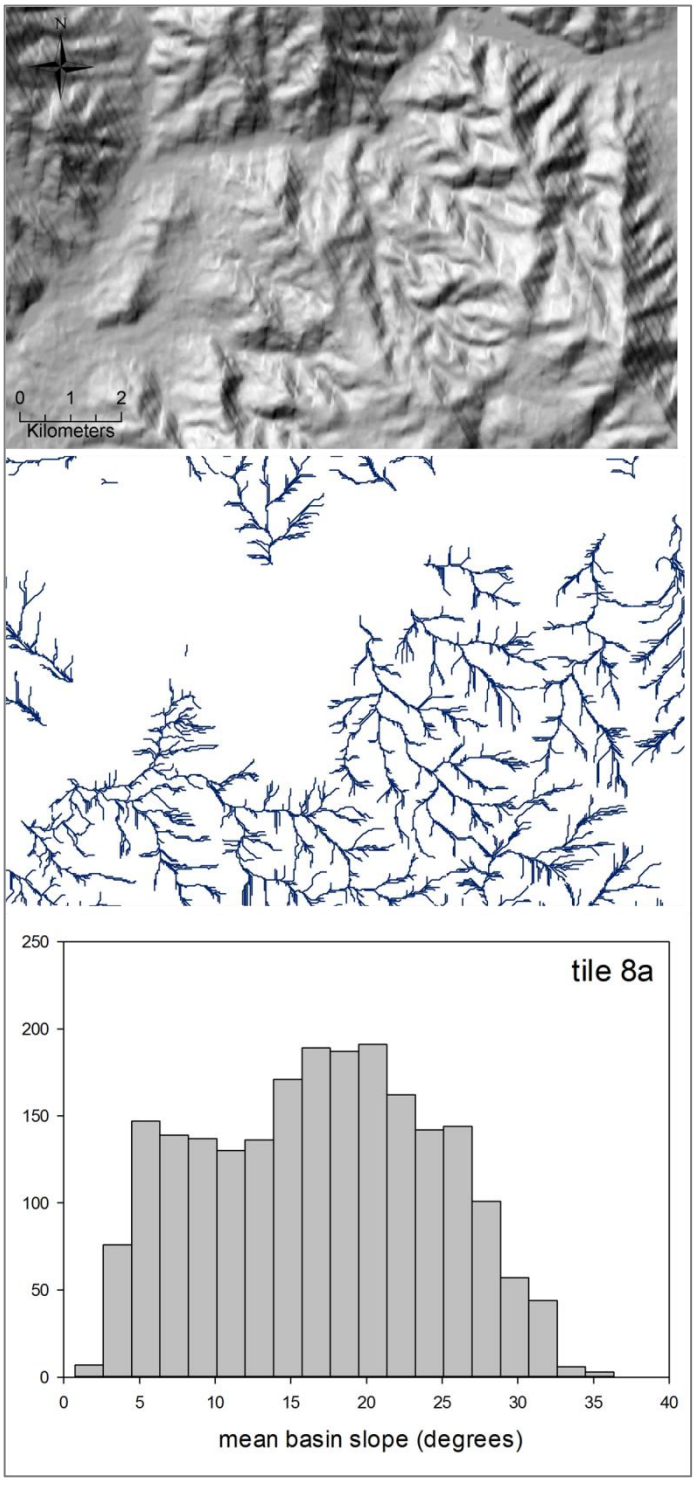

Figure 7.6 (cont.)

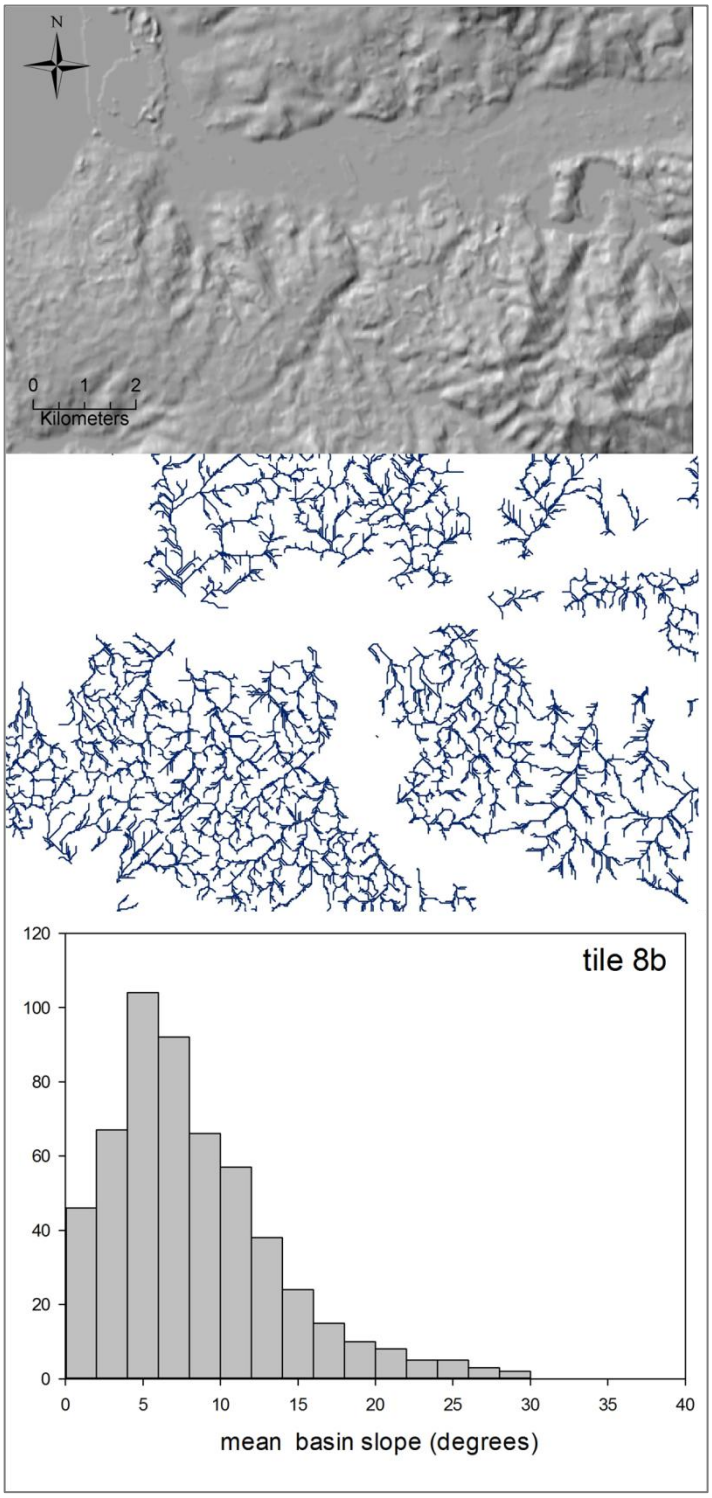

Figure 7.6 (cont.)

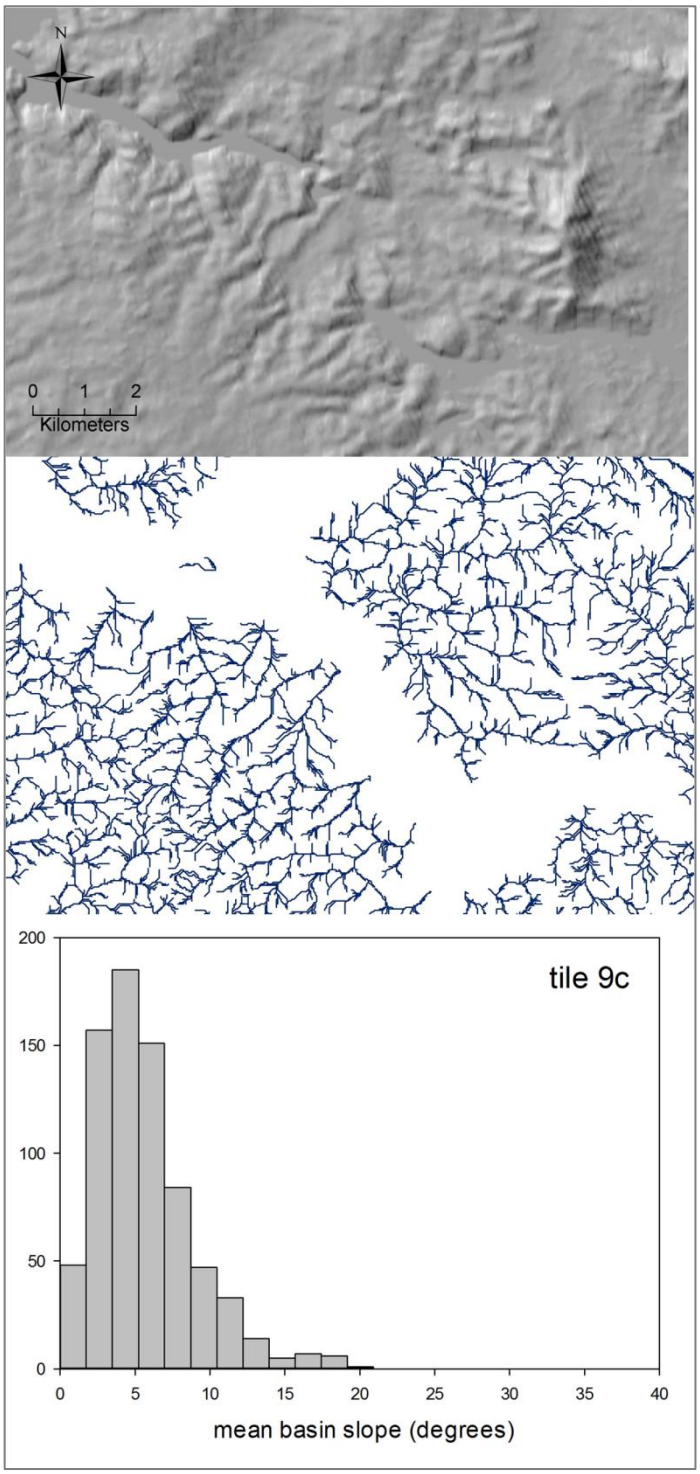

Figure 7.6 (cont.)

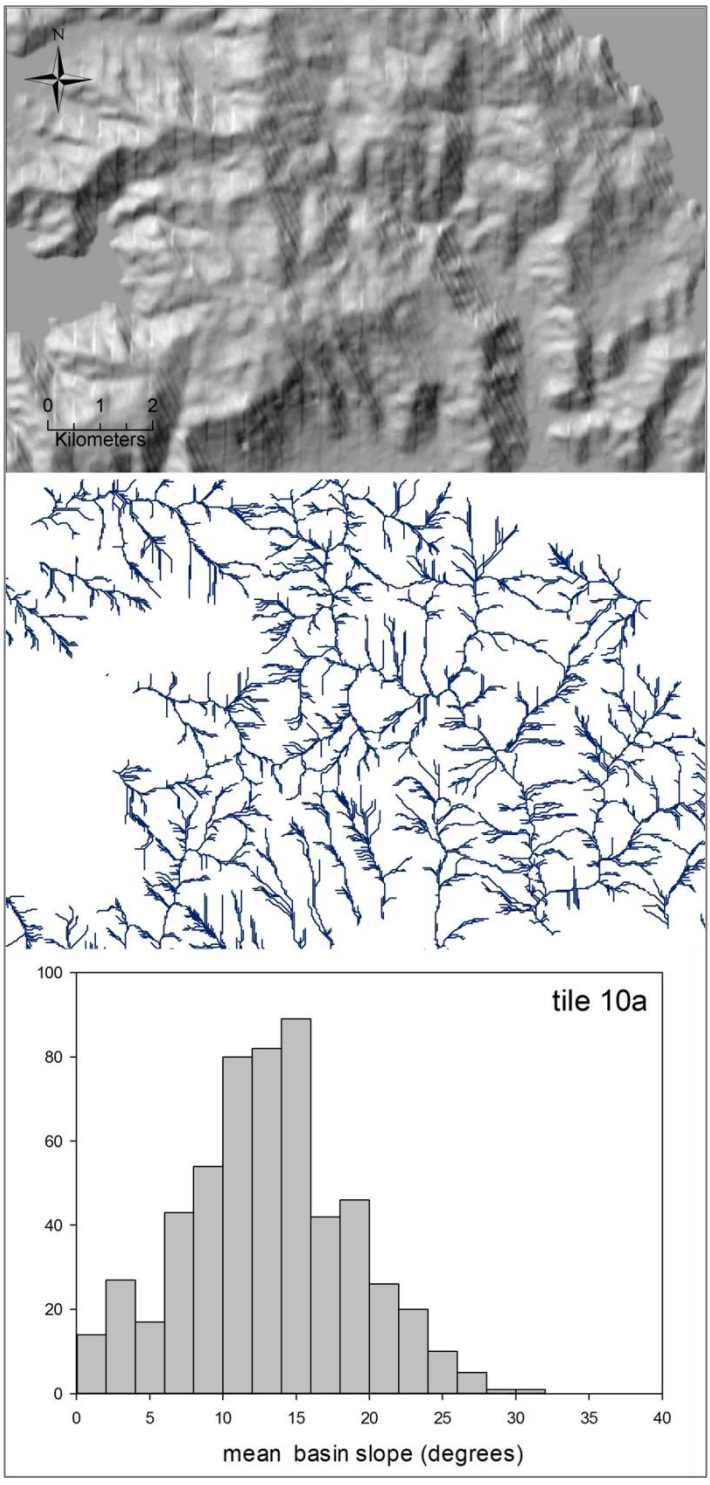

Figure 7.6 (cont.)

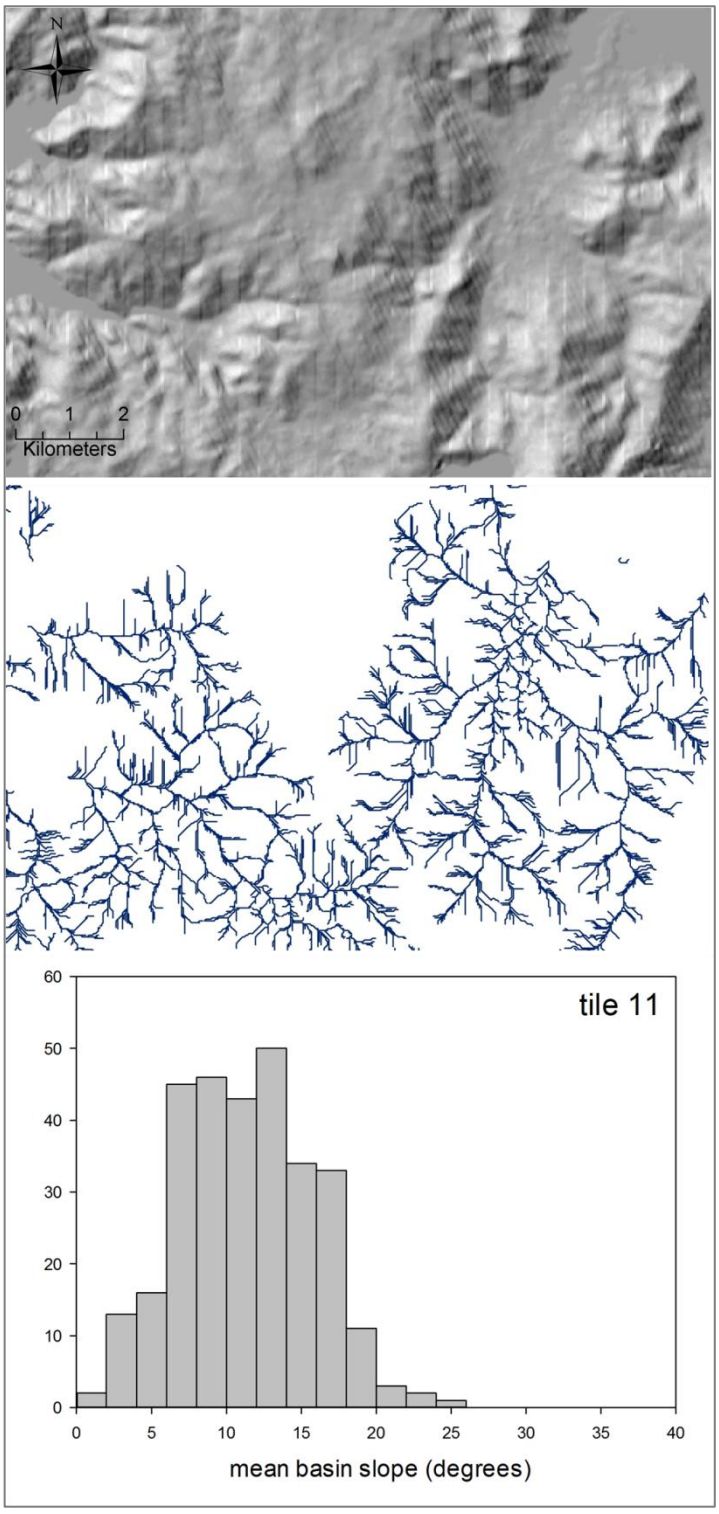

Figure 7.6 (cont.)

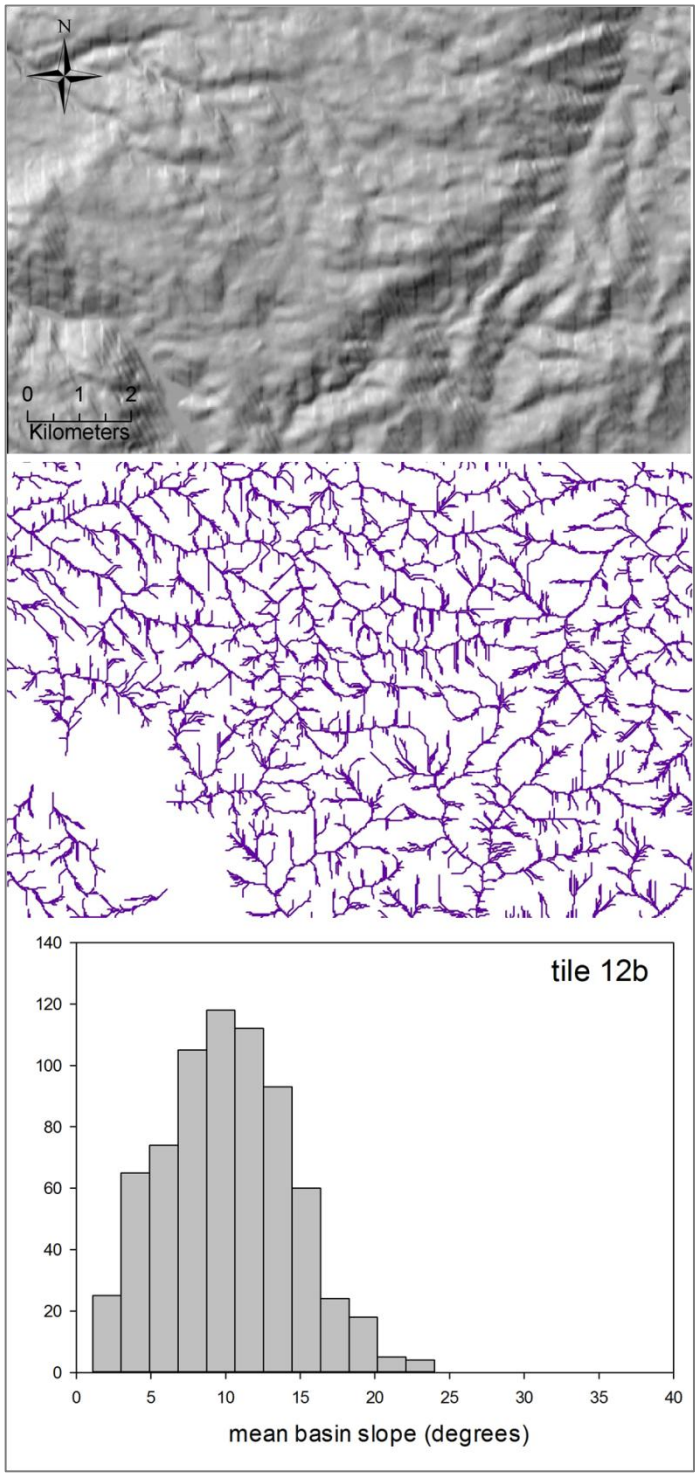

Figure 7.6 (cont.)

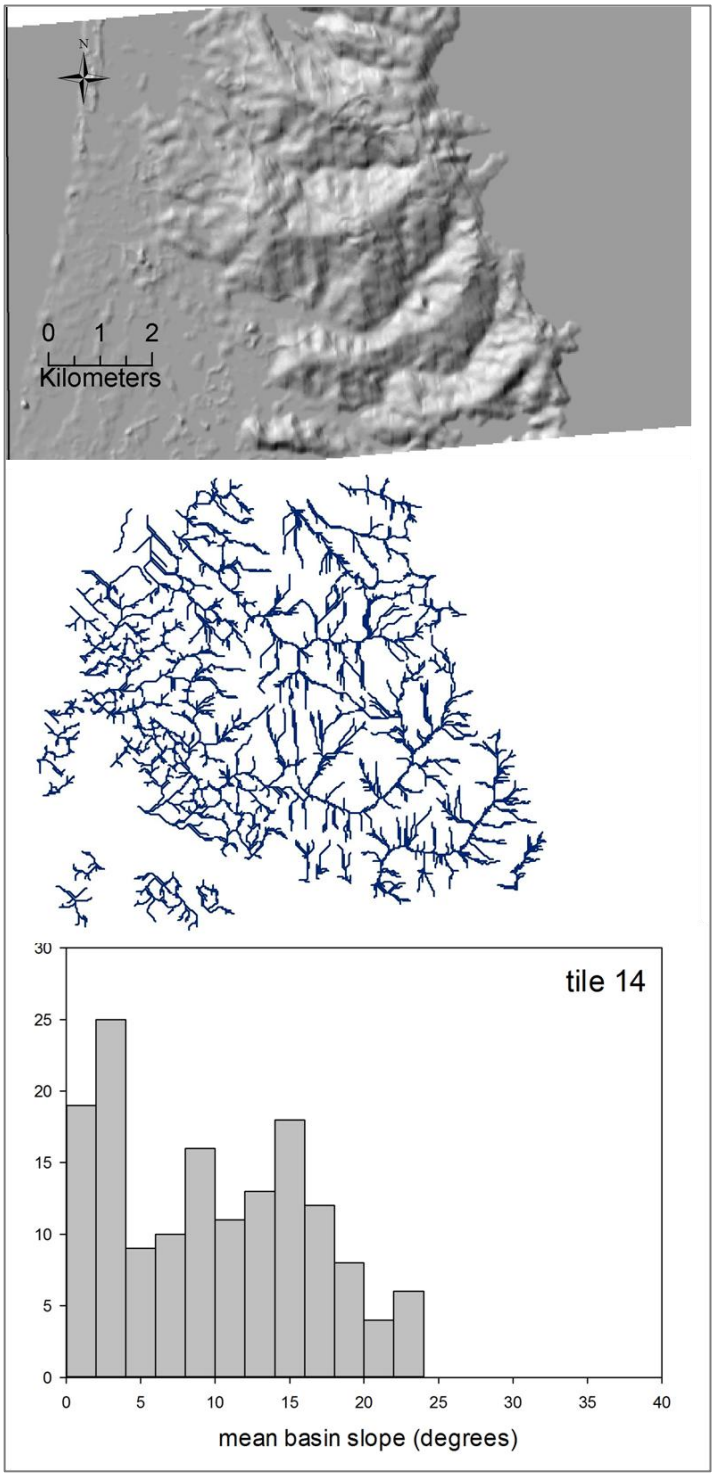

Figure 7.6 (cont.)

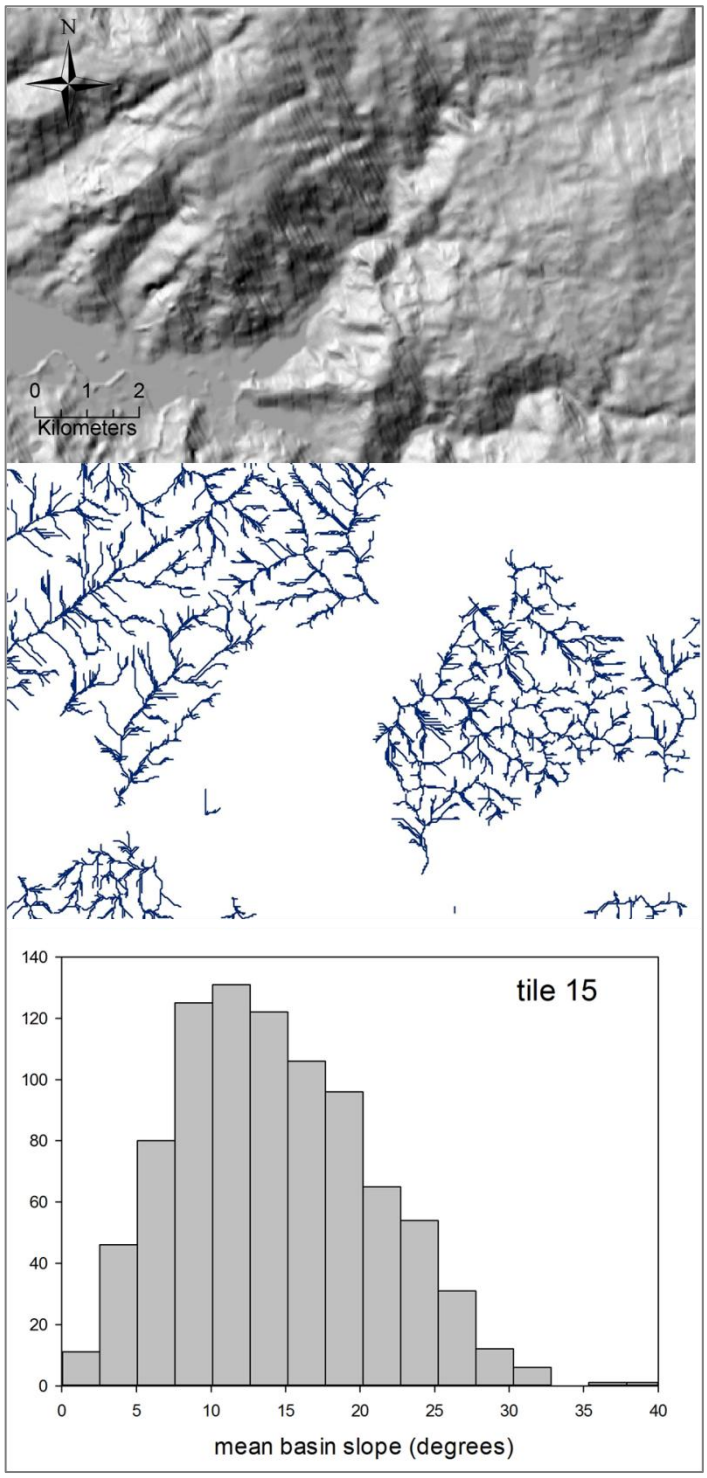

Figure 7.6 (cont.)

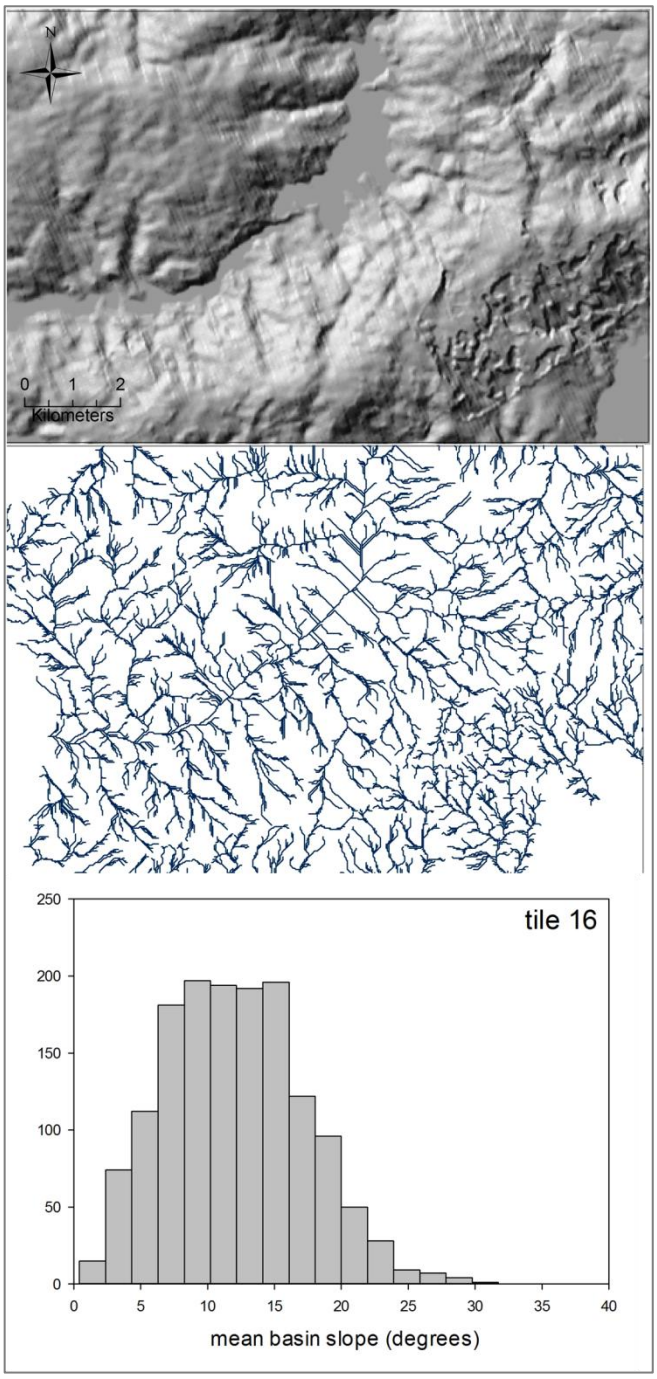

Figure 7.6 (cont.)

A qualitative change can be seen in the landscapes at the transition from tile8a to tile8b; the landscape becomes much smoother and less dissected, with lower relief and seeming to have lower slopes. This is reflected in the slope distributions, with tiles in the south of the study area having generally lower modal slopes (see Figure 7.6). Of more interest is the relationship between slope skewness and mean annual precipitation, and the links between changes in slope skewness and landscape diffusivity. According to the process based model of Wolinsky & Pratson (2005), changes in diffusivity, or K_0 in their model, should be reflected in the skewness of slope distributions. This is, to an extent, what is reflected in the landscapes of the study area, although the changes in diffusivity are by no means reflected in direct changes in skewness of slope distributions (Figure 7.7). The overall form of the relationship is similar, however. Skewness is lowest at low values of precipitation, but increases with precipitation and peaks before decreasing to a relatively constant 'background' level. Whereas the K-curve peaks at 100-200mm/yr, skewness appears to peak at ~400mm/yr. Both curves, however, appear to level out at approximately the same amount of mean annual precipitation. The skewness trend is less clear at lower values of precipitation, where data points are much more scattered, but there appears to be a general tendency towards negatively skewed distributions in the north of the study area and positively skewed in the south, with some exceptions. Negatively skewed slope distributions are only found in the north of the study area. There appears to be a transition in slope distribution skewness between tile 8a and tile 8b (~32.5˚S), from a negatively skewed distribution to a particularly positively skewed distribution.

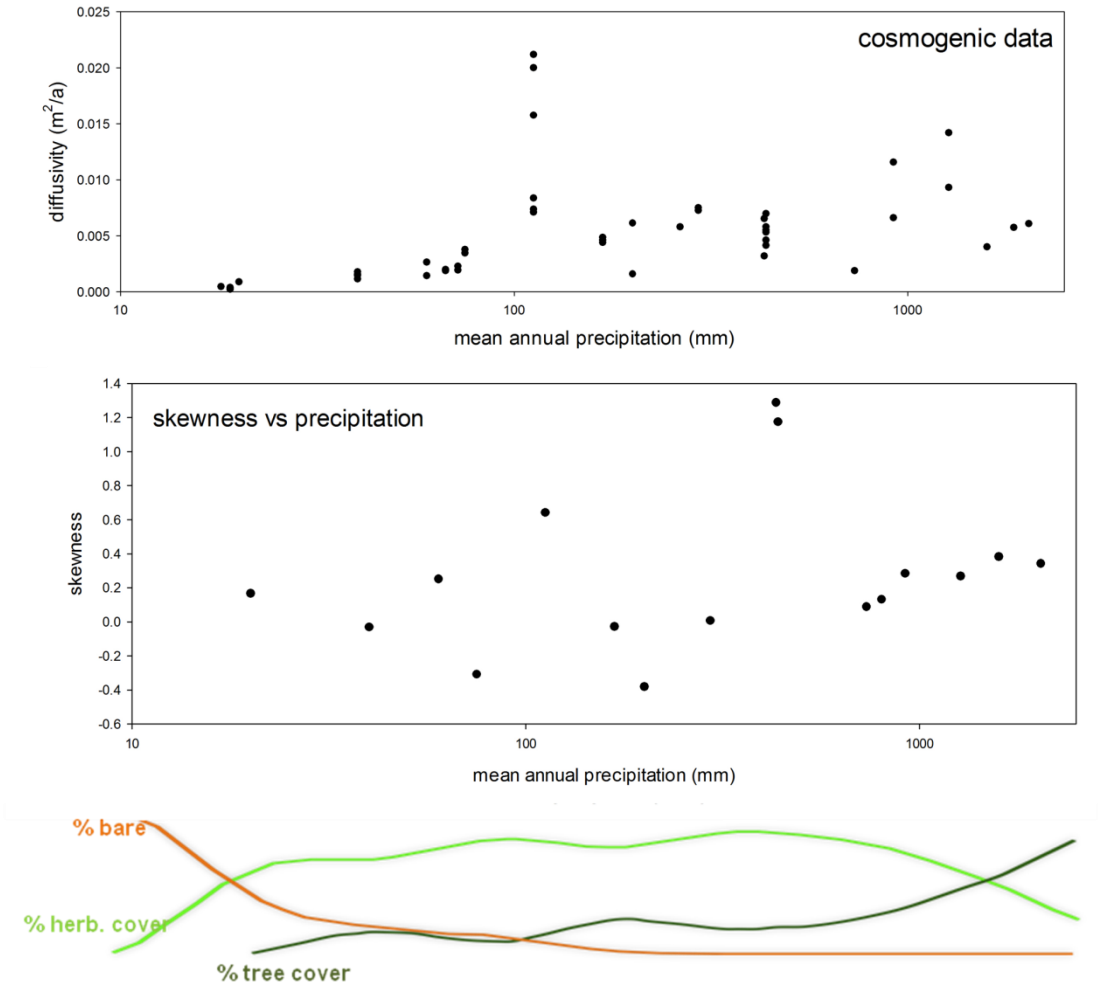

Figure 7.7: The relationship between skewness and precipitation is similar to that between diffusivity and precipitation derived in Chapter 5. Skewness is much more variable between tiles in the north of the study area, and becomes relatively constant at high values of precipitation which can support a continuous vegetation cover.

Most tiles north of this transition show a negative skew, or "slope failure" signal (Wolinsky & Pratson, 2005), with the exception of tiles 3b, 5a and 6. Tile 5a incorporates a significant area of coastal plateau, and the slope distribution in this tile obscures the overall skewness of the non-plateau regions of the tile. Both tile 3b and tile 6 are located in areas where coastal fog is particularly intense and supports a more continuous vegetation cover than the surrounding areas.

A closer examination of the relationship between skewness and precipitation suggests that there may be two distinct trends. Below ~500mm/yr precipitation, the point at which bare ground completely disappears and the percentage cover of trees begins to rise to a maximum value, small increases in precipitation lead to large increases in skewness of slope distributions, while above this level there is only a small increase in skewness over a wide range of precipitation. Above ~1000mm/yr precipitation, there appears to be little change in slope skewness with increasing precipitation; this point also corresponds to the point at which percentage tree or woody vegetation cover exceeds that of herbaceous vegetation. In addition, at lowest precipitation, the data points are much more scattered, which may reflect the heterogeneous nature of vegetation cover in the northern region; this scatter may be in part related to the inclusion of the tiles which display different characteristics to the rest of the tiles in the region.

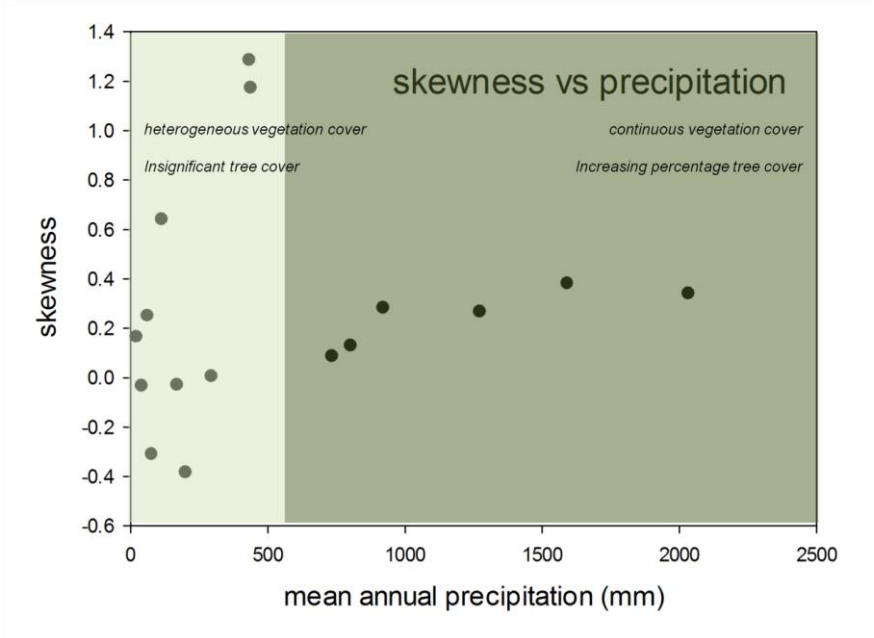

Figure 7.8: The effect of increased vegetation cover on skewness of catchment-mean slope distributions.

Comparing skewness to the percentages of bare ground, herbaceous vegetation and trees highlights some interesting relationships (Figure 7.9). Where bare ground is absent, the scatter of skewness is high and this scatter appears to decrease with increasing percentage of bare ground. The same can be said of the relationship between skewness and percentage of tree cover (increasing percentage of trees decreases scatter in the data), whereas for herbaceous cover this trend is reversed. If it is assumed that the skewness of the slope distribution reflects the processes acting on it, these relationships can be explained by considering how these percentages relate to surface cover. Tree cover tends to be high only in areas where bare ground is absent or almost absent, and thus reflects a relatively continuous vegetation cover, while the greatest percentages of herbaceous vegetation tend to occur in the vicinity of the arid-semiarid transition and therefore high percentages of herbaceous vegetation tend to be associated with a more heterogeneous vegetation cover in general.

Plotting Wolinsky & Pratson's (2005) uplift number against skewness illustrates the general decrease in uplift number with increasing skewness of slope distribution. This is as predicted by their process-based model. There are, however, a few outliers; these catchments are illustrated in Figure 7.10. There is no immediately obvious reason why these catchments may have a drastically different uplift number, but decreasing the uplift for these tiles by a factor of ten results in the outliers fitting the overall data trend (see lower plot in Figure 7.10).

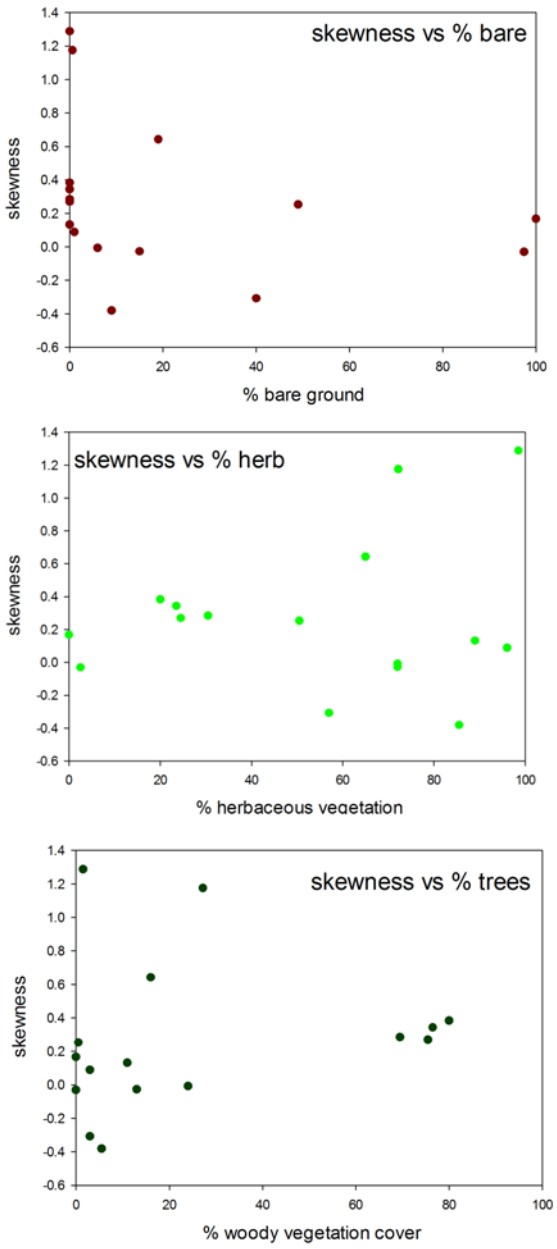

Figure 7.9: The relationship between skewness and percentage cover of different vegetation types. Scatter in skewness is high where bare ground is low, tree cover is relatively low and herbaceous cover is high, which corresponds to the arid-semiarid climatic transition.

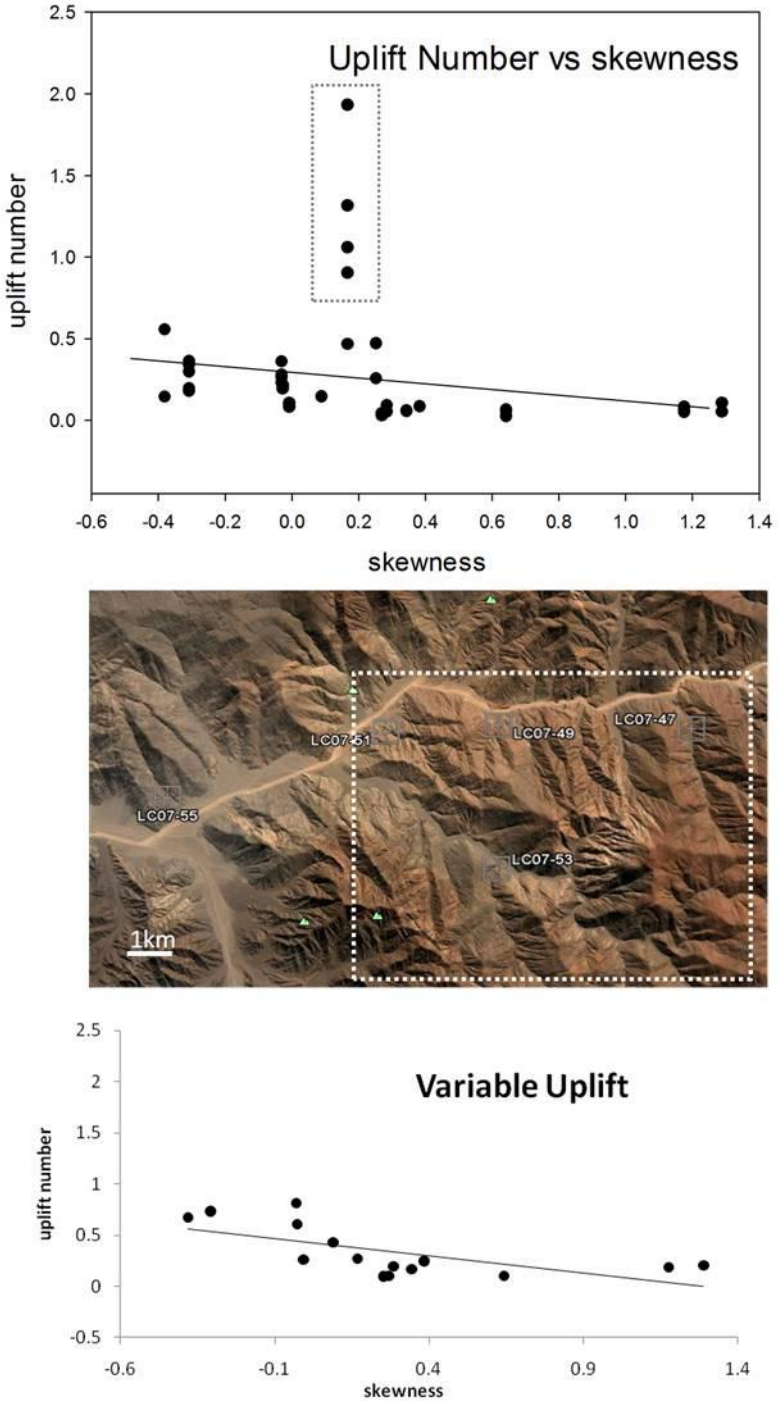

Figure 7.10: The relationship between Wolinsky & Pratson's uplift number and skewness in the study area. Grey dashed box on plot corresponds to sampled catchments enclosed by white dashed box in satellite image. The bottom plot illustrates the trend that would result if tile3b and tile5a had experienced uplift rates approximately one tenth of those in the rest of the study area.

7.5. DISCUSSION

The results presented above suggest that the skewness of slope distributions may be influenced by precipitation on a regional scale, in the same manner that sediment transport efficiency is, although the greater scatter in the slope skewness data suggests that other factors may modulate this relationship, particularly at lower levels of precipitation.

While Wolinsky & Pratson (2005) consider negatively skewed slope distributions to be primarily an indicator of failure dominated landscapes, the definition of their uplift number suggests other ways in which variations in input parameters could result in negatively skewed distributions. In particular, increases in diffusivity (or sediment transport efficiency) such as those constrained in the arid part of the study area, would decrease the uplift number and produce a negatively skewed distribution without the need to invoke failure processes. Samples for the cosmogenic analyses were deliberately chosen in areas with no evidence of landsliding and although an overall dominance of slope failure processes in the sampled DEMs cannot be ruled out, it is unlikely. It is more likely that the negatively skewed slope distributions are a result of other processes. In fact, calculating the uplift number defined by Wolinsky & Pratson (2005) for each of the areas sampled for CRN analysis illustrates (Figure 7.10) that negatively skewed slope distributions can occur in landscapes even where the uplift number is much less than 1, which they consider a sign that the landscape is dominated by creep and/or wash processes. That most of the sampled areas fall into this creep-dominated space further illustrates that the sampling of catchments for CRN analysis was suitable. Changes in the diffusivity could be directly forced by

climatic factors (e.g. increasing precipitation promoting faster sediment transport, or increased fog density promoting weathering), or could be indirectly affected by climate via changes in vegetation type and cover. The fact that the more northern tiles are largely negatively skewed may suggest that negative skew can be indicative not just of slope failure but also of any large-magnitude, low frequency events which shape the landscape. In addition, landslides are often triggered by the same infrequent but large amounts of rainfall which characterise the arid region of the study area. Furthermore, although the calculation of uplift number results in several outliers in the data set, analysis of sensitivity of uplift number to variable uplift across the study area suggests that if the tiles containing the outliers were subject to less uplift than the surrounding regions, the outliers would fit in with the general data trend. In order to fit the overall trend, these tiles (3b and 5a) would have undergone uplift rates approximately one tenth those of the surrounding areas. The geological map of the study area does not indicate the presence or absence of any major structures or changes in lithology that may explain variations in uplift, but it is generally accepted that small-scale local variations in uplift do occur, and it is therefore possible that the outliers in Figure 7.10 (top plot) are a result of using an erroneous uplift rate in the initial calculations.

Results also suggest that vegetation plays a crucial part in defining the skewness of the slope distribution. Two distinct trends in skewness with precipitation can be delineated (Figure 7.8), with the transition between the two occurring at ~500mm/yr mean annual precipitation; this coincides with the levelling off of the diffusivity curve and also with the disappearance of bare ground or, conversely, the shift to a complete vegetation cover. In fact, skewness changes very little beyond this point,

despite large increases in precipitation, which may suggest that there is a characteristic skewness in slope distributions for soil-mantled, fully vegetated landscapes such as these; however, there are too few data points in this area to extrapolate further. Qualitative evidence for the effect of vegetation on skewness of slope distributions is present in a consideration of two of the tiles in the northern part of the study area which exhibit a positively skewed distribution in contrast to the negatively skewed distributions of the surrounding tiles.

Both of these areas lie within areas with intense coastal fogs which support an almost continuous vegetation cover in places. Tile 3b lies adjacent to the Pan de Azucar NP, where coastal fogs are dense and frequent enough to support an almost-continuous cover, in comparison to the surrounding, largely barren landscapes. Tile 6 lies within the Fray Jorge NP, where coastal fogs support relict Pleistocene forests which are generally found much further south.

Further information regarding the effects of vegetation on skewness of slope distributions can be gleaned from the comparison of percentages of different ground cover classes with skewness. High percentages of tree cover tend to occur only in regions with a high percentage vegetation cover in general, and in these areas the skewness of the distribution tends to be relatively uniform (~0.3). Intermediate values of percentage of herbaceous vegetation are often associated with high percentage of tree cover (combining to represent a continuous, homogeneous vegetation cover) and skewness values here (~20-50% herbaceous cover) cluster around the same level. High percentages of tree cover and associated development of extensive root systems may allow vegetation to bind together the soil more effectively, thus making the landscape resistant to sporadic, high-magnitude events

which may lead to failure-type slope signatures. High percentages of herbaceous vegetation are often associated with patches of bare ground in the study area, such that low percentages of bare ground, low percentages of tree cover and high percentages of herbaceous vegetation are associated with a wide scatter of slope distribution skewness; this scatter is much more extensive than that seen in the diffusivity data, suggesting that in areas of landscape heterogeneity, factors other than vegetation and precipitation may play the crucial role in determining the distribution of slopes in the landscape. There is pronounced aspect sensitivity in the Mediterranean biome within the study area, but this is unlikely to result in such a large spread in slope skewness between tiles. Wolinsky & Pratson (2005) suggest that the relative input of creep and wash processes on hillslopes can also be expressed in slope distributions, but note that the interplay between these processes has little effect on skewness compared to the spectrum of creep/wash to failure processes. Landscapes in the central region are furthermore likely to contain relics of last-glacial climate and vegetation cover, so the current slopes may not necessarily be in equilibrium with the current climatic conditions.

Several of the tiles in the study area display evidence of a bimodal slope distribution; all of these except one are in the northern part of the study area, in the region of predominantly negatively skewed distributions, and may be related to differences in factors such as climatic variability/seasonality, aspect, vegetation cover, although the large differences in modal values suggest that aspect alone could not be responsible. The exception to this trend is tile 14, which is overall positively skewed and is towards the south of the study area at ~37˚S. The slightly bimodal distribution here may be explained by the inclusion of a small area of coastal plain, but may also be

related to more intense forestry activity in the area and unusually low-relief landscapes when compared to the surrounding areas.

Although it cannot be discerned from these results whether the diffusivity of a landscape has a direct effect on the skewness of slope distributions, the results do suggest that vegetation plays a crucial role on both diffusivity and skewness.

8. CONCLUSIONS

This study provides empirical evidence that climate exerts a first order control on sediment transport at the catchment scale via its effects on sediment transport efficiency, *D*, and that vegetation is a crucial modulator of sediment transport at the regional scale. Although the effects of climate and vegetation on drainage basin morphology are less clear, results of the study indicate that these factors have a significant effect on maximum basin dimensions and on slope distributions via effects on competing hillslope processes, while supporting previous evidence for an almost universal drainage basin spacing ratio.

Changes in *D* mirror those suggested by Langbein & Schumm (1958), with a peak in transport efficiency at the arid-semiarid transition and a decline in efficiency that coincides with almost complete vegetation cover. This is the first empirical evidence of such striking climate and vegetation effects on sediment transport at the catchment scale. The data presented here also provides a typical *D*-value for soil-mantled hillslopes underlain by granitoid lithologies, and illustrate how changes in climate in climatic transition zones could have a profound effect on sediment transport. The study therefore provides a useful tool for predicting erosion in environments in danger of losing their vegetative cover, whether by natural or anthropogenic means.

The study also reinforces the evidence for an almost universal, optimum spacing ratio for drainage basins, regardless of climate, vegetation cover or rates of tectonic uplift, and highlights the fact that this spacing ratio changes with stream order, with first order basins tending towards longer, narrower configurations; this is interpreted to be a consequence of a greater influence of hillslope-scale processes. In order to

satisfy the model proposed by Perron *et al* (2008), the constant width to length ratio seen in the study area necessitates a positive correlation between *D* and the advective transport term, *K*, such that the ratio of these two factors remains constant despite dramatic changes in climate and vegetation. The results presented here are not conclusive enough to postulate a cause for the uniform spacing ratio, but there is no evidence to refute claims by previous authors (e.g. Hovius, 1996) that the mechanism is the same as that which underlies Hack's Law. In addition, the results suggest that this optimum spacing may result from the interplay of diffusive and advective transport, although further work is needed to investigate this. While climate does not affect basin spacing ratio, it does have an effect on the maximum dimensions of basin similar to the climatic effects on sediment transport efficiency, and also indirectly through the development of a continuous vegetation cover which can cause fundamental changes to hydrological and erosional processes and thus restrict the maximum dimensions attainable by drainage basins.

Catchment-mean slopes were found to be negatively correlated with erosion rates in the study area, contrary to existing evidence. However, the spatially and temporally uniform uplift along the Chilean coast means that erosion rates have adapted to uplift rates, and slopes are therefore a reflection of the efficiency of sediment transport, being low in the south of the study area where transport is more efficient and relatively constant, and high in the north where transport is highly inefficient. Climate thus has an effect on catchment-mean slope via its effects on sediment transport efficiency. The data presented here also provide the first regional-scale evidence for a climatic and vegetation control on the skewness of slope distributions and support the evidence of Wolinsky & Pratson (2005) for a direct correlation

between mean slope and skewness of slope distribution. This study shows that skewness of slope distributions is affected by precipitation on a regional scale in a manner similar to that in which precipitation controls sediment transport efficiency and maximum basin length. Vegetation has also been shown to be a crucial modulator of skewness; where vegetation cover is discontinuous, scatter in the skewness trend is high, while the development of a continuous vegetation cover, in particular an increase in the percentage of tree cover, appears to bind soil, making landscapes resistant to large-magnitude sediment transport events which may result in a "failure type" slope distribution and resulting in a relatively constant skewness even when precipitation continues to increase.

REFERENCES

Aguiar, M.R. & Sala, O.E. (1999). Patch structure, dynamics and implications for the functioning of arid ecosystems, *Trends in Ecology and Evolution, 14(7),* 273-277

Ahnert, F. (1970). Functional relationships between denudation, relief and uplift in large mid-latitude drainage basins, *American Journal of Science, 268,* 243-263

Allmendinger, R.W., Gonzalez, G., Yu, J., Hoke, G & Isacks, B. (2005). Trench-parallel shortening in the Northern Chilean forearc: Tectonic and climatic implications, *GSA Bulletin, 117,* 89-104

Armesto, J.J. & Martinez, J.A. (1978). Relationship between vegetation structure and slope aspect in the Mediterranean region of Chile, *Journal of Ecology, 66(3),* 881-889

Attal, M. (2009). Rivers split as mountains grow, *Nature Geoscience, 2(11),* 747-748

Badano, E.I., Cavieres, L.A., Molina-Montenegro, M.A. & Quiroz, C.L. (2005). Slope aspect influences plant association patterns in the Mediterranean matorral of central Chile, *Journal of Arid Environments, 62,* 93-108

Balco, G., Stone, J.O., Lifton, N.A. & Dunai, T.J. (2008). A complete and easily accessible means of calculating surface exposure ages or erosion rates from ^{10}Be and ^{26}Al measurements, *Quaternary Geochronology, 3,* 174-195

Band, L.E. (1986). Topographic partition of watersheds with digital elevation models, *Water Resources Research, 22,* 15-24

Bangs, N.L. & Cande, S.C. (1997). Episodic development of a convergent margin inferred from structures and processes along the southern Chile margin, *Tectonics, 16(3),* 489-503

Barnes, J.A. & Ehlers, T.A. (2009). End member models for Andean Plateau uplift, *Earth Science Reviews, 97,* 105-132

Bartley, R., Roth, C.H., Ludwig, J., McJannet, D., Liedloff, A., Corfield, J., Hawdon, A. & Abbott, B. (2006). Runoff and erosion from Australia's tropical semiarid rangelands: Influence of ground cover for differing space and time scales, *Hyrdrological Processes, 20,* 3317-3333

Bautista, S., Mayor, A.G., Bourakhouadar, J. & Bellot, J. (2007). Plant spatial pattern predicts hillslope runoff and erosion in a semiarid Mediterranean landscape, *Ecosystems, 10,* 987-998

Bertiller, M.B., Elissalde, N.O., Rostagno, C.M. & Defosse, G.E. (1995). Environmental patterns and plant distributions along a precipitation gradient in western Patagonia, *Journal of Arid Environments, 29,* 85-97

Bertrand, S., Charlet, F., Charlier, B., Renson, V & Fagel, N. (2008). Climate variability of southern Chile since the Last Glacial Maximum: a continuous sedimentological record from Lago Puyehue (40°S), *Journal of Palaeolimnology, 39(2),* 179-195

Bierman, P.R. & Caffee, M. (2001). Slow rates of rock surface erosion and sediment production across the Namib Desert and Escarpment, South Africa, *American Journal of Science, 301,* 326-358

Bierman, P.R., Caffee, M.W., Davis, P.T., Marsella, K., Pavich, M., Colgan, P., Mickelson, D. & Larsen, J. (2002). Rates and timing of earth surface processes from in situ-produced cosmogenic Be-10, *Beryllium: Mineralogy, Petrology and Geochemistry, 50,* 147-205

Bierman, P.R. & Nichols, K.K. (2004). Rock to sediment - Slope to Sea with ^{10}Be - Rates of

landscape change, *Annual Review of Earth & Planetary Sciences, 32,* 215-255

Bierman, P.R. & Steig, E.J. (1996). Estimating rates of denudation using cosmogenic isotope abundances in sediment, *Earth Surface Processes & Landforms, 21(2),* 125-139

Binnie, S.A., 2005. Edinburgh University Cosmogenic Laboratory Protocols, Al/Be Target Preparation, unpublished.

Binnie, S.A., Phillips, W.M., Summerfield, M.A. & Fifield, L.K. (2006). Sediment mixing and basin-wide cosmogenic nuclide analysis in rapidly eroding mountainous environments, *Quaternary Geochronology, 1,* 4-14

Binnie, S.A., Phillips, W.M., Summerfield, M.A. & Fifield, L.K. (2007). Tectonic uplift, threshold hillslopes and denudation rates in a developing mountain range, *Geology, 35,* 743-746

Binnie, S.A., Phillips, W.M., Summerfield, M.A., Fifield, L.K. & Spotila, J.A. (2008). Patterns of denudation through time in the San Bernardino Mountains, California: Implications for early-stage orogenesis, *Earth & Planetary Science Letters, 276,* 62-72

Boix-Fayos, C., Calvo-Cases, A., Imeson, A.C., Soriano-Sotos, M.D. & Tiemessen, I.R. (1998). Spatial and short-term temporal variations in runoff, soil aggregation and other soil properties along a mediterranean climatological gradient, *Catena, 33,* 123-138

Bonnet, S. & Crave, A. (2003). Landscape response to climate change: Insights from experimental modelling and implications for tectonic versus climatic uplift of topography, *Geology, 31(2),* 123-126

Bonnet, S. (2009). Shrinking and splitting of drainage basins in orogenic landscapes from the migration of the main drainage divide, *Nature Geoscience, 2,* 766-771

Bourlès, D.L., 1988. Etude de la géochimie de l'isotope cosmogénique 10Be et de son isotope stable 9Be en milieu océanique. Application à la datation des sédiments marins., Paris-sud Centre d'Orsay, PhD thesis.

Braud, I., Vich, A.I.J., Zuluaga, J., Fornero, L. & Pedrani, A. (2001). Vegetation influence on runoff and sediment yield in the Andes region: observation and modelling, *Journal of Hydrology, 254,* 124-144

Brown, E.T., Stallard, R.F., Larsen, M.C., Raisbeck, G.M. & Yiou, F. (1995). Denudation rates determined from the accumulation of in situ-produced ^{10}Be in the Luquillo experimental forest, Puerto Rico, *Earth & Planetary Science Letters, 129(1-4),* 193-202

Brown, E.T., Stallard, R.F., Larsen, M.C., Bourles, D.L., Raisbeck, G.M. & Yiou, F. (1998). Determination of predevelopment denudation rates of an agricultural watershed (Cayaguas River, Puerto Rico) using in-situ-produced ^{10}Be in river-borne quartz, *Earth & Planetary Science Letters, 160(3-4),* 723-728

Buis, E., Veldkamp, A., Boeken, B. & van Breemen, N. (2009). Controls on plant functional surface cover types along a precipitation gradient in the Negev Desert of Israel, *Journal of Arid Environments, 73,* 82-90

Burbank, D.W. (1992). Geomorphology: Characteristic size of relief, *Nature, 359,* 483-484

Burbank, D.W., Leland, J., Fielding, E., Anderson, R.S., Brozovic, N., Reid, M.R. & Duncan, C. (1996). Bedrock incision, rock uplift and threshold hillslopes in the northwestern Himalayas, *Nature, 379,* 505-510

Cammeraat, E.L.H. (2004). Scale dependent thresholds in hydrological and erosion response of a semiarid catchment in southeast Spain, *Agriculture, Ecosystems and Environment, 104,* 317-332

Carson, M.A. & Kirkby, M.J. (1972). Hillslope form and process. Cambridge University Press, London

Caviedes, C.N. (1990). Rainfall variation, snowline depression and vegetational shifts in Chile during the Pleistocene, *Climatic Change, 16,* 99-114

Cembrano, J., Lavenu, A;, Yañez, G., Riquelme, R., Garcia, M., Gonzzalez, G. & Herail, G. (2007). Neotectonics. In: Moreno, T. & Gibbons, W. (Eds.), *The Geology of Chile,* Geological Society, London, pp231-261

Cerdá, A. (1997). The effect of patchy distribution of Stipa tenacissima L. on runoff and erosion, *Journal of Arid Environments, 36,* 37-51

Cerling, T.E. & Craig, H. (1994). Geomorphology and in-situ cosmogenic isotopes, *Annual Review of Earth & Planetary Sciences, 22,* 273-317

Cerveny, R. (1998). Present climates of South America. In: J.E. Hobbs, J.A. Lindesay & H.A. Bridgamn, Eds., *Climates of the Southern Continents: Present, past and future,* Wiley, West Sussex, England (1998), pp. 107-135

Clapp, E.M., Bierman, P.R., Schick, A.P., Lekach, J., Enzel, Y. & Caffee, M. (2000). Sediment yield exceeds sediment production in arid region drainage basins, *Geology, 28(11),* 995-958

Clapp. E.M., Bierman, P.R. & Caffee, M. (2002). Using ^{10}Be and ^{26}Al to determine sediment generation rates and identify sediment source areas in an arid region drainage basin, *Geomorphology, 45(1-2),* 89-104

Clapperton, C. (1993). Quaternary geology and geomorphology of South America, Elsevier, Amsterdam, 779pp

Cockburn, H.A.P. & Summerfield, M.A. (2004). Geomorphological applications of cosmogenic isotope analysis, *Progress In Physical Geography, 28(1),* 1-42

Codilean, A.T. (2006). Calculation of the cosmogenic nuclide production topographic shielding scaling factor for large areas using DEMs, *Earth Surface Processes & Landforms, 31,* 785-794

Collins, D.B.G. & Bras, R.L. (2008). Climatic control of sediment yield in dry lands following climate and land cover change, *Water Resources Research, 44,* W10405

Collins, D.B.G. & Bras, R.L. (2010). Climatic and ecological controls of equilibrium drainage density, relief and channel concavity, *Water Resources Research, 46,* W04508

Cooke, R., Warren, A. & Goudie, A. (1993). Desert geomorphology, UCL Press, London, 517pp

Dedkov, A.P. & Moszherin, V.I. (1992). Erosion and sediment yield in mountain regions of the world. In: Walling, D.E., Davies, T.R. & Hasholt, B. (Eds.), Erosion, debris flows and environment in mountain regions (Proceedings of the Chengdu Symposium, July 1992). IAHS Publ. no. 209

Delouis, B., Philip, H., Dorbath, L. & Cisternas, A. (1998). Recent crustal deformation in the Antofagasta region (northern Chile) and the subduction process, *Geophys J Int, 132,* 302-338

Densmore, A.L., Ellis, M.A. & Anderson, R.S. (1998). Landsliding and the evolution of normal-fault-bounded mountains, *Journal of Geophysical Research, 103,* 15203-15219

Desilets, D. & Zreda, M. (2003). Spatial and temporal distribution of secondary cosmic-ray nucleon intensities and applications to in situ cosmogenic dating, *Earth & Planetary Science Letters, 206(1-2),* 21-42

Desilets, D., Zreda, M. & Prabu, T. (2006). Extended scaling factors for in situ cosmogenic nuclides: New measurements at low latitude, *Earth & Planetary Science Letters, 246,* 265-276

De Batist, M., Fagel, N., Loutre, M.F. & Chapron, E. (2008). A 17,900-year multi-proxy lacustrine record of Lago Puyehue (Chilean Lake District): introduction, *Journal of Palaeolimnology, 39(2),* 151-161

del-Val, E., Armesto, J.J., Barbosa, O., Christie, D.A., Gutiérrez, A.G., Jones, C.G., Marquet, P.A. & Weathers, K.C. (2006). Rain forest islands in the Chilean semiarid region: fog-dependency, ecosystem persistence and tree regeneration, *Ecosystems, 9,* 598-608

DiBiase, R.A., Whipple, K.A., Heimsath, A.M.& Ouimet, W.B. (2010). Landscape form and millennial erosion rates in the San Gabriel Mountains, CA. *Earth & Planetary Science Letters, 289,* 134-144

Dunai, T.J. (2000). Scaling factors for production rates of in situ produced cosmogenic nuclides: a critical reevaluation, *Earth & Planetary Science Letters, 176(1),* 157-169

Dunai, T.J. (2001). Influence of secular variation of the gemoagnetic field on production rates of in situ produced cosmogenic nuclides, *Earth & Planetary Science Letters, 193(1-2),* 197-212

Dunai, T.J. (2001a). Reply to comment on 'Scaling factors for production rates of in situ produced cosmogenic nuclides: a critical reevaluation' by Darin Desilets, Marek Zreda and Nathaniel Lifton, *Earth & Planetary Science Letters, 188,* 289-298

Dunai, T.J., Lopez, G.A.G. Juez-Larre, J. (2005). Oligocene-Miocene age of aridity in the Atacama Desert, revealed by exposure dating of erosion-sensitive landforms, *Geology, 33,* 321-324

Dunkerley, D.L. & Brown, K.J. (1995). Runoff and runon areas in a patterned chenopod shrubland, arid western New South Wales, Australia: characteristics and origin, *Journal of Arid Environments, 30,* 41-55

Dunne, J., Elmore, D. & Muzikar, P. (1999). Scaling factors for the rates of production of cosmogenic nuclides for geometric shielding and attenuation at depth on sloped surfaces, *Geomorphology, 27,* 3-11

Dunne, T., Zhang, W. & Aubry, B.F. (1991). Effects of rainfall, vegetation and microtopography on infiltration and runoff, *Water Resources Research, 27(9),* 2271-2285

Dunne, T., Malmon, D.V. & Mudd, S.M. (2010). A rain splash transport equation assimilating field and laboratory measurements, *Journal of Geophysical Research, 115,* F01001

Ehlers, T.A. & Poulsen, C.J. (2009). Influence of Andean uplift on climate and palaeoaltimetry estimates, *Earth & Planetary Science Letters, 281,* 238-248

Elmore, D. & Phillips, F.M. (1987). Accelerator mass spectrometry for measurement of long-lived radioisotopes, *Science, 236,* 543-550

Encinas, A., Herve, F., Villa-Martinez, R., Nielsen, S.N., Finger, K.L. & Peterson, D.E. (2006). Finding of a Holocene marine layer in Algarrobo (33°22'S), central Chile: Implications for coastal uplift, *Revista Geologica de Chile, 33(2),* 339-345

Ewing, S.A., Sutter, B., Owen, J., Nishiizumi, K., Sharp, W., Cliff, S.C., Perry, K., Dietrich, W., McKay, C.P. & Amundson, R. (2006). A threshold in soil formation at Earth's arid-hyperarid transition, *Geochimica et Cosmochimica Acta, 70,* 5293-5322

Farias, M., Carretier, S., Charrier, R., Martinod, J., Tassara, A., Encinas, A. & Comte, D. (2008b). No

subsidence in the development of the Central Depression along the Chilean margin, *7th International Symposium on Andean Geodynamics (ISAG 2008, Nice), Extended Abstracts,* 206-209

Farías, M., Charrier, R., Carretier, S., Martinod, J., Fock, A., Campbell, D., Cáceres, J. & Comte, D. (2008). Late Miocene high and rapid surface uplift and its erosional response in the Andes of central Chile (33-35°S), *Tectonics, 27,* TC1005

Fournier, F. (1960). *Climate et erosion,* Presses Universitaires de France, Paris, pp.201

Freeman, S., Bishop, P., Bryant, C., Cook, G., Dougans, D., Ertunc, T., Fallick, A., Ganeshram, R., Maden, C., Naysmith, P., Schnabel, C., Scott, M., Summerfield, M. & Xu, S. (2007). The SUERC AMS laboratory after 3 years, *Nuclear Instruments and Methods in Physics Research B, 259,* 66-70

Freeman, S., Bishop, P., Bryant, C., Cook, G., Fallick, A., Harkness, D., Metcalfe, S., Scott, M., Scott, R. & Summerfield, M. (2004). A new environmental sciences AMS laboratory in Scotland, *Nuclear Instruments and Methods in Physics Research B, 223-223,* 31-34

Fuenzalida, R., Schneider, W., Garces-Vargas, J. & Bravo, L. (2008). Satellite altimetry data reveal jet-like dynamics of the Humboldt current, *Journal of Geophysical Research, 113,* C07043

Glodny, J., Echtler, H., Collao, S., Ardiles, M., Buron, P. & Figueroa, O. (2008b). Differential Late Palaeozoic active margin evolution in South-Central Chile (37-40°S) - the Lanalhue Fault Zone, *Journal of South American Earth Sciences, 26(4),* 397-411

Glodny, J., Gräfe, K., Echtler, H. & Rosenau, M. (2008). Mesozoic to Quaternary continental margin dynamics in South-Central Chile (36-42°S): the apatite and zircon fission track perspective, *Geologische Rundschau, 97,* 1271-1291

Gonzalez, G., Cembrano, J., Carrizo, D., Macci, A. & Schneider, H. (2003). The link between forearc ectonics and Pliocene-Quaternary deformation of the Coastal Cordillera, northern Chile, *Journal of South American Earth Sciences, 16(5),* 321-342

Gosse, J.C. & Phillips, J.M. (2001). Terrestrial in situ cosmogenic nuclides: theory and application, *Quaternary Science Reviews, 20(14),* 1475-1560

Granger, D.E., Kirchner, J.W. & Finkel, R. (1996). Spatially averaged long-term erosion rates measured from in situ-produced cosmogenic nuclides in alluvial sediment, *Journal of Geology, 104(3),* 249-257

Granger, D.E. & Riebe, C.S. (2007). Cosmogenic nuclides in weathering and erosion. In: Drever, J.I. (Ed.), *Treatise on Geochemistry, Volume 5: Surface and Ground Water, Weathering and Soils.* Elsevier, London.

Gregory-Wodzicki, K.M. (2000). Uplift history of the Central and Northern Andes: A review, *GSA Bulletin, 112(7),* 1091-1105

Gutierrez, J.R., Meserve, P.L., Kelt, D.A., Engilis, A., Previtali, M.A., Milstead, W.B. & Jaksic, F.M. (2010). Long-term research in Bosque Fray Jorge National Park: Twenty years studying the role of biotic and abiotic factors in a Chilean semiarid scrubland, *Revista Chilena de Historia Natural, 83,* 69-98

Gyssels, G., Poesen, J., Bochet, E. & Li, Y. (2005). Impact of plant roots on the resistance of soils to erosion by water: a review, *Progress in Physical Geography, 29,* 189-217

Hack, J.T. (1960). Interpretation of erosional topography in humid temperate regions, *American Journal of Science, 258,* 80-97

Hansen, M.C., Defries, R.S., Townshend, J.R.G. & Sohlberg, R. (2000). Global land cover

classification at 1km spatial resolution using a classification tree approach, *International Journal of Remote Sensing, 21,* 1331-1364

Hartley, A.J. & Chong, G. (2002). A late Pliocene age for the Atacama Desert: Implications for the desertification of western South America, *Geology, 30,* 43-46

Hartley, A.J., Chong, G., Houston, J. & Mather, A.E. (2005). 150 million years of climatic stability: Evidence from the Atacama Desert, northern Chile, *J. Geol. Soc. London, 162,* 421-424

Hartley, A.J. & Jolly, E.J. (1995). Tectonic implications of Late Cenozoic sedimentation from the Coastal Cordillera of northern Chile (22-24°S), *J. Geol. Soc. London, 152(1),* 51-63

Hebbeln, D., Lamy, F., Mohtadi, M. & Echtler, H. (2007). Tracing the impact of glacial-interglacial climate variability on erosion of the southern Andes, *Geology, 35(2),* 131-134

Hebbeln, D., Marchant, M., Freudenthal, T. & Wefer, G. (2000). Surface sediment distribution along the Chilean continental slope related to upwelling and productivity, *Marine Geology, 164,* 119-137

Heimsath, A.M., Chappell, J., Dietrich, W.E., Nishiizumi, K. & Finkel, R.C. (2000). Soil production on a retreating escarpment in southeastern Australia, *Geology, 28,* 787-790

Heisinger, B., Lal, D., Jull, A.J.T., Kubik, P., Ivy-Ochs, S., Neumaier, S., Knie, K., Lazarev, V. & Nolte, E. (2002a). Production of selected cosmogenic radionuclides by muons: 1. Fast muons, *Earth & Planetary Science Letters, 200,* 345-355

Heisinger, B., Lal, D., Jull, A.J.T., Kubik, P., Ivy-Ochs, S., Knie, K. & Nolte, E. (2002b). Production of selected cosmogenic radionuclides by muons: 2. Capture of negative muons, *Earth & Planetary Science Letters, 200,* 357-369

Hervé, F., Faundez, V., Calderón, M., Massonne, H-J. & Willner, A.P. (2007). Metamorphic and plutonic basement complexes. In : Moreno, T. & Gibbons, W. (Eds.), *The Geology of Chile,* Geological Society, London, pp5-19

Heusser, C.J. (1983). Quaternary pollen record from Laguna de Tagua Tagua, Chile, *Science, 219,* 1429-1432

Heusser, C.J. (1990). Ice age vegetation and climate of subtropical Chile, *Palaeogeog, Palaeoclim, Palaeoecol, 80,* 107-172

Heusser, C.J., Lowell, T.V., Heusser, L.E., Hauser, A., Andersen, B.G. & Denton, G.H. (1996). Full-glacial-late-glacial palaeoclimate of the southern Andes: evidence from pollen, beetle and glacial records, *Journal of Quaternary Science, 11(3),* 173-184

Heusser, C.J., Lowell, T.V., Heusser, L.E., Moreira, A. & Moreira, S. (2000). Pollen sequence from the Chilean Lake District during the Llanquihue glaciation in marine Oxygen Isotope Stages 4-2, *Journal of Quaternary Science, 15(2),* 115-125

Heusser, L., Heusser, C., Mix, A. & McManus, J. (2006a). Chilean and Southeast Pacific palaeoclimate variations during the last glacial cycle: directly correlated pollen and O-18 records from ODP Site 1234, *Quaternary Science Reviews, 25,* 3404-3415

Heusser, L., Heusser, C. & Pisias, N. (2006b). Vegetation and climate dynamics of southern Chile during the past 50,000 years: results of ODP Site 1233 pollen analysis, *Quaternary Science Reviews, 25,* 474-485

Hewawasam, T., von Blanckenburg, F., Schaller, M. & Kubik, P. (2003). Increase of human over natural erosion rates in tropical highlands constrained by cosmogenic nuclides, *Geology, 31,* 597-600

Hijmans, R.J., Cameron, S.E., Parra, J.L., Jones, P.G. & Jarvis, A. (2005). Very high resolution interpolated climate surfaces for global land areas, *International Journal of Climatology, 25,* 1965-1978

Hinojosa, L.F., Armesto, J.J. & Villagran, C. (2006). Are Chilean coastal forests pre-Pleistocene relicts? Evidence from foliar physiognomy, palaeoclimate and phytogeography, *Journal of Biogeography, 33,* 331-341

Horton, R.E. (1932). Drainage basin characteristics, *Trans. Am. Geophysical Union, 13,* 350-361

Houston, J. & Hartley, A.J. (2003). The central Andean west-slope rainshadow and its potential contribution to the origin of hyper-aridity in the Atacama Desert, *Int J Climatol, 23,* 1453-1464

Hovius, N. (1996). Regular spacing of drainage outlets from linear mountain belts, *Basin Research, 8,* 29-44

Hsu, J.T., Leonard, E.M. & Wehmiller, J.F. (1989) Aminostratigraphy of Peruvian and Chilean Quaternary marine terraces, *Quaternary Science Reviews, 8,* 255-262

Hunt, A.G. & Wu, J.Q. (2004). Climatic influences on Holocene variations in soil erosion rates on a small hill in the Mojave Desert, *Geomorphology, 58,* 263-289

Imeson, A.C & Lavee, H. (1998). Soil erosion and climate change: the transect approach and the influence of scale, *Geomorphology, 23,* 219-227

Isacks, B.L. (1988). Uplift of the central Andean Plateau and bending of the Bolivian orocline, *Journal of Geophysical Research, 93,* 3211-3231

Istanbulluoglu, E. & Bras, R.L. (2006). On the dynamics of soil moisture, vegetation and erosion: Implications of climate variability and change, *Water Resources Research, 42,* W06418

Istanbullugoglu, E., Yetemen, O., Vivoni, E.R., Gutiérrez-Jurado, H.A. & Bras, R.L. (2008). Eco-geomorphic implications of hillslope aspect: Inferences from analysis of landscape morphology in central New Mexico, *Geophysical Research Letters, 35,* L14403

Ivanov, V.Y., Bras, R.L & Vivoni, E.R. (2008). Vegetation-hydrology dynamics in complex terrain of semiarid areas: 2. Energy-water controls of vegetation spatiotemporal dynamics and topographic niches of favorability, *Water Resources Research, 44,* W03430

Kefi, S., Rietkerk, M., Alados, C.L., Pueyo, Y., Papanastasis, V.P., ElAich, A. & de Ruiter, P.C. (2007). Spatial vegetation patterns and imminent desertification in Mediterranean arid ecosystems, *Nature, 449,* 213-217

Kirchner, J.W., Finkel, R.C., Riebe, C.S., Granger, D.E., Clayton, J.L., King, J.G. & Megahan, W.F. (2001). Mountain erosion over 10 yr, 10 kyr, and 10 Myr timescales, *Geology, 29(7),* 591-594

Kirkby, M. (1995). Modelling the links between vegetation and landforms, *Geomorphology, 13,* 319-335

Kohl, C.P. & Nishiizumi, K. (1992). Chemical isolation of quartz for measurement of in situ-produced cosmogenic nuclides, *Geochimica et Cosmochimica Acta, 56,* 3583-3587

Kukowski, N. & Oncken, O. (2006). Subduction erosion – the 'normal' mode of fore-arc material transfer along the Chilean margin? In: The Andes (Frontiers In Earth Sciences)

Lal, D. (1988). In situ-produced cosmogenic isotopes in terrestrial rocks, *Annual Review of Earth & Planetary Sciences, 16,* 355-388

Lal, D. (1991). Cosmic-ray labelling of erosion surfaces - Insitu nuclide production rates and erosion models, *Earth & Planetary Science Letters, 104(2-4),* 424-439

Lal. D. & Peters, B. (1967). Cosmic ray produced radioactivity on the earth. In: *Handbuch der Physick.* Berlin, Springer Verlag, 46, pp551-612

Lamb, S. & Davis, P. (2003). Cenozoic climate change as a possible cause for the rise of the Andes, *Nature, 425,* 792-797

Lamy, F., Hebbeln, D., Röhl, U. & Wefer, G. (2001). Holocene rainfall variability in southern Chile: a marine record of latitudinal shifts of the Southern Westerlies, *Earth and Planetary Science Letters, 185,* 369-382

Lamy, F., Hebbeln, D. & Wefer, G. (1998a). Terrigenous sediment supply along the Chilean continental margin: modern regional patterns of texture and composition, *Geologische Rundschau, 87,* 477-494

Lamy, F., Hebbeln, D. & Wefer, G. (1998b). Late Quaternary precessional cycles of terrigenous sediment input off the Norte Chico, Chile (27.5°S) and palaeoclimatic implications, *Palaeogeog, Palaeoclim, Palaeoecol., 141,* 233-251

Lamy, F., Hebbeln, D. & Wefer, G. (1999). High-resolution marine record of climatic change in mid-latitude Chile during the last 28,000 years based on terrigenous sediment parameters, *Quaternary Research, 51,* 83-93

Lamy, F., Klump, J., Hebbeln, D. & Wefer, G. (2000). Late Quaternary rapid climate change in northern Chile, *Terra Nova, 12(1),* 8-13

Langbein, W.B. & Schumm, S.A. (1958). Yield of sediment in relation to mean annual precipitation, *Eos Trans AGU, 39,* 1076

Larrain, H., Velasquez, F., Cereceda, P., Espejo, R., Pinto, R., Osses, P. & Schemenauer, R.S. (2002). Fog measurements at the site Falda Verde north of Chañaral compared with other fog stations of Chile, *Atmospheric Research, 64,* 273-284

Lavee, H., Imeson, A.C. & Sarah, P. (1998). The impact of climate change on geomorphology and desertification along a Mediterranean-arid transect, *Land Degradation & Development, 9,* 407-422

Leonard, E.M. & Wehmiller, J.F. (1992). Low uplift rates and terrace reoccupation inferred from mollusk aminostratigraphy, Coquimbo Bay, Chile, *Quaternary Research, 38(2),* 246-259

Leopold, L.B. & Langbein, W.B. (1962). The concept of entropy in landscape evolutions, *USGS Professional Paper, 500-A,* pp.20

Lifton, N.A., Bieber, J.W., Clem, J.M., Duldig, M.L., Evenson, P., Humble, J.E. & Pyle, R. (2005). Addressing solar modulation and long-term uncertainties in scaling secondary cosmic rays for in situ cosmogenic nuclide applications, *Earth & Planetary Science Letters, 239(1-2),* 140-161

Lonsdale (2005) Tectonophysics

Lucassen, F., Fowler, C.M.R. & Franz, G. (1996). Formation of magmatic crust at the Andean continental margin during early Mesozoic: a geological and thermal model of the North Chilean Coast Range, *Tectonophysics, 262,* 263-279

Ludwig, J.A., Tongway, D.J., Eager, R.W., Williams, R.J. & Cook, G.D. (1999). Fine-scale vegetation patches decline in size and cover with increasing rainfall in Australian savannas, *Landscape Ecology, 14,* 557-566

Maden, C., Anastasi, P.A.F., Dougans, A., Freeman, S.P.H.T., Kitchen, R., Klody, G., Schnabel, C., Sundquist, M., Vanner, K. & Xu, S. (2007). SUERC AMS ion detection, *Nuclear Instruments and Methods in Physics Research B, 259,* 131-139

Maldonado, A. & Villagran, C. (2002). Palaeoenvironmental changes in the semiarid coast of Chile (~32°S) during the last 6200 cal yr inferred from a swamp-forest pollen record, *Quaternary Research, 58,* 130-138

Maldonado, A. & Villagran, C. (2006). Climate variability over the last 9900 cal yr BP from a swamp forest pollen record along the semiarid coast of Chile, *Quaternary Research, 66,* 246-258

Manor, A. & Shnerb, N.M. (2008). Facilitation, competition and vegetation patchiness: From scale free distribution to patterns, *Journal of Theoretical Biology, 253,* 838-842

Markgraf, V. (1998). Past climates of South America, In: Climates of the Southern continents: Present, Past and Future, Hobbs, J.E., Lindesay, J.A. & Bridgman, H.A. (Eds), John Wiley & Sons Inc, pp107-134

Marquardt, C., Lavenu, A., Ortlieb, L., Godoy, E. & Comte, D. (2004). Coastal neotectonics in southern Central Andes: uplift and deformation of marine terraces in northern Chile (27°S), *Tectonophysics, 394,* 193-219

McElroy, B. & Wilkinson, B. (2005). Climatic control of continental physiography, *Journal of Geology, 113,* 47-58

Melnick, D. & Echtler, H.P. (2006). Inversion of forearc basins in south-central Chile caused by rapid glacial age trench fill, *Geology, 34,* 709-712

Miller, A. (1976). The climate of Chile, In: Schwerdtfeger (Ed.), World Survey of Climatology, vol. 12, Elsevier, Amsterdam, pp. 113-145

Milliman, J.D., Qin, Y.S., Ren, M.E. & Saito, Y. (1987). Mans influence on the erosion and transport of sediment by Asian rivers – the Yellow River (Huanghe) example, *Journal of Geology, 95,* 751-762

Mohtadi, M. & Hebbeln, D. (2004). Mechanisms and variations of the palaeoproductivity off northern Chile (24-33°S) during the last 40,000 years, *Palaeoceanography, 19,* PA2023

Molina, A., Govers, G., Poesen, J., Van Hemelryck, H., De Biévre, B. & Vanacker, V. (2008). Environmental factors controlling spatial variation in sediment yield in a central Andean mountain area, *Geomorphology, 98,* 176-186

Montgomery, D.R., Balco, G. & Willett, S.D. (2001). Climate, tectonics and the morphology of the Andes, *Geology, 29(7),* 579-582

Montgomery, D.R. & Brandon, M.T. (2002). Topographic controls on erosion rates in tectonically active mountain ranges, *Earth & Planetary Science Letters, 201,* 481-489

Montgomery, D.R. & Dietrich, W.E. (1992). Channel initiation and the problem of landscape scale, *Science, 255,* 695-702

Mortimer, C. (1973). The Cenozoic history of the southern Atacama Desert, Chile, *J. Geol. Soc London, 129,* 505-526

Mudd, S.M. & Furbish, D.J. (2007). Response of soil-mantled hillslopes to transient channel incision rates, *Journal of Geophysical Research, 112,* F03S18

Mulligan, M. (1998). Modelling the geomorphological impact of climatic variability and extreme events in a semiarid environment, *Geomorphology, 24,* 59-78

Muñoz, J.F., Fernandez, B., Varas, E., Pasten, P., Gomez, D., Rengifo, P., Muñoz, J., Atenas, M. & Jofre, J.C. (2007). Chilean water resources. In: Moreno, T. & Gibbons, W. (Eds.), *The Geology of Chile,* Geological Society, London, pp 215-230

Muzikar, P. (2008). Cosmogenic nuclide concentrations in episodically eroding surfaces: Theoretical results, *Geomorphology, 97,* 407-413

Muzikar, P. (2009). General models for episodic surface denudation and its measurement by cosmogenic nuclides, *Quaternary Geochronology, 4(1),* 50-55

Niedermann, S. (2002). Cosmic-ray-produced noble gases in terrestrial rocks: Dating tools for surface processes. In: Porcelli, D., Ballentine, C.J. & Wieler, R. (Eds.), *Noble Gases in Geochemistry & Cosmochemistry,* Mineralogical Society of America, pp 731-784

Niemi, N.A., Oskin, M., Burbank, D.W., Heimsath, A.M. & Gabet, E.J. (2005). Effects of bedrock landslides on cosmogenically determined erosion rates, *Earth & Planetary Science Letters, 237(3-4),* 480-498

Nishiizumi, K. (2002). 10Be, 26Al, 36Cl, and 41Ca AMS standards: abstract O16-1. In: *9th Conference on Accelerator Mass Spectrometry,* p. 130.

Nishiizumi, K., Kohl, C.P., Arnold, J.R., Klein, J., Fink, D. & Middleton, R. (1991). Cosmic-ray produced ^{10}Be and ^{26}Al in Antarctic rocks - exposure and erosion history, *Earth & Planetary Science Letters, 104,* 440-454

Nishiizumi, K., Winterer, E., Kohl, C., Klein, J., Middleton, R., Lal, D. & Arnold, J. (1989). Cosmic ray production rates of 26Al and 10Be in quartz from glacially polished rocks, *Journal of Geophysical Research, 94,* 17907-17915

Norton, K.P. & Vanacker, V. (2009). Effects of terrain smoothing on topographic shielding correction factors for cosmogenic nuclide-derived estimates of basin-averaged denudation rates, *Earth Surface Processes & Landforms, 34,* 145-154

Olson, D.M., Dinerstein, E., Wikramanayake, E.D., Burgess, N.D., Powell, G.V.N., Underwood, E.C., D'Amico, J.A., Itouha, I., Strand, H.E., Morrison, J.C., Loucks, C.J., Allnutt, T.F., Ricketts, T.H., Kura, Y., Lamoreux, J.F., Wettengel, W.W., Hedao, P. & Kassem, K.R. (2001). Terrestrial ecoregions of the world: A new map of life on Earth, *BioScience, 51(11),* 933-938

Ortlieb, L., Zazo, C., Goy, J.L., Hillaire-Marcel, C., Ghaleb, B. & Cournoyer, L. (1996). Coastal deformation and sea-level changes in the Northern Chile subduction area (23°S) during the last 330 kyr, *Quaternary Science Reviews, 15,* 819-831

Ouimet, W.B., Whipple, K.X. & Granger, D.E. (2009). Beyond threshold hillslopes: Channel adjustment to base-level fall in tectonically active mountain ranges, *Geology, 37,* 579-582

Pankhurst, R.J. & Hervé, F. (2007). Introduction and overview, In: Moreno, T. & Gibbons, W. (Eds.), *The Geology of Chile,* Geological Society, London, pp1-4.

Parsons, D.U. & Moldenke, A.R. (1975). Convergence in vegetation structure along analogous climatic gradients in California and Chile, *Ecology, 56(4),* 950-957

Perron, J.T., Dietrich, W.E. & Kirchner, J.W. (2008). Controls on the spacing of first order valleys, *Journal of Geophysical Research, 113,* F04016

Perron, J.T., Kirchner, J.W. & Dietrich, W.E. (2009). Formation of evenly spaced ridges and valleys, *Nature, 460,* 502-505

Pigati, J.S. & Lifton, N.A. (2004). Geomagnetic effects on time-integrated cosmogenic nuclide production with emphasis on in situ ^{14}C and ^{10}Be, *Earth & Planetary Science Letters, 226(1-2),* 193-205

Plug, L.J., Gosse, J.C., McIntosh, J.J. & Bigley, R. (2007). Attenuation of cosmic ray flux in temperate forest, *Journal of Geophysical Research, 112,* F02022

Puigdefábregas, J. (2005). The role of vegetation patterns in structuring runoff and sediment fluxes in drylands, *Earth Surface Processes and Landforms, 30,* 133-147

Quezada, J., Gonzalez, G., Dunai, T., Jensen, A. & Juez-Larre, J. (2007). Pleistocene littoral uplift on northern Chile: Ne-21 age of the upper marine terrace of Caldera-Bahia Inglesa area, *Rev Geol Chile, 34(1),* 81-96

Reinhardt, L.J., Hoey, T.B., Barrows, T.T., Dempster, T.J., Bishop, P. & Fifield, L.K. (2007). Interpreting erosion rates from cosmogenic radionuclide concentrations measured in rapidly eroding terrain, *Earth Surface Processes & Landforms, 32(3),* 390-406

Riebe, C.S., Kirchner, J.W., Granger, D.E. & Finkel, R.C. (2001). Minimal climatic control on erosion rates in the Sierra Nevada, California, *Geology, 29(5),* 447-450

Riebe, C.S., Kirchner, J.W. & Finkel, R.C. (2003). Long-term rates of chemical weathering and physical erosion from cosmogenic nuclides and geochemical mass balance, *Geochimica et Cosmochimica Acta, 67(22),* 4411-4427

Riebe, C.S., Kirchner, J.W. & Finkel, R.C. (2004a). Sharp decrease in long-term chemical weathering rates along an altitudinal transect, *Earth & Planetary Science Letters, 218,* 421-434

Riebe, C.S., Kirchner, J.W. & Finkel, R.C. (2004b). Erosional and climatic effects on long-term chemical weathering rates in granitic landscapes spanning diverse climatic regimes, *Earth & Planetary Science Letters, 224,* 547-562

Rietkerk, M., Boerlijst, M.C., van Langevelde, F., HilleRisLambers, R., van de Koppel, J., Kumar, L., Prins, H.H.T & de Roos, A.M. (2002). Self-organisation of vegetation in arid ecosystems, *The American Naturalist, 160(4),* 524-530

Rietkerk, M., Dekker, S.C., de Ruiter, P.C. & van de Koppel, J. (2004). Self-organised patchiness and catastrophic shifts in ecosystems, *Science, 305,* 1926-1929

Rietkerk, M. & van de Koppel, J. (1997). Alternate stable states and threshold effects in semiarid grazing systems, *Oikos, 79(1),* 69-76

Rinaldo, A., Dietrich, W.E., Rigon, R., Vogel, G.K. & Rodriguez-Iturbe, I. (1995). Geomorphological signatures of varying climate, *Nature, 374,* 632-635

Riquelme, R., Martinod, J., Herail, G., Darrozes, J. & Charrier, R. (2003). A geomorphological approach to determining the Neogene to Recent tectonic deformation in the Coastal Cordillera of northern Chile (Atacama), *Tectonophysics, 361,* 255-275

Roering, J.J., Kirchner, J.W. & Dietrich, W.E. (1999). Evidence for nonlinear, diffusive sediment transport on hillslopes and implications for landscape morphology, *Water Resources Research, 35,* 853-870

Roering, J.J., Perron, J.T. & Kirchner, J.W. (2007). Functional relationships between denudation and hillslope form and relief, *Earth & Planetary Science Letters, 264,* 245-258

Romero, O.E., Kim, J-H. & Hebbeln, D. (2006). Palaeoproductivity evolution off central Chile from the Last Glacial Maximum to the Early Holocene, *Quaternary Research, 65,* 519-525

Saillard, M., Hall, S.R., Audin, L., Farber, D.L., Herail, G., Martinod, J., Regard, V., Finkel, R.C. & Bondoux, F. (2009). Non-steady long-term uplift rates and Pleistocene marine terrace development along the Andean margin of Chile (31°S) inferred from Be-10 dating, *Earth & Planetary Science Letters, 277,* 50-63

Saunders, I. & Young, A. (1983). Rates of surface processes on slopes, slope retreat and denudation, *Earth Surface Processes and Landforms, 8,* 473-501

Scanlon, T.M., Caylor, K.K., Levin, S.A. & Rodriquez-Iturbe, I. (2007). Positive feedbacks promote power-law clustering of Kalahari vegetation, *Nature, 449,* 209-212

Schaller, M. & Ehlers, T.A. (2006). Limits to quantifying climate driven changes in denudation rates with cosmogenic radionuclides, *Earth & Planetary Science Letters, 248(1-2),* 153-167

Scheffer, M. & Carpenter, S.R. (2003). Catastrophic regime shifts in ecosystems: linking theory to observation, *Trends in Ecology and Evolution, 18(12),* 648-656

Scheffer, M., Carpenter, S., Foley, J.A., Folke, C. & Walker, B. (2001). Catastrophic shifts in ecosystems, *Nature, 413,* 591-596

Segerstrom, K. (1964). Quaternary geology of Chile: Brief outline, *Geol Soc Am Bull, 75,* 157-170

SERNAGEOMIN (2003). Mapa Geológico de Chile: versión digital. *Servicio Nacional de Geología y Minería, Publicación Geológica Digital,* No. 4 (CDROM, versión 1.0, 2003). Santiago.

Sherratt, J.A. & Lord. G.J. (2007). Nonlinear dynamics and pattern bifurcations in a model for vegetation stripes in semiarid environments, *Theoretical Population Biology, 71,* 1-11

Silver, P.G., Russo, R.M. & Lithgow-Bertelloni, C. (1998). Coupling of South American and African plate motion and plate deformation, *Science, 279,* 60-63

Simpson, G. & Schlunegger, F. (2003). Topographic evolution and morphology of surfaces evolving in response to coupled fluvial and hillslope sediment transport, *Journal of Geophysical Research, 108,* 2300

Small, E.E., Anderson, R.S. & Hancock, G.S. (1999). Estimates of the rate of regolith production using ^{10}Be and ^{26}Al from an alpine hillslope, *Geomorphology, 27(1-2),* 131-150

Smith, T. & Bretherton, F.P. (1972). Stability and the conservation of mass in drainage basin evolution, *Water Resources Research, 8,* 1507-1529

Sobolev, S.V. & Babeyko, A.Y. (2005). What drives orogeny in the Andes?, *Geology, 33,* 617-620

Sobolev et al (2006) In Andes: Active Subduction Erosion.

Speight, J.G. (1971). Log-normality of slope distributions, *Zeitschrift fur Geomorphologie, 15,* 290-311

Sterken, M., Verleyen, E., Sabbe, K., Terryn, G., Charlet, F., Bertrand, S., Boes, X., Fagel, N., De Batist, M. & Vyverman, W. (2008). Late Quaternary climatic changes in southern Chile, as recorded in a diatom sequence of Lago Puyehue (40°S), *Journal of Palaeolimnology, 39(2),* 219-235

Stone, J.O. (2000). Air pressure and cosmogenic isotope production, *Journal of Geophysical Research, 105 (B10),* 23753-23759

Stuut, J.B.W. & Lamy, F. (2004). Climate variability at the southern boundaries of the Namib (SW Africa) and Atacama (northern Chile) coastal deserts during the late 120kyr, *Quaternary Research,*

62, 301-309

Talling, P.J., Stewart, M.D., Stark, C.P., Gupta, S. & Vincent, S.. (1997). Regular drainage spacing of drainage outlets from linear fault blocks, *Basin Research,* 9, 275-302

Tarboton, D.G., Bras, R.L. & Rodriguez-Iturbe, I. (1992). A physical basis for drainage density, *Geomorphology, 5,* 59-76

Tongway, D.J. (1994). Small-scale resource heterogeneity in semiarid landscapes, *Pacific Conservation Biology, 1,* 201-208

Tosdal, R.M., Clark, A.H. & Farrar, E. (1984). Cenozoic polyphase landscape and tectonic evolution of the Cordillera Occidental, southernmost Peru, *Geological Society of America Bulletin, 95,* 1318-1332

Tucker, G.E. & Bras, R.L. (2000). A stochastic approach to modelling the role of rainfall variability in drainage basin evolution, *Water Resources Research, 36(7),* 1953-1964

Tucker, G.E., Catani, F., Rinaldo, A. & Bras, R.L. (2001). Statistical analysis of drainage density from digital terrain data, *Geomorphology, 36,* 187-202

Valero-Garces, B.L., Jenny, E., Rondanelli, M., Delgado-Huertas, A., Burns, S.J., Veit, H. & Moreno, A. (2005). Palaeohydrology of Laguna de Tagua Tagua and moisture fluctuations in central Chile for the last 46kyr, *Journal of Quaternary Science, 20,* 625-641

van de Koppel, J., Rietkerk, M. & Weissing, F.J. (1997). Catastrophic vegetation shifts and soil degradation in terrestrial grazing systems, *Trend in Ecology and Evolution, 12(9),* 352-356

Vanacker, V., von Blanckenburg, F., Govers, G., Molina, A., Poesen, J., Deckers, J. & Kubik, P. (2007). Restoring dense vegetation can slow mountain erosion to near natural benchmark levels, *Geology, 35(4),* 303-306

Veblen, T.T., Donoso, C., Schlegel, F.M. & Escobar, B. (1981). Forest dynamics in south-central Chile, *Journal of Biogeography, 8(3),* 211-247

Vico, G. & Porporato, A. (2009). Probabilistic description of topographic slope and aspect, *Journal of Geophysical Research, 114,* F01011

Villagran, C. & Varela, J. (1990). Palynological evidence for increased aridity on the central Chilean coast during the Holocene, *Quaternary Research, 34,* 198-207

Villa-Martinez, R., Villagran, C. & Jenny, B. (2003). The last 7500 cal yr BP of westerly rainfall in Central Chile inferred from a high-resolution pollen record from Laguna Aculeo (34°S), *Quaternary Research, 60,* 284-293

Villa-Martinez, R., Villagran, C. & Jenny, B. (2004). Pollen evidence for late-Holocene climatic variability at Laguna de Aculeo, Central Chile (lat. 34°S), *Holocene, 14(3),* 361-367

von Blanckenburg, F. (2005). The control mechanisms of erosion and weathering at basin scale from cosmogenic nuclides in river sediment, *Earth & Planetary Science Letters, 237(3-4),* 462-479

von Huene, R. & Ranero, C.R. (2003). Subduction erosion and basal friction along the sediment-starved convergent margin off Antofagasta, Chile, *J Geophys Res, 108(B2),* pp?

Walcott, R.C. & Summerfield, M.A. (2009). Universality and variability in basin outlet spacing: Implications for the two-dimensional form of drainage basins, *Basin Research, 21,* 147-155

Whipple, K.X. (2009). The influence of climate on the tectonic evolution of mountain belts, *Nature*

Geoscience, 2, 97-104

Whipple, K.L., Kirby, E. & Brocklehurst, S.H. (1999). Geomorphic limits to climate-induced increases in topographic relief, *Nature, 401,* 39-43

Wilkinson, M.T. & Humphreys, G.S. (2006). Slope aspect, slope length and slope inclination controls of shallow soils vegetated by sclerophyllous heath - links to long-term landscape evolution, *Geomorphology, 76,* 347-362

Wilson, L. (1973). Variations in mean annual sediment yield as a function of mean annual precipitation, *American Journal of Science, 273,* 335-349

Wolinsky, M.A. & Pratson, L.F. (2005). Constraints on landscape evolution from slope histograms, *Geology, 33,* 477-480

Yair, A. & Kossovsky, A. (2002). Climate and surface properties: hydrological response of small arid and semiarid watersheds, *Geomorphology, 42,* 43-57

Yokoyama, T., Makishima, A. & Nakamura, E. (1999). Evaluation of the coprecipitation of incompatible trace elements with fluoride during silicate rock dissolution by acid digestion, *Chemical Geology, 157,* 175-187

APPENDIX 1: CRN DATA

Sample name	Latitude [°S]	Longitude [°W]	Elevation, mean [m]	Shielding correction factor	10Be/9Be	+/- 1 σ	10Be [atoms/g]	+/- 1 σ [atoms/g]	erosion rate [m/Myr]	internal error [m/Myr]; +/-1σ	K-value, mean [m^2/yr]	K-value uncertainty + [m^2/yr]	K-value uncertainty - [m^2/yr]	Bare %	Herbaceous %	Trees %	Mean Precipitation [mm/yr]
LC07_01	32.99	71.42	271	0.994	4.18E-13	8.60E-15	1.75E+05	4.1E+03	26.50	0.60	5.51E-03	3.40E-03	1.43E-03	0	80	20	437
LC07_04	32.98	71.42	193	0.995	4.42E-13	2.40E-14	1.93E+05	1.1E+04	22.60	1.30	6.99E-03	4.98E-03	2.17E-03	0	69	31	437
LC07_06	32.98	71.42	238	0.986	3.83E-13	1.70E-14	1.76E+05	8.7E+03	25.50	1.30	4.13E-03	2.79E-03	1.21E-03	0	69	31	437
LC07_08	32.94	71.43	151	0.975	2.62E-13	6.40E-15	1.71E+05	4.8E+03	24.60	0.70	4.61E-03	2.89E-03	1.19E-03	3	79	18	437
LC07_10	33.01	71.44	338	0.956	2.87E-13	1.00E-14	1.37E+05	5.7E+03	34.70	1.40	5.81E-03	3.82E-03	1.58E-03	0	96	4	437
LC07_11	31.12	71.58	475	0.975	6.24E-13	1.70E-14	3.95E+05	1.2E+04	12.20	0.40	4.62E-03	2.50E-04	1.17E-03	4	77	19	168
LC07_15	31.12	71.56	530	0.966	8.04E-13	2.70E-14	3.64E+05	1.3E+04	13.70	0.50	4.40E-03	1.39E-03	1.13E-03	13	73	14	168
LC07_17	31.12	71.55	688	0.949	6.93E-13	1.80E-14	2.96E+05	8.5E+03	18.90	0.50	4.86E-03	1.46E-03	1.20E-03	28	66	6	168
LC07_19	30.55	71.63	551	0.978	7.48E-14	2.90E-15	9.55E+04	4.8E+03	56.90	2.90	1.58E-02	7.06E-03	6.56E-03	8	65	27	112
LC07_20	30.55	71.63	526	0.986	7.29E-14	2.80E-15	1.07E+05	5.3E+03	50.20	2.50	2.12E-02	9.72E-03	8.68E-03	27	65	8	112
LC07_21	29.62	71.20	801	0.989	2.47E-13	6.10E-15	2.99E+05	8.4E+03	20.30	0.60	3.77E-03	1.49E-03	1.08E-03	28	68	4	75
LC07_22	29.62	71.20	832	0.984	2.76E-13	6.60E-15	2.96E+05	8.0E+03	20.90	0.60	3.78E-03	1.49E-03	1.08E-03	28	68	4	75
LC07_24	29.62	71.20	713	0.977	1.52E-13	4.30E-15	3.30E+05	1.1E+04	17.10	0.60	3.46E-03	1.39E-03	1.02E-03	28	68	4	75
LC07_27	29.58	71.14	970	0.981	5.29E-13	1.30E-14	6.56E+05	1.8E+04	9.86	0.27	1.99E-03	7.92E-04	5.92E-04	27	70	3	67
LC07_29	29.57	71.16	859	0.894	3.84E-13	1.20E-14	3.76E+05	1.3E+04	15.30	0.50	1.87E-03	8.02E-04	5.36E-04	33	63	4	67
LC07_31	29.22	71.18	1011	0.966	8.70E-13	2.30E-14	4.24E+05	1.2E+04	15.90	0.50	2.65E-03	1.05E-03	7.72E-04	44	55	1	60
LC07_37	29.23	71.18	857	0.818	4.66E-13	1.00E-14	3.99E+05	1.0E+04	13.40	0.30	1.44E-03	5.77E-04	4.06E-04	54	46	0	60
LC07_39	28.41	71.05	720	0.989	1.51E-13	4.00E-15	6.06E+05	1.9E+04	8.87	0.27	1.55E-03	8.12E-04	6.28E-04	91	9	0	40
LC07_41	28.40	71.06	581	0.979	2.14E-13	5.40E-15	6.11E+05	1.8E+04	7.85	0.23	1.13E-03	5.95E-04	4.57E-04	99	0	1	40
LC07_43	28.39	71.07	482	0.998	1.79E-13	4.50E-15	5.03E+05	1.5E+04	9.21	0.27	1.46E-03	7.66E-04	5.88E-04	100	0	0	40
LC07_45	28.36	71.05	442	0.969	8.44E-14	3.30E-15	3.70E+05	1.8E+04	12.30	0.60	1.77E-03	9.85E-04	7.43E-04	100	0	0	40
LC07_47	26.57	70.44	941	0.980	1.54E-12	1.30E-14	2.55E+06	3.4E+04	1.92	0.03	2.10E-04	1.12E-04	8.67E-05	100	0	0	19
LC07_49	26.56	70.48	660	0.957	4.18E-12	4.10E-14	1.80E+06	2.5E+04	2.24	0.03	3.09E-04	1.63E-04	1.25E-04	100	0	0	19
LC07_51	26.56	70.51	640	0.985	4.33E-12	9.80E-14	1.83E+06	4.5E+04	2.23	0.06	3.84E-04	2.10E-04	1.58E-04	100	0	0	19
LC07_53	26.59	70.49	889	0.988	2.17E-12	4.20E-14	1.67E+06	3.6E+04	3.10	0.07	4.49E-04	2.35E-04	1.85E-04	100	0	0	18
LC07_55	26.57	70.56	511	0.984	1.41E-12	3.40E-14	7.77E+05	2.1E+04	5.56	0.15	8.71E-04	4.58E-04	3.50E-04	100	0	0	20
LC08_01	40.58	73.69	161	0.976	6.92E-13	9.90E-15	1.52E+05	2.7E+03	30.20	0.50	5.75E-03	2.03E-03	1.45E-03	0	23	77	1860
LC08_04	40.58	73.60	341	0.980	2.72E-13	9.40E-15	1.39E+0	5.4E+03	37.70	1.50	6.09E-03	2.33E-03	1.73E-03	0	24	76	2032
LC08_05	37.90	73.28	333	0.952	9.56E-14	2.90E-15	1.17E+05	5.2E+03	42.60	1.90	4.01E-03	1.62E-03	1.08E-03	0	20	80	1590
LC08_08	36.97	73.12	187	0.964	7.15E-14	2.50E-15	8.59E+04	4.8E+03	53.80	3.00	9.32E-03	5.15E-03	3.93E-03	0	25	75	1272
LC08_09	36.97	73.12	208	0.966	1.19E-13	3.60E-15	6.52E+04	2.6E+03	72.80	2.90	1.42E-02	7.29E-03	5.75E-03	0	24	76	1272
LC08_12	35.84	72.51	525	0.984	1.27E-12	2.90E-14	3.02E+05	7.6E+03	18.00	0.50	6.61E-03	2.54E-03	2.03E-03	0	34	66	920
LC08_13	35.86	72.48	558	0.970	6.59E-13	2.40E-14	1.52E+05	5.8E+03	37.60	1.40	1.16E-02	4.65E-03	3.71E-03	0	27	73	920
LC08_20	34.61	71.58	489	0.990	1.05E-13	4.30E-15	3.11E+05	1.5E+04	16.80	0.80	1.86E-03	1.25E-03	1.05E-03	1	96	3	733
LC08_22	33.88	71.50	213	0.994	4.96E-13	1.20E-14	2.02E+05	5.4E+03	21.90	0.60	6.53E-03	4.16E-03	1.63E-03	0	99	1	432
LC08_23	33.90	71.49	258	0.973	6.15E-13	1.50E-14	2.33E+05	6.1E+03	19.10	0.50	3.20E-03	2.06E-03	7.95E-04	0	98	2	432
LC08_27	32.94	71.42	215	0.996	2.63E-13	5.70E-15	1.59E+05	4.1E+03	28.20	0.70	5.33E-03	3.34E-03	1.35E-03	0	64	36	437
LC08_28	32.27	71.41	327	0.984	3.44E-13	9.50E-15	1.81E+05	5.5E+03	26.00	0.80	7.50E-03	3.96E-03	2.30E-03	5	69	26	294
LC08_29	32.27	71.40	303	0.983	5.43E-14	3.40E-15	1.73E+05	1.5E+04	26.90	2.30	7.27E-03	4.80E-03	2.78E-03	5	69	26	294
LC08_31	32.08	71.42	298	0.970	6.62E-14	3.60E-15	1.83E+05	1.3E+04	24.90	1.80	5.79E-03	3.59E-03	2.08E-03	2	77	21	264
LC08_33	31.56	71.42	253	0.975	1.67E-13	4.40E-15	3.79E+05	1.2E+04	10.90	0.40	6.14E-03	1.45E-03	1.66E-03	8	92	0	200
LC08_34	31.52	71.42	749	0.912	5.59E-13	1.10E-14	7.52E+05	1.7E+04	6.96	0.16	1.59E-03	3.57E-04	4.20E-04	10	79	11	200
LC08_35	30.52	71.66	433	0.985	4.06E-13	9.70E-15	1.83E+05	4.9E+03	27.00	0.70	7.12E-03	2.97E-03	2.80E-03	15	55	30	112
LC08_36	30.53	71.66	518	0.993	2.00E-13	6.10E-15	1.36E+05	4.7E+03	39.20	1.40	7.37E-03	3.17E-03	2.91E-03	21	75	4	112
LC08_37	30.55	71.62	611	0.963	1.41E-13	6.10E-15	1.64E+05	8.0E+03	33.50	1.60	8.38E-03	3.80E-03	3.50E-03	18	59	23	112
LC08_38	30.57	71.63	519	0.996	1.23E-13	4.90E-15	1.30E+05	6.1E+03	41.10	1.90	2.00E-02	9.30E-03	8.20E-03	26	69	5	112
LC08_39	29.65	71.11	1180	0.981	2.30E-13	6.60E-15	5.85E+05	1.9E+04	12.90	0.40	2.28E-03	9.44E-04	6.79E-04	85	15	0	72
LC08_40	29.67	71.16	967	0.983	9.61E-13	2.00E-14	7.21E+05	1.7E+04	8.91	0.21	1.93E-03	7.71E-04	5.63E-04	51	48	1	72

APPENDIX 2: DEM TILE DATA

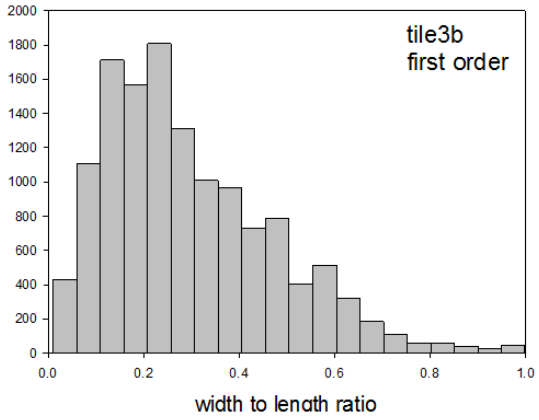
tile3b
first order
2000
1800
1600
1400
1200
1000
800
600
400
200
0
0.0
0.2
0.4
0.6
0.8
1.0
width to length ratio

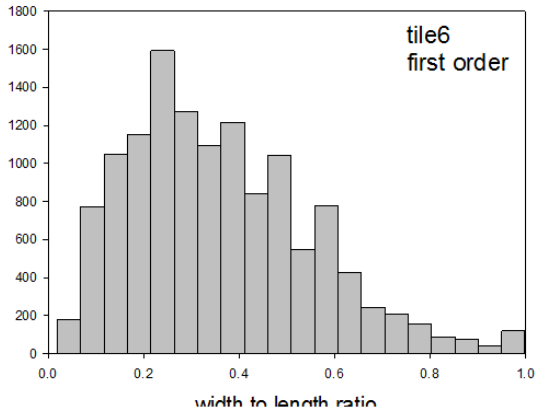
tile6
first order
1800
1600
1400
1200
1000
800
600
400
200
0
0.0
0.2
0.4
0.6
0.8
1.0

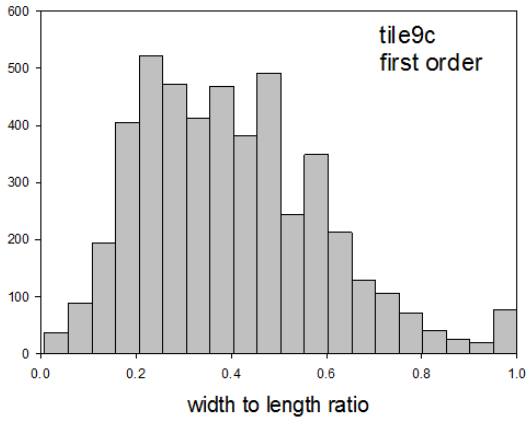
tile9c
first order
600
500
400
300
200
100
0
0.0
0.2
0.4
0.6
0.8
1.0
width to length ratio

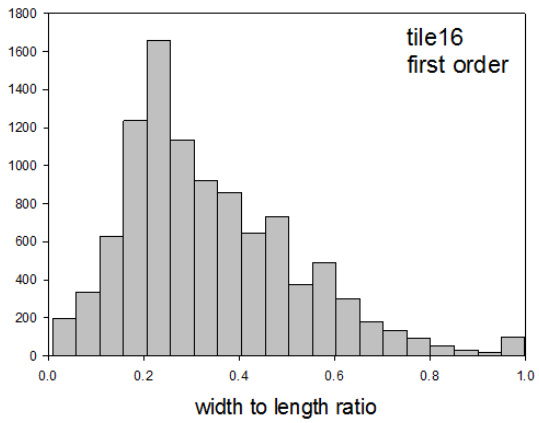
tile16
first order
1800
1600
1400
1200
1000
800
600
400
200
0
0.0
0.2
0.4
0.6
0.8
1.0
width to length ratio

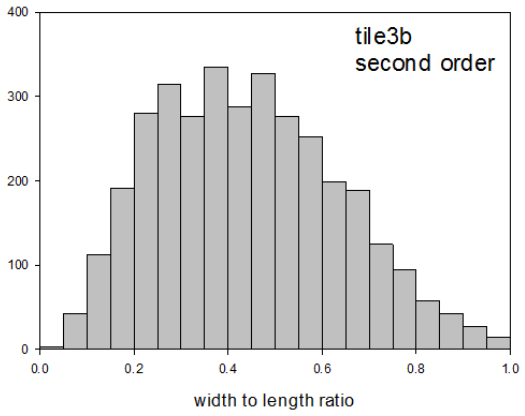
tile3b
second order
400
300
200
100
0
0.0
0.2
0.4
0.6
0.8
1.0
width to length ratio

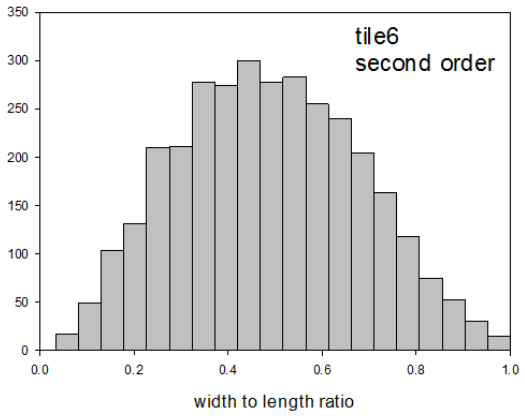
tile6
second order
350
300
250
200
150
100
50
0
0.0
0.2
0.4
0.6
0.8
1.0
width to length ratio

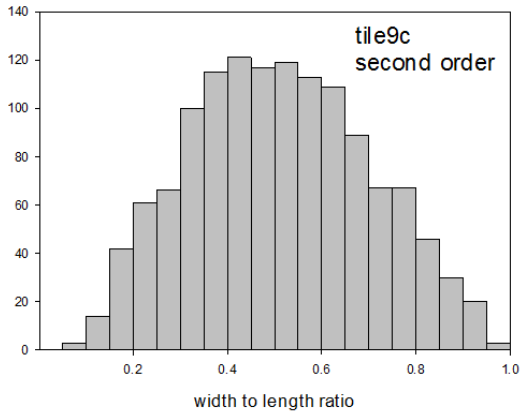
tile9c
second order
140
120
100
80
60
40
20
0
0.2
0.4
0.6
0.8
1.0
width to length ratio

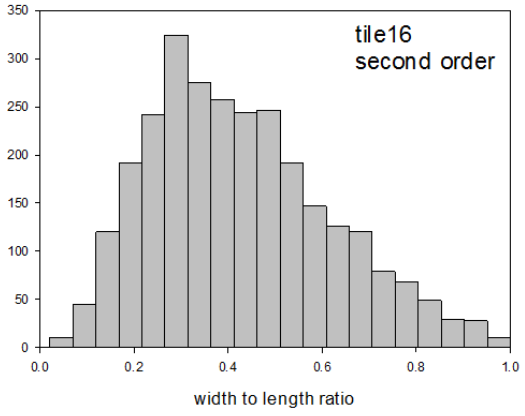
tile16
second order
350
300
250
200
150
100
50
0
0.0
0.2
0.4
0.6
0.8
1.0
width to length ratio

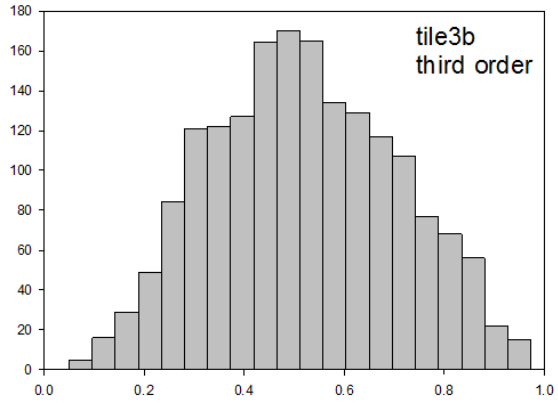
tile3b
third order
180
160
140
120
100
80
60
40
20
0
0.0
0.2
0.4
0.6
0.8
1.0

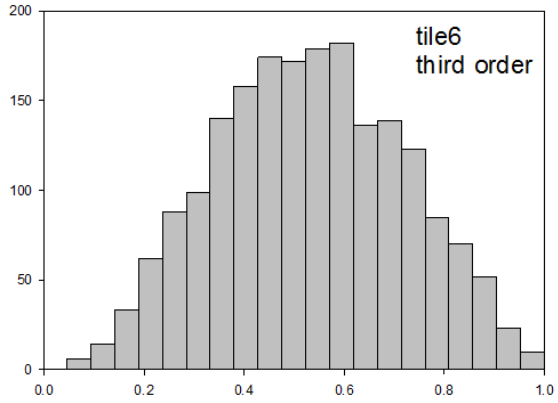
tile6
third order
200
150
100
50
0
0.0
0.2
0.4
0.6
0.8
1.0

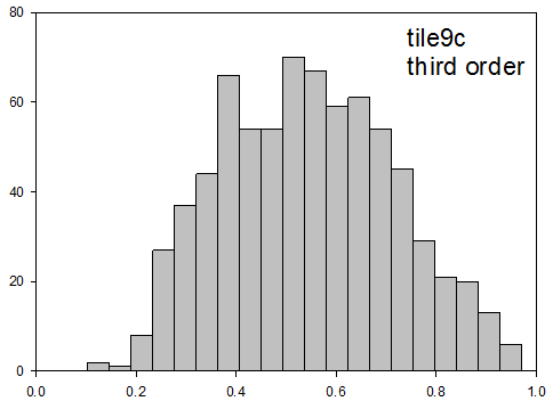
tile9c
third order
80
60
40
20
0
0.0
0.2
0.4
0.6
0.8
1.0

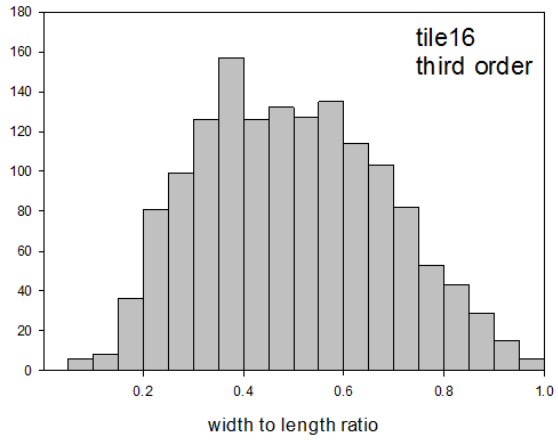
tile16
third order
180
160
140
120
100
80
60
40
20
0
0.2
0.4
0.6
0.8
1.0
width to length ratio

Tile	O1 median	25%	75%	O2 median	25%	75%	O3 median	25%	75%	O4 median	25%	75%
CHILD1	0.241	0.155	0.367	0.488	0.384	0.582	0.453	0.317	0.601	-	-	-
CHILD2	0.334	0.168	0.598	0.652	0.509	0.77	0.589	0.435	0.736	-	-	-
CHILD3	0.583	0.483	0.711	0.66	0.561	0.758	0.594	0.496	0.741	-	-	-
3b	0.256	0.16	0.405	0.43	0.287	0.58	0.512	0.384	0.654	0.496	0.376	0.625
4	0.289	0.187	0.448	0.457	0.333	0.582	0.496	0.363	0.644	0.48	0.368	0.624
5a	0.302	0.193	0.473	0.437	0.31	0.594	0.509	0.376	0.636	0.493	0.374	0.634
5b	0.243	0.156	0.369	0.397	0.269	0.553	0.5	0.364	0.645	0.473	0.347	0.622
6	0.333	0.218	0.492	0.481	0.341	0.627	0.53	0.398	0.671	0.5	0.367	0.64
7a	0.393	0.263	0.541	0.522	0.407	0.654	0.504	0.395	0.635	0.463	0.354	0.591
7b	0.403	0.268	0.548	0.532	0.418	0.666	0.5	0.392	0.631	0.451	0.36	0.575
8a	0.272	0.176	0.421	0.427	0.302	0.577	0.512	0.377	0.649	0.493	0.363	0.628
8b	0.405	0.252	0.577	0.522	0.395	0.652	0.566	0.448	0.687	0.555	0.434	0.676
9c	0.382	0.25	0.52	0.507	0.369	0.649	0.541	0.406	0.671	0.512	0.404	0.642
10a	0.252	0.16	0.394	0.392	0.262	0.523	0.466	0.325	0.627	0.498	0.375	0.627
11	0.28	0.192	0.428	0.418	0.296	0.588	0.497	0.368	0.645	0.477	0.365	0.604
12b	0.306	0.207	0.457	0.46	0.323	0.617	0.538	0.422	0.66	0.502	0.388	0.635
14	0.351	0.213	0.5	0.521	0.369	0.659	0.561	0.428	0.706	0.479	0.388	0.573
15	0.324	0.207	0.49	0.463	0.323	0.612	0.543	0.417	0.666	0.519	0.395	0.644
16	0.3	0.213	0.452	0.401	0.28	0.545	0.485	0.355	0.635	0.497	0.392	0.633

Tile	Mean Slope (degrees)	Median Slope (degrees)	Skewness
tile3b	12.954	12.673	0.167
tile4	11.754	12.194	-0.0309
tile5a	12.628	12.83	0.252
tile5b	19.701	19.95	-0.308
tile6	9.489	8.578	0.642
tile7a	14.36	14.567	-0.0275
tile7b	15.751	17.012	-0.381
tile8a	16.874	17.091	-0.0073
tile8b	8.237	7.093	1.175
tile9c	5.639	4.958	1.288
tile10a	13.111	13.195	0.0885
tile11	11.328	10.98	0.132
tile12b	10.134	9.997	0.284
tile14	9.902	9.619	0.269
tile15	14.274	13.744	0.383
tile16	12.071	11.923	0.343